TIME-EFFICIENT METHOD FOR MONITORING ELECTROCHEMICAL ENERGY CONVERSION DEVICES

Gjorgji Nusev

Doctoral Dissertation
Jožef Stefan International Postgraduate School
Ljubljana, Slovenia

Supervisor: Asst. Prof. Pavle Boškoski, Jožef Stefan International Postgraduate School and Jožef Stefan Institute, Ljubljana, Slovenia

Evaluation Board:
Prof. Dr. Đani Juričić, Chair, Jožef Stefan International Postgraduate School and Jožef Stefan Institute, Ljubljana, Slovenia
Dr. Jože Moškon, Member, National Institute of Chemistry, Ljubljana, Slovenia
Asst. Prof. Vanja Subotić, Member, Technical University of Graz, Graz, Austria

MEDNARODNA PODIPLOMSKA ŠOLA JOŽEFA STEFANA
JOŽEF STEFAN INTERNATIONAL POSTGRADUATE SCHOOL

Gjorgji Nusev

TIME-EFFICIENT METHOD FOR MONITORING ELECTROCHEMICAL ENERGY CONVERSION DEVICES

Doctoral Dissertation

ČASOVNO UČINKOVITA METODA ZA SPREMLJANJE ELEKTROKEMIJSKIH SISTEMOV ZA PRETVORBO ENERGIJE

Doktorska disertacija

Supervisor: Asst. Prof. Pavle Boškoski

Ljubljana, Slovenia, December 2021

To my wife, my brother, my parents and my family!

Acknowledgments

Everyone will say that earning a PhD degree is an individual job. That is partly true, because when you share and discuss your problems with your teammates, it is easier to find a solution than solving it all by yourself. So there are many people who have helped me get through these five long, sometimes exciting, sometimes tense years.

First and foremost, I would like to express my immense gratitude to my PhD supervisor, Assistant Professor Dr. Pavle Boškoski, for his patience and guidance through all the obstacles and difficulties during all these years. Without him, none of this would have been possible and I would not be where I am today. Also, I am very indebted to him for all the incredible opportunities he has given me and for his relentless optimism, which has greatly impacted my approach to both my career and my life. I am honoured to call him and his family my friends.

The second person to whom I would like to express my immense gratitude is Professor Dr. Đani Juričić for his support, enthusiasm, sharing his knowledge and ideas. He is a person whith whom you can have a conversation on any topic, not only in the field of science.

Furthermore, I would like to express my deepest gratitude to the members of the PhD committee, Assistant Professor Dr. Vanja Subotić and Dr. Jože Moškon, for their efforts, timely evaluation and for providing constructive comments that improved the quality of the dissertation. At the same time, I would like to thank my colleagues at the Department of Systems and Control who shared their ideas and thoughts, laughs and jokes, and enabled a relaxed working environment.

I would also like to acknowledge the support I received from Benjamin Königshofer and Michael Höber from TU Graz and Bertrand Morel from CEA. Without their expertise in conducting the experiments, this thesis would not have been possible. A special thanks goes to Mirko Ivančič from Amiteh d.o.o. who helped me with providing the right instruments to perform the experiments.

I would like to acknowledge the support of the Young Researchers Programme grant no. PR-07603, Research Programme P2-0001 of the Slovenian Research Agency, projects INSIGHT (grant agreement No. 735918), REACTT (grant agreement No. 101007175), RUBY (grant agreement No. 875047), MEMPHYS (grant agreement No 735533) which were part of Fuel Cells and Hydrogen 2 Joint Undertaking under the European Union's Horizon 2020 research and innovation programme, Hydrogen Europe and Hydrogen Europe research.

Next, I would like to thank my close friends, who helped me go through the overall PhD process and made it more enjoyable: Martin, Nikola, Aleksandar, Magdalena and Teo, Stevanče, Saško and Vera, Aleksandar and Simona, Rok, Petra and Oliver, Marija and Matjaž, my dearest friends from Sarma&Musaka facebook group Nikolče, Aco, Žuco, Ace, Dime i Jordan with their wives, Bašeto, Jošt, Rudi, Boco, Leon and many others.

Finally, this thesis would not have been possible without the closest ones, my parents Stojanče and Valentina, my brother Petar and especially my wife Anitafor for their uncon-

ditional support, encouragement and motivation. From the bottom of my hearth I would like to thank my wife Anita for believing in me and encouraging me that one day this will come to an end. Thank you very much for your motivation and for making me smile during the happiest and saddest times in the last 5 years. Also thank you very much for tolerating me. I love you very much.

Abstract

According to the EU's Green Deal plan, one of the main objectives for the EU is to become a net-zero greenhouse emission society by 2050. Achieving this goal requires advancements across many areas ranging from energy production, conversion, distribution and energy storage where the key role is taken by the electrochemical energy conversion devices (EECD). EECD is the umbrella notion for the family of the devices such as fuel cells, batteries, electrolysers, supercapacitors and hydrogen pumps. They share common fundamentals of electrochemical thermodynamics and kinetics but differ in the design and operational requirements since neither batteries, fuel cells nor other EECD can serve all applications alone. In the very nature of the EECD are complex electrochemical processes that are fundamental for their operation. On the other hand, they are the main source of the degradation that significantly affects their reliability and durability. Therefore, online health monitoring is being percepted as an indispensable integral part of the systems with EECD, which is expected to elevate their market deployment and economic exploitation.

Current state-of-the-art health monitoring approaches strongly build on electrochemical impedance spectroscopy (EIS). EIS contains the fingerprint of the dynamics of the EECD, which depends on physical and chemical processes inherent to the device. By definition, EIS is performed by perturbing EECD with mono-component, low-amplitude sinusoidal signals with the predefined frequencies. To ensure confident characterisation, the system under test has to comply with the conditions of stationarity, linearity and causality. However, as the perturbation times increase, load and environmental disturbances are more likely to cause distorting effects on the evaluation results, especially in the low-frequency region below 100 mHz. A way to alleviate the limitations of the conventional sine-based EIS is to employ broadband switching perturbation like discrete random binary sequence (DRBS). In that case all the frequencies from a wide band are excited at the same time. The approach is referred to as fast EIS method.

The aim of this dissertation is to revisit fast EIS and propose upgrade that will render the approach applicable for cost-effective in-field monitoring. The main contributions of the thesis are threefold.

First, the accuracy of the evaluated impedance spectrum is improved by applying continuous wavelet transform (CWT) with Morse mother wavelet. It is shown that at ultra-low frequencies ($<$ 1 mHz) Morse wavelet remains analytical, i.e. completely concentrated at positive frequencies despite its dispersion. That is essential for correct spectral decomposition and, consequently, correct impedance estimation. The said properties turned essential for accurate estimation of the state-of-health (SoH) and state-of-charge (SOC) of Li-ion batteries.

Second, a numerically efficient approach for the spectral deconvolution by means of the equivalent circuit model (ECM) and distribution of relaxation times (DRT) is proposed. By detecting changes in the resulting model parameters, one can track changes in the impedance spectrum and possibly identify the degradation mode. The demonstration on a case study with occasional fuel supply deficiency during solid oxide fuel cell (SOFC)

operation is performed.

Third, a concept of modular HW setup for performing EIS not only in the laboratory but also in the in-field applications is proposed. It relies on using commercially available low-cost components. The setup is rather general and applicable to a broad range of EECD. It enables the use of arbitrary excitation signals and provides great flexibility both in terms of power ranges and modes of operation.

Finally, the effectiveness of HW and algorithmic solutions is demonstrated through numerous accelerated and long-term experiments performed on various electrochemical energy devices, such as single cell SOFC, SOFC stack, single cell SOE, SOE stack, electrochemical hydrogen compressor, Li-ion battery, etc. During these experiments more than 5 TB of data was generated. Algorithms are implemented in a free open source format and made publicly available.

Povzetek

V skladu z načrtom zelenega dogovora je eden od glavnih ciljev EU postati družba z ničelnimi emisijami toplogrednih plinov do leta 2050. Za to je potreben napredek na številnih področjih, od proizvodnje energije, pretvorbe, distribucije do shranjevanja energije, pri čemer imajo eno izmed ključnih vlog naprave za elektrokemijsko pretvorbo energije (EECD, angl. electrochemical energy conversion devices). EECD predstavljajo najboljši način za reševanje problema z neskladnostjo proizvedene električne energije. Spadajo v družino naprav, kot so gorivne celice, baterije, elektrolizerji, superkondenzatorji in vodikove črpalke. Osnovni princip delovanja vseh EECD je podoben, vendar se razlikujejo v dizajnu in načinu delovanja. V sami naravi se dogajajo kompleksni elektrokemični procesi, ki predstavljajo osnovo za njihovo delovanje. Po drugi strani ti procesi predstavljajo glavni vir degradacije, ki vpliva na njihovo zanesljivost in trajnost. Nezaželeni degradacijski procesi igrajo pomembno vlogo in močno vplivajo na njihov način delovanja, tako da zmanjšajo njihovo učinkovitost ter skrajšajo njihovo življenjsko dobo. Zato je spremljanje teh degradacijskih procesov zelo pomembno.

Elektrokemijska impedančna spektroskopija (EIS, angl. electrochemical impedance spectroscopy) predstavlja enostavno in učinkovito in-situ metodo, ki se najbolj pogosto uporablja za spremljanje zdravja EECD v realnem času. Rezultat poda podrobno informacijo o dinamiki fizikalnih in kemijskih procesov, ki se pojavljajo v samih sistemih. Klasični način EIS temelji na enofrekvenčnem sinusnem vzbujanju s prej določenimi frekvencami, ki se zaporedno dodajajo na konstantno delovno točko. Težave nastopajo pri zagotavljanju pogojev stacionarnosti, linearnosti in kavzalnosti, ki zaradi kompleksnosti elektrokemičnih sistemov predstavlja najbolj zahtevno nalogo pri opravljanju EIS, še posebej za frekvence, nižje od 100 mHz. Pri nizkih frekvencah se z naraščajočim časom vzbujanja verjetnost, da bodo zunanje okoljske motnje vplivale na meritve, povečuje.

Uporaba širokopasovnih vzbujevalnih signalov, kot na primer diskretno naključno binarno zaporedje (DRBS, angl. discrete random binary sequence), predstavlja najboljši način, kako se izogniti omejitvam klasične EIS. Ta pristop se imenuje hitra EIS. Cilj te disertacije je ponovno pregledati metode hitre EIS in predlagati njeno nadgradnjo, ki bo omogočila pristop za učinkovitejšo spremljanje stanja EECD. V tej disertaciji sem predlagal tri različne izboljšave metode hitre EIS.

Prva izboljšava predstavlja implementacijo Mors valjčne funkcije v zvezni valjčni transformaciji (CWT, angl. continuous wavelet transform), ki omogoča natančno oceno impedance pri ultra nizkih frekvencah (<1 mHz). Dokazano je, da Mors valjčna funkcija ostane analitična tudi pri ultra nizkih frekvencah (<1 mHz). To pomeni, da je funkcija popolnoma koncentrirana pri pozitivnih frekvencah kljub svoji disperziji. To daje možnost natančne ocene zdravstvenega stanja (SOH, angl. state of health) in stanja napolnjenosti (SOC, angl. state of charge) Li-Ionske baterije.

Druga izboljšava predstavlja sledenj spremembam impedančnih krivulj preko kvantifikacije s pomočjo uporabe modela ekvivalentnega vezja (ECM, angl. equivalent circuit model) ali preko porazdelitvenih relaksacijskih časov (DRT, angl. distribution of relaxation

times). To ponuja možnost za pravočasno odkrivanje nezaželenega delovanja ali morebitnih degradacijskih procesov znotraj elektrokemičnih naprav za pretvorbo energije, kot na primer pomanjkljivosti v oskrbi z gorivom (angl. increased fuel utilisation).

Tretja izboljšava predstavlja izgradnjo modularne eksperimentalne proge, ki jo lahko uporabljamo za izvedbo hitre EIS z uporabo poljubnega signala za vzbujanje. Predlagana modularna proga je sestavljena iz komercialno dostopnih in cenovno učinkovitih komponent, ki zagotavljajo veliko prilagodljivost ne glede na vhodno/izhodno moč ter na način delovanja.

Učinkovitost zgornjih izboljšav sem dokazal preko številnih pospešenih in dolgotrajnih poskusov na različnih elektrokemičnih napravah, in sicer na: enoceličnem SOFC, SOFC skladih, enoceličnem SOE, SOE skladih, elektrokemičnem vodikovem kompresorju, Li-Ion bateriji itd., pri čemer smo pridobili in obdelali več kot 5 TB podatkov. Metode in kode za vsak zgoraj navedeni korak so javno dostopne.

Contents

List of Figures

List of Tables

List of Abbreviations

ADC	analogue-to-digital converter
ASR	area-specific resistance
BoP	balance-of-plant
CAES	compressed air energy storage
CLNS	complex nonlinear least square
CNLS	Complex Nonlinear Least Squares
CPE	constant phase element
CWT	continuous wavelet transform
DAQ	data acquisition
DRBS	discrete random binary sequence
DRT	distribution of relaxation times
DSS	decision support system
ECM	equivalent circuit model
EECD	electrochemical energy conversion devices
EHP	electrochemical hydrogen pump
EIS	electrochemical impedance spectroscopy
ESS	energy storage systems
FES	flywheel energy storage
FFT	Fast Fourier Transform
FOS	fractional order system
FRA	frequency response analysers
FU	fuel utilisation
IV	current-voltage
KK	Kramers-Kronig
KS	Kolmogorov-Smirnov
LTI	linear time-invariant
MCMC	Markov chain Monte Carlo
MRI	magnetic resonance imaging
OCV	open-circuit voltage
PDF	probability density function
PEM	proton exchange membrane
PHM	prognostics and health management
PHS	pumped hydroelectric storage
RBS	random binary sequence
rSOC	reverse solid oxide cells

RUL . . . . remaining useful life
SMES . . . superconducting magnetic energy storage
SMR . . . . steam methane reforming
SNG . . . . synthetic natural gas
SNR . . . . signal-to-noise ratio
SOC . . . . state-of-charge
SOE . . . . solid oxide electrolyser
SOFC . . . solid oxide fuel cell
SoH . . . . state-of-health
THDA . . . total harmonic distortion analysis
XAS . . . . X-ray absorption spectroscopy
YSZ . . . . Yttria-stabilised zirconia

Chapter 1

Introduction

The products of burning fossil fuels are considered to be the main root-cause for the environmental problems such as ozone layer depletion, acid rains, increased air pollution (PM10 and more harmful PM2.5 particles) and emission of greenhouse gases. As a consequence, the increased concentration of greenhouse gases is causing the global average temperature to rise. In order to limit the global warming trend, the Paris Agreement was signed by setting a global framework to keep the increase of the global average temperature well below 2.0 °C and to invest efforts to limit it to 1.5 °C by 2050.

To be in line with the Paris Climate Agreement and to become the first continent that is carbon neutral, EU member states have set a target to reduce the CO_2 emissions by 60 % by 2030 and become carbon neutral by 2050 [1], [2]. One way to achieve this is to increase energy production from low-carbon energy sources (wind, solar, hydro, etc.) [3]. Currently, there are many studies on whether a country's energy system can rely 100 % on renewable energy sources [4]–[8]. According to these studies, it seems that in the future, countries around the world will percept renewable energy as their main source of energy.

Renewables provide clean energy, but the problem is their weather reliance. This leads to fluctuating and intermittent power production that is inconsistent with the actual power demands. Therefore, there is an obvious need for energy storage systems capable to store the amounts of energy produced during times of surplus whilst being capable of instant on-demand delivery. Given the possibility to store the surplus energy enables the transition from centralised large energy production sites to the smaller, distributed grid-connected energy production sites. That would reduce losses in the transmission and distribution system, reduce environmental impact and, most importantly, increase the global efficiency of the entire energy production [9].

There are various energy storage systems (ESS) technologies for storing the surplus energy [10]–[12]. In recent years, batteries and hydrogen technologies moved into the focus of attention as main means of storage for renewable energies. The main reason is their high specific power and energy per unit weight (Figure 1.1), which allows them to be equally used both in power generation as well as mobility/transportation sector, without the need to make big changes in their design.

Although battery and hydrogen technologies are in the commercial use, their main weakness is related to the reliability and durability. For example, durability needs to be increased by a factor of five (at least 60000 hours for stationary applications) in order to present an alternative to the power generation technologies currently on the market [13]. The main problem with the durability are the degradation processes that occur inside the devices [14]. According to the standard EN 13306 [15], the degradation process is defined as: *"An irreversible process in one or more characteristics of an item with either time, use or an external cause"*.

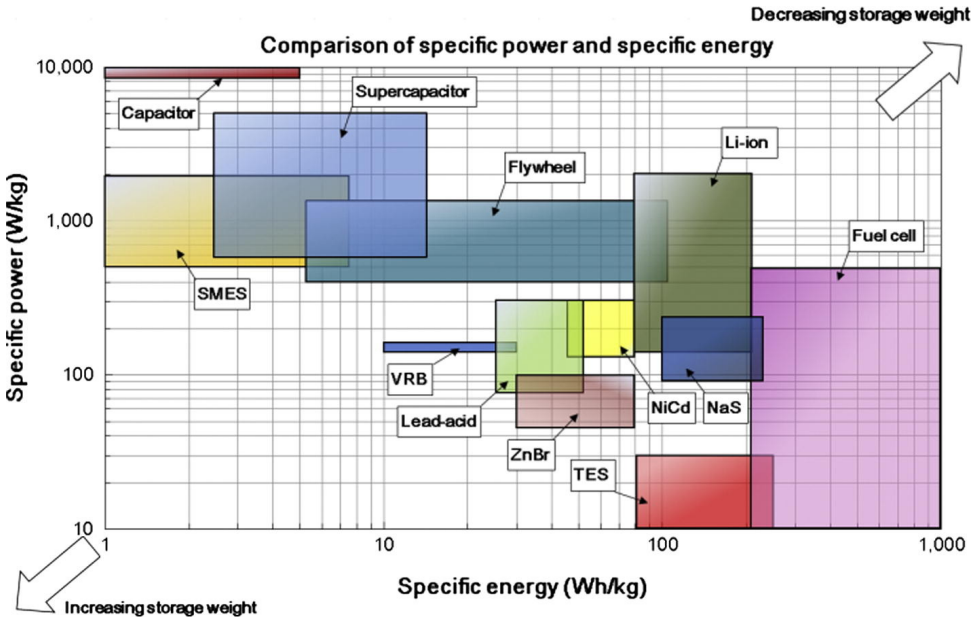

Figure 1.1: Specific energy and specific power comparison of different types of ESS technologies [12].

To increase the durability, two requirements have to be fulfilled. First, to monitor their operation, and second, to take corrective actions. The point of doing that is to detect undesirable health condition in the early stage so that there is enough room for executing adequate mitigation actions. That means to take either maintenance actions or accommodate the operating conditions in order to reduce the influence of the degradation.

1.1 Hydrogen Technologies

Hydrogen (H_2) is one of the most abundant elements in nature. It is also an energy-rich gas. So far, most of the hydrogen produced is used by industry, mainly for the production of fertilizers (ammonia) and in the metallurgical industry [16]. In the future, however, the market for hydrogen could grow strongly. This is because hydrogen is seen as a potential energy carrier for heating buildings and generating electricity. It is also expected to become an important fuel in the transportation sector [17], [18]. As a result, many analysts believe that hydrogen will replace oil as the primary source of energy and spark a whole new revolution.

Although hydrogen is the most abundant element in the universe, molecular hydrogen (H_2) is very rare in Earth's atmosphere (1 ppm by volume or less than 0.000055 % of atmospheric air). Most of the hydrogen on Earth is contained in water and other hydrocarbons. In order to use hydrogen as an energy source, it has to be separated from other elements in the molecules in which it is found. In other words, it has to be produced.

There are several methods for hydrogen production [19]. The most common one is *steam methane reforming (SMR)*. It is applied on industrial scale and it contributes more than 90 % of overall hydrogen production, of which 75 % is produced with natural gas. In this process, natural gas (methane) is pressurized and heated up to temperatures between 700 ºC and 1000 ºC in the presence of steam and nickel catalyst. The result of the endothermic reaction is carbon monoxide (CO) and hydrogen (H_2)

$$CH_4 + H_2O \longrightarrow CO + 3\,H_2.$$

Additional amounts of H_2 can be obtained in a reaction known as *water gas shift*, in which carbon monoxide reacts with water vapor to produce H_2

$$CO + H_2O \longrightarrow CO_2 + H_2.$$

Today, 6 % of natural gas is used to produce hydrogen. The major drawback of this process are its by-products (CO_2 and CO), which are released into the atmosphere as greenhouse gases. To produce 1 ton of hydrogen, 9-12 tons of CO_2 are released into the atmosphere. This type of hydrogen is called *grey* hydrogen. The average price for a kilogram of grey hydrogen is between 1.00 – 1.80 \$/kg [20].

If the produced CO_2 is captured, utilized and stored, it is called *blue* hydrogen. However, this process captures only about 80 % of the CO_2 produced. That figure can be increased up to 95 % by using a slightly more expensive process called autothermal reforming. As the greenhouse gases are captured, this contributes to the decarbonization of the planet. The average price of a kilogram of blue hydrogen is between 1.40 – 2.40 \$/kg [20].

These two types of hydrogen production (grey and blue) still release greenhouse gases and hence contribute to the global warming. However, in order to tackle the global temperature rise, there is a third option of hydrogen production known as *water electrolysis*, and the produced hydrogen is labelled as *green* hydrogen. This type of hydrogen is considered to play a major role in future energy production and decarbonisation of the planet.

1.1.1 Production of green hydrogen (storing energy)

Electrolysis is a process in which an electric current is used to split the water molecules (H_2O) to produce hydrogen. In this reaction there are no other by-products or emissions other than hydrogen and oxygen. This is only true if the electricity used for hydrogen production is coming from a renewable energy source (wind, solar, hydro, etc.). Otherwise, if the electricity is coming from fossil fuel power plants (coal, natural gas, and petroleum), the hydrogen produced is considered as grey or blue due to the indirect production of CO_2.

Currently, only 10 % of the world's hydrogen is produced by water electrolysis. That figure is likely to increase in the next decade due to rising obligations of the governments across the globe to reduce greenhouse gas emissions. On top of that, hydrogen generation sector is driven by the increased demand for long-term storage of renewable energy. For this reason, electrolysers are positioned high in this field. On a large commercial scale, this process can be referred to as *power-to-gas* [21]. That means the surplus of electrical energy can be efficiently stored for future usage.

Electrolysis is a process in which electric current is used to split water molecules (H_2O) into hydrogen and oxygen. The basic reaction of electrolysis is:

$$H_2O_{(\text{liquid})} + \underbrace{237.2\,\tfrac{\text{kJ}}{\text{mol}}}_{\text{electricity}} + \underbrace{48.6\,\tfrac{\text{kJ}}{\text{mol}}}_{\text{heat}} \longrightarrow H_2 + \tfrac{1}{2}O_2.$$

The produced hydrogen using this method can be of very high purity (> 99.999 %). There are three types of electrolysers currently in use [22]:

1. alkaline water electrolysers,
2. proton exchange membrane (PEM) electrolysers and
3. solid oxide electrolyser (SOE).

In this thesis, only SOE will be addressed.

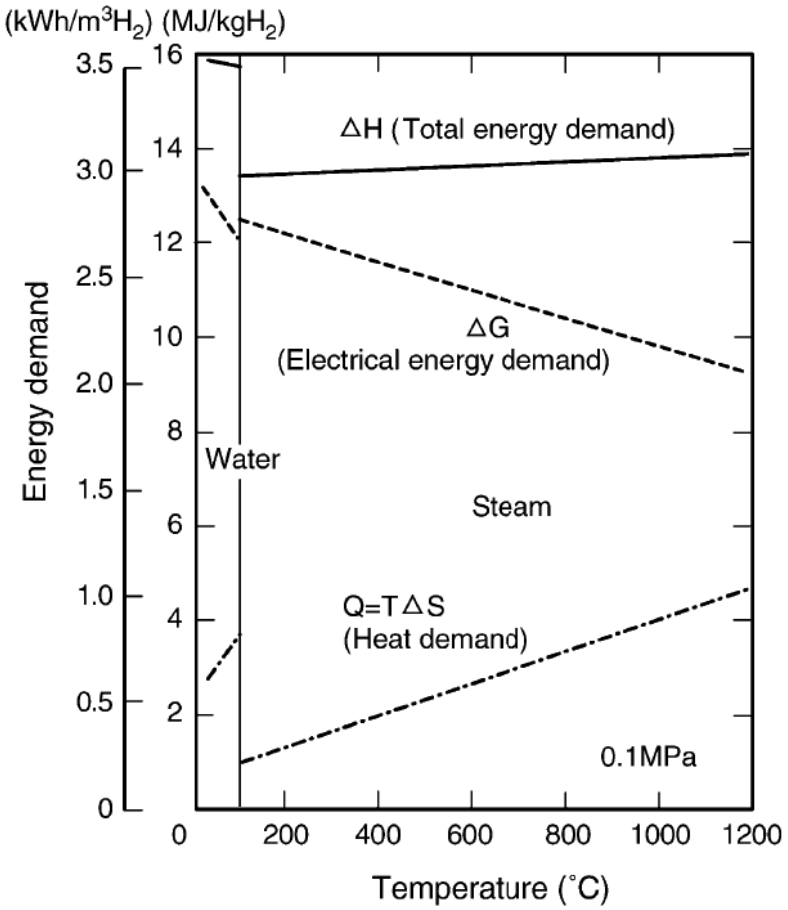

Figure 1.2: Energy demand for water and steam electrolysis [23].

Solid oxide electrolysers

SOE have attracted much attention due to their highly efficient conversion of electrical energy to the chemical energy while producing highly pure hydrogen. Figure 1.2 shows the energy demand for water and steam electrolysis. According to Hino *et al.* [23], the total energy demand (ΔH) for water and steam decomposition is the sum of Gibbs energy (ΔG) and heat energy (TΔS). The electrical energy demand ΔG decreases with increasing temperature as shown in Figure 1.2. The ratio of ΔG to ΔH is about 93% at 100 ºC and about 70% at 1000 ºC.

SOEs operate at high pressure and high temperatures around 500 – 850 ºC and use steam instead of liquid water. Due to the high operating temperatures, the electrolyte is made of Yttria-stabilised zirconia (YSZ), which is an excellent O^{2-} conductor. Its working principle is shown in Figure 1.3.

In SOE electrolysers, high-temperature steam is introduced at the cathode side, where it is split into hydrogen molecules (H_2) and oxygen ions

$$H_2O + 2\,e^- \longrightarrow H_2 + O^{2-}.$$

Since the YSZ electrolyte is ion conductive, the negative oxygen ions diffused to the anode side where they get oxidised. The free electrons are transported back to the cathode side by the external power supply, which is the driving force of the reaction. The chemical reaction that takes place on anode side is

$$O^{2-} \longrightarrow \tfrac{1}{2}O_2 + 2\,e^-.$$

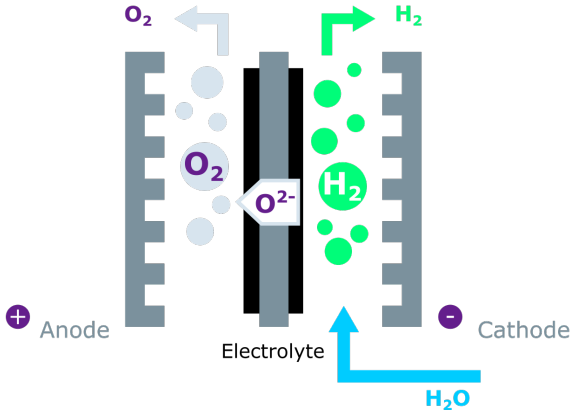

Figure 1.3: Working principle of SOE electrolyser.

Overall:

$$H_2O \longrightarrow H_2 + \frac{1}{2} O_2$$

The main advantage of the SOE electrolyser over the low-temperature electrolyser is high electrical efficiency, which can theoretically reach 100 % [23]–[25]. However, the major drawback of SOE electrolysers is the durability of the ceramic materials at high temperatures and long-term operation. It should be noted that the same stack can be used also in the fuel cell mode. In that case we are talking about reverse solid oxide cells (rSOC).

1.1.2 Gas to power (fuel cell)

Stored hydrogen can be later used in periods of high electricity demand to generate electricity. Similarly to the electrolysers, fuel cells are electrochemical devices that convert the energy of a fuel (hydrogen, natural gas, or other hydrocarbon-based fuels) directly into electricity. All fuel cells consist of an electrolyte layer in contact with an anode and a cathode on either side.

There are several types of fuel cells today [26]–[28], the most frequently used are

- Alkaline fuel cell (AFC);
- Phosphoric acid fuel cell (PAFC);
- Molten carbonate fuel cell (MCFC);
- Solid oxide fuel cell (SOFC) and
- Proton exchange membrane (PEM) fuel cell.

They differ in power output, operating temperature, electrical efficiency and type of fuel used. Each type of fuel cells has its own strengths and weaknesses, hence rendering it for a particular niche application. For example, PEM and SOFC fuel cells have the highest electrical efficiency, which makes them particularly attractive for automotive and stationary applications. Therefore, in this thesis, we will address only PEM and SOFC.

Low temperature PEM fuel cells

The excellent operating characteristics and compactness of low-temperature PEMfuel cells make them the most attractive candidate for the automotive industry. Currently, a number of forklifts are powered by PEM fuel cells, and this number will increase in the future.

The building blocks of PEM fuel cell are similar to that of the PEM electrolyser. The electrolyte is made of a Nafion and allows only protons to pass through it. The working principal of the PEM fuel cell is shown in Figure 1.4.

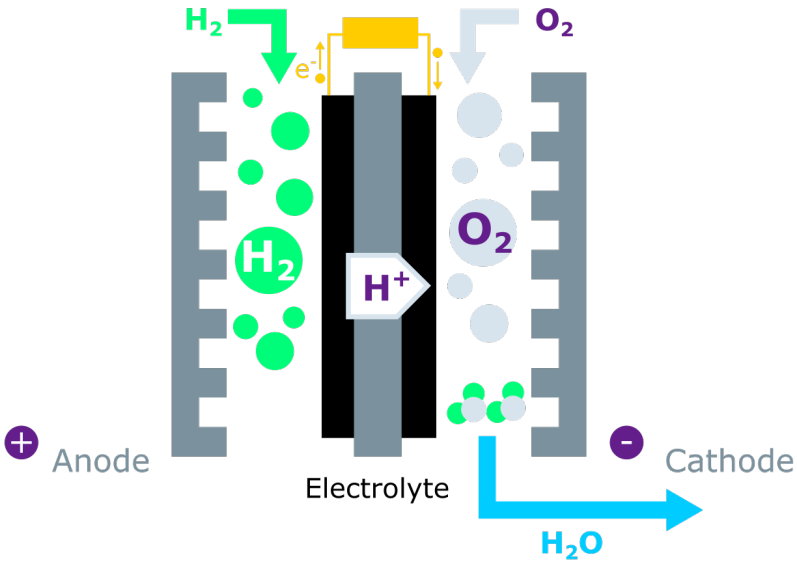

Figure 1.4: Working principle of PEM fuel cell.

At the anode side, hydrogen is oxidized and split into electrons and protons

$$\mathrm{H_2} \longrightarrow 2\,\mathrm{H^+} + 2\,\mathrm{e^-}.$$

Then the protons migrate through the electrolyte, which is conductive only for the protons, while the electrons are forced through the external circuit all the way to the cathode. On the cathode side, protons are recombined with electrons to form molecular hydrogen $\mathrm{H_2}$ which reacts with the oxygen. A product of this reaction is pure water. The chemical reaction at the cathode side reads

$$\mathrm{O_2} + 4\,\mathrm{H^+} + 4\,\mathrm{e^-} \longrightarrow 2\,\mathrm{H_2O}.$$

The overall reaction in the fuel cell can be written as

$$\mathrm{H_2} + \tfrac{1}{2}\mathrm{O_2} \longrightarrow \mathrm{H_2O} + \mathrm{W_{elec}} + \mathrm{Q_{heat}},$$

where W_{elec} is the produced electrical energy delivered to the load and Q_{heat} is the produced heat. Heat and water must be continuously removed in order to maintain the ideal working condition and to avoid unwanted failures of the components.

According to Sharaf *et al.* [13], the main advantages of PEM fuel cells are high power density, compact structure, rapid start-up due to low temperature operation (60 – 80 $^{\mathrm{o}}$C), excellent dynamic response, etc. However, the main drawbacks are: complex water and thermal management, low-grade heat, high sensitivity to contaminants (carbon monoxide CO and hydrogen sulphide $\mathrm{H_2S}$) and expensive catalyst (platinum).

High temperature solid oxide fuel cell (SOFC)

High temperature SOFC are considered as the prime candidate for stationary power generation. High temperature of (700 – 1000 $^{\mathrm{o}}$C) enables them to operate at high electrical

efficiency up to 80 % [29]. Additionally these temperatures allow operation with a variety of fuels, such as hydrogen, carbon monoxide, methane and other hydrocarbon fuels [30]–[32]. Moreover, the exhaust energy gives an opportunity to be used (recuperated) via e.g. gas turbine, or heat exchangers, thus ranging the overall efficiency of the SOFC system up to 90 % [33].

The structure of the SOFC is similar to that of the solid oxide electrolyser. High operating temperatures make YSZ electrolyte excellent O^{2-} conductor, while nickel-based electrodes act as an excellent catalyst material. The working principal of the SOFC is shown in Figure 1.5.

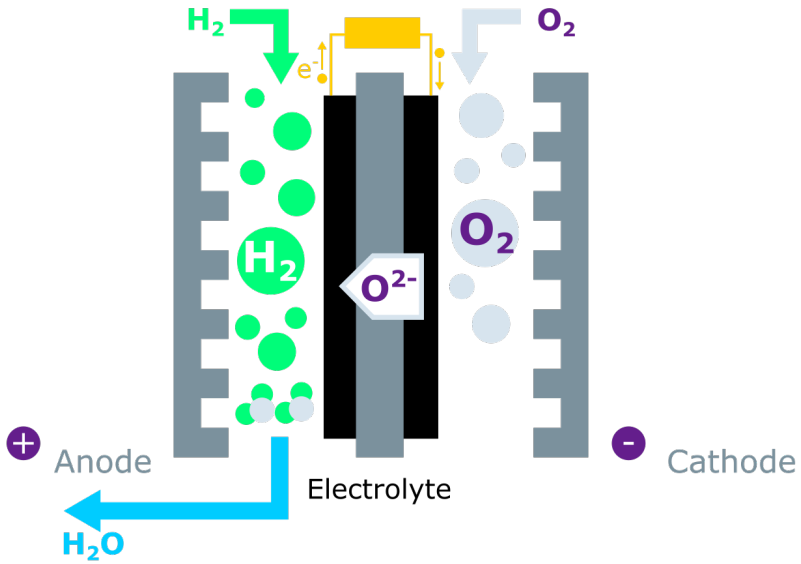

Figure 1.5: Working principle of SOFC fuel cell.

On the cathode side O^{2-} ions are formed by reduction

$$\tfrac{1}{2}O_2 + 2\,e^- \longrightarrow O^{2-}.$$

Since the YSZ electrolyte is ion conductive, negative O^{2-} ions are transported through the electrolyte to the anode site where they are oxidised. Molecular oxygen (O_2) then reacts with the hydrogen to form water

$$H_2 + O^{2-} \longrightarrow H_2O + 2\,e^-.$$

The main advantages are: high electrical efficiency, high tolerance to contaminants, fuel flexibility, inexpensive Ni catalyst, etc. However, the main drawbacks are: slow start-up, high thermal stresses, sealing issues, durability issues, etc.

1.2 Battery Technology

Batteries are electrochemical energy devices that can store chemical energy and convert it directly into electrical energy when needed. Unlike fuel cells, where power is generated from external fuel, the power from batteries is generated from the previously stored chemical energy. A typical battery cell consists of two electrodes (anode and cathode) separated by electrolyte, which can take solid, liquid or ropy/viscous state [34]. The two electrodes are compounded by materials having different electrochemical potentials that spontaneously

induce a redox reaction. This potentials difference generates current when connected to an external load. The desired battery voltage and current are achieved by electrically connecting the cells either in series or in parallel.

Nowadays, batteries are used in many different applications, ranging from transportation to power grid management. Compared to other types, Li-ion batteries exhibit the greatest potential due to high energy density and storage efficiency of 83 % [35].

A single lithium-ion cell consists of a cathode, an anode, an electrolyte, and a separator (Figure 1.6). The cathode of the lithium-ion battery is made of lithium metal oxide, such as lithium cobalt oxide ($LiCoO_2$), which is the main supplier of lithium ions. The anode, on the other hand, consists of lithium-carbon (graphite) compounds. The electrolyte serves only as a conductor for the positive lithium ions from the anode to the cathode and vice versa through the separator. Finally, the separator has the task of blocking the flow of electrons within the battery.

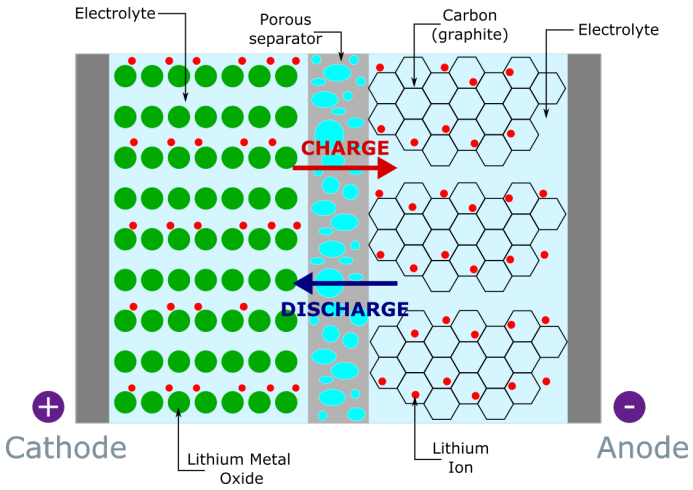

Figure 1.6: Working principle of a Lithium-ion battery.

The movement of lithium ions from anode to cathode creates free electrons. Therefore, the current flows from anode to the cathode via external load. When the battery is charging, the opposite happens. Lithium ions are released by the cathode and received by the anode. The basic chemical reactions occurring inside the lithium-ion battery for $LiCoO_2$ as positive electrode reads:

Cathode reaction :

$$LiCoO_2 \underset{\text{discharge}}{\overset{\text{charge}}{\rightleftharpoons}} CoO_2 + Li^+ + e^-,$$

Anode reaction:

$$C_6 + Li^+ + e^- \underset{\text{discharge}}{\overset{\text{charge}}{\rightleftharpoons}} LiC_6,$$

Overall:

$$LiCoO_2 + C_6 \underset{\text{discharge}}{\overset{\text{charge}}{\rightleftharpoons}} CoO_2 + LiC_6.$$

According to Amirante *et al.* [9], the main advantages of lithium-ion batteries are: high energy density (160 – 200 Wh/kg), potential for yet higher capacities, fast response time (milliseconds), low self-discharge rate and high efficiency. However, the main drawbacks include requirement for external circuit to maintain voltage and current within the safe limits and high temperature dependency.

1.3 Common Features of Electrochemical Energy Conversion Devices (EECD)

Although the construction and operating principles of EECD differ, the underlying electrochemical processes share a great deal of similarity. During energy conversion, numerous sub-processes associated with diffusion, ion and electron transport, redox reactions and other processes take place. They span from ultra low frequencies (<1 mHz) to ultra high frequencies (>1 MHz). During operation, undesirable internal degradation processes may evolve, leading to the reduction in EECD performance. In turn that leads to a reduced state-of-health (SoH) and hence, reduction of the remaining useful life (RUL) [36]–[40]. Since all of these processes occur at the molecular level, the main question is *how can the degradation processes be inferred on the macroscopic (or system) level non-invasively, i.e. without intruding the structure?*

For the sake of high efficiency and low operating costs, in situ/operando monitoring of EECD turns out to be of utmost importance. There are multiple in situ characterization techniques such as magnetic resonance imaging (MRI) [41], [42] and X-ray absorption spectroscopy (XAS) [43], however due to the complexity and price of the equipment they cannot be used to perform on site monitoring on a mass scale. The simplest and the most cost-efficient methods for performing real-time monitoring rely on electrochemical techniques such as analysis of polarisation curves and EIS. Polarisation curve represents the steady-state relationship between current and voltage, without giving any information about the dynamic characteristics of the system. In contrast, EIS represents a linear dynamic method that provides information about the dynamics of the physical and chemical processes occurring inside the EECDs.

By performing EIS, it is possible to cover the whole frequency spectra of interest, obtain information about the main processes occurring inside the EECD under test, and possibility to detect unwanted degradation phenomena as illustrated in Figure 1.7. Therefore the EIS spectrum represents a common feature for condition monitoring and prognostics and health management (PHM) of EECD.

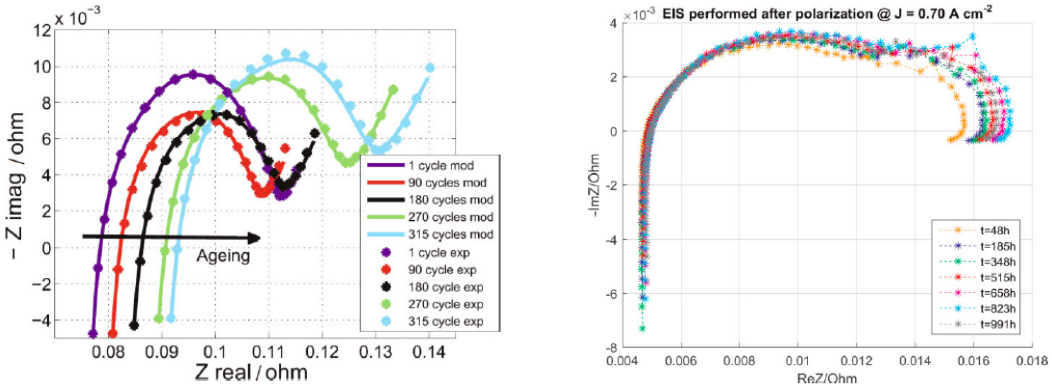

(a) (b)

Figure 1.7: Effect of ageing on the EIS spectrum on (a) Li-ion battery and (b) PEM fuel cell [44]. Visible changes in EIS associated with change in the internal health can be observed.

1.4 Dissertation in the Context of PHM

Prognostics and health management (PHM) represents a general framework focused on performing health monitoring of technical systems, prognostics of their remaining operational life and designing the mitigation actions [45]. The general concept is depicted in Figure 1.8.

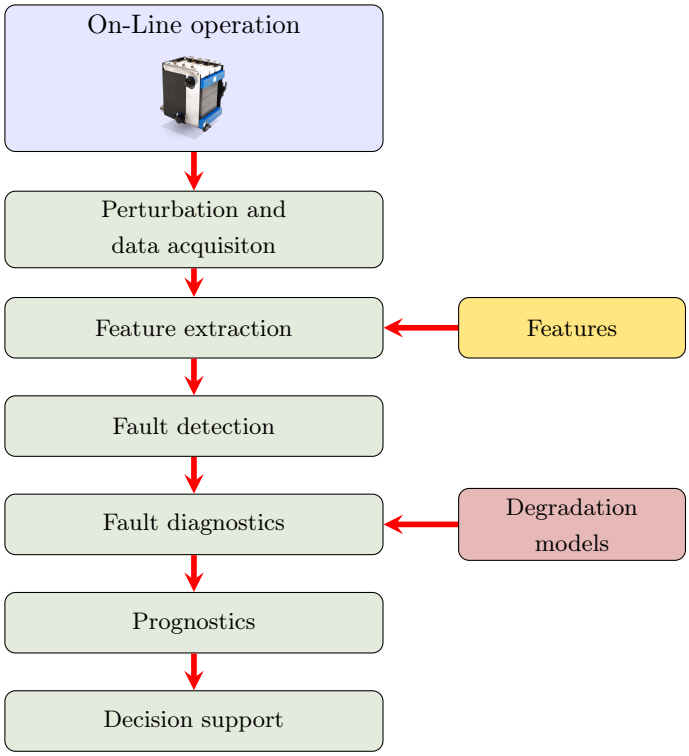

Figure 1.8: General concept of prognostics and health management (PHM) of technical systems slightly accommodated for EECD.

To perform PHM, the system design partly requires substantial off-line experimental data and models built thereupon. These models are normally very detailed. They are aimed to analyse important issues related to the conditions leading to degradation, the evolution of degradation and impact on reliability. The same data sets and models are important in devising models for support in online processing. The main steps of PHM system are briefly reviewed in the sequel.

Perturbation and data acquisition

Characterisation of EECD or any devices in general requires an external perturbation signal to obtain its response. This dissertation will largely exploit the potential of unconventional DRBS perturbation instead of the classical mono-component sinusoidal perturbation. The advantages are twofold. First, from the electronics point of view the excitation circuit is much simpler than the one required for generation of the sinusoidal waveforms. Consequently, such a module is cost-effective and relatively easy to build. At the same time, the quality of the perturbation signals is comparable with those in the commercially available laboratory equipment. Second, due to its broad-band frequency content, shorter perturbation times may suffice for full characterisation of an EECD.

Feature extraction

Feature extraction is a procedure aimed to unfold information out of the measured signals. It is usually performed by various signal processing techniques. The result are features, which, ideally, depend only on the system internal health condition and are independent of the external and operating conditions. Hence the pattern of the features in the features space represents the fingerprint of the system degradation modes and fault modes.

In this thesis, the features are acquired by applying the wavelet transform using the recently developed Morse wavelet [46], [47]. Compared to the other wavelets, Morse wavelet has superior accuracy even at ultra-low frequencies (<100 mHz) without losing its analytical properties. Unlike the current state-of-the-art techniques that usually provide only a dozen of points per decade, the result of this approach is an impedance spectrum (Nyquist curve) calculated with almost continuous frequency resolution without the need for additional excitation cycles. This greatly reduces the excitation time while, at the same time, improving the quality of the results.

Fault detection

Basically, it performs analysis of change in the feature space by comparing the actual feature pattern with the reference one. Reference patterns can be structured in terms of models or be available in the data format. Typically, one or more faults in the EECD under test will result in a change of the feature pattern.

Fault diagnostics

Diagnostics represents a process of isolating the source (cause) of the fault. That means pointing out the root-cause of the fault. To do so, a sort of fault-symptom model is needed. Such a model can be obtained by analysing the causal relationship between faults and features of classification techniques applied to the available data records.

Prognostics

The anticipated evolution of the system condition is evaluated and the remaining useful life (RUL) is estimated. Information from reliability models or other priors on hidden degradation processes can be used to predict the future condition of the monitored system, subsystem or component. The goal is to infer how long the EECD can continue operating even in the presence of a degradation trend due to the previously detected fault.

Decision support

As soon as fault condition is inferred and the RUL anticipated, alerts to the operators should be triggered along with the suggested corrective and maintenance to take.

1.5 The purpose of the Dissertation

The main purpose of this thesis is to contribute to the first three components as presented in Figure 1.8, in particular the perturbation and data acquisition, feature extraction and the fault detection step. In the conventional PHM, system perturbation as an accompanying step in the data acquisition is not particularly addressed. In this thesis, a strong emphasis will be on a novel way of perturbation for the sake of quality feature extraction.

The classical approach relies on superimposing a mono-component sinusoidal perturbation signal to a constant operating point (DC). The amplitude of the signal has to be

small so that the perturbation remains in the linear range, but still large enough to ensure a suitable output signal-to-noise ratio. By changing the frequency of the perturbation signal, the impedance is measured over a selected set of frequencies. The most challenging task of performing EIS on EECDs is satisfying the conditions of linearity, causality, and stability. This is especially true at low frequencies (<100 mHz), since perturbation times might be of order of an hour. Therefore, during this time, the chances for environmental disturbances to corrupt the measurement increase with increasing perturbation time.

A way to solve this issue is by using broad-band stochastic perturbation signals [40], [48]–[51]. There are several publications that provide solutions to this question [48], [49], [52]. However, some accuracy issues at ultra low frequencies occur. Furthermore, the possibility of using dedicated and cost-effective perturbation circuit has been neglected. Finally, to show the broad applicability of this idea, the complete concept has to be evaluated over a wide variety of EECD.

1.6 Goals

The ambition of the dissertation is to develop a method and apparatus that will improve the process of on-line in-operando characterisation of EECD. The goals are the following:

- Cost-efficient perturbation circuit enabling broad frequency excitation;
- Increase by an order of magnitude the frequency resolution of EIS spectra compared to the mono-component sinusoidal based EIS approaches;
- Achieving accurate lowest observable frequency down in the mHz range;
- Detection of fuel starvation at SOFC;
- Estimate the uncertainties of inferred EIS characteristics; That is completely neglected by the researchers in the field.

Due to the novel perturbation and signal processing approaches, it is impossible to use equipment produced by the established manufacturers in the field of electrochemical impedance spectroscopy. Consequently, new perturbation and data acquisition infrastructure should be devised for use in long-term run-to-failure experiments. It has to be capable to cope with large amounts of data, typically several TBytes monthly. Furthermore, the infrastructure has to be cost-effective and provide a similar quality of signals as the laboratory-scale equipment.

Besides the methodological development, a strong additional goal is to evaluate the proposed method and apparatus on different families of electrochemical energy systems such as: PEM fuel cells, SOFC, SOE, lithium-ion battery and supercapacitors.

1.7 Hypotheses

The thesis is based on the following hypotheses:

Hypothesis 1. The quality of impedance spectra obtained by broad-band DRBS excitations is comparable with the those obtained using commercially available state-of-the-art laboratory equipment.

Hypothesis 2. By using DRBS perturbation signal together with the Morse mother wavelet, the number of frequency points at which the impedance is calculated can be significantly increased without extending the measurement time.

Hypothesis 3. Changes in the internal condition of the EECD can be associated with the characteristic changes in the parameters of the equivalent circuit model (ECM).

1.8 Scientific Contribution

The contributions of this thesis are the following:

- It is shown that broadband perturbation signal such as DRBS results in almost continuous frequency resolution of the evaluated spectra, without the need of increasing the measurement perturbation time. The number of frequency points is limited only by the number of samples in the signal.
- Implementation of the Morse wavelet for accurate evaluation of the impedance spectra at ultra-low frequencies (<1 mHz).
- Estimation of the impedance uncertainty at each frequency point in order to ensure the validity of the measurements.
- Associating qualitative changes in the internal condition with quantitative changes in the ECM parameters. The possibility of the approach to detect issues in fuel supply is demonstrated on real data. However, it seems the unambiguous isolation is not possible in that case since different faults exhibit similar configurations of the features.
- A modular experimental setup which consists of commercially available and cost effective components. It is capable of performing EIS by using arbitrary excitation signals. This contributes to a great flexibility both in terms of power ranges and modes of operation.

1.9 Structure of the Thesis

The remainder of the thesis is organised as follows.

Chapter 2 first describes the basics of performing EIS. That is followed by the description of a method for fast EIS based on unconventional DRBS excitation. The basics for wavelet transform for processing current and voltage signals are also presented. In the second part of the chapter, the practical aspects of performing EIS are discussed. In the last part of the chapter, different architectures for EIS on different EECD are presented.

Chapter 3 gives a detailed presentation of the fast EIS, with the focus on ultra-low frequencies. The advantages of using Morse mother wavelet over the other complex mother wavelets are explained.

Chapter 4 presents different methods for feature extraction from measured impedance spectra, which are used to perform condition monitoring on various EECDs.

And finally, Chapter 5 summarises the thesis and provides directions for future work.

Chapter 2

Electrochemical Impedance Spectroscopy (EIS)

EIS is a nondestructive characterisation technique widely used in the fields of electrochemistry [53] like batteries [54], fuel-cells [55], electrolysers [56], materials [57], etc. The result of EIS is system impedance (system transfer function), which carries the information about the internal health of the system under test. Quality EIS evaluation requires good data acquisition system, precise signal generators, low-noise sensors and effective signal processing techniques. Each of these segments is addressed in the remainder of this chapter.

2.1 The Definition of Electrical Impedance

The impedance $Z(\omega)$ of a linear electrical circuit is defined as the ratio between Fourier transforms of the voltage $u(t)$ and the current $i(t)$

$$\begin{aligned} Z(j\omega) &= \frac{\mathcal{F}\{u(t)\}}{\mathcal{F}\{i(t)\}} = \frac{\mathcal{F}\{U_0 \sin(\omega t)\}}{\mathcal{F}\{I_0 \sin(\omega t + \varphi)\}} = \frac{U_0 e^{j\omega t}}{I_0 e^{j(\omega t+\varphi)}} = Z_0 e^{j\varphi} \\ &= Z_0 \cos(\varphi) + j Z_0 \sin(\varphi) = Z' + jZ''. \end{aligned} \tag{2.1}$$

where U_0 and I_0 represent the amplitudes of voltage and current signal respectively, ω represents the angular frequency of excitation and φ represents the phase shift. The concept is illustrated in Figure 2.1.

The impedance spectra is divided into two main components: **resistance**, which represents the real part of the impedance and is denoted as Z' (2.1) in the electorhemical books and **reactance**, which represents the imaginary part of the impedance (Z''). The measuring unit of impedance is in Ohms [Ω].

2.1.1 Graphical representation of impedance

Since the result of the impedance measurement is a frequency-dependent complex function, it is usually visualised in either a **Nyquist plot** (Figure 2.2a), in which the real and imaginary part of the impedance are plotted, or a **Bode plot** (Figure 2.2b) in which the phase and the magnitude (or the real and imaginary parts of the impedance) are plotted versus the logarithm of the frequency.

2.1.2 Classical impedance spectroscopy

Classical method for performing impedance spectroscopy includes mono-component sinusoidal excitation signals. In order to cover the whole impedance spectrum of interest of

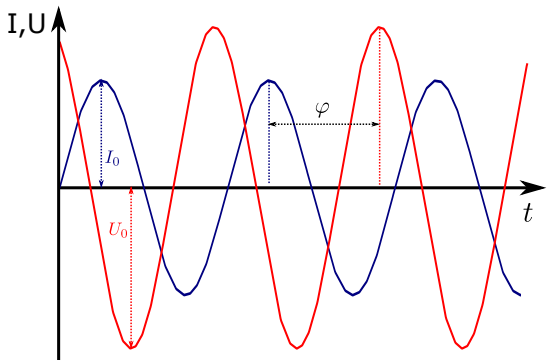

Figure 2.1: Sinusoidal current signal $i(t)$, corresponding voltage response $u(t)$, and phase shift φ.

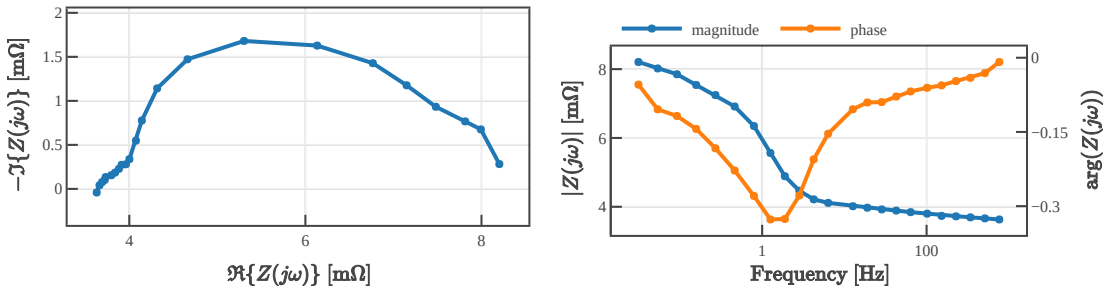

(a) (b)

Figure 2.2: Different representations of EIS spectra: (a) Nyquist plot and (b) Bode plot.

the system under test, it has to be excited at multiple predefined frequencies.

The impedance of the system under test is calculated by applying the Fourier transformation to the measured voltage $u(t)$ and current $i(t)$ signal correspondingly

$$U(j\omega) = \int_{-\infty}^{\infty} u(t) e^{j\omega t} dt.$$

Similarly, the real and imaginary parts of the signals can be obtained separately by splitting the above integral using the Euler's formula as:

$$\begin{aligned} \Re\{U(j\omega)\} &= \int_{-\infty}^{\infty} u(t)\cos(\omega t) dt \\ \Im\{U(j\omega)\} &= \int_{-\infty}^{\infty} u(t)\sin(\omega t) dt. \end{aligned} \tag{2.2}$$

The integrals (2.2) are then solved for each discrete frequency ω at which the system was excited.

In order to avoid possible discontinuities, the obtained signals are first multiplied with a windowing function $w(t)$. A window function is zero-valued outside of some chosen interval, normally symmetric around the middle of the interval. This is especially important, since most of the measured signals on real systems do not start from zero or end at zero, and

such discontinuities at the beginning or at the end can influence the final result. Therefore, (2.2) gets the following form:

$$\Re\{U(j\omega)\} = \int_{-\infty}^{\infty} u(t)w(t)\cos(\omega t)dt$$
$$\Im\{U(j\omega)\} = \int_{-\infty}^{\infty} u(t)w(t)\sin(\omega t)dt.$$

2.1.3 Influence of the number of periods of the sinusoidal excitation on the accuracy of the results

The number of periods used in sinusoidal excitation determines the accuracy of the results. It is especially important when performing EIS in a noisy environment. The accuracy of the final result can be significantly improved by making more than one signal cycle subject to integration.

This can be easily demonstrated by solving (2.2) for a certain f_0, which for demonstration purposes is set to $f_0 = 10$ Hz. The frequency accuracy depending on the number of periods is shown in Figure 2.3. For short excitation signals, typically with less than 5 periods (top left plot in Figure 2.3), frequency resolution is too wide, thus reducing the precision of the resulting EIS. This means the influence from neighbouring frequencies will have a significant impact on the values of the integrals (2.2).

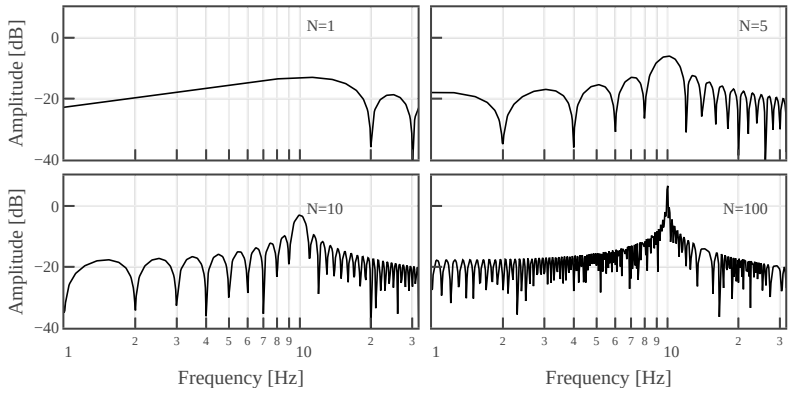

Figure 2.3: Frequency accuracy of single sine excitation for a different number of periods N for a "sine" filter at $f_0 = 10$ Hz calculated using the integrals (2.2).

2.2 Conditions to be Met in Impedance Spectroscopy

To correctly evaluate EIS, the system under test has to satisfy the following conditions:

- linearity,
- causality and
- stability.

2.2.1 Linearity

In linear dynamic systems sinusoidal signal on input causes sinusoidal signal on the output. The amplitude of the output has to be directly proportional to the amplitude of the input signal.

Generally, EECDs are nonlinear systems. To meet the linearity conditions, the amplitude of the input excitation signal should be small enough in order not to excite non-linear modes of the system, but big enough to ensure a suitable signal-to-noise ratio output. The attribute small depends very much on the operating point. That is illustrated on a static characteristic of a fuel cell in Figure 2.4. In Figure 2.4a, the operating point falls in the linear part of the characteristic. A small-amplitude sinusoidal perturbation causes a small-amplitude response which is almost sinusoidal as well. However, the same amplitude of the perturbation applied to the operating point in Figure 2.4b causes a response, which is no longer mono-component but contains higher harmonics. To reduce the amount of higher harmonics, the amplitude of the input signal should be significantly reduced.

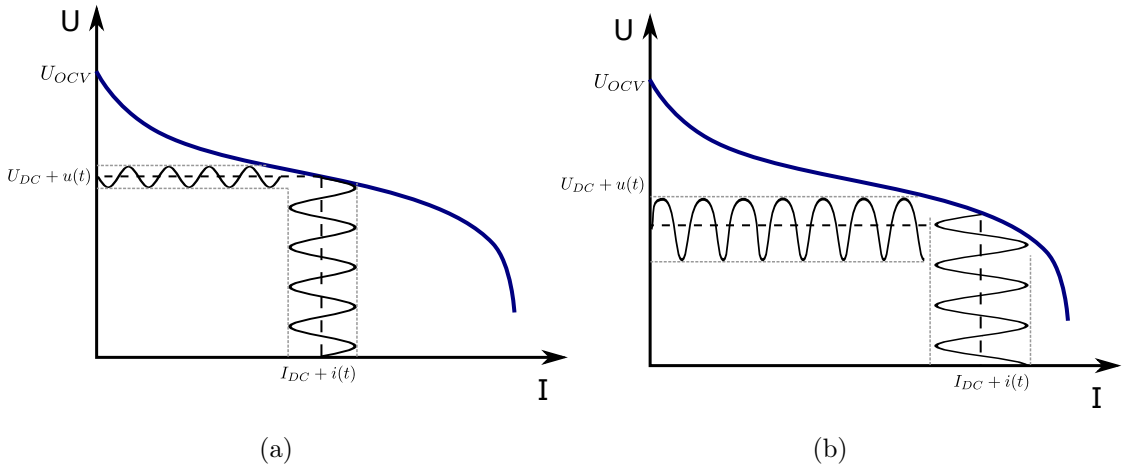

(a) (b)

Figure 2.4: Impedance spectroscopy performed at different operating points of a nonlinear system: (a) operating point is within the linear region and (b) operating point is within the nonlinear region.

One should also note that EIS based on linearisation results in different EIS characteristics for different operating points.

2.2.2 Causality

The notion of causality stands for the presumption that the system response is a result only of the perturbation signal at the input. However an EECD is normally subjected to various perturbations of different origin. For example, fluctuations in fuel flow in a fuel cell can disturb the EIS measurement and hence result in corrupted values of the evaluated impedance.

2.2.3 Stability

The notion of stability in the context of EIS refers to the system property according to which a system subjected to a perturbation returns to its original state once the perturbation is removed. If the state of the system under test changes during the experiment, the results are not valid and they should not be taken into account. A typical example are batteries. If EIS is performed under higher charging/discharging rates, the state of charge at the beginning and the end of the experiment might differ, which means that the battery's internal condition has changed. Consequently, the EIS properties might have changed as well.

Particular attention should be devoted when impedance spectroscopy takes long perturbation times, especially in the low-frequency region. Although a mono-component sinusoidal excitation leads to the increased accuracy of the evaluated EIS, yet 3 to 10 periods are required to achieve sufficient frequency resolution [58]–[60]. During this time, drifts and environmental disturbances may occur, which can significantly affect the accuracy of the final result.

Ensuring stability conditions becomes especially challenging when performing characterisation at the frequencies below 1 mHz. At these frequencies, the time required to perform the excitation can be notoriously long. For example, using mono-component sinusoidal excitation at 1 mHz with recommended 3–10 periods would take from 3,000 to 10,000 seconds of perturbation. That is where broadband excitation signals come at their best since they may substantially reduce the time required for performing EIS.

2.2.4 Broadband excitation signals

A broadband signal is composed of many sinusoidal signals with frequencies taking values from a broad interval. If a linear system is excited with such a signal, then thanks to the superposition principle, the overall system response is a sum of the partial responses

$$I = \sum_k I_k e^{j\omega_k t}$$
$$U = \sum_k U_k e^{j(\omega_k t + \varphi_k)}$$

The EIS characteristic is then evaluated as follows

$$Z(\omega_k) = \frac{U(\omega_k)}{I(\omega_k)} e^{j\varphi_k}$$

Signal generators used for excitation can generate signals with a finite amount of power. In case of a mono-component sinusoidal signal, the entire power is concentrated at one frequency. However, in broadband signals, the same power of the signal is distributed across many frequencies in a broad range. A component in a broadband signal can bear only a fraction of power of the overall signal, which is substantially lower compared to the mono-component case. Because of that, the broadband excitation signals are more susceptible to lower values of SNR.

To use a broadband signal as excitation signal, the following properties must be fulfilled [61], [62]:

- its bandwidth must include the highest frequency of interest,
- the amplitude must be large enough to guarantee an appropriate signal-to-noise ratio.

Broadband excitation signals can be deterministic, such as multisine and chirp, or stochastic, such as DRBS. Stochastic excitation signals, however, must be stationary in order to be used for performing EIS.

Multisine excitation signal uses the sum of sinusoidal signals to form a broadband signal [63], [64]. It is defined as $u(t) = \sum_{k=1}^{N} A_k \sin(2\pi f_k t + \phi_k)$, where A_k are the amplitudes, f_k frequencies and ϕ_k the phases of the sinusoidal functions applied. Time needed to take the measurements is defined by the lowest frequency used in the signal. In Figure 2.5, an example of a multisine signal in time-domain and its corresponding power spectrum is shown. Multisine signal is often used for performing EIS on different electrochemical conversion devices [65]–[67]. However, in order not to exceed the maximum allowed amplitude of the signal in the linear region, the amplitude of the sinusoidal signals should be carefully used. One way to do it is by performing phase optimisation of each of the signals.

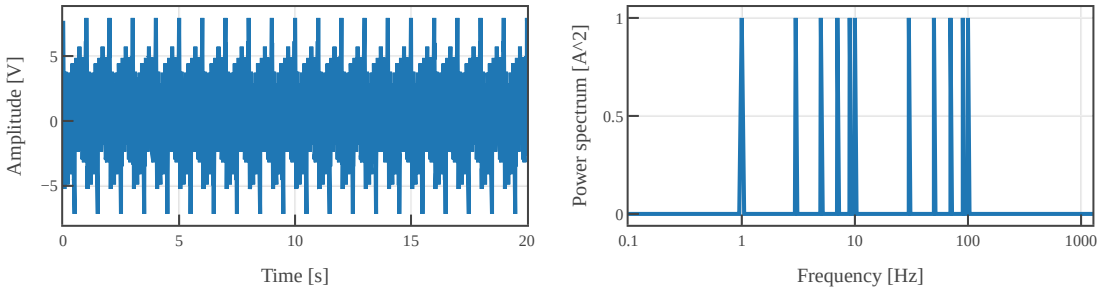

(a) (b)

Figure 2.5: (a) Multi-sine signal in time domain and (b) its amplitude power spectrum.

Chirp represents a sinusoidal signal in which the frequency is swept up and/or down during the measurement. It is defined as

$$u(t) = \sin\left[\left(\frac{\pi(f_2 - f_1)}{T}t + 2\pi f_1\right)t\right],$$

where f_1 and f_2 represent the minimum and maximum used frequency, respectively, and T represents the measurement period. In Figure 2.6, an example of a chirp signal in time-domain and its corresponding power spectrum is shown. Chirp signal has also been used for performing EIS on EECD [68], [69].

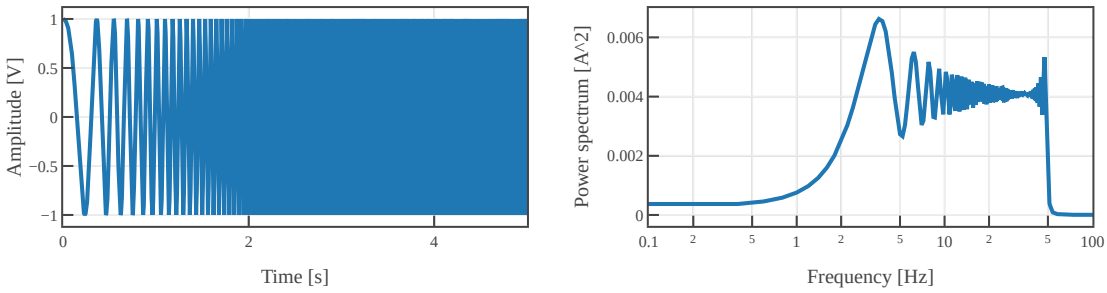

(a) (b)

Figure 2.6: Chirp signal in (a) time domain and (b) its power spectrum.

DRBS signal is designed to match white noise properties [62]. Its value switches between $-a$ and $+a$ at the discrete time points $k\lambda$ ($k \in \mathbb{N}^0$), where λ is minimal time between the two switchings [61, pp. 161–162]. λ also determines the effective bandwidth of the DRBS, which is defined as $f_b = \frac{1}{3\lambda}$. This means that all of the frequencies are on average excited with the same power (more precisely, power density). Power spectral density $\Phi_X^d(\omega)$ of the DRBS is defined as:

$$\Phi_X^d(\omega) = a^2\lambda\left|\frac{\sin\left(\frac{\omega\lambda}{2}\right)}{\frac{\omega\lambda}{2}}\right|^2.$$

where ω represents the angular frequency and a is the amplitude of the generated signal. In Figure 2.7, an example is shown of a DRBS signal in time-domain and its corresponding

power spectrum density. In the interval $[0, f_B]$, the power spectrum of the signal is rather flat and hence pretty much similar to power spectrum of the white noise.

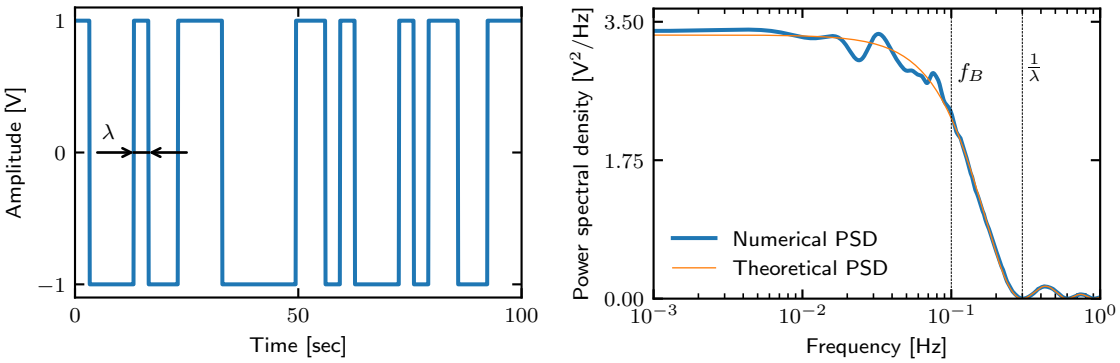

(a) (b)

Figure 2.7: DRBS signal in (a) time domain and (b) its power spectrum.

2.3 Impedance Evaluation by Means of Continuous Wavelet Transform

When applying Fourier transform to the measured signals, their local time properties and details of interest die out due to averaging. If the details matter, it is more suitable to use the *time-frequency spectral decomposition*. Time-frequency methods enable analysis in a two-dimensional time-frequency plane. In turn, the signal's spectral evolution in time can be observed. A simple way is to use short-time Fourier transform, which is defined as follows:

$$F(\tau, \omega) = \int_{-\infty}^{+\infty} f_m(t) g(t - \tau) e^{-j\omega t} dt, \tag{2.3}$$

where $g(t)$ is a window function and τ denotes time.

Expression (2.3) is a time-localised Fourier transform. Fourier transform is performed at each position of the sliding window $g(t)$, which results in a sequence of spectra. The main problem with the short-time Fourier transform is limited time-frequency resolution, which is related to the choice of the time window shown on the left-hand side in Figure 2.8.

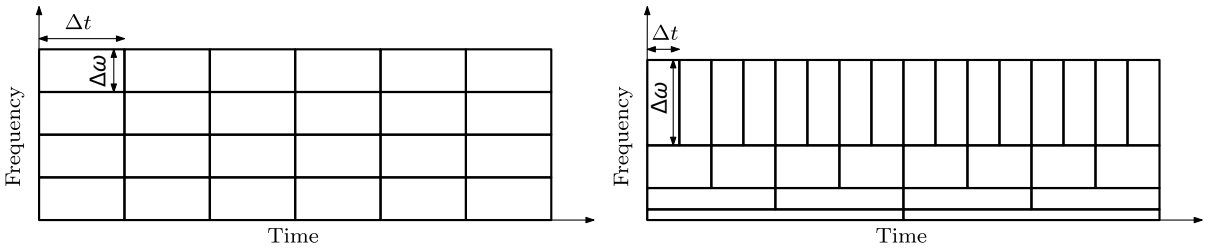

Figure 2.8: The concept of time-frequency resolution. The left-hand graph shows constant time-frequency resolution typical for the short-time Fourier transform. The right-hand plot shows adaptive time-frequency resolution, a partitioning that is typical for the wavelet transform.

Continuous wavelet transform (CWT), on the other hand, allows flexible time-frequency resolution, which is achieved through the concepts of scaling of mother wavelet $\psi_{u,s}(t)$. Mother wavelet functions represent an orthogonal set of function, which are used to represent any finite energy signal $f(t)$. CWT is defined as [70]:

$$Wf(s,u) = \int_{-\infty}^{\infty} f(t)\psi_{u,s}^{*}(t)\,dt,$$

where $\psi_{u,s}^{*}(t) = \frac{1}{\sqrt{s}}\psi^{*}(\frac{t-u}{s})$ denotes the complex conjugate and u and s are the translation and scaling parameters. The u and s parameters can be easily transformed in time and frequency based on the properties of the selected wavelet function.

There are many different mother wavelet functions available, but only complex mother wavelet functions are applicable for EIS evaluation such as: the Bump wavelet, the Morlet wavelet [71], [72] and the Lognormal wavelet [73].

However, due to its outstanding high time localization properties, the generalised Morse mother wavelet is considered as the best candidate for impedance analysis [74]. In frequency domain it is defined as:

$$\Psi(\omega) = U(\omega)K_{\alpha,\beta}\omega^{\beta}e^{-\omega^{\alpha}}$$

Details on the use of CWT with the Morse wavelet in the context of EIS can be found in Chapter 3.

It should be noted that having a finite number of samples, certain wavelet coefficients become corrupted due to the edge effects at the beginning and the end of the observation window. These coefficients must be omitted from further analysis. The effect is a direct consequence of the so-called cone of influence [75].

The impedance values can be obtained by CWT in a pretty much similar way as with the Fourier transform. CWT analysis of the voltage $u(t)$ and current $i(t)$ will result in a set of complex wavelet coefficients:

$$\begin{aligned} Wi(t,f) &= \Re\{Wi(t,f)\} + j\Im\{Wi(t,f)\}, \\ Wu(t,f) &= \Re\{Wu(t,f)\} + j\Im\{Wu(t,f)\}. \end{aligned}$$

where $Wx(t,f)$ denotes the wavelet of a signal $x(t)$ and its function of time t and frequency f. The impedance is the ratio of the wavelet coefficients:

$$Z(t,f) = \frac{Wu(t,f)}{Wi(t,f)}. \tag{2.4}$$

It should be noted that the impedance calculated in (2.4) is defined with time and frequency and provides *instantaneous* amplitude and phase at every time-frequency point. This means that one can track the evolution of the phase and amplitude of the impedance for each frequency over time. Having the time evolution of the complex impedance, it becomes possible to perform a more detailed analysis on the impedance values.

2.4 Data Validation

System impedance represents a complex analytic function in the upper half-plane. Moreover, real and imaginary part are not independent as they emerge from the same signals. This strong property is expressed by means of the Kramers-Kronig relations, which render possible to reconstruct the imaginary part of the impedance spectra from the real part and

vice versa [76], [77]

$$\begin{aligned}\Im\{\hat{Z}(\omega)\} &= -\frac{2\omega}{\pi}\int_0^\infty \frac{\Re\{Z(x)\}-\Re\{Z(\omega)\}}{x^2-\omega^2}\mathrm{d}x \\ \Re\{\hat{Z}(\omega)\} &= \Re\{Z(\infty)\}-\frac{2}{\pi}\int_0^\infty \frac{x\Im\{Z(x)\}-\omega\Im\{Z(\omega)\}}{x^2-\omega^2}\mathrm{d}x.\end{aligned} \tag{2.5}$$

KK can be used as a tool to check whether the measured system satisfies the condition of stability, causality and linearity.

The infinite integration in (2.5) leads to the inevitable numerical errors. Ehm *et al.* [78] provided a solution to this numerical problem and proposed a Z-HIT method. In Z-HIT, the amplitude spectrum can be reconstructed from the phase spectrum as follows

$$\log|\hat{Z}(\omega_0)| \approx a + \frac{2}{\pi}\int_{\omega_{min}}^{\omega_0}\phi(\omega)\mathrm{d}\log\omega + \gamma\frac{\mathrm{d}\phi(\omega_0)}{\mathrm{d}\log\omega_0} \tag{2.6}$$

where $\phi(\omega)$ is the phase spectrum, $\gamma = -\frac{\pi}{6}$ and $\omega_0 \in [\omega_{min}, \omega_{max}]$. The derivation $\frac{\mathrm{d}\phi(\omega_0)}{\mathrm{d}\log\omega}$ can be evaluated numerically by means of the Savitzky-Golay filter [79]. The constant a is determined by a least squares fit. It is done in a way where the region in which it is calculated is immune to external disturbances.

Using (2.6), impedance data are valid if the difference $||Z(\omega)|-|\hat{Z}(\omega)||$ is small enough. If either system dynamics, experimental conditions or data acquisition violate linearity, causality and stability, the reconstruction via Z-HIT may fail in certain frequency regions. These regions should be excluded from further EIS analysis.

2.5 Practical Aspects of EIS Measurement

In the context of electrochemical systems, two kinds of excitation modes apply, i.e. *potentiostatic* mode and *galvanostatic* mode. In potentiostatic mode, the manipulated input is voltage and the system response (output) is current, while in the galvanostatic mode, current is the manipulated input and voltage is the output. Potentiostatic mode is often used in cases of high impedances, for example in corrosion. In that case, currents cannot go unintentionally high but remain limited. On the other hand, the galvanostatic mode is particularly suitable for measuring very low impedances (e.g. batteries, fuel-cells and electrolysers) since in that case, limited currents result in limited voltages.

Most of the conventional EIS devices currently available on the market are referred to as *frequency response analysers (FRA)*. FRA generates sinusoidal excitation for a selected frequency, acquires current and voltage samples and evaluates the value of impedance at that particular frequency. The perturbation is repeated for a selected set of frequencies across the frequency band of interest. The main advantage of these devices is their reliability, accuracy, and the ability to operate in both potentiostatic and galvanostatic modes. However, these devices are not modular in a sense that if EIS measurements at higher power ranges are needed, one cannot simply apply multiple items of the same device (in parallel or in series) but has to purchase a new item designed for higher power range. A constraint often encountered in FRA concerns the lack of freedom in choosing the excitation waveforms and the inability to have access to time-domain data. This makes it unattractive for performing fast impedance spectroscopy.

A problem addressed in this thesis concerns modularity and flexibility of the hardware equipment to be used in applications. As demonstrated in the sequel, that can be achieved by using low-cost *standard laboratory devices*, such as digital loads, power supplies, and signal generators. If the required power, current or voltage range of the EECD exceeds

the range supported by a single device, several such devices can be put together either in parallel or in series to meet the specified range. The key requirement for standard devices to be employable for impedance spectroscopy is that they can be synchronized one with another. That is crucial because all the devices that contribute to the final excitation signal have to generate exactly the same waveform in the time domain. In some cases, the equipment dedicated to EIS measurements might not provide the opportunity to the user to apply a user-defined, arbitrary excitation waveform.

In order to obtain good quality data, the following modules are required:

- Current sensors,
- DAQ system,
- Device for inducing excitation signals,
- Control and processing unit.

The role for each of the modules described above is explained in detail in the sections that follow.

2.5.1 Current sensors

Current can be measured directly or indirectly. The simplest (direct) method uses the *shunt resistor* shown in Figure 2.9a. Although accurate and relatively inexpensive, it suffers from three weaknesses:

1. To implement a shunt, one needs to break the electrical circuit in order to physically embed in the circuit. That can be rather impractical in some cases.

2. For small currents, the voltage drop across the shunt is very small and has to be amplified using an external instrumentation amplifier.

3. With increasing currents, the energy dissipation increases, thus leading to the increase of the resistance and, consequently, to a higher voltage drop. Hence a bias appears in the deduced current values.

Indirect methods rely on sensing magnetic field that is generated by a current passing through the cable. The magnitude of the magnetic field is proportional to the magnitude of the electric current. There are two options, one is *Hall probe* (Figure 2.9b) and the other is *Flux-gate* sensor (Figure 2.9c).

The *Hall probe* is based on the Hall effect. A voltage difference is generated across an electrical conductor placed in a magnetic field. The main advantage of using Hall probe is that it is galvanically separated between the primary and secondary circuit, easy to install, relatively immune to external disturbances and it has high bandwidth.

Flux-gate current sensor is similar to a Hall effect current sensor, except that it uses a magnetic coil instead of a Hall effect system. The magnetic core is built using a high permeability material, which is immersed in the magnetic field to be measured. It is based on a closed-loop technology that allows accurate and precise monitoring of DC and AC currents with high bandwidth, very low noise and negligible drift. Due to its higher accuracy, it makes these sensors ideally suited for industrial, aerospace, and other applications that require high accuracy measurements. Details about the operating principle of the Flux-gate can be found in [80], [81].

The main advantage of flux-gate sensors is that their primary and secondary circuit are galvanically separated, they have very high SNR and can be used for both AC and DC measurements.

In our experiments, EIS was performed with two different types of current sensors:

(a) (b) (c)

Figure 2.9: Different sensors for measuring current: (a) shunt resistor, (b) Hall probe and (c) Flux-gate.

- LEM HASS-50S[1] which represents a Hall probe and
- CAENels CT-100[2] transducer which represents a flux-gate current sensor.

As mentioned before, current measurements performed using CAENels CT-100 sensor are by far superior when compared with the measurements performed using LEM HASS-50S. A comparison of the noise levels between both sensors is shown in Figure 2.10.

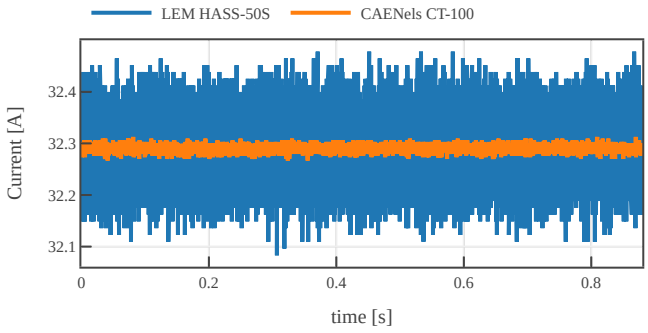

Figure 2.10: Comparison of current signals obtained with Hall current sensor and flux-gate current sensor. Note the substantially higher noise level in the former sensor.

2.5.2 Data acquisition system

Signal measurement

There are two types of signal measurements: *single-ended* and *differential*. They are illustrated in Figure 2.11.

In a single-ended measurement, the potential difference between a point of interest in the circuit and ground is observed. In contrast, a differential measurement represents a

[1]Datasheet of LEM HASS-50S sensor can be found on `https://www.lem.com/sites/default/files/products_datasheets/hass_50_600-s.pdf`

[2]Datasheet of CAENels CT-100 transducer can be found on `https://www.caenels.com/wp-content/uploads/2015/04/CT-100_CT-150_UsersManual_V1.5.pdf`

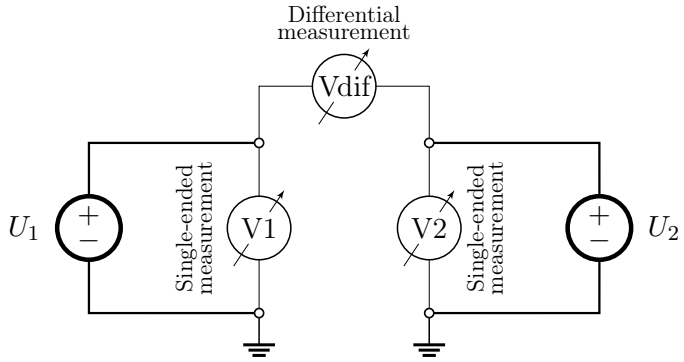

Figure 2.11: Comparison between single-ended measurement and differential measurement.

measurement of the voltage difference between the two voltage signals. The main advantage of the differential measurement is noise rejection. Namely, a problem with single-ended measurements is that noise in the signal might be amplified prior to the transmission to the entry of DAQ system. In the differential measurement, noise is added to both signals and filtered out by the common-mode rejection filter of the data acquisition system.

When performing EIS on EECDs, most of them are not connected to the ground, which means that their voltage is floating. Therefore, the voltage and current signals coming from the device under test should be measured differentially.

To prevent one measurement channel interfering with the other, each single channel must be isolated from the rest of the system, e.g. the system's power supply, chassis ground, and so on. If all the channels are mutually isolated, they are isolated from the ground.

Analogue-to-digital converters (ADCs)

Depending on the DAQ system, the analog-to-digital conversion can be *multiplexed* or *simultaneous*. In a multiplexed DAQ system, such as NI USB-6215, a single ADC is used to convert multiple signals from analog to digital domain. This is done by multiplexing the analog signals, meaning only one channel at a time can be processed by the ADC (Figure 2.12).

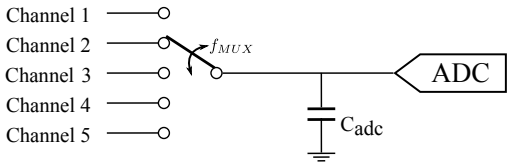

Figure 2.12: Schematic of a multiplexed DAQ system.

For example, the multiplexer frequency f_{MUX} of NI USB-6215 is 250 kHz. It can measure up to 8 differential signals with adjustable sampling frequency f_s. If only one signal is measured, the maximal sampling frequency f_s is 250 kHz. When all 8 channels need to be sampled, the maximal sampling frequency is $250/8 = 31.25$ kHz.

The main problem of multiplexed DAQ systems is the time delay that occurs during sampling. For example, if ADC conversion on the channel no. 1 starts at time t, the time to complete ADC equals $\Delta t_{MUX} = \frac{1}{f_{MUX}}$. That means the next channel (say no. 2) can start with sampling at Δt_{MUX}. Although sampled with a delay, the DAQ system associates

the sampled value with time t, which is not quite correct especially when sampling high frequency signals. From Figure 2.13a it can be seen that for low frequency signals the time delay caused by the multiplexer does not influence the end result significantly. However, this is not the case when high frequency signals are measured. In such a case, the time delay caused by the multiplexer can significantly influence the final result. Therefore, the final result of the impedance measurement will fail to fulfil the KK relations.

An example of sampling two signals using multiplexed DAQ system is shown in Figure 2.13a.

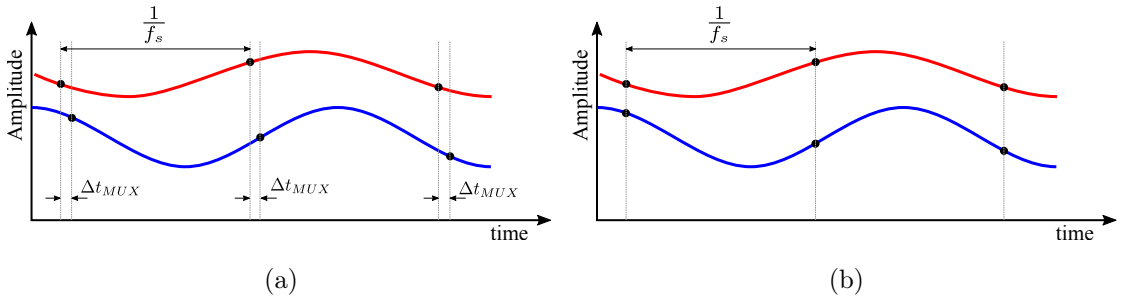

Figure 2.13: Sampling two signals using (a) multiplexed DAQ system and (b) simultaneous DAQ system. The black dots represent samples. Note that in case (a), the sampled value of the second signal is not taken at t but with a delay.

In applications where information about the phase between signals is essential, the best solution is a DAQ system with *simultaneous sampling*. In a simultaneous DAQ system, each channel has its own ADC chip. Since there is no multiplexer, the $\Delta t_{MUX} = 0$ s. The process of simultaneous sampling is shown in Figure 2.13b.

Another issue related to the multiplexed DAQ systems are the transients that occur when sampling signals with different DC voltages. Between consecutive switching from one channel to another, the multiplexer capacitor is charged and discharged depending on the DC value of the input signals. The charging/discharging rate is equal to $\tau_{input} = C_{adc}Z_{channel}$, where C_{adc} is the capacitance of the multiplexer and $Z_{channel}$ is the output impedance of the signal. To avoid transients, the value of τ_{input} has to be as low as possible. Since C_{adc} is fixed and typically in the range of several hundred picofarads (∼100 pF), the only variable parameter is the output impedance of the input signal channels. This impedance has to be as low as possible. One way to circumvent this problem is to use DAQ systems with simultaneous sampling, which by default have separate capacitors at each ADC.

In the experiments, we used two simultaneous DAQ, i.e. Keysight DAQ970A and Dewesoft Sirius HS - LV. Keysight DAQ970A can simultaneously measure 12 signals, which are acquired using 24-bit sigma-delta ADC with a sampling frequency f_s=800 kHz. The isolation voltage of this system is 48 V. On the other hand, Dewesoft Sirius HS-LV can simultaneously measure 8 signals that are acquired using 16-bit ADC with a sampling frequency f_s=1 MHz. However, due to the high isolation voltage 1000 V, Dewesoft Sirius HS-LV is used for more demanding applications that exceed voltages of 48 V.

Filtering

Before the analogue signal is sampled, it is filtered using a low-pass filter. In order to satisfy the Nyquist–Shannon sampling theorem over the band of interest, the filter cut-off frequency (f_c) must be $f_c < \frac{f_s}{2}$.

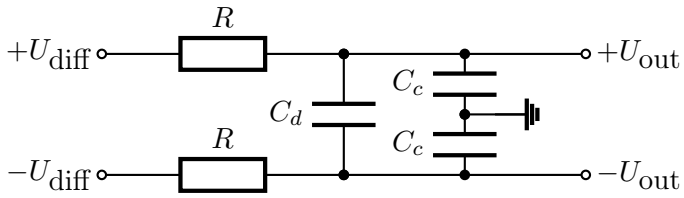

Figure 2.14: First-order differential low-pass anti-aliasing filter.

Since most of the signals used to perform EIS are differential, a passive differential low-pass filter is used. The electrical scheme of the filter is shown in Figure 2.14. The cut-off frequency is $f_c = \frac{1}{4\pi R C_d}$. Capacitors C_c have at least ten times lower capacity than C_d and are used as common-mode filters.

Wiring

4-point sensing is an EIS measurement technique that uses separate pairs of current-carrying and voltage-sensing electrodes to increase accuracy of the measurement. Typically, twisted pair cables are used to minimise the influence of the external disturbances and avoid the creation of a ground loop. Also, twisted pair wiring significantly reduces the noise currents induced by the coupling of electric or magnetic fields. The idea is that the currents induced in each of the two wires are almost equal. Since differential voltages are only measured, the common-mode noise at the input of the ADC is automatically cancelled. Therefore, any inductance that appears in the result is due to the properties of the device being measured and is physically present. In fact, the inductance does not appear as a result of the wiring.

2.5.3 Devices for inducing excitation signals

There are two different concepts of inducing excitation signals for performing EIS on any electrochemical energy conversion device (Figure 2.15).

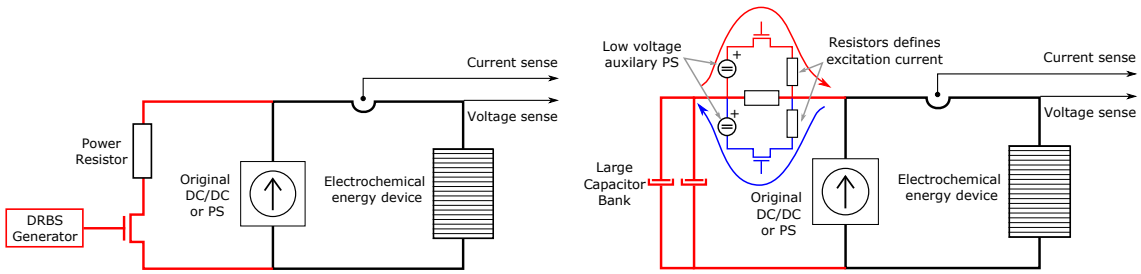

(a) Unidirectional excitation with only digital signals.

(b) Bidirectional excitation with any arbitrary excitation signal.

Figure 2.15: Different concepts for performing EIS on any electrochemical energy conversion device using custom-made arbitrary excitation signals.

The first concept shown in Figure 2.15a is the simplest version to create. It allows only unidirectional excitation that is imposed through the MOSFET transistor via external generator. Any digital port of any computer can also be used as an external generator.

However, the main drawbacks of this concept are low efficiency and inability to perform sinusoidal excitation.

This concept is realised in a more sophisticated manner in Rigol DL3031A electronic digital load[3]. It contains a current drain controller, which means that it is capable to execute any current waveform according to the user-defined signal generator. It is a single channel programmable electronic load designed for power ranges up to 350 W with a maximum current of 60 A. The accuracy of the build in arbitrary generator is ±1 mA. By adding more digital loads in parallel, higher power (or current) ranges that exceed the maximum power (or current) of a single Rigol DL3031A can be achieved.

The second concept shown in Figure 2.15b allows symmetric excitation in both directions. It is realised by using MOSFET transistors for switching together with external resistors and a bootstrapped auxiliary power supply. There are two main advantages of this version:

1. While draining, the energy is not lost but stored in external capacitors, and later returned back to the system. Therefore the energy consumption is significantly reduced when compared to the first concept, which corresponds to increased overall efficiency.

2. Ability to generate any form of user-defined continuous signals.

However, the main disadvantage of this concept is the large capacitor storage required to store the excess amount of energy. So far, this concept has been used only in charging mode.

2.6 Different Architectures for Performing EIS

2.6.1 Discharging mode (fuel cell, battery, capacitor)

In the discharge mode, the electrochemical energy conversion device represents a power source. Performing EIS is a simple task. It is done using a single digital load (Rigol DL3031A) or multiple loads depending on power requirements, which are connected in series with the fuel cell, a DAQ system and a control unit. The task of the digital load is to regulate the electric current drawn from the fuel cell and superimpose user-defined arbitrary signals to it. The block scheme of the measurement system is shown in Figure 2.16a.

When the voltage of the fuel cell falls below a certain threshold, additional excitation can destabilize electronic load. For example, the voltage at the input terminals of Rigol DL3031A must be above 5 V to perform excitation. Otherwise the device faces serious risk to go unstable. To avoid such a behaviour, an additional voltage booster is introduced to artificially increase the voltage at the input terminals. The block scheme of the measurement system including the voltage booster is shown in Figure 2.16a. The voltage booster represents a power supply in voltage mode that has a sufficiently high bandwidth. High bandwidth is important to avoid unwanted artefacts that affect the final result. For example, the Itech IT6512C power supply used as a voltage booster has a cutoff frequency of 50 kHz.

This architecture was used to obtain impedance results from the experiments explained in Section 4.1 and partly in Section 4.3.

[3]for details of the device, see `https://beyondmeasure.rigoltech.com/acton/attachment/1579/f-0778/1/-/-/-/-/DL3000_DataSheet_EN.pdf`

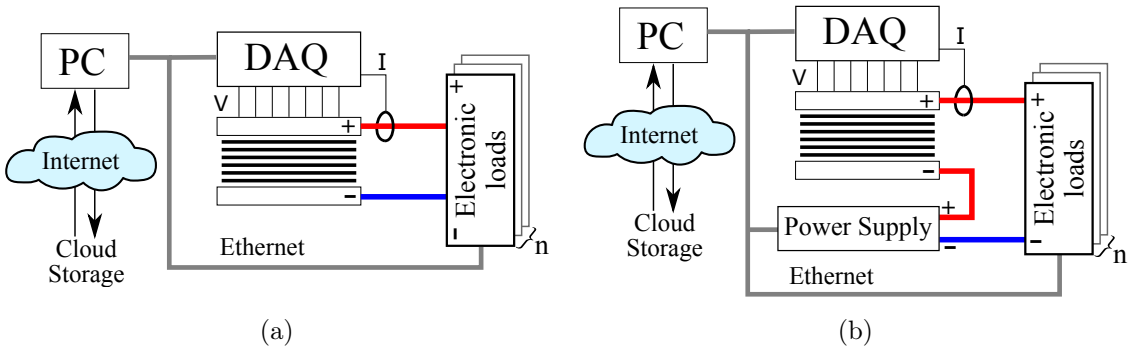

Figure 2.16: Conceptual set-up in galvanostatic mode for performing EIS on fuel cells, batteries or supercapacitors in (a) normal mode or (b) with included voltage booster.

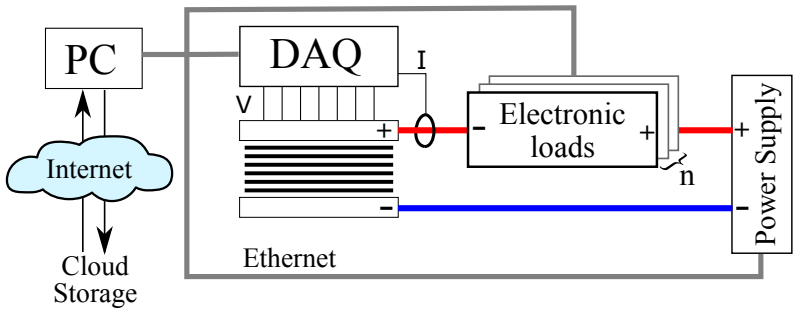

Figure 2.17: Conceptual set-up in galvanostatic mode for performing EIS on electrolysers, batteries and supercapacitors.

2.6.2 Charging mode (electrolyser, battery, supercapacitor)

In the charging mode, power supply is required to provide power to the electrochemical system under test. It must have a sufficient bandwidth to avoid unwanted artefacts in the results. Such power supply is Itech IT6512C, which was used in most of the experiments. It is designed for power ranges up to 1800 W with a maximum current of 120 A and a maximum voltage of 80 V. The current is controlled by one or more digital electronic loads (Rigol DL3031A), depending on the application, which are connected in series with the power supply. Similar to discharge/fuel cell operation mode, it is used to control the current flow in the circuit and superimpose user-defined arbitrary signals. The block scheme of the measurement system for performing EIS in charging/electrolysis mode is shown in Figure 2.17.

This architecture was used to obtain the impedance result from the experiments explained in Section 4.2.

Chapter 3

EIS at Ultra-Low Frequencies

Measuring impedance at ultra-low frequencies (<10 mHz) is a challenging task. At low frequencies, the measurement time required for accurate impedance estimation has to be sufficiently long, as it is shown in Figure 2.8. During this time, it is hard to avoid internal and external disturbances that could significantly affect the accuracy of the final result.

As mentioned before, one way to reduce the measuring time for impedance spectroscopy and to possibly avoid drifts and external disturbances is to use DRBS excitation signal together with CWT for signal analysis. Selecting a proper mother wavelet for CWT greatly influences the results.

A mother wavelet function $\psi(t)$ represents a bandpass filter that is used to preserve the main characteristics of the signals such as amplitude and phase [82]. By definition, a mother wavelet function has localized oscillatory features with zero mean and finite energy.

$$\int_{-\infty}^{+\infty} \psi(t)\, dt = 0$$
$$\int_{-\infty}^{+\infty} |\psi(t)|^2\, dt < \infty$$

Since impedance of the system represents a complex function, only analytical (complex) wavelets are suitable for this task, such as Morlet, Morse, lognormal and Bump wavelet [48]. An analytical wavelet is the one whose spectrum has only positive frequencies [83]:

$$\Psi(\omega) = 0 \qquad \text{for} \qquad \omega < 0$$

where $\Psi(\omega)$ represents the Fourier transform of the mother wavelet.

3.1 Comparison Between Morlet and Morse Wavelet

The most commonly used mother wavelet for impedance analysis is the Morlet wavelet [71], [84]. It represents a Gaussian envelope modulated by a complex-valued carrier wave at radian frequency ω_0. The time domain of the Morlet wavelet $\psi_{\omega_0}(t)$ and its Fourier transform $\Psi_{\omega_0}(\omega)$ are defined as followed:

$$\begin{aligned} \psi_{\omega_0}(t) &= \pi^{-1/4} \left(e^{j\omega_0 t} - e^{-\frac{\omega_0^2}{2}} \right) e^{-\frac{t^2}{2}} \\ \Psi_{\omega_0}(\omega) &= \pi^{1/4} e^{-\frac{(\omega-\omega_0)^2}{2}} \left(1 - e^{-\omega\omega_0}\right) \end{aligned}$$

where ω_0 represents the central frequency. By changing the central frequency ω_0, a compromise is made between localisation in time and localisation in frequency. Smaller values

of ω_0 enable accurate localisation of short time events, while large values of ω_0 increase the number of oscillations inside the envelope, leading to increased localisation in frequency domain.

As mentioned in Chapter 2, the lowest observable frequency component (f_{low}) from a signal is defined by its length T, i.e. $f_{low} = 1/T$. During the time T of the signal, the f_{low} frequency component has performed at one oscillation. Because of the limited measuring time, low frequency components of the acquired signal are highly time-localised. However, high frequency events appear more frequently and are more frequency-localised.

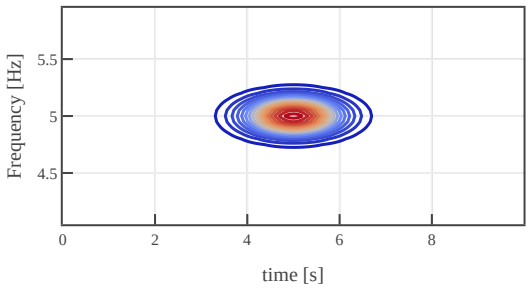

(a) Morlet wavelet for higher values of central frequency.

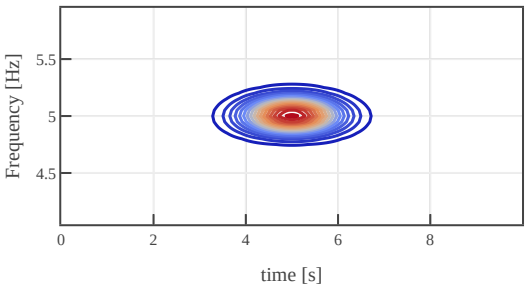

(b) Morse wavelet for higher values of central frequency.

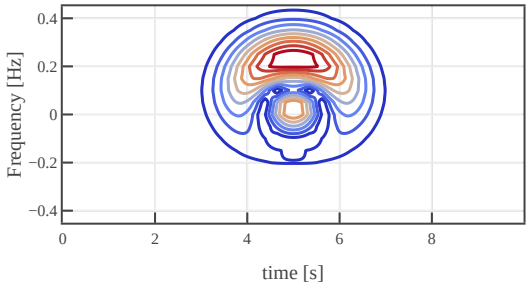

(c) Morlet wavelet for lower values of central frequency.

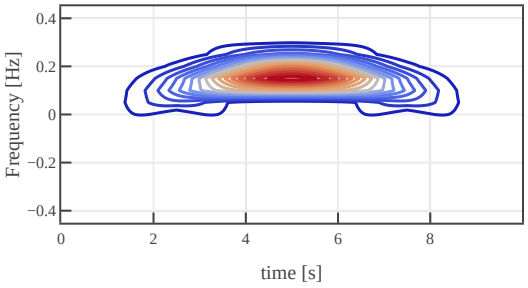

(d) Morse wavelet for lower values of central frequency.

Figure 3.1: Comparison of the Wigner-Ville transform of the Morlet wavelet and Morse wavelet. Parameters of both wavelets are chosen in a way that their central frequency is the same. (c) Morlet wavelet loses its analytic properties due to leakage to negative frequencies, while (d) the Morse wavelet remains analytic even for highly time-localized parameter settings.

The biggest disadvantage of the Morlet wavelet is that it is only approximately analytic for sufficiently large values of the central frequency $\omega_0 > 5\,\mathrm{s}^{-1}$ (Figure 3.1c). As we can see from Figure 3.1c, the Morlet wavelet loses its analytic properties due to leakage to the negative frequencies, for lower value of the central frequency parameter ω_0.

The Morse wavelet, on the other hand, is a two-parameter wavelet, which according to Lilly *et al.* [74] has been successfully used to estimate properties of a number of different non-stationary signals, including blood flow data, seismic and solar magnetic field data, neurophysiological time series, drifting oceanographic float records, and has also been used in image analysis. Due to its two free parameters, the Morse wavelet has an additional degree of freedom. These great properties have not been exploited so far in the domain of EIS analysis, so the results presented below are the first such attempt in the field of

electrochemistry.

The general form of the Morse wavelet in frequency domain is defined as follows [83]:

$$\Psi(\omega) = U(\omega) K_{\beta,\lambda} \omega^{\beta} e^{-\omega^{\lambda}}$$

where $U(\omega)$ is the Heaviside unit step function and $K_{\beta,\lambda}$ is the normalizing factor. The roles of β and λ parameters in shaping the Morse wavelet are examined in detail by Lilly *et al.* [74]. However, for more computationally efficient calculation, the following form of the Morse wavelet is used in the analysis that follows [85]:

$$\psi(\omega) = U(\omega) e^{-\omega^{a} + q\left(\log\omega + \frac{1}{a}\log\frac{ae}{q}\right)},$$

where parameter q is related to the central frequency ω_0 as $\omega_0 = \frac{q}{a}^{(1/a)}$ and e represents the Euler's number.

Unlike the Morlet wavelet, which loses its analyticity for low values of the central frequency, the Morse wavelet remains analytic for all values of its central frequency. A comparison between the Morse and Morlet wavelets about their analyticity can be seen from their Wigner-Ville distributions shown in Figure 3.1. In Figure 3.1a and 3.1b, parameters of both wavelets are chosen in a way that their central frequency is the same. It can be seen that the two wavelets appear indistinguishable, and their Wigner-Ville distributions are nearly identical.

In contrast to the Morlet wavelet, Morse wavelet remains analytic even for highly time-localized parameter settings (Figure 3.1d). In Figure 3.1d, the Wigner-Ville transform of the Morse wavelet remains completely concentrated at positive frequencies despite its dispersion. This is particularly important for extracting low-frequency components, where the wavelets must be narrow in time to match the modulation time scale.

The outstanding properties of the Morse wavelet together with the DRBS excitation have been successfully used to accurately measure the impedance of the Li-ion battery at ultra low frequencies ($<$ 1 mHz), which are shown in Section 3.3.

3.2 Noise Influence

When performing EIS measurement, there are three main sources of disturbances. The first source of disturbances comes from random phenomena in the excitation circuit as well as from the noise present in the current sensor, which is denoted as $n_i(t) \sim \mathcal{N}(0, \sigma_i^2)$ in Figure 3.2. Note that for the sake of simplicity we assume the noise n_i is normally distributed. The second and the third source of disturbances act together on the voltage signal. One is measurement noise $n_u(t) \sim \mathcal{N}(0, \sigma_u^2)$ and the other is the term n_{dist}, which aggregates the effects of disturbances originating in balance-of-plant (BoP) and system environment. Examples include fluctuations in fuel and air flow (for instance due to control system issues), fluctuations in the temperatures, etc. In terms of the frequency content $n_{dist}(t)$ is much slower than $n_u(t)$, therefore it results in slowly time-varying EIS characteristics. That should be keep in mind, especially when performing in-field applications. In case of EIS measurements in the laboratory conditions, one can take all the measures to minimise the presence of $n_{env}(t)$ and hence ensure the causality condition for EIS to be fully valid.

The influence of noise components n_i and n_u is shown by simulating a simple electrical circuit shown in Figure 3.2. EIS is evaluated from simulated inputs and outputs assuming galvanostatic mode applies. The noise components are $(n_i(t) \sim \mathcal{N}(0, \sigma_i^2))$ as well and $(n_u(t) \sim \mathcal{N}(0, \sigma_u^2))$. The parameters of the theoretical system used for simulation are given in Table 3.1.

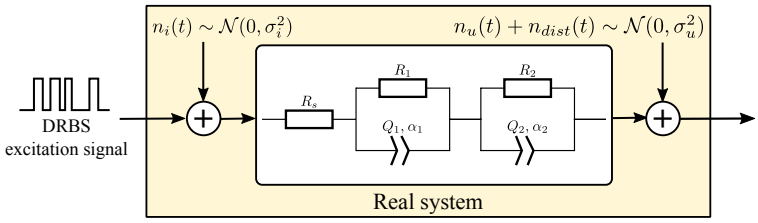

Figure 3.2: Schematic of a general measurement system for performing EIS in galvanostatic mode with $n_i(t)$ is the input noise and system uncertainties and $n_u(t)$ is the measurement noise.

Table 3.1: Parameters of the simulation circuit.

Parameter	R_s [Ω]	R_1 [Ω]	Q_1 [$\Omega^{-1}s^{\alpha}$]	α_1	R_2 [Ω]	Q_2 [$\Omega^{-1}s^{\alpha}$]	α_2
Value	0.5	1	0.005	0.8	2	0.1	0.95

The time domain simulation was performed using three different DRBS excitation signals, with $f_b \in \{10, 100, 1000\}$ Hz. The time domain response was simulated using closed-form solutions of linear fractional-order differential equations as explained in [86]. A snapshot of the current excitation and voltage response signal is shown in Figure 3.3a. Obtained signals are time-frequency decomposed using CWT with Morse mother wavelet. The absolute values of the wavelet coefficients of the current signal are shown in Figure 3.3b.

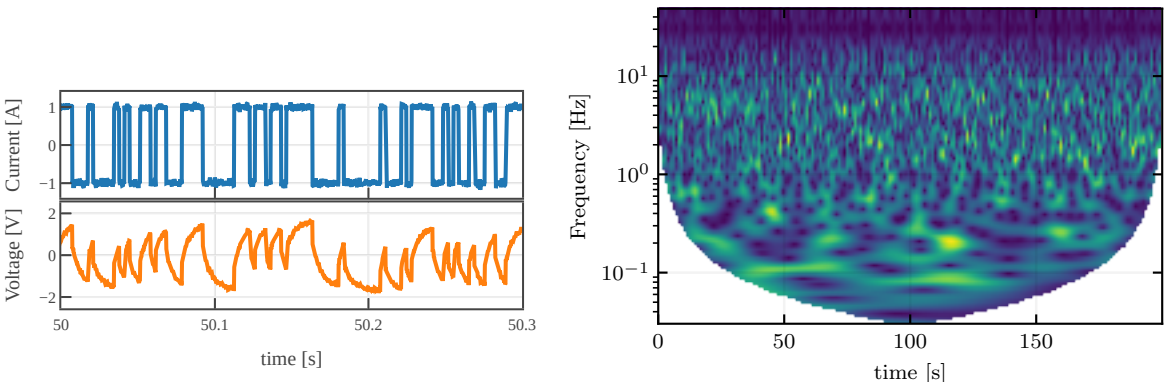

(a) (b)

Figure 3.3: Results of simulation of the system shown in Figure 3.2 with parameters in Table 3.1. (a) Snapshot of the current excitation and voltage response signal and (b) time-frequency evolution of the absolute value of the wavelet coefficients of the current signal.

The statistical properties of both excitation and response signals are preserved within the wavelet coefficients. As a result, the wavelet coefficients of the voltage and current signal follow the statistical properties of a zero-mean Gaussian circular complex random

variable [87], with the following properties:

$$\begin{aligned}
\Re\left[W_i(t,f)\right] &\sim \mathcal{N}(\Re\left[\bar{W}_i(t,f)\right], \sigma_i^2) \\
\Im\left[W_i(t,f)\right] &\sim \mathcal{N}(\Im\left[\bar{W}_i(t,f)\right], \sigma_i^2) \\
\Re\left[W_u(t,f)\right] &\sim \mathcal{N}(\Re\left[\bar{W}_u(t,f)\right], \sigma_u^2) \\
\Im\left[W_u(t,f)\right] &\sim \mathcal{N}(\Im\left[\bar{W}_u(t,f)\right], \sigma_u^2)
\end{aligned}$$

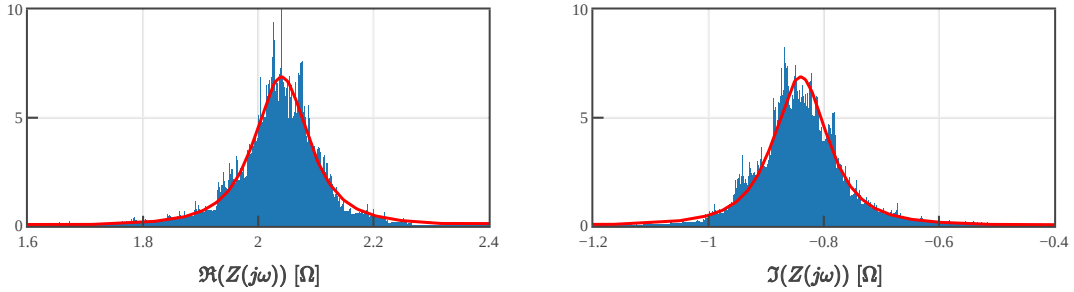

(a) (b)

Figure 3.4: Comparison between the histogram of the calculated impedances and the corresponding probability distribution of different impedance components. (a) Real part of the impedance. (b) Imaginary part of the impedance.

The impedance of the system represents a ratio between the wavelet coefficients of the current and the voltage. Therefore, for linear system, the wavelet coefficients of the voltage $Wu(t,f)$ and the current $Wi(t,f)$ are correlated using the following covariance matrix:

$$\Sigma = \begin{bmatrix} \sigma_u^2 & \rho\sigma_u\sigma_i \\ \rho^*\sigma_u\sigma_i & \sigma_i^2 \end{bmatrix},$$

where $\rho = \rho_r + j\rho_i$ is the complex correlation coefficient such that $|\rho| \leq 1$. The resulting distribution can be derived in a closed form as [71], [88]:

$$f_Z(z) = \frac{1-|\rho|^2}{\pi\sigma_u^2\sigma_i^2}\left(\frac{|z|^2}{\sigma_u^2} + \frac{1}{\sigma_i^2} - 2\frac{\rho_r z_r - \rho_i z_i}{\sigma_u\sigma_i}\right)^{-2}, \tag{3.2}$$

where z_r and z_i are real and imaginary components of the random variable Z. In Figure 3.4, the comparison between the calculated histogram of the real and imaginary part of the impedance at selected frequency and the corresponding probability distribution of the real and the imaginary part of (3.2) is shown .

Figure 3.5 shows a comparison of the calculated impedance together with the uncertainty region and the theoretical impedance of the system. It can be seen that the variance of the impedance, especially the variance of the imaginary part, increases significantly at frequencies near the system's poles. This is a consequence of the fact that the mother wavelet functions used for CWT are not ideal bandpass filters. As a result, neighbouring frequencies affect the overall result. Small changes in the frequency can significantly influence the impedance result, hence the increased variance.

There are two additional effects that have to be discussed. The first one is shown in Figure 3.6a, where the variance of the calculated impedance changes due to changes in the sampling frequency. The second effect is increased variance shown in Figure 3.6b, which is caused by the decreased effective values of the amplitude of the excitation that leads to reduced SNR, thus to an increase of measurement uncertainty.

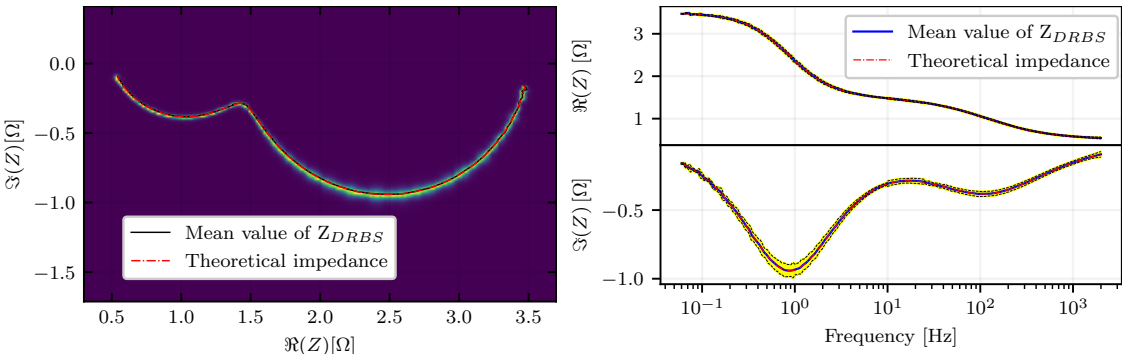

(a) (b)

Figure 3.5: Comparison between the impedance calculated using DRBS excitation signals with Morse wavelet and the theoretical impedance of the system with parameters given in Table 3.1. (a) Yellow represents the noise influence on the measured Nyquist plot. (b) Bode plot of the measured real and imaginary part of the impedance within the 90 % confidence interval (yellow area).

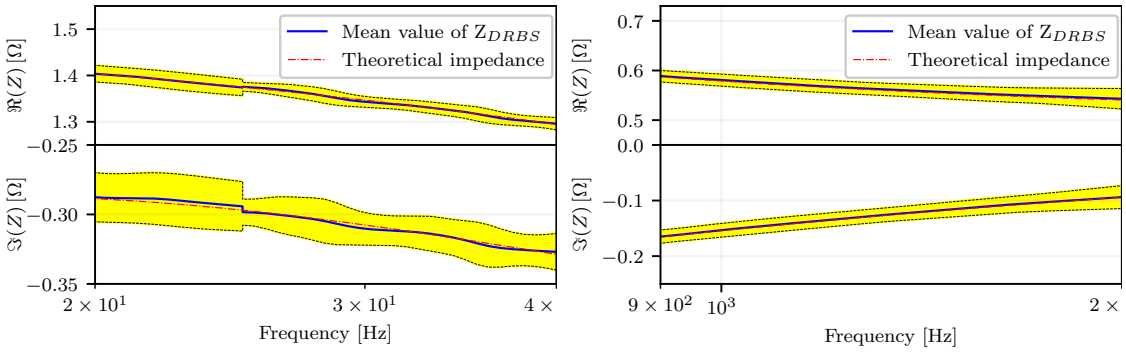

(a) (b)

Figure 3.6: (a) Zoomed parts of graphs in Figure 3.5b showing two regions analysed with different sampling frequencies. (b) High frequency part where the variance of the real and imaginary part starts to increase due to the lower effective values of the amplitude of the excitation.

3.3 Performing EIS at Ultra-Low Frequencies Using DRBS and Morse Wavelet

IEEE Access
Multidisciplinary ⋮ Rapid Review ⋮ Open Access Journal

Received January 15, 2021, accepted February 5, 2021, date of publication February 10, 2021, date of current version March 30, 2021.

Digital Object Identifier 10.1109/ACCESS.2021.3058368

Fast Impedance Measurement of Li-Ion Battery Using Discrete Random Binary Excitation and Wavelet Transform

GJORGJI NUSEV[1,2], ĐANI JURIČIĆ[2], MIRAN GABERŠČEK[3], JOŽE MOŠKON[3], AND PAVLE BOŠKOSKI[2]

[1]Jožef Stefan International Postgraduate School, 1000 Ljubljana, Slovenia
[2]Jožef Stefan Institute, 1000 Ljubljana, Slovenia
[3]National Institute of Chemistry, 1001 Ljubljana, Slovenia

Corresponding author: Gjorgji Nusev (gjorgji.nusev@ijs.si)

This work was supported by the Slovenian Research Agency through the programme under Grant P2-0001.

ABSTRACT Electrochemical impedance spectroscopy (EIS) is a widely used means for characterization of the dynamics of batteries and electrochemical energy conversion systems in general. EIS is useful for on-line condition monitoring since it contains valuable information on the internal condition of the batteries. The conventional approach to the EIS of batteries relies on their successive excitation with mono-component sinusoidal signals at the pre-defined frequencies. When inferring about the battery's state-of-health, the low-frequency part of the impedance characteristic is of particular interest. Excitation in the low-frequency region can take an excessively long time. Moreover, maintaining stable experimental conditions over long time intervals i na way that the external disturbances will not affect the estimated impedance, might be demanding, especially in the in-field applications. To alleviate the said limitations, and to minimally intrude the process operation, in this paper we apply broadband electrochemical impedance spectroscopy based on a discrete random binary sequence for perturbation of the battery input. The impedance is evaluated by processing voltage and current signals with continuous Morse wavelet transform. The main contributions of the paper refer to (i) the accurate evaluation of the impedance spectra from μHz to kHz range with high-frequency resolution (more than 200 points per decade) and (ii) the evaluation of the uncertainty region of the impedance characteristic. The entire characterisation takes only a fraction of the time required by the classical sine-based electrochemical impedance spectroscopy. The algorithm is successfully demonstrated on a commercial Li-ion battery, which, together with the all datasets are available for download at https://repo.ijs.si/gnusev/supplementary_material.git.

INDEX TERMS Discrete random binary sequence, continuous wavelet transform, variance estimation, Li-ion battery.

I. INTRODUCTION

Thanks to their high energy and power density, Li-ion batteries have become indispensable in a broad range of stationary and automotive applications as well as in portable devices [1]. Reliable indication of the change in the internal state of health of all the main battery components (cathode, anode, electrolyte) and remaining useful life could be gained by EIS since change in the patterns of the impedance spectra could be related with the change in the internal condition. In the recent paper from Zhang *et al.* [2], it was demonstrated on a huge set of long-term experiment data that information contained in EIS is very useful in diagnosing the degradation modes as well as assessing the remaining useful life.

EIS is performed by applying small amplitude perturbation signal to the battery input and then measuring its response on the output. Typically EIS measurements use mono-component sinusoidal excitation [3]–[9]. Hence the impedance is calculated only at a limited number of frequency points (usually ten frequencies per decade).

It has been shown that in the sub-millihertz region the Nyquist curve contains valuable information for estimating

The associate editor coordinating the review of this manuscript and approving it for publication was Bernardo Tellini.

the actual capacity of the battery, i.e. state of health (SOH), and its state of charge (SOC) [3], [9]. Therefore, performing accurate measurement in the low frequency region is of great interest.

EIS using sinusoidal excitation usually requires 3 to 10 periods [10]–[12]. Consequently, for low frequencies the time required to perform excitation might become notoriously long. For example, the time required to measure EIS at 1 mHz, by following the recommended 3-10 periods, would take 3000 to 10000 seconds. During long excitation period it is non-trivial to avoid drifts and environmental disturbances that might significantly impact the accuracy of the final result. Moreover, in the ultra-low frequency region (<10 mHz), a reasonable resolution would require excessive overall measurement times. On top of that, the information about the uncertainty of the measured impedance spectra is mainly ignored.

To evaluate EIS with high resolution over a dense set of frequency points, while, at the same time, reducing the excitation times to the shortest possible duration, we propose the application of broadband excitation signals [13]–[19]. From the reported cases, the lowest frequency at which EIS was measured was 100 mHz requiring approximately 90 seconds of excitation time [13], [15].

The contribution of this paper to the EIS evaluation for Li-ion batteries is twofold. The first is adoption of discrete random binary sequence (DRBS) for battery excitation. DRBS could be viewed as composited of an infinite number of sinusoids over a continuum of frequencies. Second, the approach enables straightforward estimation of the confidence region of the evaluated EIS.

Small-amplitude DRBS guarantees that linearity assumption, the experiment is based on, is valid. However, instead of exciting the system with consecutive mono-component sinusoids, *simultaneous* excitation over a range of frequencies is performed. The linearity assumption guarantees that the output is sum of responses obtained at the particular sinusoidal inputs. DRBS was successfully applied to the EIS evaluation of fuel cells [20], [21]. The same approach was used by Li *et al.* [22] for estimating Warburg-like impedance spectra. All of them used Morlet wavelet as mother wavelet. However, the main disadvantage of the Morlet wavelet is that it looses its analytical properties for low values of the central frequency parameter [23], which makes it ineffective for calculating impedance at low frequencies (below 10 mHz).

In the proposed approach, particular attention is paid to the accurate estimation of impedance at low frequencies. The original approach from [20], [21] is further improved so that the loss of analytical properties of Morlet wavelet is overcome by using Morse wavelet for impedance calculation.

Validation of the proposed EIS approach was done on a commercial 3.0 Ah 811 NMC-Graphite 18650 cylindrical Li-ion battery type LG18650HG2 (LG Chem). The same battery was then characterised using the DRBS excitation and evaluation of the Nyquist characteristic by processing voltage and current signals with the Morse wavelet transform. The main goal is to show that by using time-domain signals we get results comparable with those obtained with the established high-end laboratory equipment. We go beyond the state of the art as our approach is capable to estimate the confidence intervals of the measured impedance. The signal processing code is available in the supplementary material.

The organization of the paper is as follows. The main properties of the excitation waveform and the signal processing approach are presented in section III. Validation of the approach by using a simulated equivalent circuit model is presented in section IV. Description of the experiment is given in section V. Finally, section VI presents the experimental validation of the approach.

II. EXCITATION SIGNAL

Conventional EIS in batteries is done by using a sequence of mono- or multi-component sine waves, thus obtaining the EIS values at a discrete set of frequencies. From the system identification perspective, a broad-band noise-like signal can excite the system dynamics over a broad frequency range. Such a signal must fulfil several properties [24], [25]:

- it must be stationary,
- its bandwidth must include the highest frequency of interest,
- the power spectral density must be large enough to guarantee an appropriate signal-to-noise ratio.

A signal that satisfies the above properties and whose generation is fairly simple is the *random binary sequence*. Its value switches between $-a$ and $+a$ at random time instances. The number of changes over a period of time is Poisson-distributed, where the intensity parameter of the Poisson distribution determines the signal bandwidth.

For the case of discrete time signals, changes can not occur at arbitrary time instances, but only at the discrete time points $k\lambda$ ($k \in \mathbb{N}^0$), where λ is minimal time between the two switchings [24, pp. 161–162]. Such a signal is referred to as discrete random binary sequence (DRBS). A time realisation of the DRBS and its frequency spectrum are shown in FIGURE 1.

The main idea of using DRBS for system excitation is to simultaneously excite the system with almost all frequencies of interest. In an ideal scenario this would mean using band-pass limited white noise. DRBS is a signal with close statistical resemblance with white noise. The power spectral density $\Phi_X^d(\omega)$ of the DRBS is shown in FIGURE 1b and reads:

$$\Phi_X^d(\omega) = a^2\lambda \left| \frac{\sin\left(\frac{\omega\lambda}{2}\right)}{\frac{\omega\lambda}{2}} \right|^2 . \tag{1}$$

where λ represents the minimal time between the two switchings, ω represents the angular frequency and a represents the amplitude of the generated signal. Power spectrum has zeros exactly at integer multiples of $1/\lambda$. Useful, near-flat part of the frequency band f_B is approximately determined by

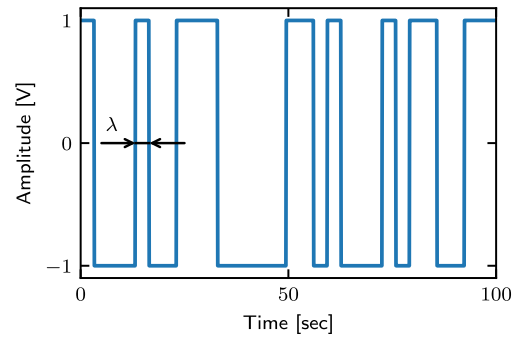

(a)

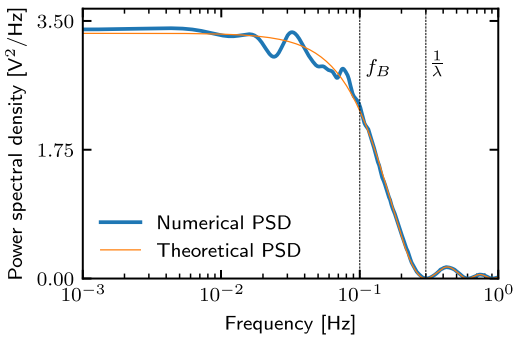

(b)

FIGURE 1. (a) Discrete random binary sequence waveform generated with λ = 3.3 seconds with the effective band $f_B = 0.1$Hz. (b) Power spectral density of the discrete random binary sequence. Numerical plot is calculated using a 300 seconds long realisation of the DRBS signal and Welch method for power spectral density estimation.

the −3 dB crossover frequency $f_B = \frac{1}{3\lambda}$ [26]. The complete derivation of (1) is given in Appendix A.

III. CONTINUOUS WAVELET TRANSFORM

Continuous wavelet transform (CWT) belongs to the group of time-frequency analysis methods. The simplest example of the time-frequency analysis is the short-time Fourier transform. It segments the measured signal $f_m(t)$ by using sliding window $g(t)$ in the time domain. The short-time Fourier transform is defined as:

$$F(\tau, \omega) = \int_{-\infty}^{+\infty} f_m(t) g(t-\tau) e^{-j\omega t} dt, \tag{2}$$

where $g(t)$ is window function.

As such, (2) can be regarded as a time localised Fourier transform. Fourier transform is performed at each position of the sliding window $g(t)$, which results in a sequence of spectra, hence the name time-frequency analysis.

A challenge with time-frequency analysis concerns the limits of resolution expressed by the Heisenberg-Gabor inequality [27]. We assume $f(t) = f_m(t) \cdot g(t)$ and its Fourier transform $F(\omega)$ are well localized functions. The center in time of the function f is defined as

$$\mu_t = \frac{1}{||f||^2} \int_{-\infty}^{\infty} t|f(t)|^2 dt$$

The concentration of the function around the center is expressed with the spread Δt

$$\Delta t = \frac{1}{||f||} \left(\int_{-\infty}^{\infty} (t-\mu_t)^2 |f(t)|^2 dt \right)^{\frac{1}{2}} \tag{3}$$

In the same spirit the center μ_ω and the spread $\Delta\omega$ are defined

$$\mu_\omega = \frac{1}{||F||^2} \int_{-\infty}^{\infty} \omega |F(\omega)|^2 d\omega$$

$$\Delta\omega = \frac{1}{||F||} \left(\int_{-\infty}^{\infty} (\omega-\mu_\omega)^2 |F(\omega)|^2 dt \right)^{\frac{1}{2}} \tag{4}$$

Then the Heisenberg-Gabor inequality reads [28]

$$\gamma = \Delta t \cdot \Delta\omega \geq \frac{1}{2} \tag{5}$$

and γ stands for the area of the Heisenberg box described with the rectangle $[\omega, \omega + \Delta\omega] \times [t, t + \Delta t]$.

Message contained in (5) is illustrated in FIGURE 2 by indicating the bounds of the selected time-frequency resolution. For more detailed definition of the joint time-frequency resolution one may refer to [29, Chapter 2].

The left-hand plot represents the case of the short-time Fourier transform (2) where the time-frequency resolution is kept constant. The shape of the rectangle is determined by the selected window function $g(t)$. The right-hand graph depicts the so-called adaptive time-frequency resolution. In this case, at high frequencies, higher precision in time localisation is achieved at the cost of lower frequency resolution. The opposite is true for the low-frequency region, where high frequency resolution is traded for the low time resolution. Regardless of the partitioning, the area of the "rectangles" remains constant as guided by (5).

Fixed length time window in short-time Fourier transform (2) results in an inflexible time-frequency partitioning (plot on the left in FIGURE 2). Better results can be achieved by using more sophisticated functions that define orthogonal space capable of describing the transient signals in a more efficient manner [30]. One such transform is *continuous wavelet transform*, in which any finite energy signal $f(t)$ can be represented with a set of orthogonal functions $\psi(t)$ referred to as wavelets:

$$Wf(u, s) = \frac{1}{\sqrt{s}} \int_{-\infty}^{\infty} f(t) \psi^* \left(\frac{t-u}{s} \right) dt, \tag{6}$$

where u represents time shift parameter and s is a scaling parameter. The scaling parameter contracts and expands the mother wavelet thus achieving adaptive time-frequency resolution, cf. the right-hand part of FIGURE 2.

There are numerous families of mother wavelets each with their own strengths and weaknesses. Since the goal is to analyse impedance data, only complex mother wavelets can be considered for this task. The most notable mother

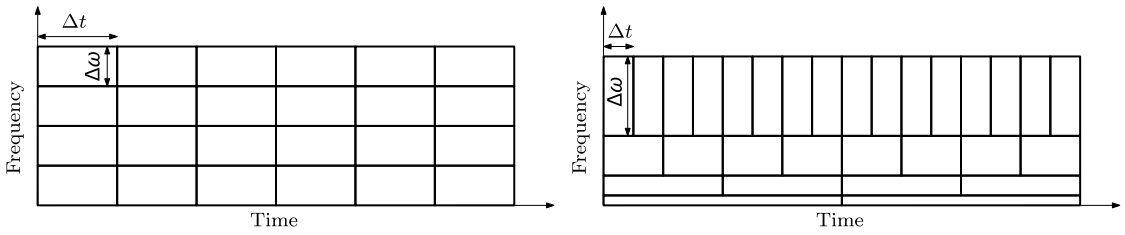

FIGURE 2. Schematic representation of the general concepts of time-frequency resolution. The left-hand graph shows constant time-frequency resolution typical for the short-time Fourier transform. The right-hand plot shows adaptive time-frequency resolution, a partitioning that is typical for the wavelet transform.

wavelets for performing CWT are Morlet [31], Bump wavelet, the Morse wavelet [32], [33] and the Lognormal wavelet [34].

A. SELECTION OF MOTHER WAVELET

The most common criterion for selecting the mother wavelet is its time-frequency resolution [29], [30], [34]. The time and frequency resolution of a wavelet function defines the minimal time and frequency difference for which two mono-component sinusoidal signals can be still reliably distinguished [29]. In the sequel we will analyse the time and frequency resolution separately as well as joint time-frequency resolution.

The Morlet wavelet and its Fourier transform are given respectively by

$$\psi_{\omega_0}(t) = \pi^{-1/4}\left(e^{j\omega_0 t} - e^{-\frac{\omega_0^2}{2}}\right)e^{-\frac{t^2}{2}} \tag{7a}$$

$$\Psi_{\omega_0}(\omega) = \pi^{1/4}e^{-\frac{(\omega-\omega_0)^2}{2}}\left(1 - e^{-\omega\omega_0}\right) \tag{7b}$$

where ω_0 is the central frequency.

The Morlet wavelet has optimal joint time-frequency concentration i.e. the Heisenberg box area reaches its lower bound $\Delta t\Delta\omega = \frac{2\pi}{\sqrt{2}}$. However, in spite of strong properties, the Morlet wavelet suffers from some weaknesses. In particular, it depends only on one parameter ω_0. Also, we are also limited with the parameter choices it cannot be considered analytic for $\omega_0 < 5\ \mathrm{s}^{-1}$.

The Morse wavelet is designed as a two-parameter family of wavelets aimed to achieve optimal localization in the sense that the eigenvalues of a joint time-frequency localization operator are maximized. The general form of the Morse wavelet in frequency domain is defined as follows [35]:

$$\Psi(\omega) = U(\omega)K_{\alpha,\beta}\omega^{\beta}e^{-\omega^{\alpha}} \tag{8}$$

where $U(\omega)$ is Heaviside unit step function and $K_{\alpha,\beta}$ is normalizing factor. However, for more computationally efficient calculation the following form of the Morse wavelet is used in the analysis that follows [29]:

$$\psi(\omega) = U(\omega)e^{-\omega^a + q\left(\log\omega + \frac{1}{a}\log\frac{ae}{q}\right)}, \tag{9}$$

where parameter q is related to the central frequency ω_0 as $\omega_0 = \frac{q^{(1/a)}}{a}$ and e represents the Euler's number. Due to its complexity, the wavelet transform is performed by a simple multiplication in the frequency domain by using FFT algorithm. The computational complexity is $n\log(n)$, where n is the number of samples in the signal. For that reason the time-domain waveform of the Morse wavelet is not required.

In can be noticed that in the cases of Morlet as well as Morse wavelet the parameter $\omega_0 = 2\pi f_0$ directly affects the wavelet's frequency resolution $\Delta\omega$. A comparison of the features of the Morlet and Morse wavelet is presented in FIGURE 3. Three aspects are analysed:

a) the frequency resolution depending on the central frequency parameter $\omega_0 = 2\pi f_0$,
b) time resolution (minimal time $\Delta\tau$) in which two consecutive impulses can be distinguished depending on the frequency resolution, and
c) the variation of the joint time-frequency resolution γ with respect to the frequency resolution. The value of γ is related to the minimal resolvable area in which two signals can be reliably distinguished both in time and in frequency.

Regarding the first aspect, addressed in FIGURE 3(a), the Morlet wavelet reaches a plateau for the frequencies below $\omega_0 = 3\ \mathrm{s}^{-1}$, which is not the case for the Morse wavelet. This effect is mainly due to the fact that for the low values of central frequency ω_0 the Morlet wavelet looses the analytical properties [23]. The time resolution of both wavelets is similar, as shown in FIGURE 3(b). The joint time-frequency resolution γ, shown in FIGURE 3(c), is slightly lower in the case of Morlet wavelet.

For the case of battery EIS, the goal is to achieve sufficiently accurate results at the low frequencies. Since the Morse wavelet preserves the analytical properties even at the ultra-low frequencies [23], all of the subsequent analysis is performed using Morse wavelet as the mother wavelet.

B. IMPEDANCE EVALUATION USING CWT

The impedance values can be obtained by CWT in a pretty much similar way as with the Fourier transform. CWT analysis of the voltage $u(t)$ and current $i(t)$ will result in a set of complex wavelet coefficients:

$$\begin{aligned} Wi(t,f) &= \Re\{Wi(t,f)\} + j\Im\{Wi(t,f)\}, \\ Wu(t,f) &= \Re\{Wu(t,f)\} + j\Im\{Wu(t,f)\}. \end{aligned} \tag{10}$$

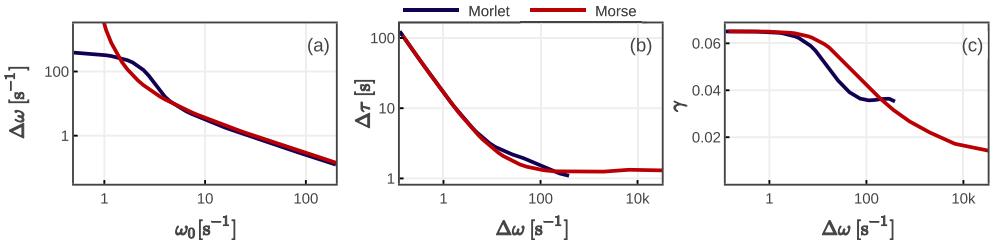

FIGURE 3. Comparison of time-frequency characteristics between the Morlet and the Morse wavelet. The notation is adopted from [34]. (a) the minimal resolvable frequency depending on the central frequency parameter ω_0, (b) the minimal time $\Delta\tau$ required for distinguishing two impulses and (c) the joint time-frequency resolution, which is related to the minimal resolvable area in which two signals can be reliably distinguished both in time and in frequency.

where $Wx(t,f)$ denotes wavelet of a signal $x(t)$ and is function of time t and frequency f. The impedance is the ratio of the wavelet coefficients:

$$Z(t,f) = \frac{Wu(t,f)}{Wi(t,f)}. \tag{11}$$

It should be noted that the impedance calculated in (11) is defined by time and frequency and provides *instantaneous* amplitude and phase at every time-frequency point. This means that one can track the evolution of the phase and amplitude of the impedance for each frequency over time. Conversely, the impedance calculated through FFT provides only *time-averaged values* of the amplitude and phase for each frequency. Hence, having the time evolution of the complex impedance, it becomes possible to perform more detailed analysis on the impedance values, a task that renders impossible when the impedance is calculated through FFT.

IV. A SIMULATED EXAMPLE

Method described in Section III is validated on a simulated Randles circuit, shown in FIGURE 4. Such a circuit is commonly used to simulate impedance of lithium-ion batteries [36]–[38]. The theoretical impedance of the Randles circuit reads:

$$Z(j\omega) = R_s + \frac{1}{(j\omega)^{\alpha_1} Q_1 + \frac{1}{R_1 + Z_w}} + j\omega L \tag{12}$$

where R_s is the series resistance, R_1, Q_1 and α_1 are the parameters of the pole, where $Q_1 \in \mathbb{R}^+$ and $\alpha_1 \in [0, 1]$, Z_w is the Warburg impedance $Z_w = \frac{1}{Q_w(j\omega)^{0.5}}$ and L is the inductance.

The goal is to estimate the impedance characteristic of Randles circuit (12) in the frequency band between 600 μHz and 2 kHz using time domain excitation and response signals. Since the DRBS has almost flat power spectrum approximately up to $\frac{1}{3\lambda}$ (see FIGURE 1b), one might assume that only one waveform with large enough λ will suffice. However, an almost flat power spectrum can be achieved only with an infinitely long signal. We suggest to split the required bandwidth into decades and for each decade use a DRBS excitation with different λ. In such a way, each frequency band will be excited with sufficient energy allowing for accurate spectral

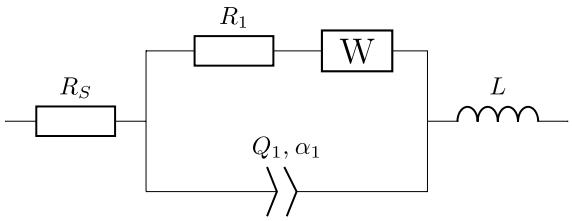

FIGURE 4. Schematic representation of the Randles circuit (12).

estimation. So, for the required numerical validation, the system was excited with 6 DRBS signals whose bandwidths and duration are listed in Table 1.

TABLE 1. Time needed for each DRBS signal used for excitation.

	1	2	3	4	5	6
Bandwidth [Hz]	0.01	0.1	1	10	100	1000
Duration [s]	5000.0	300.0	200.0	30	3.0	1.0
f_s [Hz]	200	500	500	1000	5000	50000

The simulation of the model (12) was performed in potentiostatic mode. The DRBS excitation was applied to the voltage $u(t)$ and the response was recorded through the output current $i(t)$. Since the simulation was done in time domain, the time response of (12) was simulated using closed-form solutions of linear fractional-order differential equations [39]. The sampling frequency was different for each simulated signal and is given in Table 1. The waveforms of the voltage $u(t)$ and current $i(t)$ are shown in FIGURE 5.

With 6 excitation signals, the overall impedance was obtained by merging results of the CWT from each DRBS excitation and the corresponding response $i(t)$, see FIGURE 6. The estimated characteristic almost ideally matches the theoretical impedance, shown with grey markers.

From the Table 1 it can be seen that approximately 97 minutes of excitation is required to evaluate the whole impedance. Also, it should be noted that by using our approach the impedance spectrum is evaluated with a frequency resolution of 122 frequency points per decade. The length of the lowest DRBS bandwidth dictates the lowest frequency, at which the

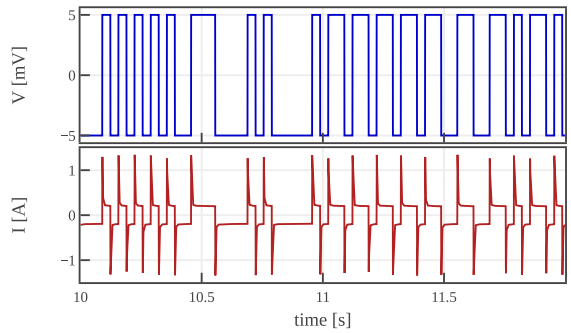

FIGURE 5. DRBS voltage excitation signal and the theoretical current response signal of the Randles circuit to the DRBS excitation.

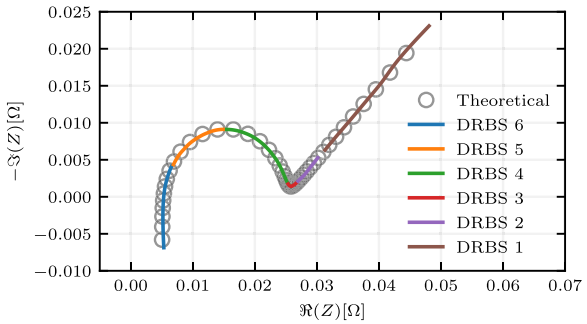

FIGURE 6. Comparison between the theoretical impedance and calculated impedance by applying the method proposed in Section III. In order to calculate the impedance 6 different DRBS signals (Table 1) were used.

impedance can be calculated. In the particular simulation the length of the DRBS with the bandwidth 0.01 Hz corresponds to the 3 periods of the lowest frequency for which the impedance is calculated (600 μHz). If the same number of points had to be evaluated by using the classical single sine-wave excitation signal with only 2 periods, that would overall take around 54 hours of excitation. For comparison, by using the standard 10 points per decade the time needed for impedance evaluation by 10 mono-component sinusoidal signals in the same frequency bandwidth from 600 μHz to 2 kHz, will take around 4.7 hours of excitation time. This example clearly indicates that the method described in Section III accurately determines the low frequency spectra in spite of a shorter excitation time.

V. EXPERIMENTAL VALIDATION

The method for fast EIS measurement was experimentally validated using 811 NMC-Graphite 18650 cylindrical Li-ion battery (LG18650HG2, LG Chem). During measurements the battery was held fixed under constant applied force as shown in the lower part of the FIGURE 7.

A. EXPERIMENTAL SET-UP

Since the application of the method described in Section III requires access to the time domain data, the excitation and measurement equipment include high-precision data acquisition system, electronic load with built-in arbitrary waveform

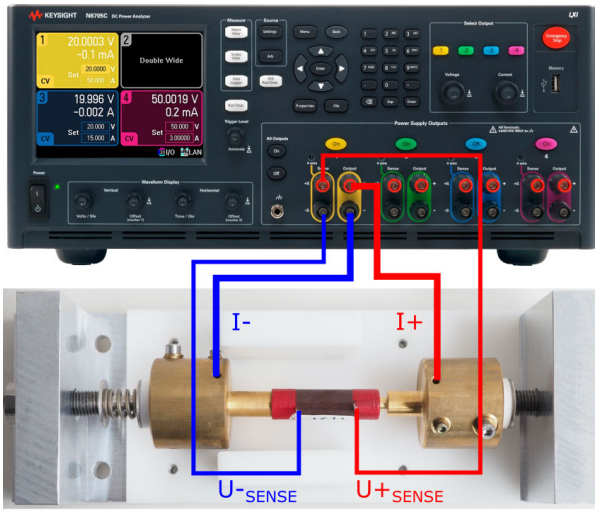

FIGURE 7. Block scheme of the experimental set-up for fast battery characterization.

generator and control unit. We used the Keysight N6705C DC power analyser together with the N6781A Source/Measure Unit module, which allows access to the time-domain signals. This device is a multi-functional power supply system that combines the functions of a DC voltage/current source together with built-in data acquisition system. The output of the device also includes arbitrary waveform generator. In order not to surpass the 5 mV voltage change of the battery, the experiment was performed in potentiostatic mode. The requirement of the restricted magnitude of imposed voltage perturbation when determining impedance response of a Li-ion battery is explained and clarified in the Supplementary Appendix D A block scheme of the set-up is shown in FIGURE 7.

B. EXPERIMENTAL PROTOCOL

Prior to impedance measurements the battery cell was preconditioned. At the side of positive terminal and at the lower part of the battery steel housing (negative pole) we have carefully spot-welded two nickel tab strips that served for connecting the sense (U+, U−) ports (FIGURE 7). Battery cell was placed in a specially designed measurement rack that exerts constant mechanical force of 150 N at the positive terminal and bottom of the housing via two massive brass electrodes that are connected with the current (I+, I−) ports. This means we can perform true 4-electrode measurements where all the resistances of the measuring wires (cables) and contact resistances at the two battery terminals are effectively eliminated. We placed the battery together with the rack in a temperature chamber and allowed for 2 hours for the temperature of the battery to equilibrate at 23 °C. We performed five initial galvanostatic ±3 A charge/discharge cycles in voltage range from 2.5 V up to 4.2 V, followed by a half-charge up to 3.705 V and 3 hours of voltage hold

whereby the current dropped below 1.5 mA. By applying this pre-conditioning procedure the battery was driven to be in thermal and electrochemical equilibrium at State of Charge 0.5. The impedance of the battery was measured in the frequency region 600 μHz to 1.1 kHz. Experiments were performed in potentiostatic mode by using DRBS excitation signals with amplitude $V_{AC} = 5$ mV. The amplitude was chosen in a way to guarantee linearity, but still big enough to maintain sufficient signal-to-noise ratio. The EIS was measured using 6 DRBS excitation signals as listed in TABLE 1. The pause between each DRBS sequences was 30 seconds.

As stated in the previous section, the lowest observable frequency in the spectra is determined by the duration of the excitation signal ($f_{min} = \frac{3}{T}$), where T represents the length of the acquired signal. In our case the lower observable frequency is $f_{min} = 600$ μHz. On the other hand, the highest observable frequency is determined by the sampling frequency of the acquired signal.

VI. RESULTS AND DISCUSSION

The same battery sample was measured using three different approaches:

1. **Initial measurements** Initially, the battery was measured using standard laboratory equipment BioLogic SP-200 by performing mono-component sinusoidal signal excitation in the frequency range between 1 mHz and 10 kHz with frequency resolution of 10 points per decade. These measurements are only used as a reference.
2. **Single sine measurements** For validation purposes using the equipment described in Section V, the EIS curve was measured using single sine excitation in the frequency interval between 1 mHz and 1 kHz. This might seem as a repetition of the first step. However, the goal was to reconstruct the original results using standard method so that we can check validity of the measurement equipment.
3. **DRBS based EIS** Using the same equipment as in the second step, the battery's EIS was measured in the same frequency band between 600μ Hz and 1.1 kHz using the proposed DRBS and CWT based approach.

The implementation of the approaches is available as supplementary material the details of which are presented in Appendix E.

A. INITIAL REFERENCE MEASUREMENTS

The EIS curve of the initial measurements is shown with black $\times$ in FIGURE 9. The EIS was measured after 5 initial charge/discharge cycles and comprises 68 frequency points (10 points per decade) in the frequency region between 1 mHz and 10 kHz. Excitation at each frequency point took 1 period. The whole characterisation process took 96 minutes together with pauses between the frequency points. The impedance characteristics, as expected, contain one semi-circle in the frequency region between 3 Hz and 5 kHz and constant-phase capacitive properties at frequencies below 3 Hz.

B. IMPEDANCE CALCULATION USING MONO-COMPONENT SINUSOIDAL EXCITATION

In order to validate the proposed approach, additional measurements were performed using the classical mono-component sinusoidal excitation in the same frequency band 1 mHz to 2 kHz with the resolution of 10 points per decade. The length of the sinusoidal excitation signal was 3 periods for the frequencies below 1 Hz and 10 periods for the frequencies above 1 Hz. The overall excitation time, without pauses between the frequency points, was 157.53 minutes. The obtained EIS curve is shown in FIGURE 9, along with the results of the DRBS based approach.

C. IMPEDANCE EVALUATION USING DRBS EXCITATION

With the DRBS excitation the EIS curve was evaluated in the frequency range 600 μHz and 1.1 kHz by using 6 different DRBS signals, as described in TABLE 1. The voltage excitation signal and the battery current response are shown in FIGURE 8. The characterisation was performed at $V_{DC} = 3.705$ V with amplitude $V_{AC} = \pm 5$ mV. The main rationale for using potentiostatic mode was to fulfill the requirement not to exceed the 5 mV voltage change, when performing characterization on battery. The amplitude of the noise in the voltage signal was estimated $V_{\text{noise}} = 114$ μV and the signal-to-noise ratio SNR = 90 dB. When calculating the impedance values, the parameters of the Morse wavelet in equation (9) were $a = 3$ and $q = 1.224$.

The obtained EIS curve is shown in FIGURE 9. By using the proposed method, the impedance is calculated at 862 frequency points, which amounts to approximately 100 points per decade. It should be noted that this can be easily increased by up to 3000 points per decade without changing the duration of the excitation. The total length of the excitation signals is 97 minutes. In order to accurately estimate impedance for the frequencies lower than 10 mHz, the length of the DRBS signal has to be at least 3 periods of the lowest frequency. Hence, in our example the length of the longest DRBS signal with 10 mHz bandwidth is 5000 seconds, which corresponds to 3 periods of the lowest observable frequency $f = 600$ μHz.

FIGURE 9 shows the comparison between initial impedance measurement performed with BioLogic SP-200, the impedance measured using DRBS signals and the impedance measured using classical single-sine excitation signals. It can be seen that the impedances obtained by the two approaches are identical.

It should be noted that the inductive part of the impedance exhibits a higher variance. This is due to a hardware's attenuation at higher frequencies. More details about the measured impedance spectra at frequencies higher than 1 kHz are given in Appendix C.

The key result is that by using the method described in section III, it becomes possible to estimate the probability distribution of the impedance values at the

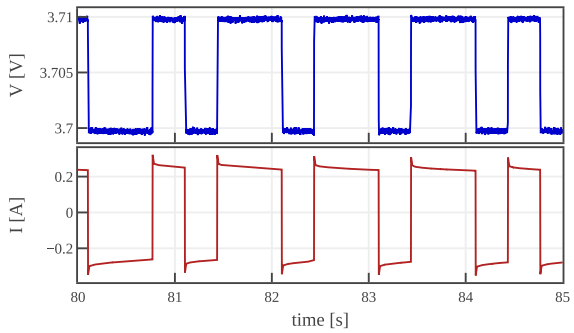

FIGURE 8. Voltage excitation signal and the current response of the battery.

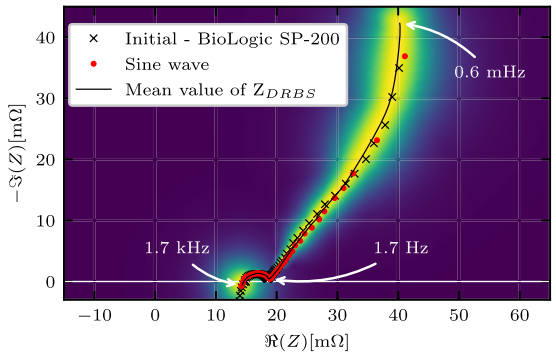

FIGURE 9. Comparison of impedance calculated using DRBS and classical single-sine excitation signals. The uncertainty region of the estimated impedance are represented with yellow colour.

calculated frequency points. This provides information regarding the confidence interval of the measurements. The uncertainty region of the estimated impedance is represented with brighter colours (yellow) in FIGURE 9. The details of the method for estimating impedance distribution are presented in Appendix B.

D. DISCUSSION

With classical sine-based EIS measurements the impedance is calculated at a discrete set of frequencies. Broadband excitation, combined with a sophisticated signal processing, allows the evaluation of the impedance at a high frequency resolution. The theoretical limit of the number of points N, in which the impedance can be calculated using the proposed approach, is $\mathrm{T} = \frac{1}{f_s} \times \mathrm{N}$, where T is duration of excitation and f_s is the sampling frequency. For example, in our case the sampling frequency is $f_s = 24.45$ kHz and the duration of measurement is 5834 seconds. That means with only 5834 seconds of measurement the impedance can be evaluated for the frequency range 600 μHz to 1.5 kHz at almost 200 million points using only single excitation signal.

As shown in FIGURE 9, the uncertainty of the impedance estimation at lower frequencies increases i.e. the spread of the confidence is getting larger for lower frequencies. Instead of analysing only time-averaged impedance values when using sine-based excitation, with the proposed approach it becomes possible to estimate the uncertainty of the measured impedance as explained in Appendix B. It should be pointed out that this uncertainty includes both unavoidable measurement errors, as well as the inherent randomness of the processes occurring during battery's operation. The uncertainty region is a valuable information reflecting the quality of the measurement, which is in field of EIS measurements usually neglected.

VII. CONCLUSION

The paper demonstrates the advantages of using DRBS excitation with Morse wavelet for broadband EIS compared to the conventional sine-based approach. The EIS is estimated at almost the continuum of frequency points without the need of additional excitation cycles. This greatly reduces the excitation time while in the same time improves the quality of the results.

Furthermore, having broad-band excitation as input, it becomes possible to assess the uncertainty of the measured impedance at each frequency point. This is a feature that is unavailable in classical sine-based approaches and has not been exploited yet.

Having a tool capable to get fast and accurate impedance values at ultra-low frequencies it will become possible to address the issues of SOH estimation in more details. The complete approach has computationally efficient implementation. The proposed CWT based impedance can be easily calculated as series of Fourier transforms. All these properties show the practical merit of proposed CWT based EIS.

APPENDIX A
AUTOCORRELATION AND POWER SPECTRAL DENSITY OF THE DRBS

The imposed DRBS voltage variation is denoted as $u(t)$ and its realisation reads [40]

$$u(t) = \sum_n U_n w\left(\frac{t - n\lambda - D}{\lambda}\right), \tag{13}$$

where U_n is the amplitude of the n^{th} pulse, which can be either $-a$ or a, D is the initial displacement (delay) of the initial pulse, λ is the minimal width of the pulse and $w(t)$ is a rectangular pulse defined as:

$$w(t) = \begin{cases} 1 & \text{for } |t| \le \frac{1}{2} \\ 0 & \text{elsewhere.} \end{cases} \tag{14}$$

The autocorrelation function of (13) can be written as:

$$R_{uu}(t_1, t_2) = E\left[\sum_n \sum_l U_n U_l \, w\left(\frac{t_1 - n\lambda - D}{\lambda}\right) \times w\left(\frac{t_2 - n\lambda - D}{\lambda}\right)\right]. \tag{15}$$

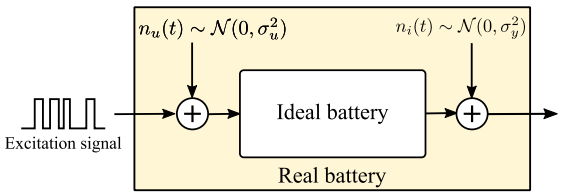

FIGURE 10. Schematic of a general measurement system form performing EIS with $n_u(t)$ is the input noise and system uncertainties and $n_i(t)$ is the measurement noise.

Since the amplitudes of different pulses $l \neq n$ are independent, and are also independent of the displacement D then the above relation becomes:

$$R_{uu}(t_1, t_2) = a^2 \sum_n E\left[w\left(\frac{t_1 - n\lambda - D}{\lambda}\right) \times w\left(\frac{t_2 - n\lambda - D}{\lambda}\right)\right] + \sum_{n \neq l} \sum_l E[U_n]E[U_l] \times E\left[w\left(\frac{t_1 - n\lambda - D}{\lambda}\right) w\left(\frac{t_2 - n\lambda - D}{\lambda}\right)\right]. \tag{16}$$

For equiprobable values of $-a$ and a the second term is zero. The first term is an autocorrelation of two rectangular signals. Consequently, it can be easily shown that the autocorrelation of the DRBS with equiprobable states $-a$ and a reads:

$$R_{uu}(\tau) = \begin{cases} a^2\left(1 - \frac{|\tau|}{\lambda}\right) & \text{for } |t| \leq \lambda \\ 0 & \text{elsewhere,} \end{cases} \tag{17}$$

where $\tau = t_2 - t_1$. The power spectral density (1) can be easily derived as a Fourier transform of the autocorrelation (17).

APPENDIX B
ESTIMATING THE PROBABILITY DISTRIBUTION OF THE MEASURED EIS VALUES

The schematic of the measurement setup is shown in FIGURE 10. The battery under test can be regarded as an ideal system. When performing characterisation we have two sources of disturbances. The first one are the disturbances imposed on the excitation signal denoted as $n_u(t) \sim \mathcal{N}(0, \sigma_u^2)$. These disturbances include any noise from the excitation circuit as well as any influence of inherent random processes within the battery. The second source is the measurement noise $n_i(t) \sim \mathcal{N}(0, \sigma_i^2)$. Consequently, the time evolution of the wavelet coefficients (10) at each frequency follow the statistical properties of a zero-mean Gaussian circular complex random variable [41]. Since the wavelet coefficients of the voltage $Wu(t, f)$ and the current $Wi(t, f)$ are linked through a linear system,[1] they are correlated. The resulting bivariate complex Gaussian distribution has the following covariance matrix:

$$\Sigma = \begin{bmatrix} \sigma_u^2 & \rho\sigma_u\sigma_i \\ \rho^*\sigma_u\sigma_i & \sigma_i^2 \end{bmatrix}, \tag{18}$$

where $\rho = \rho_r + j\rho_i$ is the complex correlation coefficient such that $|\rho| \leq 1$. The resulting distribution can be derived in a closed form as [20], [42]

$$f_Z(z) = \frac{1 - |\rho|^2}{\pi\sigma_u^2\sigma_i^2}\left(\frac{|z|^2}{\sigma_u^2} + \frac{1}{\sigma_i^2} - 2\frac{\rho_r z_r - \rho_i z_i}{\sigma_u\sigma_i}\right)^{-2}, \tag{19}$$

where z_r and z_i are real and imaginary components of the random variable Z. The location of the mode of $f_Z(z)$ depends on the correlation coefficient ρ.

APPENDIX C
FREQUENCY DOMAIN ANALYSIS OF THE OBTAINED RESULTS

The Nyquist plot of the measured impedance spectra of the battery shown in FIGURE 9 describes the joint behaviour of the real and imaginary parts. To get a better overview of the accuracy of the proposed approach, the variance of the real and imaginary impedance components over frequency are shown in FIGURE 11 and FIGURE 11, respectively. FIGURE 12, respectively. As already shown in the analysis of the Nyquist plot, the uncertainty of the measured impedance is higher at lower frequencies.

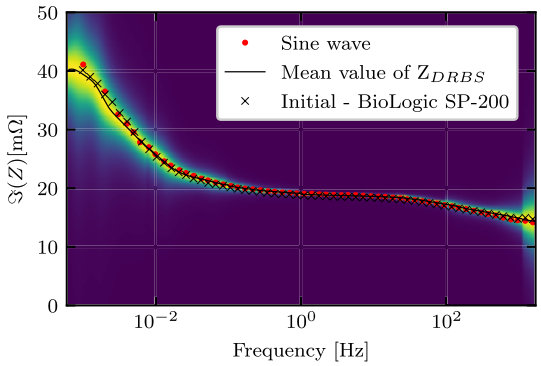

FIGURE 11. Comparison of real part of the impedance calculated using DRBS and classical single-sine excitation signals. The uncertainty region of the estimated real part of the impedance is represented with yellow colour.

There is an additional effect of increased uncertainty at higher frequencies (1kHz). This is a direct result of the frequency characteristics of the data acquisition system. FIGURE 13 shows the comparison between the bandwidths of the theoretical and calculated power spectral density (PSD) of each excitation signal DRBS used to perform EIS. It is clear that the measured PSD for all DRBS excitation signals are identical to the theoretical PSD, except for DRBS 1000 Hz (FIGURE 13f). Above 1 kHz, the effective amplitude of the measured signal is significantly lower. This leads to a reduced SNR and thus to an increase of the measurement uncertainty.

[1] When using small amplitude excitation the battery's characteristic can be regarded as piecewise linear.

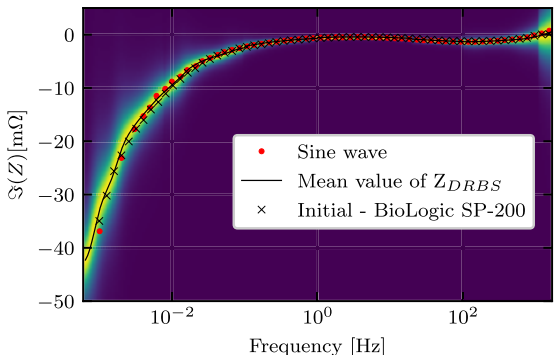

FIGURE 12. Comparison of imaginary part of the impedance calculated using DRBS and classical single-sine excitation signals. The uncertainty region of the estimated imaginary part of the impedance is represented with yellow colour.

This effect can be clearly seen in FIGURE 14, which is a zoomed part of the FIGURE 9 at high frequencies.

APPENDIX D
RESTRICTION OF THE MAGNITUDE OF THE INPUT EXCITATION SIGNAL

During the impedance response measurements of Li-ion batteries, we are subject to the constraint of the maximum magnitude of the voltage (and current) perturbation. The limitation is of electrochemical in origin. First, it is important to distinguish between two fundamentally different aspects of impedance measurements. The first is the accuracy of the imposed (excitation) signal and the obtained response signal, which determines the "quality" of the obtained impedance data and is directly related to the measurement parameters such as SNR, etc. The second aspect, which is not related to instrumentation and signal processing, is the aspect of electrochemical stability of the tested system (battery) during the measurement. In general, tests on Li-ion battery systems (e.g. the LG18650HG2 used here) have to be considered with great care when performing good quality impedance measurements over a wide frequency range (down to very low frequencies).

Moreover, it should be noted that Li-ion batteries can exhibit significant (long-lasting) relaxation times when approaching equilibrium (for selected SOC). In our particular case of the LG18650HG2 battery, which consists of an 811 Ni rich NMC cathode and a graphite anode, corresponding relaxation times of the two active electrode materials have been observed in the range of (at least) several hours. For example, in a recent study of the 811 NMC cathode at Galvanostatic Intermittent Titration Technique (GITT), it was observed that the typical relaxation times of this material ranged from 2 hours to more than 4 hours (depending on SOC) [43]. Therefore, a reasonable relaxation time must be allowed prior to the impedance measurement. There are two ways to implement this: either by introducing a classical open-circuit period or by applying a suitable selected constant voltage to the battery cell. In this work, we used the second approach because we wanted the battery to operate at the selected SOC = 0.5, which in our particular case of the 811 NMC graphite battery corresponds to 3.705 V. The decision that

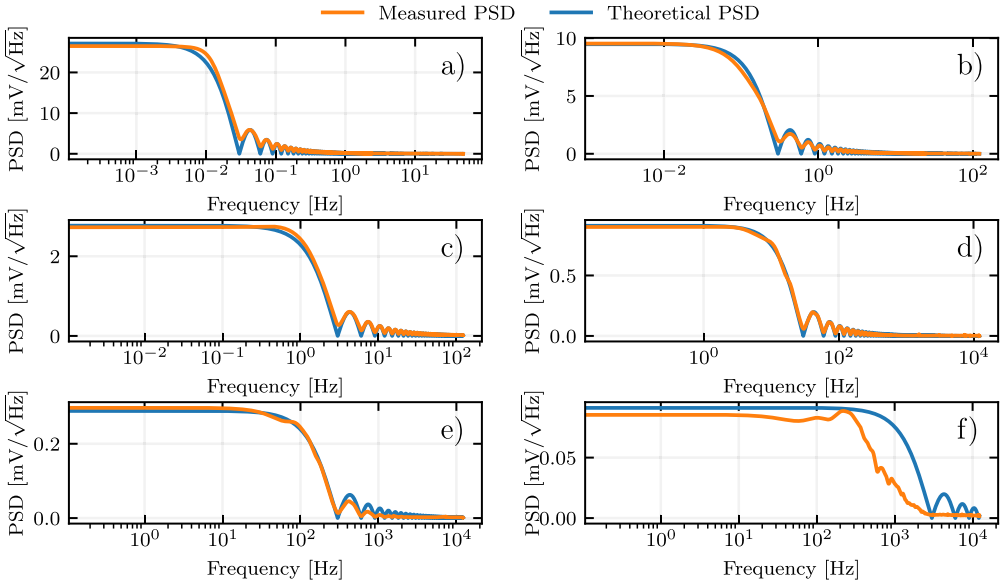

FIGURE 13. Comparison between the bandwidths of the theoretical and measured power spectral density (PSD) of each excitation DRBS signal used to perform EIS. In the figure a) represents DRBS 0.01 Hz, b) represents DRBS 0.1 Hz, c) represents DRBS 1 Hz, d) represents DRBS 10 Hz, e) represents DRBS 100 Hz and f) represents DRBS 1000 Hz. Above 1 kHz, the effective amplitude of the measured signal is significantly lower leading to a reduced SNR which corresponds to an increased measurement uncertainty.

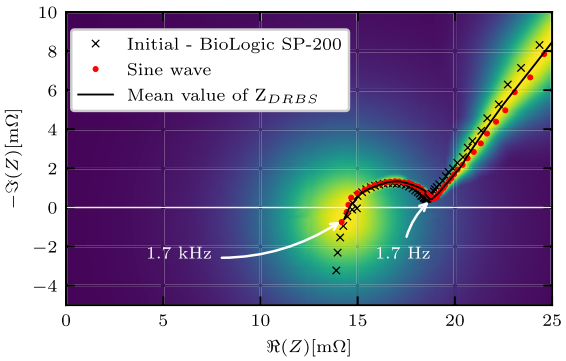

FIGURE 14. Zoomed part of the FIGURE 9 in which the inductive effect is visible. The increased variance in the inductive part is due to the limited acquisition bandwidth, as can be seen from the results in FIGURE 13.

the SOC should be close to 0.5 was made based on the fact that at this SOC the battery (with all its internal components) is electrochemically and chemically most stable. In other words, for the case of LG18650HG2, the choice of a SOC = 0.5 ensures that the system will not change over long periods of time, allowing a systematic and reliable study of the corresponding impedance. In contrast, Ni-rich NMC active materials are subject to strong side electrochemical processes when approaching the upper limit voltage (e.g., 4.2 V), leading to degradation of the cathode during long-term charge/discharge cycles [44].

With the above considerations in mind, we can move on to the important point of whether to use a (small) applied voltage perturbation or a current-controlled perturbation. Li-ion insertion materials possess exactly defined (relaxed) open-circuit voltage (V_{OC}) as a function of SOC. The value of V_{OC} is determined by the difference in the chemical potential of lithium in the two host materials (cathode-anode). In other words, when a battery is allowed to relax for a sufficiently long period of time at open-circuit voltage (or, alternatively, for a sufficiently long period at constant voltage so that the corresponding current drops to a very low level), it is considered to be very close to the true thermodynamic equilibrium state. In this case, the corresponding voltage V_{OC} is very close to $V_{eq}(\mathrm{SOC}, T)$ (this notation shows that the equilibrium voltage is a function of both SOC and temperature T). Thus, for accurate electrochemical measurements, both SOC and temperature have to be accurately controlled (temperature control is realized by placing the tested battery in an appropriate temperature chamber or dipping it in a thermostatic bath).

FIGURE 15 shows measured voltage profiles of the galvanostatic charge/discharge cycle for the 811 NMC-Li cell (C/20 obtained by GITT sequence) and the LG18650HG2 battery cell, obtained at a current density of C/50 (the C rate corresponds to reaching a full nominal capacity in 50 hours of charging or discharging, i.e., nominally 60 mA). The measured voltage of the battery LG is about 100 mV lower compared to the 811 NMC-Li cell, which is due to the fact that the main operating voltage of the graphite anode is about +100 mV compared to the metallic lithium anode. We can observe that for the selected SOC = 0.5, the voltage hysteresis of the NMC-Li cell is ±9 mV relative to the V_{eq} (3.805 V) and the voltage hysteresis of the LG18650HG2 battery is ±12 mV relative to the V_{eq} (3.705 V). The intrinsic voltage hysteresis of the two compared cells is indeed even lower and could be determined, for example, by "quasi-static" measurements at extremely low rates [45]. Let us define the maximum voltage deviation from the equilibrium voltage as: $\Delta V_{max} = V - V_{eq}$, where V is the applied voltage. The measured voltage hysteresis at finite current density sets the upper bound on the limited (maximum) voltage deviation we can afford in impedance measurements. Namely, if we increase or decrease the applied voltage V by more than $\pm\delta V_{max}$ relative to V_{eq}, we push the system out of voltage hysteresis. So in this particular case, if the applied voltage perturbation is greater than about ±9 mV, the system (battery) slips out of linearity. Thus, one of the basic conditions for impedance determination will no longer be satisfied. In voltage-controlled experiments, we must be careful not to exceed the range of voltage hysteresis. In the present work, we decided to limit the maximum voltage deviation to ±5 mV. In this way we have ensured that the linearity of the system is maintained at all tested frequencies.

An exception to the above rule is possible for cases where experiments are of very short duration (mainly high frequency). In particular, if the time/frequency is short/high enough that the storage of energy (charge) in the interior of solid-state particles of the active material has not yet started, then higher voltage perturbations can be used. In the present case of NMC graphite battery, this cut-off frequency is about 0.3 Hz [43].

On the other hand, when performing measurements by using current-driven (so-called galvanostatic) perturbations, we have to be very careful not to exceed the minimum frequency (f_{min}) at which we would push the system under test out of voltage hysteresis. As described and discussed above for the currently under tested LG18650HG2 battery, the largest input perturbation at SOC = 0.5 should definitely be less than $\Delta V_{max} = \pm 12$ mV. Also, to ensure that we stay within the linear response of the system, we choose the maximum perturbation smaller than ΔV_{max} of the 811 NMC cathode material (±9 mV) by taking the narrower bound of ±5 mV. We directly obtain the maximum current amplitude ($I_{a,max}$) that can be applied to the battery under test by the relation:

$$I_{a,max} = \frac{\Delta V_{max}}{|Z(f)|} \tag{20}$$

where $|Z(f)|$ is the magnitude of the impedance at a chosen frequency f. Specifically, in the present work, for the case of LG18650HG2 battery at SOC = 0.5, we found the following values for $|Z(f)|$: 18.4 mΩ (1 Hz), 20.1 mΩ (100 mHz), 27.5 mΩ (10 mHz) and 55.8 mΩ (1 mHz). According to the above relation, we obtain the corresponding limits of

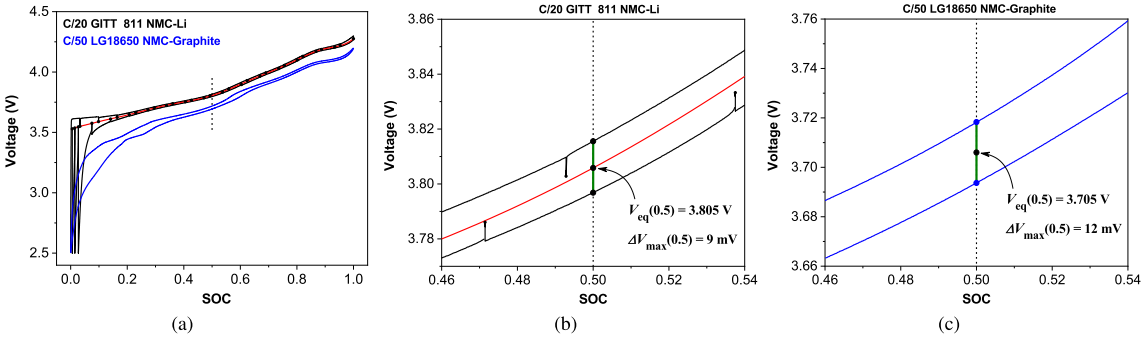

FIGURE 15. **(a) Comparison of measured voltage hysteresis for 811 NMC-Li cell (C/20 GITT) and LG18650HG2 battery cell (C/50). (b) and (c) Enlarged view of the reading out of the corresponding overvoltage $\Delta V_{max}(0.5)$ at the selected SOC = 0.5.**

current amplitude $I_{a,max}$: 271 mA (1 Hz), 249 mA (100 mHz), 182 mA (10 mHz) and 90 mA (1 mHz).

In summary, for impedance measurements performed down to very low frequencies, we have defined a constraint on the maximum magnitude of the current perturbation that we can apply without violating the linearity of the system. For the battery studied in this work (LG18650HG2), the current perturbation has to be limited to below 90 mA for measurements below 1 mHz. Since we were also interested in impedance behavior at low (or even ultra-low) frequencies in this work, we decided to use voltage-controlled perturbations to safely avoid problems with the limited current. Also, as mentioned earlier, most measurements were made using the Keysight N6705C DC power analyser. The accuracy of the system output voltage is 0.025% + 600 μV, while the accuracy of the current is 0.04% + 300 μA.

APPENDIX E
DESCRIPTION OF THE SUPPLEMENTARY MATERIAL

The supplementary material contains all the necessary data and `Python notebook` required for the reconstruction of the presented results. The entry point is the notebook `Supplementary_material.ipynb`. This notebook contains all the necessary guidelines and referenced libraries, which are readily available as open source versions. The corresponding `git` references are given in the notebook. All scripts and datasets are available for download at `https://repo.ijs.si/gnusev/supplementary_material.git`.

Voltage was used as an excitation signal to test the battery. The amplitude of the DRBS signal was U_{AC} = 5 mV The dataset used for calculation of impedance spectra consist of 6 different files, named:

- `DRBS_0.01hz.mat`
- `DRBS_0.1hz.mat`
- `DRBS_1hz.mat`
- `DRBS_10hz.mat`
- `DRBS_100hz.mat`
- `DRBS_1000hz.mat`

Each file consists of the time-domain voltage (u) and current signal (i), their sampling frequency (f_s) and minimum (f_{min}) and maximum (f_{max}) frequency in which the CWT is calculated. Additionally the measured impedance spectra from BioLogic SP-200 is also provided in order to compare measured impedance spectra.

REFERENCES

[1] X. Hu, C. Zou, C. Zhang, and Y. Li, "Technological developments in batteries: A survey of principal roles, types, and management needs," *IEEE Power Energy Mag.*, vol. 15, no. 5, pp. 20–31, Sep. 2017.

[2] Y. Zhang, Q. Tang, Y. Zhang, J. Wang, U. Stimming, and A. A. Lee, "Identifying degradation patterns of lithium ion batteries from impedance spectroscopy using machine learning," *Nature Commun.*, vol. 11, no. 1, pp. 1–6, Dec. 2020.

[3] M. Oldenburger, B. Bedürftig, A. Gruhle, F. Grimsmann, E. Richter, R. Findeisen, and A. Hintennach, "Investigation of the low frequency warburg impedance of Li-ion cells by frequency domain measurements," *J. Energy Storage*, vol. 21, pp. 272–280, Feb. 2019.

[4] M. Spielbauer, P. Berg, M. Ringat, O. Bohlen, and A. Jossen, "Experimental study of the impedance behavior of 18650 lithium-ion battery cells under deforming mechanical abuse," *J. Energy Storage*, vol. 26, Dec. 2019, Art. no. 101039.

[5] H. Dai, B. Jiang, and X. Wei, "Impedance characterization and modeling of lithium-ion batteries considering the internal temperature gradient," *Energies*, vol. 11, no. 1, p. 220, Jan. 2018.

[6] J. Fang, W. Shen, S. H. S. Cheng, S. Ghashghaie, H. KhurramShahzad, and C. Chung, "Four-electrode symmetric setup for electrochemical impedance spectroscopy study of lithium–sulfur batteries," *J. Power Sources*, vol. 441, Nov. 2019, Art. no. 227202.

[7] I. J. Gordon, S. Genies, G. S. Larbi, A. Boulineau, L. Daniel, and M. Alias, "Original implementation of electrochemical impedance spectroscopy (EIS) in symmetric cells: Evaluation of post-mortem protocols applied to characterize electrode materials for Li-ion batteries," *J. Power Sources*, vol. 307, pp. 788–795, Mar. 2016.

[8] J. Li, D. Sun, X. Jin, W. Shi, and C. Sun, "Lithium-ion battery overcharging thermal characteristics analysis and an impedance-based electrothermal coupled model simulation," *Appl. Energy*, vol. 254, Nov. 2019, Art. no. 113574.

[9] X. Wang, X. Wei, H. Dai, and Q. Wu, "State estimation of lithium ion battery based on electrochemical impedance spectroscopy with on-board impedance measurement system," in *Proc. IEEE Vehicle Power Propuls. Conf. (VPPC)*, Oct. 2015, pp. 1–5.

[10] A. Barai, G. H. Chouchelamane, Y. Guo, A. McGordon, and P. Jennings, "A study on the impact of lithium-ion cell relaxation on electrochemical impedance spectroscopy," *J. Power Sources*, vol. 280, pp. 74–80, Apr. 2015.

[11] F. M. Kindermann, A. Noel, S. V. Erhard, and A. Jossen, "Long-term equalization effects in Li-ion batteries due to local state of charge inhomogeneities and their impact on impedance measurements," *Electrochim. Acta*, vol. 185, pp. 107–116, Dec. 2015.

[12] U. Westerhoff, T. Kroker, K. Kurbach, and M. Kurrat, "Electrochemical impedance spectroscopy based estimation of the state of charge of lithium-ion batteries," *J. Energy Storage*, vol. 8, pp. 244–256, Nov. 2016.

[13] Y. Hoshi, N. Yakabe, K. Isobe, T. Saito, I. Shitanda, and M. Itagaki, "Wavelet transformation to determine impedance spectra of lithium-ion rechargeable battery," *J. Power Sources*, vol. 315, pp. 351–358, May 2016.

[14] A. J. Fairweather, M. P. Foster, and D. A. Stone, "VRLA battery parameter identification using pseudo random binary sequences (PRBS)," in *Proc. 5th IET Int. Conf. Power Electron., Mach. Drives (PEMD)*, 2010, pp. 1–6.

[15] M. Itagaki, M. Ueno, Y. Hoshi, and I. Shitanda, "Simultaneous determination of electrochemical impedance of lithium-ion rechargeable batteries with measurement of charge-discharge curves by wavelet transformation," *Electrochim. Acta*, vol. 235, pp. 384–389, May 2017.

[16] S. M. M. Alavi, C. R. Birkl, and D. A. Howey, "Time-domain fitting of battery electrochemical impedance models," *J. Power Sources*, vol. 288, pp. 345–352, Aug. 2015.

[17] N. Lohmann, P. Weßkamp, P. Haußmann, J. Melbert, and T. Musch, "Electrochemical impedance spectroscopy for lithium-ion cells: Test equipment and procedures for aging and fast characterization in time and frequency domain," *J. Power Sources*, vol. 273, pp. 613–623, Jan. 2015.

[18] Y. Li, J. Bao, M. Skyllas-Kazacos, M. P. Akter, X. Zhang, and J. Fletcher, "Studies on dynamic responses and impedance of the vanadium redox flow battery," *Appl. Energy*, vol. 237, pp. 91–102, Mar. 2019.

[19] B. Bullecks, R. Suresh, and R. Rengaswamy, "Rapid impedance measurement using chirp signals for electrochemical system analysis," *Comput. Chem. Eng.*, vol. 106, pp. 421–436, Nov. 2017.

[20] P. Boškoski, A. Debenjak, and B. M. Boshkoska, "Fast electrochemical impedance spectroscopy," in *Fast Electrochemical Impedance Spectroscopy*. Cham, Switzerland: Springer, 2017, pp. 9–22.

[21] A. Debenjak, P. Boškoski, B. Musizza, J. Petrovčič, and D. Juričić, "Fast measurement of proton exchange membrane fuel cell impedance based on pseudo-random binary sequence perturbation signals and continuous wavelet transform," *J. Power Sources*, vol. 254, pp. 112–118, May 2014.

[22] W. Li, Q.-A. Huang, C. Yang, J. Chen, Z. Tang, F. Zhang, A. Li, L. Zhang, and J. Zhang, "A fast measurement of warburg-like impedance spectra with Morlet wavelet transform for electrochemical energy devices," *Electrochim. Acta*, vol. 322, Nov. 2019, Art. no. 134760.

[23] J. M. Lilly and S. C. Olhede, "Higher-order properties of analytic wavelets," *IEEE Trans. Signal Process.*, vol. 57, no. 1, pp. 146–160, Jan. 2009.

[24] R. Isermann and M. Münchhof, *Identification of Dynamic Systems: An Introduction With Applications* (Advanced Textbooks in Control and Signal Processing). Berlin, Germany: Springer-Verlag, 2011.

[25] L. Ljung, *System Identification: Theory for the User* (Prentice-Hall Information and System Sciences Series), 2nd ed. Upper Saddle River, NJ, USA: Prentice-Hall, 1999.

[26] W. D. T. Davies, *System Identification for Self-Adaptive Control*. New York, NY, USA: Wiley, 1970.

[27] Y. Meyer and P. Flandrin, "The time-frequency problem," in *Time-Frequency/Time-Scale Analysis*, vol. 10, P. Flandrin, Ed. New York, NY, USA: Academic, 1999, ch. 1, pp. 9–47.

[28] E. Wilczok, "New uncertainty principles for the continuous Gabor transform and the continuous wavelet transform," *Documenta Mathematica*, vol. 5, pp. 201–226, Jan. 2000.

[29] D. Iatsenko, *Nonlinear Mode Decomposition*. Lancashire, U.K.: Lancaster Univ., 2015.

[30] S. Mallat, *A Wavelet Tour of Signal Processing: The Sparse Way*, 3rd ed. Burlington, MA, USA: Academic, 2008.

[31] I. Daubechies, *Ten Lectures on Wavelets*, vol. 61. Philadelphia, PA, USA: SIAM, 1992.

[32] J. M. Lilly and S. C. Olhede, "Generalized morse wavelets as a superfamily of analytic wavelets," *IEEE Trans. Signal Process.*, vol. 60, no. 11, pp. 6036–6041, Nov. 2012.

[33] S. C. Olhede and A. T. Walden, "Generalized morse wavelets," *IEEE Trans. Signal Process.*, vol. 50, no. 11, pp. 2661–2670, Nov. 2002.

[34] D. Iatsenko, P. V. E. McClintock, and A. Stefanovska, "Linear and synchrosqueezed time–frequency representations revisited: Overview, standards of use, resolution, reconstruction, concentration, and algorithms," *Digit. Signal Process.*, vol. 42, pp. 1–26, Jul. 2015.

[35] J. M. Lilly and S. C. Olhede, "On the analytic wavelet transform," *IEEE Trans. Inf. Theory*, vol. 56, no. 8, pp. 4135–4156, Aug. 2010.

[36] J. E. B. Randles, "Kinetics of rapid electrode reactions," *Discussions Faraday Soc.*, vol. 1, pp. 11–19, Mar. 1947.

[37] B. Wang, S. E. Li, H. Peng, and Z. Liu, "Fractional-order modeling and parameter identification for lithium-ion batteries," *J. Power Sources*, vol. 293, pp. 151–161, Oct. 2015.

[38] N. E. Ghossein, J. P. Salameh, N. Karami, M. E. Hassan, and M. B. Najjar, "Survey on electrical modeling methods applied on different battery types," in *Proc. 3rd Int. Conf. Technol. Adv. Electr., Electron. Comput. Eng. (TAEECE)*, Apr. 2015, pp. 39–44.

[39] C. A. Monje, Y. Chen, B. M. Vinagre, D. Xue, and V. Feliu-Batlle, "Numerical issues and MATLAB implementations for fractional-order control systems," in *Fractional-Order Systems and Controls: Fundamentals and Applications*. London, U.K.: Springer, 2010, ch. 13.

[40] H. Stark and J. Woods, *Probability, Statistics, and Random Processes for Engineers*, 4th ed. London, U.K.: Pearson, 2011.

[41] P. O. Amblard, M. Gaeta, and J. L. Lacoume, "Statistics for complex variables and signals—Part I: Variables," *Signal Process.*, vol. 53, no. 1, pp. 1–13, Aug. 1996.

[42] R. J. Baxley, B. T. Walkenhorst, and G. Acosta-Marum, "Complex Gaussian ratio distribution with applications for error rate calculation in fading channels with imperfect CSI," in *Proc. IEEE GLOBECOM*, Dec. 2010, pp. 1–5.

[43] J. Moškon, J. Žuntar, S. D. Talian, R. Dominko, and M. Gaberšček, "A powerful transmission line model for analysis of impedance of insertion battery cells: A case study on the NMC-Li system," *J. Electrochem. Soc.*, vol. 167, no. 14, Nov. 2020, Art. no. 140539.

[44] C. Xu, K. Märker, J. Lee, A. Mahadevegowda, P. J. Reeves, S. J. Day, M. F. Groh, S. P. Emge, C. Ducati, B. L. Mehdi, C. C. Tang, and C. P. Grey, "Bulk fatigue induced by surface reconstruction in layered ni-rich cathodes for Li-ion batteries," *Nature Mater.*, vol. 20, no. 1, pp. 84–92, 2021.

[45] W. Dreyer, J. Jamnik, C. Guhlke, R. Huth, J. Moškon, and M. Gaberšček, "The thermodynamic origin of hysteresis in insertion batteries," *Nature Mater.*, vol. 9, no. 5, pp. 448–453, May 2010.

GJORGJI NUSEV received the M.S. degree in electrical engineering from the Faculty of Electrical Engineering, University of Ljubljana, Ljubljana, Slovenia, in 2014. He is currently pursuing the Ph.D. degree with the Jožef Stefan International Postgraduate School, Ljubljana. Since 2016, he has been enrolled at the Jožef Stefan International Postgraduate School. He is also employed as a Researcher with the Department of Systems and Control, Jožef Stefan Institute. His research interests include the development of methods for characterisation and diagnostics of electrochemical energy systems with main focus on electrochemical impedance spectroscopy.

ĐANI JURIČIĆ received the Ph.D. degree in automatic control from the University of Ljubljana, Ljubljana, Slovenia, in 1990.

Since 1981, he has been affiliated with the Jožef Stefan Institute as the Deputy Head of the Department of Systems and Control. Since 2013, he has also been a Full Professor with the University of Nova Gorica, Nova Gorica, Slovenia. He is the (co)author of more than 200 journal and conference papers with peer review and has delivered ten invited talks. He has been the coordinator or person responsible for nearly 40 research projects and projects for industry. His research interests include condition monitoring, with particular focus on fault detection, diagnosis, and prognosis; nonlinear dynamic system identification; statistical signal processing; and optimal control. He is also a member of IFAC Technical Committee SAFEPROCESS and the General Assembly and Council of the European Control Association. He received several awards, including DAAD Fellowship in 2001 and the ISA Transactions Best Paper Award for 2009.

MIRAN GABERŠČEK has been the Director of the Centre of Excellence for Low Carbon Technologies, Ljubljana, Slovenia, (the Centre joins four academic institutions and ten industrial partners in Slovenia) since 2009. Since 2003, he has also been affiliated to the University of Ljubljana, where he currently holds the position of Full Professor for the field of materials science. He is also a Professor of materials science and the Head of the Department for Materials Chemistry, National Institute of Chemistry, Ljubljana. His research interests include novel electrochemical systems for energy storage and conversion (more specifically: primary and secondary batteries and fuel cells). In particular, he has been focused on explanation of complex charge transport and reaction mechanisms in these devices. Together with coworkers, he has invented various novels or significantly improved active materials. He has published about 214 articles in international journals, some of them in most prestigious journals, such as *Nature Materials*, *Angewandte Chemie*, *Advanced Materials*, and others. His works have been cited 8900 times (his H-index is 49). His group regularly cooperates with the most prestigious international research institutes as well as with prominent industrial partners, such as Brightsource, Alanod, Renault, Volvo, Saft, Honda, and others.

JOŽE MOŠKON received the Ph.D. degree from the Faculty of Natural Sciences and Engineering, University of Ljubljana, for study of electrochemical mechanisms in Li ion batteries, in 2010.

Since 2006, he has been employed with the National Institute of Chemistry, Ljubljana, Slovenia. He is currently a Researcher with the Department for Materials Chemistry, National Institute of Chemistry. He has been actively involved in carrying out of several European projects in the field of supercapacitors and Li ion batteries. In parallel, he has occasionally collaborated in the tasks within the Centre of Excellence for Low Carbon Technologies, Ljubljana. His research interest includes electrochemical systems for energy storage, where he has focused to studies of transport and kinetic processes as well as thermodynamic phenomena in novel battery systems (in particular Li-ion and Li-Sulfur). In particular, he has specialized in combining standard electrochemical techniques with electrochemical impedance spectroscopy for studies of interfacial phenomena. He has published about 25 articles in international journals, some of them in most prestigious journals, such as *Nature Materials* and *Chemistry of Materials*. His works have been cited about 1000 times (his H-index is 10).

PAVLE BOŠKOSKI received the Ph.D. degree with the topic ''Condition monitoring of mechanical drives,'' from the Jožef Stefan International Postgraduate School, Ljubljana, Slovenia. Since 2011, he has been employed with the Department of Systems and Control, Jožef Stefan Institute, Ljubljana. His research interests include the development of signal processing methods for prognostics and health management of mechanical drives. Since 2012, his work has been focused on the development of methods for diagnostics of fuel cell-based systems. He has authored or coauthored more than 30 journal and conference papers.

Chapter 4

Condition Monitoring of Different EECD by Means of Fast EIS

Condition monitoring of the EECD is essential for ensuring reliable operation. Changes in the pattern of the impedance curve may indicate the presence of a fault or a degradation mode. To minimise the effect of the degradation process one needs to analyse the change in the impedance curve in order to undertake proper mitigation and maintenance actions to help increase system reliability and extend its useful life.

Typically, changes in EIS characteristics are quantified by using parametric models such as ECM [89], [90], DRT [91]–[93].

Equivalent circuit model

ECM is a well-established method for analysing impedance data. It uses passive elements, such as resistors, capacitors, and inductors as building blocks. Also, it uses fractional-order components capable of describing processes occurring in electrochemical energy conversion systems, such as [94], [95]:

CPE also known as Q-element, is usually used to describe the impedance of a double layer capacitance. The impedance of the CPE represents a general form of the impedance of the capacitor and reads:

$$Z_{CPE}(j\omega) = \frac{1}{(j\omega)^{\alpha}Q}$$

where $\alpha \in (0, 1]$ and represents the fractional order coefficient. When $\alpha = 1$, the CPE describes an ideal capacitor. The Nyquist plot of the CPE element for different values of the α is shown in Figure 4.1.

Cole-Cole (RQ) element is the most commonly used element in ECM for describing processes in electrochemistry. It represents a parallel connection of a resistor and CPE element. Its impedance reads:

$$Z_{RQ}(j\omega) = \frac{R}{1 + (j\omega)^{\alpha}QR} = \frac{R}{1 + (j\omega\tau)^{\alpha}},$$

where $\tau = \sqrt[\alpha]{RQ}$. The Nyquist plot of the RQ element for different values of the α is shown in Figure 4.2.

Gerischer element impedance is given in Equation (4.1) and reads:

$$Z_{GER}(j\omega) = \frac{R}{\sqrt{1 + j\omega QR}} \tag{4.1}$$

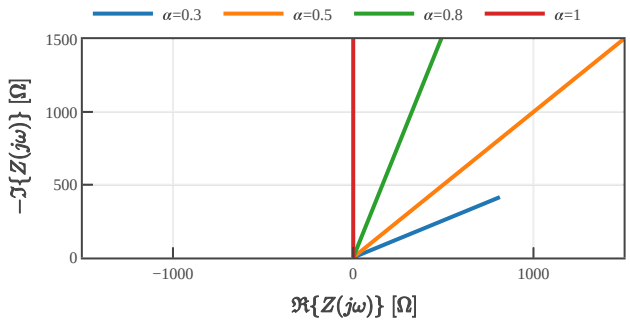

Figure 4.1: Nyquist plot of a CPE element for different values of fractional order parameter α.

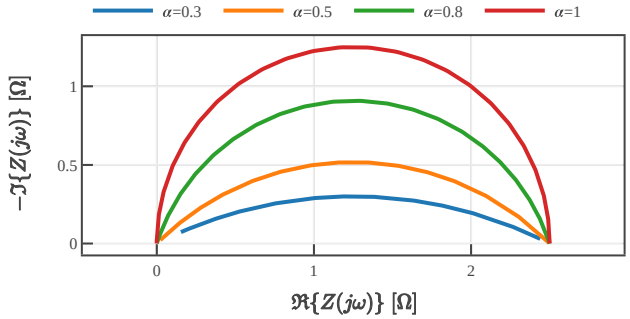

Figure 4.2: An example of the Nyquist plot of a Cole-Cole (RQ) element for different values of fractional order parameter α.

A more general form is referred to as Cole–Davidson element. Its impedance reads:

$$Z_{Cole-Davidson}(j\omega) = \frac{R}{(1+(j\omega)QR)^{\beta}}$$

where $\beta \in (0, 1]$ and represents the fractional order coefficient. The Nyquist plot for different values of β of the Cole–Davidson element, including the Gerischer element, is shown in Figure 4.3.

Generalised Warburg element is used to describe diffusion. There are two types of Warburg elements: *finite length Warburg (FLW)*, which is typically used to describe impedances of fuel cells, and the *finite space Warburg (FSW)*, which is typically used to describe impedances of Li-ion batteries. Sometimes FLW and FSW are called the short and open Warburg elements, respectively. Impedance equation of FLW is given in (4.2), while impedance equation of FSW is given in (4.3).

$$\begin{aligned} Z_{FLW}(j\omega) &= \frac{Z_0}{\sqrt{j\omega\tau}} \tanh\sqrt{j\omega\tau} \\ Z_{FLS}(j\omega) &= \frac{Z_0}{\sqrt{j\omega\tau}} \coth\sqrt{j\omega\tau} \end{aligned}$$

Their impedance curve is given in Figure 4.4.

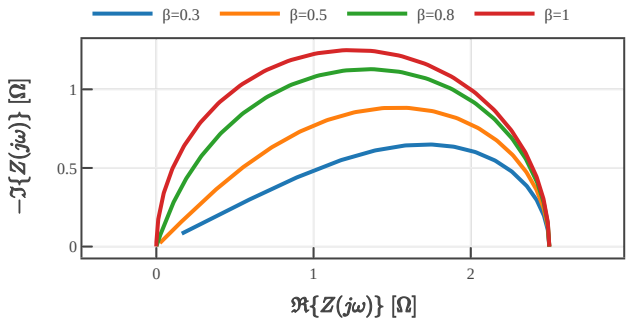

Figure 4.3: An example of the Nyquist plot of a Cole–Davidson element for different values of the fractional order parameter β, including the Gerischer element.

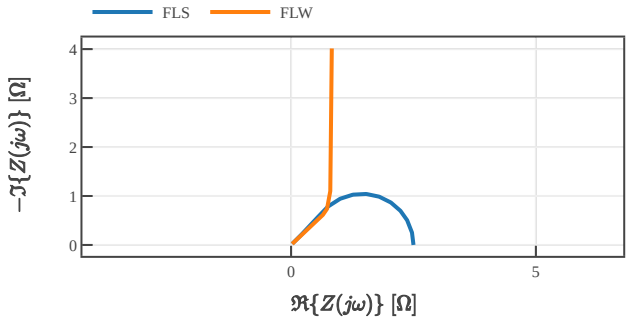

Figure 4.4: An example of the Nyquist plot of a finite length Warburg (FLW) and finite space Warburg (FSW) element.

Havriliak-Negami is the most general form of the ECM element. Its impedance is defined as:

$$Z(j\omega) = \frac{R}{(1 + (j\omega\tau)^{\alpha})^{\beta}}$$

and depicted in Figure 4.5.

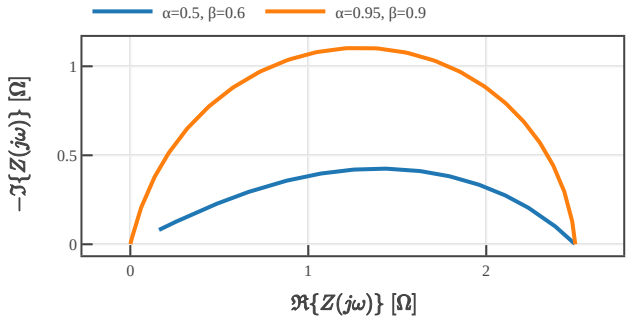

Figure 4.5: An example of the Nyquist plot of a Havriliak-Negami general element.

Each component above can be associated with a physical process that occurs within the cell. Combining various elements in a circuit leads to an ECM that describes the transfer

function of the analysed system. The idea of ECM is to keep the electrical model as simple as possible while providing a good enough fit to the measured impedance. However, the main drawback of ECM is that generally we have no unique solution. In some cases, two different equivalent circuits may result in the same transfer function.

Values of the ECM parameters are determined by means of optimisation. The most commonly used method for parameter estimation is complex nonlinear least square (CLNS) [96]. To get the optimal values reliably, it is important to have good initial estimates. To circumvent this problem, more sophisticated optimisation methods were used for parameter estimation, such as evolutionary algorithms [97], variational Bayes approach [90], Markov chain Monte Carlo (MCMC) approach [98] and others.

Sections 4.1 and 4.2 present a study in which the evolution of ECM parameters over time was used to perform condition monitoring on short SOFC stack and PEM hydrogen compressor, respectively. Moreover, the measuring equipment presented in Chapter 2 was used to perform EIS on them. During their operation, different faulty operation modes were introduced, which are later successfully detected.

Distribution of relaxation times

The distribution of relaxation times (DRT) represents a well established method for impedance deconvolution, which separates the polarisation processes with different time constants directly from the non-parametrically estimated impedance data. It is a linear transformation used to estimate the number of time constants present in the transfer function.

The DRT method states that any impedance satisfying the KK relations can be represented as a sum of an infinite number of RC-elements connected in series, as shown in Figure 4.6. This type of circuit is known as a chain of Voigt elements [99]. The impedance of a single RC-element is given by $Z(\omega) = \frac{R}{1+j\omega RC}$, with relaxation time constant $\tau = RC$. For an infinite number of RC-elements with continuously increasing relaxation times τ from 0 to ∞, its impedance is:

$$Z(\omega) = R_\infty + \int_0^\infty \frac{G(\tau)}{1 + j\omega\tau} d\tau \tag{4.4}$$

where R_∞ represents the ohmic (serial) resistance.

The distribution of relaxation times represents the function $G(\tau)$. It is an integral function which gives the value of the overall polarisation resistance R_{pol}. This can be demonstrated for $\omega \to 0$ by solving Equation (4.4)

$$\lim_{\omega\to 0} \int_0^\infty \frac{G(\tau)}{1 + j\omega\tau} d\tau = \int_0^\infty G(\tau) d\tau = \lim_{\omega\to 0} Z(\omega) - R_\infty = R_{pol} \tag{4.5}$$

In order for (4.5) to be valid, the distribution function $G(\tau)$ has to satisfy the following normalisation condition:

$$\int_0^\infty \frac{G(\tau)}{R_{pol}} d\tau = 1$$

According to Klotz [100], the area under each peak in the DRT equals the polarization resistance of that particular loss mechanism.

Calculation of the DRT for known transfer function is a straightforward task as derived by Fuoss *et al.* [101]. In order to calculate the DRT from the known impedance function $Z(j\omega)$, it is separated into its real and imaginary part, as follows:

$$Z(j\omega) = J(x) - jH(x)$$

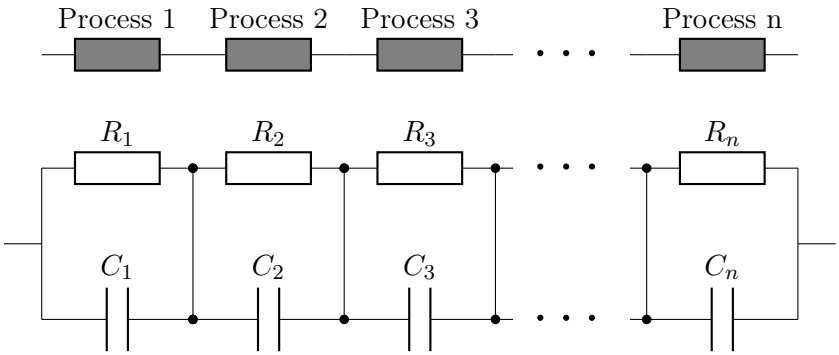

Figure 4.6: In general, DRT method assumes a chain of Voigt elements connected in series. Each element indicates a process that occurs at a specific time constant, $\tau_i = R_i C_i$.

where $x = \log\left(\frac{\omega_m}{\omega}\right)$, ω_m represents the frequency at maximum $H(x)$ and $H(x) = -\Im(Z(x))$. Taking all this into account, the original DRT function $\tau G(\tau)$ can be expressed using the following expression:

$$\tau G(\tau) = \tfrac{1}{\pi}\left(H(s + j\tfrac{\pi}{2}) + H(s - j\tfrac{\pi}{2})\right) \qquad \text{where} \qquad s = \log(\tau\omega_m) \tag{4.6}$$

Therefore, if we include the substitutions for the variables s and x into the (4.6), we get a new expression for the DRT:

$$\tau G(\tau) = -\tfrac{1}{\pi}\left(\Im(Z(e^{-\log\tau - j\frac{\pi}{2}})) + \Im(Z(e^{-\log\tau + j\frac{\pi}{2}}))\right)$$

Details about the mathematical derivation of the transform can be found in [101].

Figure 4.7 shows how the fractional order parameter α of the CPE element influences the DRT. A two-pole fractional transfer function was chosen with time constants $\tau_1 = 0.01$ s and $\tau_2 = 1$ s, representing two different processes. This can be represented using a serial connection of two R-CPEs elements. **In case** when the fractional order parameters $\alpha_1 = 1$ and $\alpha_2 = 1$, the transfer function reduces to a simple serial connection of two RC elements. The corresponding DRT represents two Dirac pulses (peaks) at locations of the time constants. In cases when $\alpha_1 < 1$ and $\alpha_2 < 1$, the shape of the DRT peaks starts to widen for lower values of the fractional order parameter. The area below the DRT is equal to the polarisation resistance.

However, in practice, determining the DRT is not an easy task, since knowledge about the transfer function is missing. Also, due to finite measurement, Equation (4.4) is approximated using discrete function for G_n for N serial RC elements. The discrete DRT function reads:

$$Z(j\omega) = R_\infty + \sum_{n=0}^{N} \frac{G_n}{1 + j\omega\tau_n}$$

The contribution of each RC element is logarithmically distributed for predefined values of τ_n. The problem of finding the DRT of an unknown function represents an ill-posed problem. In order to solve it, regularization methods, such as Tikhonov or Lasso regularisation, are required [102], [103]. More detailed information about the DRT calculation can be found in [103].

Since changes in the DRT peaks are indirectly associated with changes of the impedance spectra and therefore with the changes of the electrochemical energy conversion device under test, it can be used as a tool for monitoring its performances. As a result, Section 4.3 presents a study where the DRT method is used to perform assessment and evaluation of

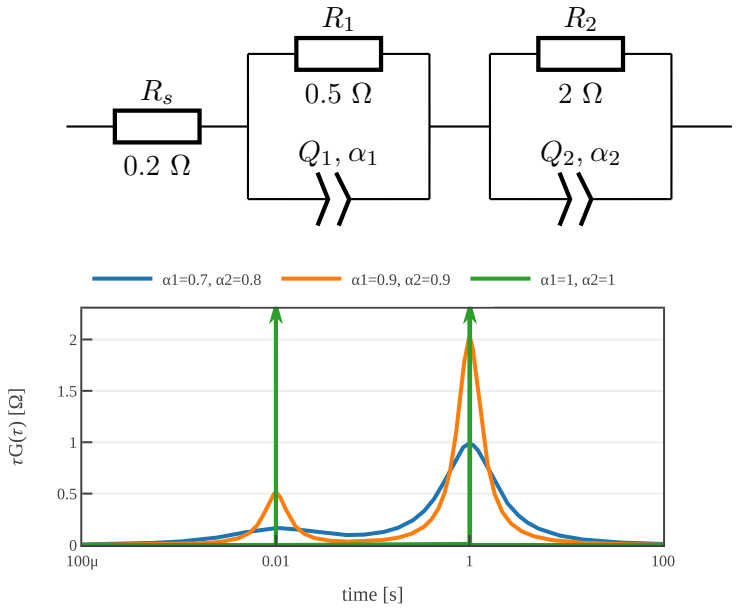

Figure 4.7: DRT plot of a two-pole fractional order system, shown in the upper figure, where the values of Q_1 and Q_2 were chosen in a way so that the time constants would be $\tau_1 = 0.01$ s and $\tau_2 = 1$ s. By changing the fractional order parameters α of the transfer function, the shape of the curve changes.

SOE stacks designed for application in a reversible operation. In this study, the measuring equipment presented in Chapter 2 has been used to perform EIS.

4.1 Condition Monitoring of Solid Oxide Fuel Cell Stacks

Journal of Power Sources 489 (2021) 229491

Contents lists available at ScienceDirect

Journal of Power Sources

journal homepage: www.elsevier.com/locate/jpowsour

Condition monitoring of solid oxide fuel cells by fast electrochemical impedance spectroscopy: A case example of detecting deficiencies in fuel supply

Gjorgji Nusev [a,b,*], Bertrand Morel [c], Julie Mougin [c], Đani Juričić [a], Pavle Boškoski [a]

[a] Jožef Stefan Institute, Jamova cesta 39, SI-1000, Ljubljana, Slovenia
[b] Jožef Stefan International Postgraduate School, Jamova cesta 39, SI-1000, Ljubljana, Slovenia
[c] Commissariat à l'énergie atomique et aux énergies alternatives - CEA, CEA/LITEN/DTBH/STHB/LTH, 17 rue des Martyrs, 38054, Grenoble Cedex 9, France

ARTICLE INFO

Keywords:
Solid oxide fuel cell
Fuel utilisation
Non-linear optimisation
Electrochemical impedance spectroscopy
Monitoring

ABSTRACT

This paper deals with the monitoring of the internal condition of a 6-cell solid oxide fuel cell stack during a 3600-hour test with short fuel starvation intervals. The relationship between change in condition and change of impedance spectra as well as the parameters of the equivalent circuit models are analysed. Tentative features indicating reduced fuel supply are identified. The analysis uses discrete random binary sequence, a stochastic broadband excitation signal that allows much shorter perturbation times. More than 600 electrochemical impedance spectroscopy curves and the associated equivalent circuit model parameters were analysed. High fuel utilisation interval is detected in two ways: (i) by violating the Z-HIT test in the low-frequency part (below ≈ 1 Hz) and (ii) significant change of the area-specific resistance parameter. The degradation after fuel cut-offs is clearly reflected in the change in area-specific resistance and the serial resistance. The numerical implementation of the proposed algorithms is available at: https://repo.ijs.si/pboskoski/py_eis.git.

1. Introduction

One of the most active areas in the field of SOFC is the development of advanced health monitoring approaches together with the design of optimised control strategies [1]. The aim was to improve the performance of SOFC technology by operating the equipment at the limit of usability.

Electrochemical voltammetry and EIS are still the most widely used *in-operando* characterisation approaches [2]. The former focuses on the detection of voltage drops (assuming constant current) but is unable to identify the root cause. The Nyquist curve is more informative, and conclusions about system condition can be drawn, for example, by identifying the ECM parameters [3–8] or by identifying the distribution of relaxation times (DRT) [9–11].

Conventional EIS is based on the successive use of low-amplitude mono-component sinusoidal signals to excite only locally linearised system dynamics. The impedance is evaluated for a selected discrete set of frequencies [12–14]. The amplitude should be carefully chosen to ensure an appropriate signal-to-noise ratio of the system output response. However, in order to correctly capture the essential characteristics of the impedance curve, especially in the low frequency range (<100 mHz), excessive perturbation times (in the range of hours) are applied. The selection of the perturbation frequencies is therefore a compromise between the time in which the process is disturbed and the resolution of the Nyquist curve.

An alternative to the successive sinusoidal perturbation in impedance spectroscopy refers to the application of broadband stochastic excitation signals [15–18]. However, evaluating the impedance from these signals requires more sophisticated signal processing approaches, e.g. the continuous wavelet transform (CWT). Despite advances in signal processing, these results have been mostly neglected by electrochemical experts. One of the goals of this work is to demonstrate the effectiveness of a fast characterisation approach for SOFC stack diagnosis. It is shown that not only the required perturbation could be significantly reduced, but also the impedance can be evaluated with high resolution on a dense set of frequencies.[1] Better resolution of the impedance curve allows more reliable parameter estimates of the ECM. The estimates are obtained by a constrained optimisation approach that addresses the problem of ill-conditioned Hessian of the criterion function.

* Corresponding author at: Jožef Stefan Institute, Jamova cesta 39, SI-1000, Ljubljana, Slovenia.
E-mail address: gjorgji.nusev@ijs.si (G. Nusev).

[1] The maximum number is limited to the number of samples in the acquired data. However, since the sampling frequency f_s is usually in the range of 100 kHz, the impedance curves can be calculated with almost at continuous resolution.

https://doi.org/10.1016/j.jpowsour.2021.229491
Received 22 October 2020; Received in revised form 14 December 2020; Accepted 6 January 2021

A further contribution of this paper is related to the application of fast impedance spectroscopy for the detection of increased fuel utilisation and fuel cut-off. That is one of the main concerns in the operation of SOFC stacks. The fuel shortage can cause a local oxidant environment, i.e. very low concentrations of H_2 and CO, resulting in oxidation of Ni and formation of NiO. The nickel oxidation causes an irreversible mechanical degradation of the electrolyte and electrode interface due to the dimensional expansion of the anode support [19].

Despite a solid understanding of degradation mechanisms due to insufficient fuel supply [20–23] there is an obvious need for efficient online monitoring tools capable of providing early warning of the onset of Ni oxidation in the anode. Several approaches have been proposed so far, based on the fact that insufficient fuel supply moves the operating point into the nonlinear region of the voltage–current characteristic. An idea how to detect the nonlinearity was proposed by Esposito et al. [24] who applied CWT to the SOFC voltage signal and showed the qualitative change in the transform in the presence of anode reoxidation caused by high fuel utilisation (i.e. local fuel starvation). A simple method for detecting non-linearity is contained in total harmonic distortion analysis (THDA), a method originating from the power engineering industry, which was first used to monitor the fuel utilisation of PEM fuel cells [25]. Later on, it was applied by [26,27] to SOFC stacks. In a recent comprehensive study, THDA was used for early detection of various degradation mechanisms in SOFC [28], including Ni oxidation. The results show that THDA can be used online to provide a consistent and reliable indicator of the fuel utilisation rate on the SOFC stack. Implementation of the THDA method is simple and inexpensive, which is important for online applications. However, the approach requires invasive excitation, typically on the minute scale in the frequency range of 0.01–1 Hz, i.e. in the range where gas transport processes dominate.

By applying the proposed DRBS excitation coupled with the CWT analysis, it is shown that accurate results can be obtained in a fraction of the time required by the state of the art methods. To evaluate the proposed approach, a rapid characterisation of the 6-cell SOFC stack was performed every 6 h, resulting in more than 600 EIS curves for each cell of the stack. It is shown that high fuel utilisation problems can be identified from the pattern of changes in the parameters of the ECM.

The paper is structured as follows. The complete methodology is presented in Section 2. Details are presented on the impedance evaluation by means of complex CWT and impedance validation through KK relationships as well as the optimisation procedure for ECM parameter estimation. The description of the experimental setup is provided in Section 3. Finally, Section 4 discusses the results obtained with the experiment.

2. Methodology

The aim of this section is to describe the entire procedure from system perturbation and signal processing up to the determination of diagnostic features. The core of the approach is fast electrochemical impedance spectroscopy proposed by Boškoski et al. [29] and now applied for the first time to SOFCs. It is based on the idea of overcoming the limitations of the conventional EIS by using broadband excitation together with powerful signal processing techniques.

Conventional EIS typically uses single and sometimes multi-component sine waveforms for system excitation [30]. Consequently, the impedance is assessed for a set of selected frequencies. To obtain sufficiently accurate results, several periods of a sinusoidal excitation signal are required for each desired frequency.

The selection of amplitude of the perturbation signal for EIS is always a result of compromise. On the one hand, it must be low, so that only linearised system dynamic modes are excited at a selected operating point. On the other hand, the amplitude should be high enough to ensure a sufficient signal-to-noise ratio. The *random binary signal* has proved to be a suitable candidate for the excitation signal [31]. It takes either of the two values, $-a$ or a, and alternates from one to another at random time instances. Such a signal could be regarded as composed of an infinite ensemble of sinusoids defined at all possible frequencies and with amplitudes adjusted accordingly. Thanks to the linearity assumption, each perturbing sinusoid on input causes a sinusoid of the same frequency on the output. From the superposition principle an ensemble of the sinusoidal inputs creates an ensemble of the sinusoids on the output which together constitute the system response. To find out the system gain and phase characteristic at a particular frequency we have to unfold the adequate sinusoidal components with that frequency both from input and output signal. For this reason, a spectral decomposition is absolutely mandatory.

A random binary signal can in theory switch from one value to another at any instance of time. In reality, however, the switching is only possible at *discrete times* that coincide with the sampling time instances. Such a signal is referred to as a *discrete binary random signal* (DRBS [32]). The minimum time between the two successive switching operations determines the effective bandwidth of the DRBS, which is denoted as f_b. This means that all of the frequencies are on average excited with the same power (more precisely, power density). As a result, it becomes possible to calculate EIS at (almost) any desired frequency point just from a single measurement. Detailed derivation of the statistical properties of DRBS is given in [32,33].

2.1. Impedance evaluation by means of continuous wavelet transform

When performing EIS with single-component signals, all energy of the input and output signals is concentrated on the excitation frequency. Assuming strict stationarity condition, the impedance can be obtained from the amplitude and phase relationships. In practice, due to the noise in the signals, the Fourier transformation proves to be a better solution.

For broadband excitation and under less restrictive stationary conditions, time–frequency spectral decomposition appears to be a more suitable tool. A typical approach is the short-time Fourier transform. The problem with Fourier-based approaches is the limitation of the time–frequency resolution, which is related to the choice of the time window function. CWT allows a flexible time–frequency resolution, which is achieved through the concepts of scaling of the mother-wavelet $\psi_{u,s}(t)$. It is defined as [34]

$$W f(s,u) = \int_{-\infty}^{\infty} f(t)\psi_{u,s}^{*}(t)\,dt, \tag{1}$$

where $\psi_{u,s}^{*}(t)$ denotes the complex conjugate and u and s are the translation and scaling parameters. The u and s parameters can be easily transformed in time and frequency based on the properties of the selected wavelet function.

From the plethora of available wavelet functions, only complex mother wavelet functions are applicable for EIS evaluation. The subsequent analysis is performed with the Morlet wavelet [29,35], defined as

$$\psi(t) = \pi^{-\frac{1}{4}}\left(e^{-j\omega_0 t} - e^{-\frac{\omega_0}{2}}\right)e^{-\frac{t^2}{2}}. \tag{2}$$

Details on the use of CWT with the Morlet wavelet in the context of EIS can be found in [17,29].

It should be noted that having finite number of samples, certain wavelet coefficients are corrupted due to edge effects at the beginning and the end of the observation window. These coefficients must be omitted from further analysis. This effect is a direct consequence of the so-called cone of influence [36].

The impedance based on CWT can be calculated in a similar way as in the case of the Fourier transform, i.e. as the ratio of the wavelet coefficients of the voltage $u(t)$ and the current $i(t)$:

$$Z(t,f) = \frac{W u_{\mathrm{cell}}(t,f)}{W i_{\mathrm{cell}}(t,f)}, \tag{3}$$

where $Wu_{\text{cell}}(t,f)$ and $Wi_{\text{cell}}(t,f)$ are the wavelet coefficients of $u(t)$ and $i(t)$ calculated using (1). Note that unlike Fourier transform, in the CWT analysis, both time and frequency are needed to define the instantaneous transfer function $Z(t,f)$ in (3). Possible fluctuations during the experiment and drifts, especially in the low-frequency part of the spectrum, cannot remain unnoticed since they are clearly seen in $Z(t,f)$. As a corollary, Fourier transform at a frequency f could be obtained by averaging the $Z(t,f)$ over time.

2.2. Validation of impedance data

In order to ensure a valid EIS evaluation, the measured system under test has to comply with the conditions of stability, causality and linearity. Since the transfer function of the SOFC represents a complex analytic function in the upper half-plane, validity of the EIS measurements can be checked with Kramers–Kronig relations. KK relations render possible to reconstruct the imaginary part of the impedance spectra from the real part and vice versa [37,38]:

$$\begin{aligned}\Im\{Z(\omega)\} &= -\frac{2\omega}{\pi}\int_0^\infty \frac{\Re\{Z(x)\}-\Re\{Z(\omega)\}}{x^2-\omega^2}\mathrm{d}x \\ \Re\{Z(\omega)\} &= \Re\{Z(\infty)\} - \frac{2}{\pi}\int_0^\infty \frac{x\Im\{Z(x)\}-\omega\Im\{Z(\omega)\}}{x^2-\omega^2}\mathrm{d}x.\end{aligned} \tag{4}$$

The infinite integration in (4) leads to inevitable numerical errors. Ehm et al. [39] provided a solution to this numerical problem and proposed a Z-HIT method. In such a case, the amplitude spectrum can be reconstructed from the phase spectrum as follows

$$\log|\hat{Z}(\omega_0)| \approx a + \frac{2}{\pi}\int_{\omega_{min}}^{\omega_0}\phi(\omega)\mathrm{d}\log\omega + \gamma\frac{\mathrm{d}\phi(\omega_0)}{\mathrm{d}\log\omega_0} \tag{5}$$

where $\phi(\omega)$ is the phase spectrum, $\gamma = -\frac{\pi}{6}$ and $\omega_0 \in [\omega_{min}, \omega_{max}]$. The derivation $\frac{\mathrm{d}\phi(\omega_0)}{\mathrm{d}\log\omega}$ can be evaluated numerically by means of the Savitzky–Golay filter. The constant a is determined by a least squares fit.

Using (5), impedance data is valid if the difference $\|Z(\omega)| - |\hat{Z}(\omega)\|$ is small enough. If either system dynamics, experimental conditions or data acquisition are not compliant with the assumption the EIS is based on, the reconstruction via Z-HIT will fail in certain frequency regions. These regions should be excluded from the parameter estimation process.

2.3. Deconvolution of the EIS spectra

2.3.1. Equivalent circuit models

ECMs consist of both simple and frequency-dependent elements (fractional-order), which together form a transfer function that should best fit the impedance curve. The simplest fractional-order element is the constant phase element (Q), which describes the double-layer capacitance at the electrodes. Its impedance is defined as [12]. There are various definitions of the impedance of the constant phase element [40]. This analysis adopts the notation of Sluyters-Rehbach [41]:

$$Z_Q(j\omega) = \frac{1}{(j\omega)^\alpha Q}, \tag{6}$$

where $\alpha \in [0,1]$ represents the fractional order of the pole. The impedance of a capacitor is the special case of the impedance of the constant phase element at $\alpha = 1$. There are also other elements that could be used, such as the Warburg element to describe mass transport losses or a more general Havriliak–Negami element [30].

Note that the selection of the ECM structure can be ambiguous. Since a model is only an approximation of reality, different ECM structures can in practice lead to a comparable matching quality of the measured impedance curve. In our approach we adopt the view that the main diffusion and polarisation can be described by the class of models [10,11,42] represented by a serial connection of parallel connected resistors R and constant phase elements Q:

$$Z(j\omega) = R_S + \sum_{i=1}^{n}\frac{R_i}{1+(j\omega)^{\alpha_i}R_iQ_i} + j\omega L, \tag{7}$$

where R_S is serial resistance, L is the inductance, R_i and Q_i are the parameter values of each pole and $\alpha_i \in \mathbb{R}^+$ and $\alpha_i \in [0,1]$ is the fractional order of the ith pole. Each component can be associated with a physical process in the cell. The goal is to keep the ECM as simple as possible while providing a sufficiently close fit to the modelled and measured impedance [43]. It should be noted that an ECM model can be directly associated with the corresponding DRT curve because they represent two equivalent descriptions of the same system [44].

2.3.2. Selecting structure of the ECM for SOFC systems

The first step in system identification is the selection of the model structure, i.e. determining the number of poles in the model (7). The structural identification of fractional order models (7) is a rather challenging task, which is insufficiently treated in the literature. In the absence of rigorous approaches, one way to solve the task is to use background knowledge to infer the number n in (7).

In hydrogen-powered SOFC fuelled by hydrogen one could expect five dominant processes whose time constants span the frequency band from 0.1 Hz to 1 MHz [45,46]. These processes can be divided into three main groups [47]: gas conversion, cathode processes and anode processes. The gas conversion processes contribute to the low frequency part of the EIS curve, the cathode processes are mostly pronounced in the mid-frequency range and the high-frequency part can be attributed to the anode related processes.

The contribution of the gas conversion impedance to the overall impedance is strongly influenced by the flow rate and the concentration of the fuel gas over the anode (humidification rate of the fuel gas). The gas conversion impedance should be considered as an effect of the passage of current at an electrode under finite gas flow rate [48]. According to Klotz [49], the dynamic characteristic of the gas impedance is that it is strongly dependent on the time required for the gas to pass through the anodic gas channel at the corresponding flow rate. Various experiments provide empirical evidence positioning the influence of this process below 1 Hz [48]. Furthermore, the gas conversion impedance is not related to the anode performance itself, but is a function of the setup geometry, the position of the electrodes and the gas flow rate.

Cathode processes are controlled by the oxygen surface exchange kinetics [46]. The time constant of these processes lies between the time constant of gas conversion and the time constant related to the anode processes. Experiments with SOFC, based on variations of the oxidant gas composition, typically place the cathode processes in the frequency interval between 3 Hz and 300 Hz [46,50]. Anode processes are mainly associated with charge transfer reaction and ion transport.

2.3.3. Estimation of ECM parameters

Finding the optimal parameters of the ECM means solving the nonlinear optimisation problem with constraints

$$\begin{aligned}\mathbf{x}^* &= \arg\min_{\mathbf{x}}\varepsilon(\mathbf{x}) \\ \mathbf{x}_L &\le \mathbf{x} \le \mathbf{x}_U\end{aligned}$$

where

$$\varepsilon(\mathbf{x}) = \sum_{i=0}^{N}\left|\frac{Z_M(f_i)-\hat{Z}_S(\mathbf{x},f_i)}{Z_M(f_i)}\right|^2 \tag{8}$$

where $Z_M(f_i)$ represents the measured impedance at the frequency f_i, $\hat{Z}_S(\mathbf{x},f_i)$ represents the estimated impedance given $\mathbf{x}$ at the frequency f_i. The vector $\mathbf{x}$ contains all ECM parameters and $\mathbf{x}_L$ and $\mathbf{x}_U$ are vectors of the lower and upper bounds of the ECM parameters respectively.

The search for an optimum might turn non-trivial since the criterion function (8) exhibits substantially different sensitivity to different ECM

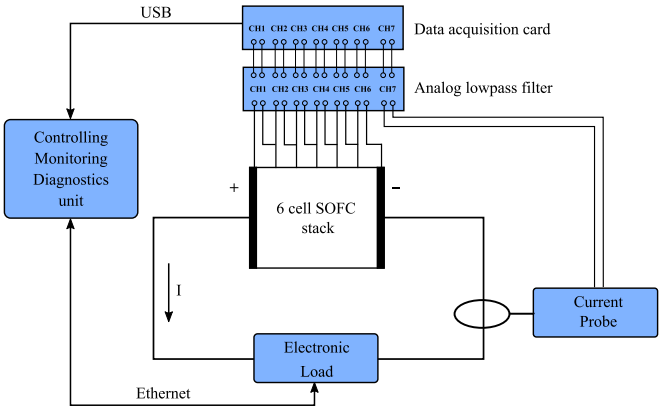

Fig. 1. Block scheme of the system for fast characterisation of SOFC stack.

parameters. In order to guarantee reliable convergence of the search, regardless of the initial conditions, a combination of global and local search strategies is used. The global search is performed by a genetic algorithm, while the refined local search is performed by the simplex method.

Algorithm 1: Pseudo code of the proposed algorithm for parameter estimation

Input : Measured impedance data, ECM topology, Threshold, number of iterations (N)
Output: Values of ECM parameters
k=0;
repeat
  GA optimisation;
  x are sorted by ascending order of the $\epsilon(\mathbf{x})$;
  Bounded simplex method for the **M** best **x**;
  choose **x** with lowest value of $\epsilon(x)$;
  k=k+1;
until *(ϵ<Threshold)* ***or*** *(k>N)* ***or*** *(change **x** <5%)*;
Solution

Genetic algorithm creates several starting points within the range of permissible parameters. The result is a rough estimate of the position of the global minimum. The obtained intermediate result is later used as a starting point for the bounded simplex optimisation method. After completion of the simplex optimisation, the best candidate solutions are transferred to the next generation, where others are mutated or discarded. The optimisation process is finished when one of the following conditions is met:

- the value of the $\epsilon(\mathbf{x})$ is lower than the threshold value that is predefined;
- relative change of the $\epsilon(\mathbf{x})$ between the last 3 iterations is less than 5%;
- relative change of the parameters **x** in the last 3 iterations is below some predefined percentage.

The implementation of all the algorithms above in Python is available at https://repo.ijs.si/pboskoski/py_eis.

3. Experiment

In order to demonstrate the potential of the proposed methodology, the experimental campaign was performed on a short SOFC stack from SOLIDpower S.p.a. operated in an electric furnace at 750 °C. The stack comprises 6 anode-supported cells. Each cell has an active area of 80 cm^2. The flow rate of the hydrogen and nitrogen fuel mixture was H_2/N_2 = 0.216/0.144 Nl h^{-1} cm^{-2}, while the air flow rate was 4 Nl h^{-1} cm^{-2}. The stack was operated with a nominal current of 32 A. (0.4 A cm^{-2}) and FU = 77.5% for most of the time. Deviations from the nominal regime were made in two ways. First, the stack was subjected to the intentional increase of fuel utilisation on two occasions. Secondly, there were several unplanned failures in the fuel supply, which proved to be quite harmful to the stack condition. The stack was operated for a total of 4500 h, but for the sake of consistency we will present the results up to t = 3600 h, since at 3600 h of stack operation an upgrade of the measurement equipment was performed.

3.1. Measurement system

Due to the unconventional excitation signals a measurement test rig was entirely custom designed. It comprised a digital load, data acquisition devices and a control unit. The block scheme of the measurement system is shown in Fig. 1. The electronic load, Rigol DL3031A, was connected in series with the SOFC stack. Its task was to control the electrical current drawn from the stack. Consequently, the device was used to perturb the stack by superimposing excitation signals with an accuracy of ±1 mA. The electric current was measured with the LEM HASS 50-S Hall probe sensor. Such a measurement technique did not affect the performance of the system under test and provides sufficient accuracy. In addition, the selected sensor with the cut-off frequency of 240 kHz has a sufficiently wide bandwidth. The cell voltages were measured independently with a differential 16-bit data acquisition system NI USB-6215. The analog signals were first low-pass filtered at 10.8 kHz and sampled with sampling frequency f_s = 50 kHz.

3.2. Experimental protocol

The protocol included two intervals of the experiment (referred to as events) in which FU was increased in four steps from 77.5% to 92.5%. At the end of each interval, the stack was brought back to 77.5%. During the first interval of increased FU, the duration of each step was 24 h. Each FU step was performed by keeping the current density constant while reducing the H_2 flow rate. The second interval of increased FU was of equal duration (the duration of each step was 24 h). It was realised by keeping the flow rate H_2 constant while step increments of current density were performed according to the following sequence 32 A, 34.06 A, 36.15 A, 38.2 A.

Throughout the experiment, EIS was performed every 6 h. At nominal operating conditions and during the first interval of increased FU, the short stack impedance at I_{DC} =32 A was evaluated based on DRBS with amplitude a = ±1 A (peak-to-peak amplitude a_{pp} =2 A. During the second interval of increased FU fuel utilisation, the peak-to-peak amplitude of the superimposed DRBS signal was set to 6% of DC current. The amplitude was chosen low enough to ensure a

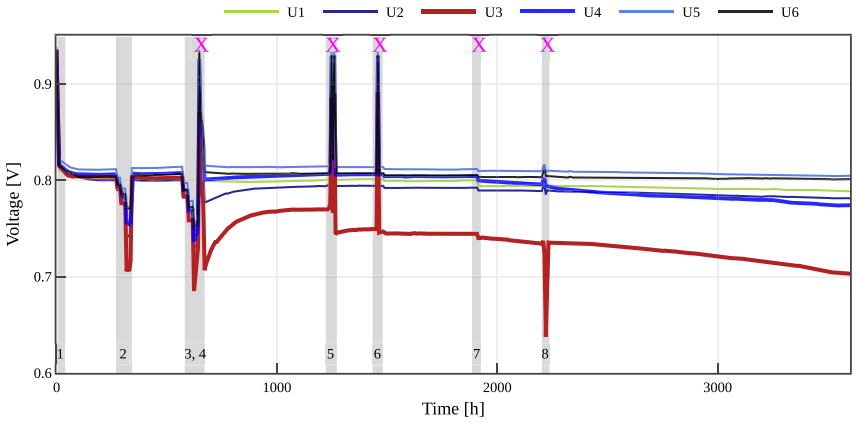

Fig. 2. Evolution of the cell voltages during the duration of the experiment together with all events that occurred..

Table 1
Experiment events.

Event number	Experiment time [h]	Description
E1	0–40	Start up
E2	270–342	Increased fuel utilisation (decreased fuel flow rate)
E3	582–648	Increased fuel utilisation (increased current)
E4	654–672	Emergency shutdown due to H_2 shortage
E5	1242	Power loss due to thunderstorms
E6	1434	Emergency shutdown due to H_2 shortage
E7	1884–1890	Moving into the new building
E8	2202	Emergency shutdown due to H_2 shortage

linear response, but high enough to maintain a sufficient signal-to-noise ratio. During the 3600 h of the experiment, 600 EIS curves and the corresponding ECM models were evaluated.

Unexpected interruptions

During the experiment, 5 unforeseen events occurred. On three occasions the experiment was abruptly halted due to H_2 cut-off. There was a power outage due to interruptions in the external power grid. Finally, at a certain time point, the test bench had to be relocated, which included a complete shutdown and restart of the SOFC stack. All events that occurred during the experiment are listed in Table 1.

4. Results and discussion

4.1. Checking validity of the impedance data

Since the fuel cell stack was operated under different FU modes, special attention was paid to checking the validity of the measurements. Before the estimation of the ECM parameters was performed, the Z-HIT test was applied to the measured EIS data. Only data from the frequency band where the relative error of the Z-HIT test was less than 5% were considered. The remaining frequency points were omitted.

It was found that for frequencies above 1100 Hz the Z-HIT test showed higher error levels. That is due to a data acquisition system with interlaced sampling. As a result, at higher frequencies there is an inherent phase error introduced by the measurement equipment delay. Therefore, the entire subsequent analysis was performed using only the EIS data up to 1 kHz. It is important to note that in cases of high FU the measurements show inconsistent values in the low-frequency range, which is suggested as an additional indicator of increased FU issues. These cases are described in detail in Section 4.3.

4.2. ECM parameter estimation results

Although five poles [45,46] are believed to be necessary to describe the main processes in SOFC, due to the limited range of validated impedance data ($f < 1100$ Hz) only three poles remain identifiable [51, 52]. In such a case, we could observe at most the three dominant processes discussed in Section 2.3 modelled by the three RQ elements. Consequently, the selected ECM has 11 parameters: the three RQ elements (each parameterised with three parameters R_i, Q_i, and α_i), the serial resistance R_S, and the inductance L. In addition, the parameter area-specific resistance (ASR) is defined as the sum of all resistances or the total resistance of the cell.

ECM parameters were obtained with the optimisation algorithm presented in Section 2.3. All ECM parameters were identified using impedance characteristics obtained by DRBS excitation. Each EIS curve contained 50 points per decade with a total of 201 points. The impedance characteristics spanned the frequency band from 0.1 Hz to 1.1 kHz.

The identification results are displayed in Fig. 3. Fig. 3(a) shows the comparison between the impedances calculated with DRBS, sinusoidal excitation and the impedance calculated from the estimated parameters. The fit is sufficiently accurate, as confirmed by the residuals shown in Fig. 3(b), where the error of the real and imaginary parts is less than 2%.

4.3. Evolution of ECM parameters during intervals of increased FU

Warmup stage — E1

Due to non-stationary temperature condition, this section of the experiment is excluded from the analysis.

The first FU variation — E2

The first FU event was performed by successively decreasing the H_2 flow rate according to the following sequence 77.5%, 82.5%, 87.5%

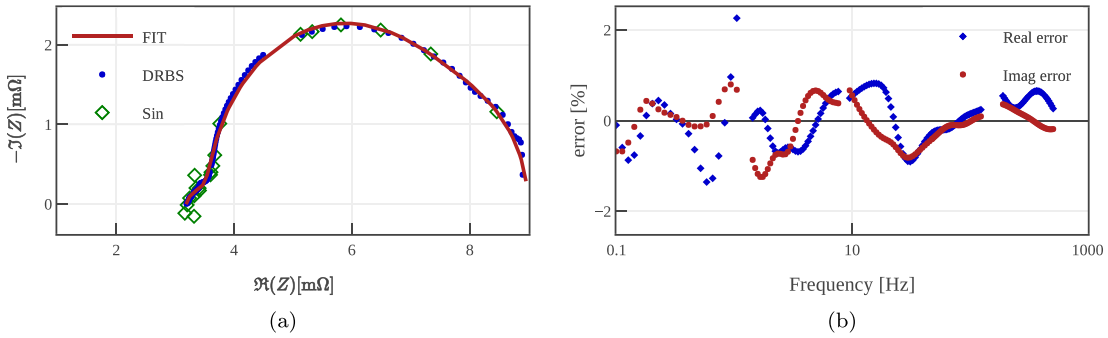

Fig. 3. (a) Comparison of impedance characteristics obtained by fitting, conventional sinusoidal excitation and DRBS based excitation. (b) Relative error of the DRBS-based ECM.

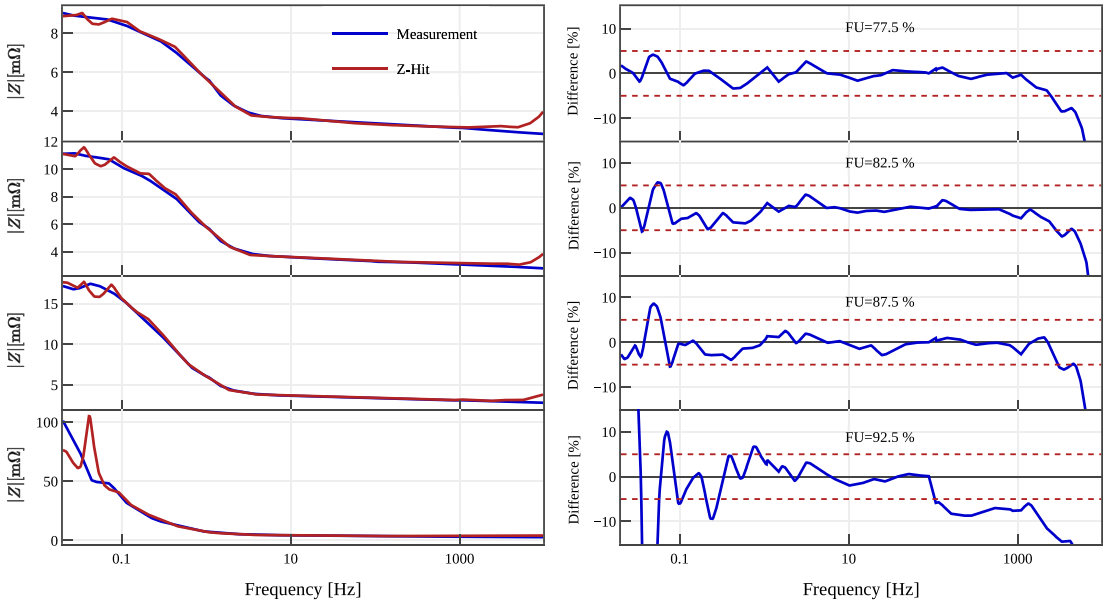

Fig. 4. Z-HIT evaluation at increased FU. Figures on the left-hand side show comparison between the original and *Z-Hit* implementation of KK recreated impedance. Figures on the right-hand side show the relative error between the original and *Z-Hit* implementation of KK recreated impedance and 5% threshold limit indicated with red dashed line. It can be seen that the results are valid up to ~1100 Hz. Data for frequencies higher than 1100 Hz are omitted.

and 92.5% while keeping the current constant. The duration of each elevated FU interval was 24 h.

First, as shown in Fig. 4, high FU affects the Z-HIT test in the frequency region below 0.1 Hz. The relative error of the Z-HIT in that region amounts to over 20% in the case of highest FU. This is a clear indication of the presence of nonlinear behaviour of the fuel cell.

Second, the FU variations affect the values of the identified ECM parameters displayed in Fig. 5. Since the FU is directly connected to the gas conversion impedance, a significant change in the parameters of the middle-frequency pole (Q_2 and R_2) and the low-frequency pole (R_3) was observed. When different FUs were applied, the resistances R_2 and R_3 increased significantly by 20 times in some cases, since their value is reciprocal to the gas flow rate and proportional to the time it takes for the gas to pass through the anode gas channel. The high frequency pole parameters (R_1 and Q_1) have also responded to the increased FU. The high frequency pole describes both anode- and cathode-related processes that take place within the cells.

The value of the serial resistance R_S decreased during the period of higher FU (Fig. 5, events E2 and E3). The reason for such a behaviour is that the increased FU causes the stack to produce more heat and the temperature to rise locally, especially at the anode/electrolyte interface. The increased temperature affects the electrolyte properties by improving its ionic conductivity, resulting in a decrease of R_S. During the events with increased FU the 3rd cell was most affected. According to Comminges et al. [52], increased temperature increases the dilatation of ceramics and interconnects, resulting in increased contact force and an improvement of the metal/ceramic interfacial contact.

Anode re-oxidation after the second FU variation E3 and fuel shortage E4

The second FU event (E3) was induced by increasing the current density according to the following sequence 32 A, 34.06 A, 36.15 A, 38.2 A while keeping the H_2 flow rate constant as shown in Fig. 6a. Each current step lasted 24 h. During the 24-hour period, four impedance measurements were made at each current step.

During the entire E3 event and especially during the last step at FU = 92.5% (I = 38.2 A), three different behaviours can be distinguished: (i)reduction of the cell serial resistance R_S, (ii) improvement of the cell voltage and (iii) small anode reoxidation. Compared to the event E2, the decrease in the R_S value was significantly higher. This is mainly due to the increased power output during the second FU event (E3) compared to E2. As mentioned above, this effect is a consequence of the

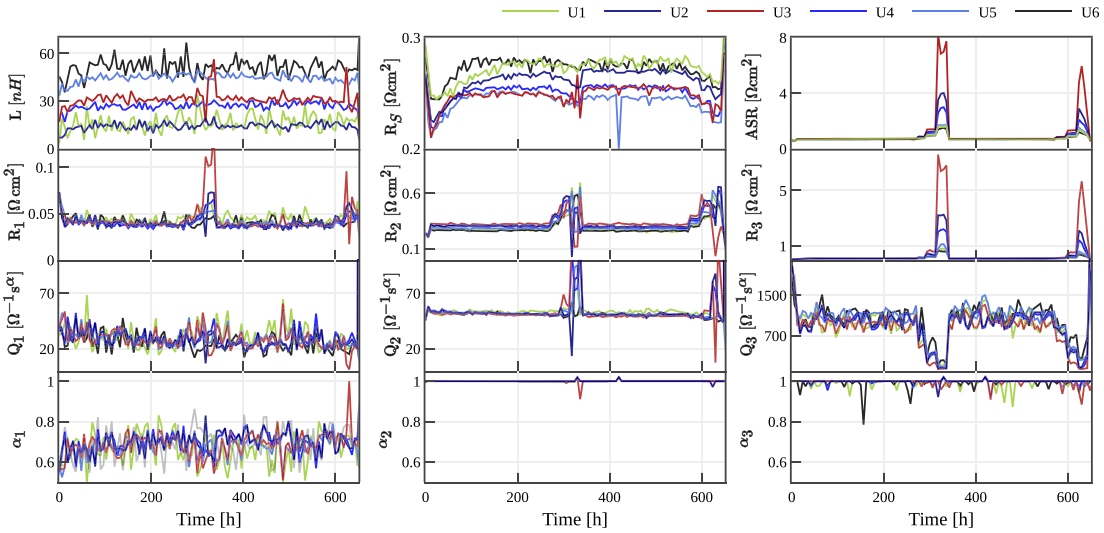

Fig. 5. Time evolution of the ECM parameters during intervals of increased FU. R_1, Q_1 and α_1 represent the high frequency ECM parameters, R_2, Q_2 and α_2 represent the medium frequency ECM parameters and R_3, Q_3, α_3 represent the low frequency ECM parameters. Calculated parameters are shown up to 670 hour.

increased heat production, which causes an increase of YSZ electrolyte conductivity.

During the last step at FU = 92.5% (I = 38.2 A) a recovery of the cell voltages was observed (Fig. 6b). This is due to the decrease in ASR (Fig. 5), which is mainly caused by the decrease in polarisation resistance. In contrast, the serial resistance R_S of the cells (especially for the 2nd and 3rd cell) remained unchanged during the impedance measurements, which was also observed by Laurencin et al. [53]. These effects can be seen in the measured impedances, which are shown in Fig. 5. There are three possible explanations for why the voltage of the cells recovered during the last FU step.

The first explanation could be sought in the decrease of air inlet temperature, probably caused by external disturbances on the test bench. The second possible explanation concerns the redistribution of the current density on the surface of each cell. During the last step, at I=38.2 A, a small anode reoxidation occurred, which was most pronounced in the 2nd and 3rd cell (see Fig. 6b). The 2nd and 3rd cells exhibited voltages of less than 0.73 V at 750 °C. According to Larrain et al. [54] the threshold voltage of anode reoxidation of 0.73 V is calculated considering the thermodynamic equilibrium of Ni/NiO at 750 °C. Other cells were largely unaffected during this event. During this step the reoxidation of the anode started abruptly when moving from 36.1 A to 38.2 A. From this point on, the Ni reoxidation becomes weaker and weaker due to the current density redistribution in the stack. The last, third, explanation could be related to the nickel redistribution in the anode.

4.4. Fuel shortage events — E4, E6 and E8

Until E4 all 6 cells show a similar behaviour during the first two variations of FU. The unforeseen events of fuel shortage led to an emergency shutdown of the experiment. Only the first of these three, i.e. E4, occurred under high FU (see Fig. 6c). During this event, due to empty H_2 tanks, the voltage of all cells dropped below 0.73 V, causing massive Ni reoxidation. In Fig. 6c is shown more clear insight of what happened during the fuel shortage event. At t = 652 h, the flow rate H_2 begins to decrease, but the DC current drawn from the stack was kept constant at I = 38.2 A. The safety mechanism caused the switch to OCV at t = 652.6. Thus, operation under constant DC load without sufficient fuel causes the use of Ni as fuel and reoxidation to NiO. The greatest short-term effect of the event E4 had the 3rd cell (Fig. 2) After this event, a sharp increase in the low frequency pole parameter R_3 and the middle frequency pole parameters R_2 and Q_2 associated with gas conversion is observed, indicating abnormal operation (Fig. 5 and 7). After this event, the values recovered slowly, but never reached the initial values from before the abrupt event E3. The same behaviour was observed with the high frequency pole parameter R_1. In contrast, other parameters (α_i, Q_1 and Q_3) did not respond and did not change their value. The two other fuel shortage events (E6 and E8) had no long-term effects on the overall condition of the SOFC stack.

4.4.1. Back to the nominal operating current

After the fuel supply fault E4, the operating conditions of the stack were brought back to normal i.e. FU=77.5% and I=32 A. From this event on, the experiment lasted for additional 3000 h. The evolution of the parameters during the durability test is shown in Fig. 7. The parameters in Fig. 7 represent continuation of the parameters shown in Fig. 5. During this phase of the experiment, three long-term phenomena can be observed. First, only the serial resistance R_S of the 3rd cell shows a clearly increasing trend over time, cf. Fig. 7. Second, a similar degradation at a much slower rate can be observed in the 2nd and 4th cells (Fig. 2). Finally, the fuel shortage event E4 has changed the behaviour of the 1st and the 6th cell (U1 and U6). As can be seen from Fig. 7, the values of the parameters α_1, R_1, Q_1 and R_s have augmented spread compared to the other cells. All these parameters are related to the high-frequency part of the impedance characteristics. After E7 and E8, however, the values of these parameters return to their initial range and become comparable with the other cells in the stack. Even with post-mortem analysis it was not possible to give a clear explanation for the observed behaviour of these two cells.

For the 3rd cell, the most likely reason for the increasing trend of the R_S increase is mechanical damage along the anode/electrolyte interface, which occurred during the FU step E3 and the interruption of the fuel supply E4. In the case of the adjacent 2nd and 4th cells, the increase of R_S is a consequence of the damaged 3rd cell.

In the similar manner, the event E4 influenced the 3rd cell, the relocation event E7 seems to have accelerated the degradation rate of the 4th cell. As in the previous case, the degradation rate is related with the rate of increase of the serial resistance R_S (Fig. 7).

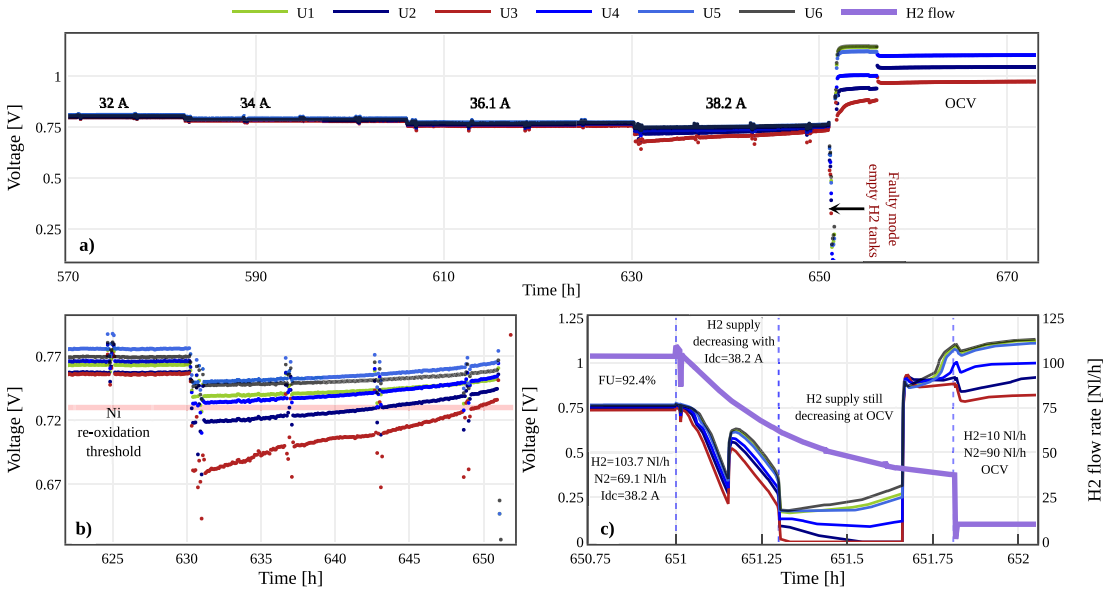

Fig. 6. (a) Detailed view of evolution of cell voltages during the second event of increased FU from FU = 87.5% to FU = 92.5% (event E3). During this step increased FU is achieved by increasing the current density, while keeping the H_2 flow rate constant. b) Improvement of the voltage of the cells during last step of the increased FU at I = 38.2 A. c) Detailed time evolution of all parameters including H_2 flow rate during E4 event.

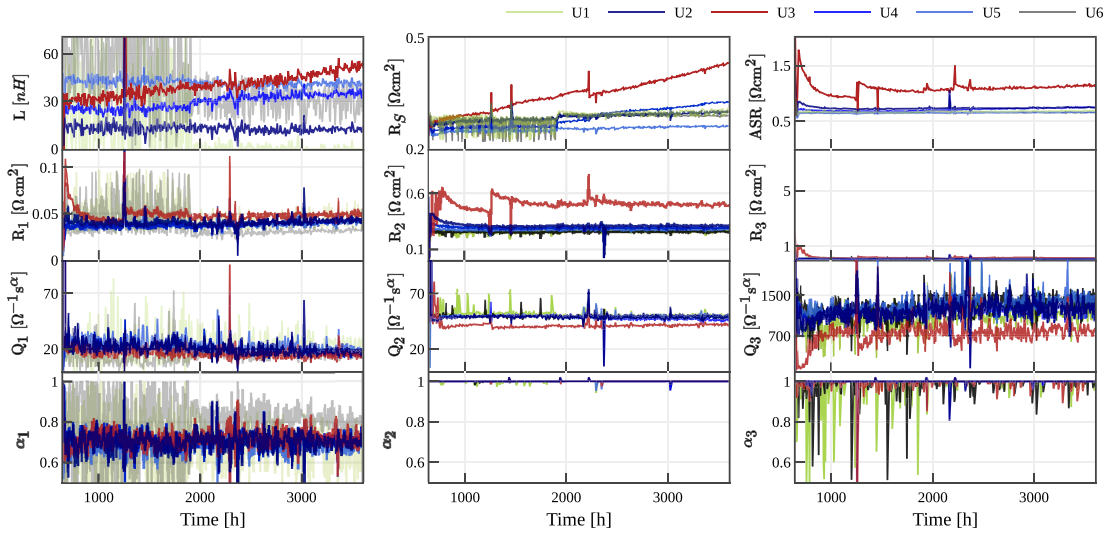

Fig. 7. Time evolution of the ECM parameters during the durability test. R_1, Q_1 and α_1 represent the high frequency ECM parameters, R_2, Q_2 and α_2 represent the medium frequency ECM parameters and R_3, Q_3, α_3 represent the low frequency ECM parameters. Calculated parameters are shown from 670 to 3600 h.

4.5. Evolution of the inductance L

The presence of the inductive artefacts is due to the mutual inductance and the geometrical set-up of the stack and does not describe the operation of the fuel cell [55]. In our case also the inductance L of the cells was estimated during the whole experiment. The evolution of the inductance of the middle cells is shown in Figs. 5 and 7. During the first 650 h the inductance of the cells was constant. After the E4 event, however, the inductance of the 3rd cell shows a markedly increasing trend over time, similar to the increasing trend of the serial resistance R_S. This behaviour corresponds to the reoxidation of the anode at the fuel outlet and the increase of the serial resistance of this cell due to NiO instead of Ni. Event E4 (fuel shortage) caused unusually large spread of the estimated parameters L of the 1st and the 6th cell which indicates abnormal behaviour at high frequencies. A similar pattern can be observed in the 4th cell immediately after the reallocation event E7, which is also similar to the behaviour of the serial resistance R_S of the same cell.

4.6. Post-mortem micro structural analysis

After the end of the experiment a post-mortem analysis of the stack cells was performed. It included a leakage test of the stack, followed by a disassembly of the stack elements to observe the quality of the cells and the sealants and to look for other particularities.

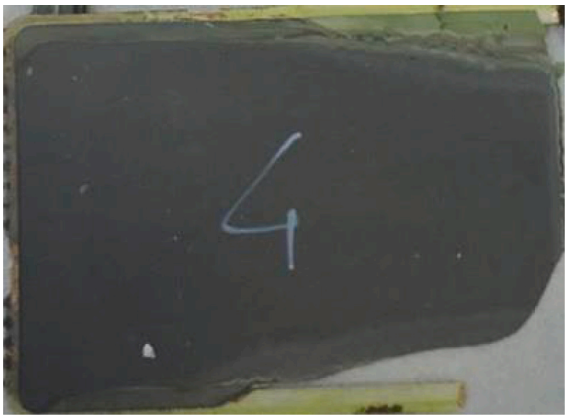

Fig. 8. Post mortem analysis on 3rd cell, which was denoted as the 4th by the stack supplier, where anode oxidation occurred (black/grey Ni has become green NiO) at the fuel exhaust side. (For interpretation of the references to color in this figure legend, the reader is referred to the web version of this article.)

The leakage test indicated out-of-scale leakage. Detailed inspection of the stack elements also revealed that the quality of the sealant was poor. In addition, the oxidation patterns on the cells (especially cell 3) indicated that the cells experienced fuel shortage. In Fig. 8 there is a photo of the 3rd (supplier designated as the 4th cell), which indicates strong anode oxidation (black/grey Ni has become green NiO) on the fuel outlet side. This strong anode oxidation, which occurred after the second FU event (E4), caused the monotone increase of R_S.

5. Conclusion

Fast impedance spectroscopy is used to detect gas shortage problems during a long-term experiment on a short stack. Firstly, it is shown that fast EIS, thanks to the short DRBS perturbations together with CWT analysis, bring two important advantages over classical EIS. The duration of EIS measurements is an order of magnitude shorter than that of classical sinusoidal EIS. (less than 2 min). This made it possible to increase the rate of characterisation runs when important changes in the stack need to be tracked.

Secondly, the resulting EIS curves are calculated with an almost continuous frequency resolution without affecting the measurement time. This is a significant improvement over the classic EIS, which typically have 10 points per decade.

More than 600 impedance curves were evaluated during the experiment. To the best of the authors' knowledge, this is the first such application in the field of durability testing of SOFC systems. The results indicate that increased fuel utilisation results in violated Z-HIT conditions and increased ASR. The main reason for the increased ASR is the resistance associated with the slowest pole of the model. When the FU conditions are brought back to the nominal value, the presence of degradation can be observed by an increasing serial resistance R_S.

CRediT authorship contribution statement

Gjorgji Nusev: Conceptualisation, Methodology, Software, Hardware, Investigation, Writing. **Bertrand Morel:** Investigation, Conceptualisation, Experimental, Writing. **Julie Mougin:** Resources, Experimental. **Đani Juričić:** Resources, Supervision. **Pavle Boškoski:** Resources, Supervision, Writing.

Declaration of competing interest

The authors declare that they have no known competing financial interests or personal relationships that could have appeared to influence the work reported in this paper.

Acknowledgments

The authors would like to acknowledge support received in part from the Slovenian Research Agency through the project J2-9441, BI-Fr/CEA/18-20-003 and research programme P2-0001. Part of the support through the project INSIGHT (grant agreement No. 735918) within the framework of the Fuel Cells and Hydrogen 2 Joint Undertaking under the European Union's Horizon 2020 research and innovation programme, Hydrogen Europe and Hydrogen Europe research is acknowledged. Our warmest thanks go to the SOLIDpower team, in particular Jan Pieter Ouweltjes for valuable comments and the post-mortem analysis. We are also indebted to the anonymous referees for the valuable feedback on the earlier version of the manuscript.

References

[1] European Energy Research Alliance, Joint research programme on fuel cells and hydrogen technologies (jp fch): Implementation plan 2018-2030, 2019, URL: https://www.eera-set.eu/component/attachments/?task=download&id=253, (Accessed 13 October 2020).
[2] A. Baldinelli, L. Barelli, G. Bidini, A. Di Cicco, R. Gunnella, M. Minicucci, A. Trapananti, Advancements regarding in-operando diagnosis techniques for solid oxide cells niysz cermets, in: AIP Conference Proceedings, vol. 2191, AIP Publishing LLC, 2019, 020012.
[3] P. Polverino, M. Sorrentino, C. Pianese, A model-based diagnostic technique to enhance faults isolability in solid oxide fuel cell systems, Appl. Energy 204 (2017) 1198–1214.
[4] S.M.R. Niya, R.K. Phillips, M. Hoorfar, Process modeling of the impedance characteristics of proton exchange membrane fuel cells, Electrochim. Acta 191 (2016) 594–605.
[5] Z. Hu, L. Xu, J. Li, Q. Gan, X. Xu, Z. Song, Y. Shao, M. Ouyang, A novel diagnostic methodology for fuel cell stack health: performance, consistency and uniformity, Energy Convers. Manage. 185 (2019) 611–621.
[6] M. Wang, M. Chen, Z. Yang, Y. Wang, Y. Wang, G. Liu, J.K. Lee, X. Wang, A study on fuel additive of methanol for room temperature direct methanol fuel cells, Energy Convers. Manage. 168 (2018) 270–275.
[7] Y. Gu, Y. Zhang, L. Ge, Y. Zheng, H. Chen, L. Guo, Ysz electrolyte support with novel symmetric structure by phase inversion process for solid oxide fuel cells, Energy Convers. Manage. 177 (2018) 11–18.
[8] L. Vichard, R. Petrone, F. Harel, A. Ravey, P. Venet, D. Hissel, Long term durability test of open-cathode fuel cell system under actual operating conditions, Energy Convers. Manage. 212 (2020) 112813.
[9] B. Liu, H. Muroyama, T. Matsui, K. Tomida, T. Kabata, K. Eguchi, Analysis of impedance spectra for segmented-in-series tubular solid oxide fuel cells, J. Electrochem. Soc. 157 (2010) B1858–B1864.
[10] A.D. Franklin, H.J. De Bruin, The fourier analysis of impedance spectra for electroded solid electrolytes, Phys. Status Solidi a 75 (1983) 647–656.
[11] M. Heinzmann, A. Weber, E. Ivers-Tiffée, Advanced impedance study of polymer electrolyte membrane single cells by means of distribution of relaxation times, J. Power Sources 402 (2018) 24–33.
[12] A. Lasia, Electrochemical Impedance Spectroscopy and Its Applications, Springer-Verlag, New York, 2014.
[13] X.-Z. Yuan, C. Sons, H. Wang, J. Zhang, Electrochemical Impedance Spectroscopy in PEM Fuel Cells, Fundamentals and Applications, Springer, London, 2010.
[14] M.E. Orazem, B. Tribollet, Electrochemical Impedance Spectroscopy, John Wiley & Sons, Inc., 2008.
[15] P. Boškoski, A. Debenjak, B.M. Boshkoska, Rayleigh copula for describing impedance data–with application to condition monitoring of proton exchange membrane fuel cells, European J. Oper. Res. 266 (2018) 269–277.
[16] P. Boškoski, A. Debenjak, Optimal selection of proton exchange membrane fuel cell condition monitoring thresholds, J. Power Sources 268 (2014) 692–699.
[17] M. Stepančič, Đ. Juričić, P. Boškoski, Fault detection of fuel cell systems based on statistical assessment of impedance data, Energy Convers. Manage. 195 (2019) 76–85.
[18] J. Schoukens, M. Vaes, R. Pintelon, Linear system identification in a nonlinear setting: Nonparametric analysis of the nonlinear distortions and their impact on the best linear approximation, IEEE Control Syst. Mag. 36 (2016) 38–69.
[19] D. Sarantaridis, R. Rudkin, A. Atkinson, Oxidation failure modes of anode-supported solid oxide fuel cells, J. Power Sources 180 (2008) 704–710.
[20] T.-H. Lee, K.-Y. Park, J.-T. Kim, Y. Seo, K.B. Kim, S.-J. Song, B. Park, J.-Y. Park, Degradation analysis of anode-supported intermediate temperature-solid oxide fuel cells under various failure modes, J. Power Sources 276 (2015) 120–132.
[21] J. Laurencin, G. Delette, B. Morel, F. Lefebvre-Joud, M. Dupeux, Solid oxide fuel cells damage mechanisms due to ni-ysz re-oxidation: case of the anode supported cell, J. Power Sources 192 (2009) 344–352.
[22] M. Angeloni, P. Lisbona, R. Bove, A pde model for microscopic simulation of solid oxide fuel cells, J. Power Sources 201 (2012) 184–195.

[23] G. Brus, K. Miyoshi, H. Iwai, M. Saito, H. Yoshida, Change of an anode's microstructure morphology during the fuel starvation of an anode-supported solid oxide fuel cell, Int. J. Hydrogen Energy 40 (2015) 6927–6934.

[24] A. Esposito, L. Russo, C. Kändler, C. Pianese, B. Ludwig, N.Y. Steiner, High fuel utilization in solid oxide fuel cells: experimental characterization and data analysis with continuous wavelet transform, J. Power Sources 317 (2016) 159–168.

[25] E. Ramschak, V. Peinecke, P. Prenninger, T. Schaffer, V. Hacker, Detection of fuel cell critical status by stack voltage analysis, J. Power Sources 157 (2006) 837–840.

[26] R.R. Mosbæk, Solid Oxide Fuel Cell Stack Diagnostics (Ph.D. thesis), Technical University of Denmark., 2014.

[27] L. Malafronte, B. Morel, A. Pohjoranta, Online total harmonic distortion analysis for solid oxide fuel cell stack monitoring in system applications, Fuel Cells 18 (2018) 476–489.

[28] V. Subotić, N.H. Menzler, V. Lawlor, Q. Fang, S. Pofahl, P. Harter, H. Schroettner, C. Hochenauer, On the origin of degradation in fuel cells and its fast identification by applying unconventional online-monitoring tools, Appl. Energy 277 (2020) 115603.

[29] P. Boškoski, A. Debenjak, B.M. Boshkoska, Fast Electrochemical Impedance Spectroscopy: As a Statistical Condition Monitoring Tool, Springer, 2017.

[30] E. Barsoukov, J. Macdonald, Impedance Spectroscopy: Theory, Experiment, and Applications, Wiley, 2018.

[31] L. Ljung, System Identification: Theory for the User, Prentice Hall Information and System Sciences Series, Prentice Hall PTR, 1999.

[32] R. Isermann, M. Münchhof, Identification of Dynamic Systems: An Introduction with Applications, Advanced Textbooks in Control and Signal Processing, Springer-Verlag Berlin Heidelberg, 2011.

[33] H. Stark, J. Woods, Probability, Statistics, and Random Processes for Engineers, fourth ed., Pearson, 2011.

[34] S. Mallat, A Wavelet Tour of Signal Processing: The Sparse Way, third ed., Elsevier Academic Press, 2008.

[35] D. Iatsenko, Nonlinear Mode Decomposition (Springer theses), Springer International Publishing, 2015.

[36] C. Torrence, G.P. Compo, A practical guide to wavelet analysis, Bull. Am. Meteorol. Soc. 79 (1998) 61–78.

[37] P. Agarwal, M.E. Orazem, L.H. Garcia-Rubio, Application of measurement models to impedance spectroscopy III. Evaluation of consistency with the Kramers–Kronig relations, J. Electrochem. Soc. 142 (1995) 4159–4168.

[38] H.W. Bode, et al., Network Analysis and Feedback Amplifier Design, van Nostrand New York, 1945.

[39] W. Ehm, R. Kaus, C.-A.S.W. Strunz, Z-hit – a simple relation between impedance modulus and phase angle. providing a new way to the validation of electrochemical impedance spectra, in: F. Mansfeld, F. Huet, O. Mattos (Eds.), New Trends in Electrochemical Impedance Spectroscopy and Electrochemical Noise Analysis, Electrochemical Society Inc, 2001, pp. 1–10, URL: http://zahner.de/pdf/zhitehm.pdf.

[40] P. Zoltowski, On the electrical capacitance of interfaces exhibiting constant phase element behaviour, J. Electroanal. Soc. 443 (1998) 149–154.

[41] M. Sluyters-Rehbach, Impedances of electrochemical systems: Terminology, nomenclature and representation part I: Cells with metal electrodes and liquid solutions, Pure Appl. Chem. 66 (1994) 1831–1891.

[42] H. Schichlein, A. Müller, M. Voigts, A. Krügel, E. Ivers-Tiffée, Deconvolution of electrochemical impedance spectra for the identification of electrode reaction mechanisms in solid oxide fuel cells, J. Appl. Electrochem. 32 (2002) 875–882.

[43] X.-Z.R. Yuan, C. Song, H. Wang, J. Zhang, Electrochemical Impedance Spectroscopy in PEM Fuel Cells: Fundamentals and Applications, Springer Science & Business Media, 2009.

[44] R.M. Fuoss, J.G. Kirkwood, Electrical properties of solids. VIII. Dipole moments in polyvinyl chloride-diphenyl systems, J. Am. Chem. Soc. 63 (1941) 385–394.

[45] A. Leonide, V. Sonn, A. Weber, E. Ivers-Tiffée, Evaluation and modeling of the cell resistance in anode-supported solid oxide fuel cells, J. Electrochem. Soc. 155 (2008) B36–B41.

[46] A. Leonide, B. Rüger, A. Weber, W. Meulenberg, E. Ivers-Tiffée, Impedance study of alternative (la, sr) feo3- δ and (la, sr)(co, fe) o3- δ miec cathode compositions, J. Electrochem. Soc. 157 (2010) B234–B239.

[47] M. Lang, C. Auer, A. Eismann, P. Szabo, N. Wagner, Investigation of solid oxide fuel cell short stacks for mobile applications by electrochemical impedance spectroscopy, Electrochim. Acta 53 (2008) 7509–7513.

[48] S. Primdahl, M. Mogensen, Gas conversion impedance: A test geometry effect in characterization of solid oxide fuel cell anodes, J. Electrochem. Soc. 145 (1998) 2431–2438.

[49] D. Klotz, Characterization and Modeling of Electrochemical Energy Conversion Systems By Impedance Techniques, KIT Scientific Publishing, 2014.

[50] L. Almar, J. Szász, A. Weber, E. Ivers-Tiffée, Oxygen transport kinetics of mixed ionic-electronic conductors by coupling focused ion beam tomography and electrochemical impedance spectroscopy, J. Electrochem. Soc. 164 (2017) F289.

[51] V. Subotić, B. Stoeckl, V. Lawlor, J. Strasser, H. Schroettner, C. Hochenauer, Towards a practical tool for online monitoring of solid oxide fuel cell operation: An experimental study and application of advanced data analysis approaches, Appl. Energy 222 (2018) 748–761.

[52] C. Comminges, Q. Fu, M. Zahid, N.Y. Steiner, O. Bucheli, Monitoring the degradation of a solid oxide fuel cell stack during 10, 000 h via electrochemical impedance spectroscopy, Electrochim. Acta 59 (2012) 367–375.

[53] J. Laurencin, G. Delette, O. Sicardy, S. Rosini, F. Lefebvre-Joud, Impact of 'redox'cycles on performances of solid oxide fuel cells: case of the electrolyte supported cells, J. Power Sources 195 (2010) 2747–2753.

[54] D. Larrain, D. Favrat, et al., Simulation of sofc stack and repeat elements including interconnect degradation and anode reoxidation risk, J. Power Sources 161 (2006) 392–403.

[55] R.R. Mosbæk, J. Hjelm, R. Barfod, J. Høgh, P.V. Hendriksen, Electrochemical characterization and degradation analysis of large sofc stacks by impedance spectroscopy, Fuel Cells 13 (2013) 605–611.

4.2 Condition Monitoring of Proton Exchange Membrane Hydrogen Compressor Using EIS

Fractional Order System Identification Method for Online Monitoring of Humidity of Electrochemical Hydrogen Pumps

Gjorgji Nusev, Pavle Boškoski, and Gregor Dolanc

Abstract Electrochemical hydrogen pump (EHP) is a promising technology capable of extracting hydrogen from miscellaneous gas mixture and compresses it to very high pressures. The basic working principles are similar to that of a proton exchange membrane (PEM) fuel cell. Consequently, its performance is heavily dependent on humidity level of the membrane. Unlike PEM fuel cells where water is generated as a by-product, in the case of EHP the humidity has to be delivered via external humidifier. Therefore, it is paramount to have accurate information regarding the humidity in order to achieve optimal exploitation. Inaccessibility of the membranes makes it almost impossible to perform direct humidity measurements. Addressing this issue, this paper presents a method for online estimation of humidity levels based on the parameters of an equivalent circuit model (ECM). The parameter estimation is performed through a combination of evolutionary algorithm and simplex optimization. The method is evaluated on a market ready EHP device with capacity of pumping 1.4118 stl/min of H_2.

1 Introduction

Numerous studies on future energy development predict hydrogen as a main source for energy storage. In that manner it is expected that the hydrogen production will continue to increase in the years that follow [1, 2]. According to Fraile [2] the global demand for hydrogen in 2010 was around 43 Mtons and is foreseen to reach 50 Mtons by 2025. In the complete production chain one of the most

G. Nusev (✉)
Department of System and Control, Jožef Stefan Institute, Ljubljana, Slovenia

Jožef Stefan International Postgraduate School, Ljubljana, Slovenia
e-mail: gjorgji.nusev@ijs.si

P. Boškoski · G. Dolanc
Department of System and Control, Jožef Stefan Institute, Ljubljana, Slovenia
e-mail: pavle.boskoski@ijs.si; gregor.dolanc@ijs.si

W. Zamboni, G. Petrone (eds.), *ELECTRIMACS 2019*, Lecture Notes
in Electrical Engineering 615, https://doi.org/10.1007/978-3-030-37161-6_28

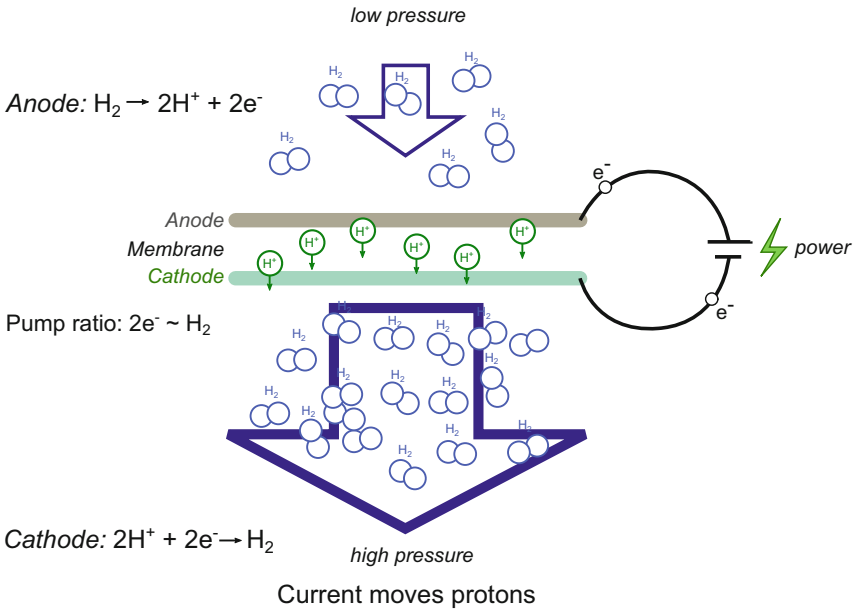

Fig. 1 Basic concept of how EHP works. It uses direct current to pull hydrogen through an impermeable membrane, very efficiently and highly selective for hydrogen [4]

energy consuming steps is the compression. There are two categories of hydrogen compressors: *mechanical* which uses adiabatic process and *non-mechanical* which mainly uses isothermal process for compression.

Non-mechanical compressors such as EHP use electricity to extract hydrogen from miscellaneous gas mixtures and compress it in order to meet different application requirements. Also the absence of moving parts makes them more efficient when comparing with the conventional mechanical compressors which are noisy and less effective than the non-mechanical [3]. The structure of EHP is similar to that of a proton exchange membrane fuel cells (PEMFC). The basic principles about how EHP works are shown in Fig. 1.

The hydrogen molecules enter the anode side (the low pressure side) of the cell where they are oxidized to protons and electrons. Due to the external voltage potential, hydrogen protons are driven through the membrane to the cathode side while the electrons are forced through an external circuit also to the cathode side, where they are recombined to form molecular hydrogen. As a result of the applied external voltage through time, the pressure at the cathode side increases with the increased number of transported hydrogen molecules. Inside the EHP, the total pressure at the cathode is larger than that at the anode, with $P_A < P_C$.

Although EHP technology has many advantages and possible applications, it is mainly used as a diagnostic test for measuring the crossover in fuel cells. Strobel et al. [5] was the first one to recognize the possibilities of the PEM-based structure for EHP. Hao et al. [6] performed ectrochemical impedance spectroscopy (EIS) on EHP with included internal humidifier with dead-end anode. Nguyen et al. [7] has

shown how the temperatures of the humidifier and the temperature of the stack are influencing the performance of the stack. Common issue in the reported analysis is the control of the membrane's humidification levels.

Humidification of the membrane plays an important role in proton conduction and is tightly connected to the overall performance of the EHP. Shortage of water reduces the proton conductance, whereas flooding decreases the active surface area. Unlike PEM fuel cells, EHP does not produce water and therefore it has to be delivered via an external humidifier.

Due to physical limitations it is impractical to perform direct humidity measurements. Therefore, EIS is the only available option to perform online humidification estimation. For that purpose, this study employs an approach for fast impedance analysis that is based on discrete random binary sequence (DRBS) excitation [8]. The main advantage of DRBS excitation over the classical single-sine excitation is the time needed to perform the measurement. The impedance characteristic in the frequency band from 0.1 to 500 Hz is identified in 60 s, approximately five times faster compared to the conventional single-sine approach. Based on this impedance data, parameters of ECM are estimated. The humidity level is inferred based on the variation of parameters of the ECM parameters. Parameters estimation is performed using a hybrid optimization method comprising of genetic algorithm and simplex method.

2 Methodology

ECMs represent one approach for analysis of impedance data. Typically, the analysis is based on the link between the parameters of an ECM and the underlying chemical reactions occurring inside the electrochemical energy devices [9–11]. The accuracy of the analysis is directly related to the accuracy of the method used for the parameter estimation of the selected ECM.

There are many different methods for parameter estimation. On the one hand, there are methods which are based on complex nonlinear least squares (CNLS) deterministic algorithms such as Levenberg–Marquardt and Gauss Newton algorithm [12, 13]. The main issue with this method is the selection of good initial conditions which are crucial to provide good convergence towards the best solution. On the other hand there are different methods which are based on evolutionary algorithms (genetic algorithm). Evolutionary algorithms when compared to the CNLS are more suitable for solving general-purpose problems where prior knowledge of the parameters is not required or limited. The biggest challenge with these approaches is designing a cost function and optimization method that will converge to the global minimum of the cost function.

For the presented approach the following cost function is selected:

$$C(\mathbf{x}) = \sum_{i=0}^{N} \left[\Re(Z_M(f_i) - \hat{Z}_S(\mathbf{x}, f_i))\right]^2 + \left[\Im(Z_M(f_i) - \hat{Z}_S(\mathbf{x}, f_i))\right]^2, \quad (1)$$

where $Z_M(f_i)$ represents the measured impedance value at frequency f_i and $\hat{Z}_S(\mathbf{x}, f_i)$ represents the estimated impedance using parameters $\mathbf{x}$ at frequency f_i. Equation (1) represents a Manhattan distance and it is mainly used as an optimization function for any complex functions [14]. In our case the complex function represents the impedance.

In order to reach the global minimum in a least number of steps, the proposed approach relies on a hybrid optimization that comprises:

- Genetic algorithm;
- Bounded simplex optimization.

A block scheme of the method is shown in Fig. 2. Through the genetic algorithm multiple starting points are randomly distributed in previously defined search area. This is done in order to roughly estimate the location of the global minimum. Before it continues with the next iteration (generation), the best solutions from the current iteration are then used as an initial condition for the simplex optimization method for fine tuning. The obtained parameters from the simplex method are then sorted according to its corresponding cost function value in ascending order. Afterwards, the best individuals are propagated to the next generation. Each subsequent generation is mutated by adding a small amount of noise [13]. The process terminates when all of the following conditions are met:

- the best value of the criterion function is less than previously defined one;
- absolute change of the criterion function value during the last couple of iterations is less than 5%;
- change of the estimated parameters through each iteration is less than some predefined percent.

3 Experimental Setup

The approach was evaluated on a 5-cell EHP stack. A schematic diagram of the test bed is shown in Fig. 3.

Humidification level is controlled by altering the hydrogen supply via three solenoid valves. Solenoid valve V3 is used to deliver the hydrogen mixture to the stack directly, without humidification, while valves V4 and V10 deliver the hydrogen mixture to the stack through a humidifier. On the high pressure side there is a buffer to accumulate the pumped hydrogen and backpressure regulator V9 to control the pressure in the tank and at the high pressure side of the stack at constant value.

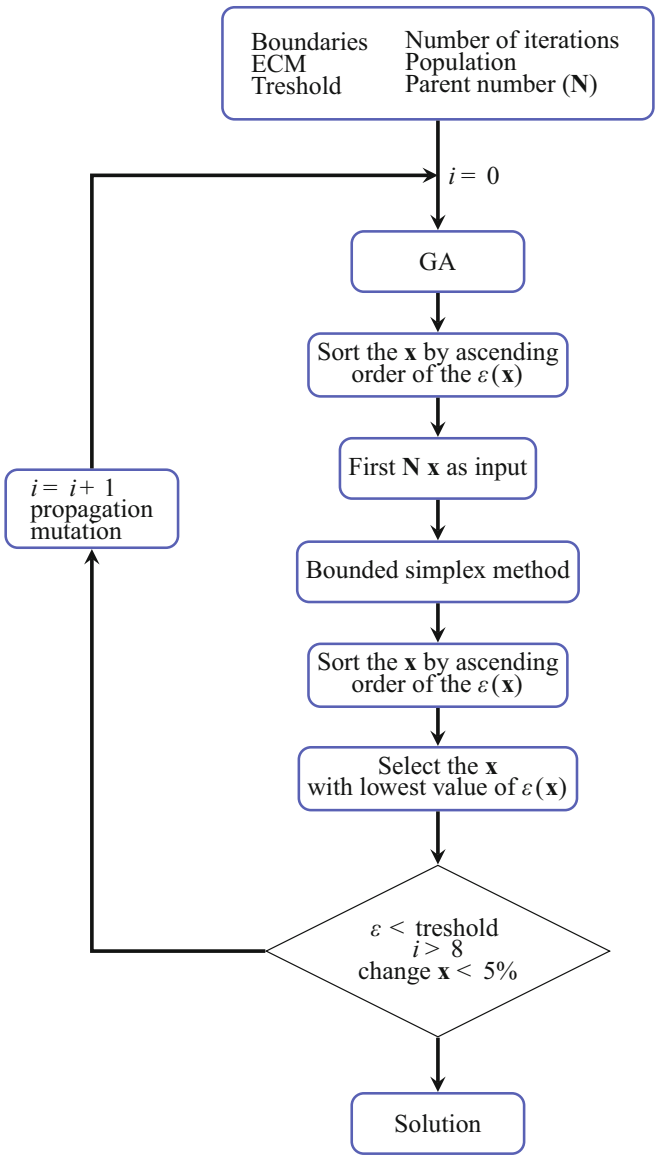

Fig. 2 Block scheme of the proposed optimization algorithm

Electrical connections on the EHP are shown in Fig. 4. Characterization of the stack is performed at DC currents $I_{DC} = 20\,\text{A}$ with peak-to-peak amplitude $I_{AC} = 1\,\text{A}$ by using DRBS excitation [8]. The perturbed current is induced using programmable digital electric load (Rigol DL3031A) with excitation frequencies starting from 0.1 Hz up to 1000 Hz. The voltage response of the cells together with the current is sampled with sampling frequency $fs = 50$ kHz using 16-bit data acquisition card (NI USB 6215). Before DAQ signals are low pass filtered at $f_c = 10.8$ kHz.

When performing EIS measurements all other controllable variables are kept constant. Due to the fact that we were not able to directly measure the humidification

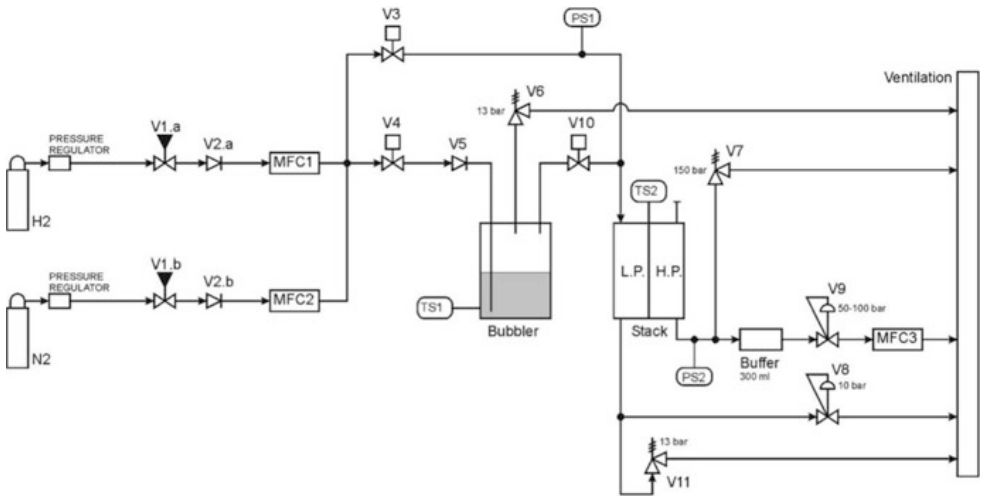

Fig. 3 Gas connections of the experimental setup for performing diagnostic experiments on EHP

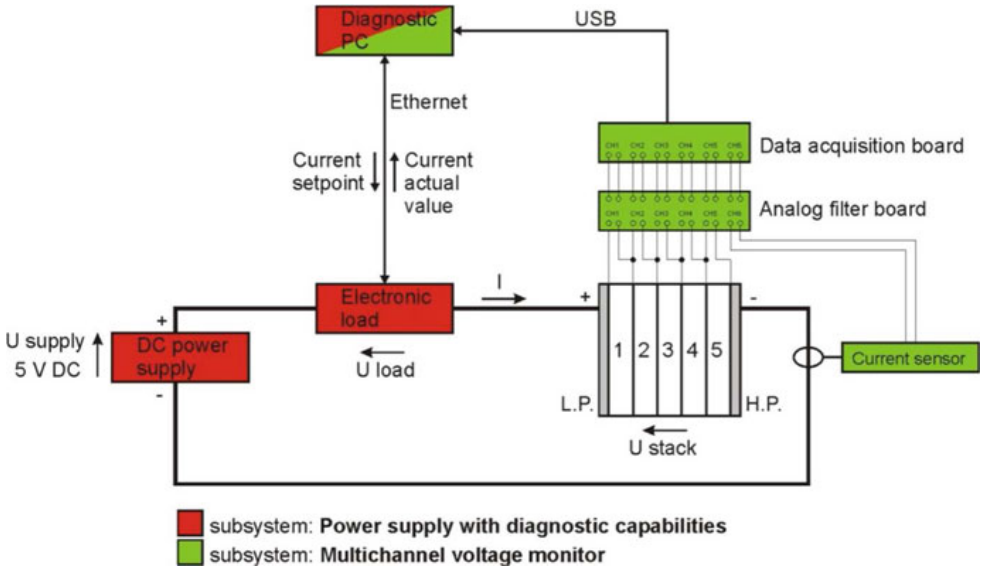

Fig. 4 Electrical connection of the EHP for performing electrochemical impedance spectroscopy

level, the first experiment was performed with the humidifier being turned on and the second experiment was performed when the humidifier turned off. The main goal was to detect the effects of membrane's humidification levels on the measured impedance.

4 Results

Since the EIS is a linear technique, the operating condition of the EHP must fulfill the linearity conditions. These conditions are associated to the value of the amplitude of the excitation signal. It states that the amplitude must be small enough in order to operate within the linear region; however, it has to be big enough to measure its response. For that reason before performing the EIS, an IV curve of the EHP was first measured (Fig. 5) in order to determine the value of the AC amplitude at desired DC point.

From the IV curve (Fig. 5) it was decided to perform EIS measurements at $I_{DC} = 20\,\text{A}$ with peak-to-peak amplitude $I_{AC} = 1\,\text{A}$ at two different operating conditions:

1. Nominal mode—with turned on humidification;
2. Drying mode—with turned off humidification.

Calculated impedances of all the 5 cells are given in Figs. 6 and 7. Solid lines are impedances at nominal conditions; dotted lines are the impedances when the cells are in drying mode. There are several effects that have to be analyzed separately.

First, the impedance of the 5th cell differs from the others. There are two different reasons. The 5th cell is located the furthest from the input and receives the least amount of humidity. Additionally, due to the connectors for measuring the cell voltage introduce additional resistance, especially the negative wire which is connected directly to the cathode where wire of the power supply is connected. The effect of this additional resistance is seen in the impedance measurement.

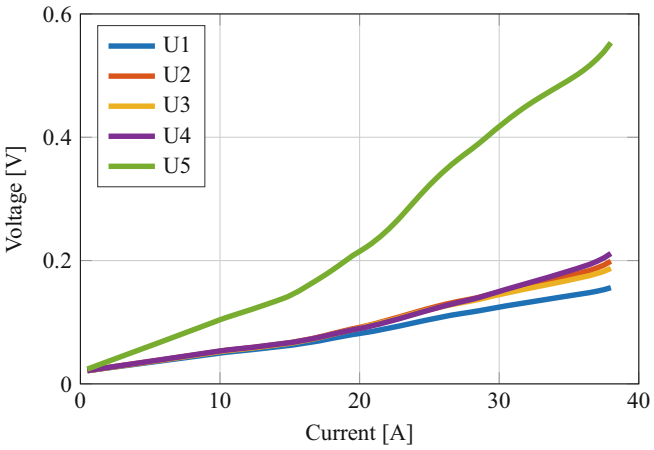

Fig. 5 IV curve of the HyET electrochemical hydrogen pump

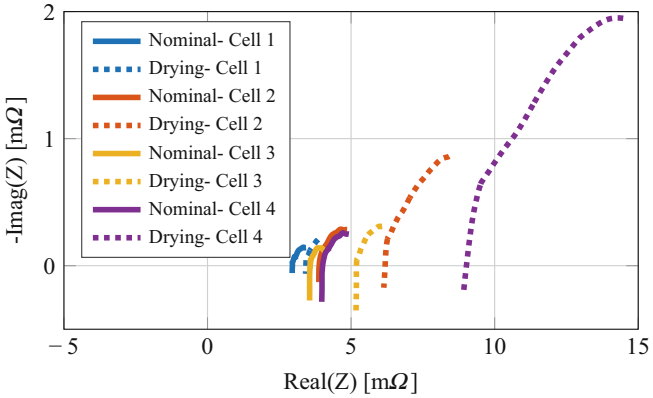

Fig. 6 Measured impedance of the first four cells in the stack at different conditions (normal and drying)

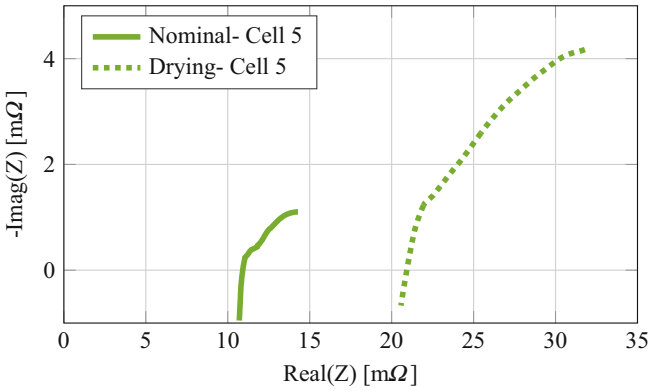

Fig. 7 Measured impedance of the fifth cells in the stack at different conditions (normal and drying)

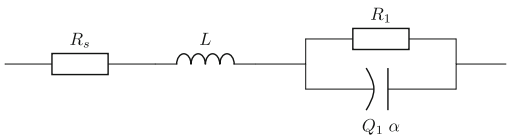

Fig. 8 Equivalent circuit model of EHP

4.1 Equivalent Circuit Model Selection

For the process of parameter estimation, the ECM topology shown in Fig. 8 has been selected for detailed analysis. The selected ECM is consisted of three elements connected in series. Resistor R_s represents the losses inside the membrane, parallel connection between resistor R_1 and constant phase element Q_1 represents the losses at the electrode, and inductance L appears due to internal wire connection between the cells inside the stack. Theoretical impedance of the selected ECM is given with the following equation:

$$Z_{SIM}(j\omega) = j\omega L + R_s + \frac{R_1}{1 + (j\omega\tau)^{\alpha}}, \qquad \tau^{\alpha} = R_1 Q_1 \tag{2}$$

4.2 Parameter Estimation

After evaluation of the hybrid optimization algorithm on the measured impedances, the parameters of the selected ECM were estimated. The values for all 5 cells in both working modes (nominal and drying) are given in Table 1. The comparison of the measured impedances in both modes, nominal and drying, and the impedance of its fitted model are shown in Figs. 9 and 10. Figure 9 shows the measured and fitted impedance of the 2nd cell in nominal mode, whereas Fig. 10 shows the impedances of the same cell in drying mode.

Drying of the cells did not have big impact on the fractional order coefficient α. Also the changes of the inductance L are insignificant. On the other hand, resistances R_S and R_1 have increased significantly, 56% and 247%, respectively. For the 4th cell the time constant τ has increased significantly.

The reason for the conductivity decrease of the membrane when in drying mode is connected to the size of the water clusters within the polymer microstructure. Dehydration of the EHP membranes leads to narrowing of the interconnecting

Table 1 ECM parameters at different operation conditions

	Parameters	Nominal mode	Drying mode
Cell 1	L [nH]	12.7	12.4
	R_S [mΩ]	2.9179	3.4068
	R_1 [mΩ]	0.94147	1.417
	τ [s]	1.317	2.7919
	α	0.38	0.40
Cell 2	L [nH]	29.5	46.8
	R_S [mΩ]	3.8012	5.9447
	R_1 [mΩ]	2.0094	6.9781
	τ [s]	1.8084	2.8614
	α	0.36	0.34
Cell 3	L [nH]	52.9	64.5
	R_S [mΩ]	3.5231	5.151
	R_1 [mΩ]	0.8457	1.853
	τ [s]	0.5	0.574
	α	0.41	0.47
Cell 4	L [nH]	58.3	90.7
	R_S [mΩ]	3.8897	7.9873
	R_1 [mΩ]	2.029	30.558
	τ [s]	2.3775	80.498
	α	0.32	0.25
Cell 5	L [nH]	198	192
	R_S [mΩ]	10.27	19.019
	R_1 [mΩ]	14.53	65.108
	τ [s]	100	100
	α	0.24	0.26

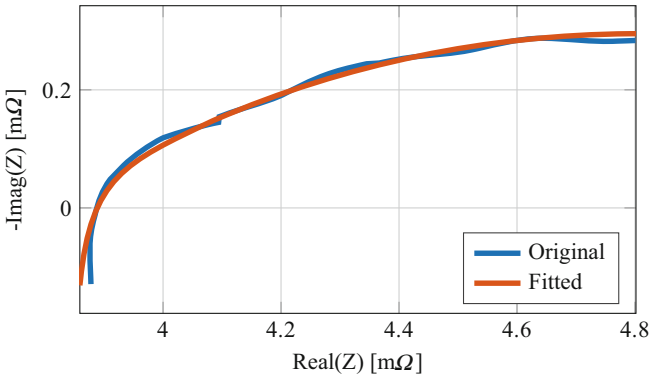

Fig. 9 Measured impedance of the cell 2 (blue line) and its fit (red line) in nominal mode

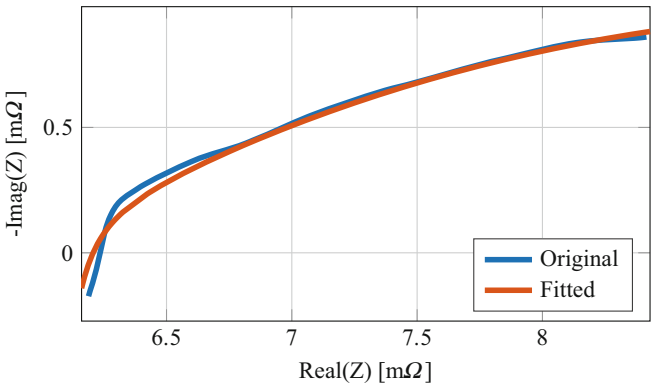

Fig. 10 Measured impedance of the cell 2 (blue line) and its fit (red line) in drying mode

channels which decreases the mobility of the protons and increases the electrical resistance [15]. On the other hand, when the EHP membranes are well humidified the microporous structure swells which leads to increase of the ionic conductance.

5 Conclusions

Performances of the EHP are highly dependent on the level of humidity presented inside the membrane. For that reason two experiments were performed, one at nominal conditions when humidification was turned on and the second at drying conditions when the humidification was turned off. By using electrochemical impedance spectroscopy, based on DRBS excitation signals, we were able to detect changes in the parameters of the selected ECM after the experiments were performed. Impedance of the EHP was measured in the frequency interval between 0.1 and 1000 Hz. Parameters of the ECM were estimated using hybrid optimization method.

From the obtained results it can be seen that drying increased the serial resistance R_S and the resistance R_1 of each of the cells. From this assumption can be concluded

that by monitoring the changes of these two variables it is possible to measure the level of humidification inside the membrane while it is in operating mode. By measuring the level of humidification it is possible to prevent the drying or flooding of the EHP.

Acknowledgements The authors acknowledge the project L2-7663, and research core funding No. P2-0001 that were financially supported by the Slovenian Research Agency. The authors acknowledge financial support through the project MEMPHYS (grant agreement No 735533) within the framework of the Fuel Cells and Hydrogen 2 Joint Undertaking under the European Union's Horizon 2020 research and innovation programme, Hydrogen Europe and Hydrogen Europe research.

References

1. D. S. Satyapal, Hydrogen and fuel cells overview, U.S. Department of Energy Fuel Cell Technologies office, April 2017. [Online]. Available: https://www.energy.gov/sites/prod/les/2017/06/f34/fcto-h2-fc-overview-dla-worldwide-energy-conf-2017-satyapal.pdf
2. D. Fraile, J. Lanoix, P. Maio, A. Rangel, A. Torres, Overview of the market segmentation for hydrogen across potential customer groups, based on key application areas. CertifHy (2015)
3. K. Onda, K. Ichihara, M. Nagahama, Y. Minamoto, T. Araki, Separation and compression characteristics of hydrogen by use of proton exchange membrane. J. Power Sources **164**(1), 1–8 (2007)
4. P. Bouwman, Electrochemical hydrogen compression (EHC) solutions for hydrogen infrastructure. Fuel Cells Bullet. **2014**(5), 12–16 (2014)
5. R. Ströbel, M. Oszcipok, M. Fasil, B. Rohland, L. Jörissen, J. Garche, The compression of hydrogen in an electrochemical cell based on a PE fuel cell design. J. Power Sources **105**(2), 208–215 (2002)
6. Y. Hao, H. Nakajima, H. Yoshizumi, A. Inada, K. Sasaki, K. Ito, Characterization of an electrochemical hydrogen pump with internal humidifier and dead-end anode channel. Int. J. Hydrog. Energy **41**(32), 13879–13887 (2016)
7. M.-T. Nguyen, S. Grigoriev, A. Kalinnikov, A. Filippov, P. Millet, V. Fateev, Characterisation of a electrochemical hydrogen pump using electrochemical impedance spectroscopy. J. Appl. Electrochem. **41**(9), 1033 (2011)
8. A. Debenjak, P. Boškoski, B. Musizza, J. Petrovčič, Đ. Juričić, Fast measurement of proton exchange membrane fuel cell impedance based on pseudo-random binary sequence perturbation signals and continuous wavelet transform. J. Power Sources **254**, 112–118 (2014)
9. A. Leonide, Y. Apel, E. Ivers-Tiffee, SOFC modeling and parameter identification by means of impedance spectroscopy. ECS Trans. **19**(20), 81–109 (2009)
10. M. Hinaje, S. Raël, P. Noiying, D.A. Nguyen, B. Davat, An equivalent electrical circuit model of proton exchange membrane fuel cells based on mathematical modelling. Energies **5**(8), 2724–2744 (2012)
11. Z. Ilhan, A. Ansar, and N. Wagner, Using equivalent circuit models in understanding theperformance change of metal supported sofcs in static and dynamic conditions, in *In 8th European SOFC Forum*, (2008)
12. M. Shamsipur, S.H. Kazemi, M.F. Mousavi, Impedance studies of a nano-structured conducting polymer and its application to the design of reliable scaffolds for impedimetric biosensors. Biosens. Bioelectron. **24**(1), 104–110 (2008)

13. O. Kanoun, U. Tröltzsch, H.-R. Tränkler, Benefits of evolutionary strategy in modeling of impedance spectra. Electrochim. Acta **51**(8–9), 1453–1461 (2006)
14. A. Lasia, Modeling of experimental data, ch. 14, in *Electrochemical Impedance Spectroscopy and its Applications* (Springer, New York, 2014), pp. 301–321
15. P.D. Beattie, F.P. Orfino, V.I. Basura, K. Zychowska, J. Ding, C. Chuy, J. Schmeisser, S. Holdcroft, Ionic conductivity of proton exchange membranes. J. Electroanal. Chem. **503**(1–2), 45–56 (2001)

4.3 Condition Monitoring of Solid Oxide Electrolyser Stacks Designed for Reversed Operation

Applied Energy 283 (2021) 116372

Contents lists available at ScienceDirect

Applied Energy

journal homepage: www.elsevier.com/locate/apenergy

Performance assessment and evaluation of SOC stacks designed for application in a reversible operated 150 kW rSOC power plant

Benjamin Königshofer [a,*], Pavle Boškoski [b], Gjorgji Nusev [b,c], Markus Koroschetz [d], Martin Hochfellner [d], Marcel Schwaiger [a], Đani Juričić [b], Christoph Hochenauer [a], Vanja Subotić [a]

[a] Institute of Thermal Engineering, Graz University of Technology, Inffeldgasse 25/B, 8010 Graz, Austria
[b] Jožef Stefan Institute, Jamova Cesta 39, 1000 Ljubljana, Slovenia
[c] Jožef Stefan International Postgraduate School, Jamova Cesta 39, 1000 Ljubljana, Slovenia
[d] VERBUND Thermal Power GmbH, Weissenegger Str. 1, 8410 Wildon, Austria

ARTICLE INFO

Keywords:
Solid oxide fuel cell (SOFC)
Solid oxide electrolysis cell (SOEC)
Stack
Electrochemical analysis
Distribution of relaxation times (DRT)

ABSTRACT

The coupling of renewable energy sources with reversible operated high temperature solid oxide cells (rSOC) seems to be a promising option to store and supply clean energy in the future. This work provides the results of experimental investigations on the performance of a rSOC stack as a main unit of a large-scale module installed at a real industrial power plant. In order to determine the requirements as well as to propose strategies for safe and stable operation of the large-scale module the stack was tested under system relevant gas mixtures and operational conditions. Hereby, the focus was on steam electrolysis (EC) and fuel cell (FC) operation utilizing a $H_2/H_2O/CO/CO_2/N_2$ gas mixture, predefined by the reformer installed within the module at the power plant. Furthermore, the alternating operation between EC and FC mode was analyzed. The comprehensive analysis of the performance of the stack includes polarization curves, electrochemical impedance spectroscopy (EIS), distribution of relaxation times (DRT), gas analysis and temperature measurements. Thus, numerous combinations of operational parameters are linked to the individual processes within the stack. During EC operation higher hydrogen partial pressures presented significantly lower diffusion losses especially at low current densities, whereby in FC mode low fuel flows presented increased concentration losses. During alternating operation, prolonged voltage stabilization periods with increasing operation time were observed. Additionally, the processes represented by the peaks calculated from the DRT showed enhanced unstable behavior and presented a significant shift towards higher frequencies compared to constant mode operation.

1. Introduction

In order to reduce the consumption of fossil fuels and the negative impact on the environment, the global energy supply requires the introduction of new and innovative ways of environmentally friendly and high-efficient energy production. Additional challenges resulting from the increase of intermittent alternative energy sources, like solar and wind energy, demand flexible energy storage solutions to utilize the entirety of the available energy [1].

The coupling of renewable energy sources with reversible operated high temperature solid oxide cells (rSOC) are a promising option for highly efficient energy supply and generation of a variety of valuable fuels [2,3]. rSOCs are electrochemical units that can either be operated in fuel cell (FC) mode to generate electricity and heat [4] or in electrolysis (EC) mode to convert surplus electrical energy and H_2O/CO_2 in valuable fuels for further utilization [5,6]. Generally, rSOCs operate at very high temperatures in the range of 600–1000 °C. In FC mode, rSOCs directly convert the chemical energy of a gaseous fuel and an oxidant to electrical energy without intermediate conversion steps. Beside the by-products heat and water, only very low emissions are produced. Additionally, a wide variety of fuels beside pure hydrogen such as methane or various reforming products like diesel or ethanol can be utilized [4,7]. Similarly, when operated in EC mode, rSOCs are capable of producing more complex fuels beside hydrogen such as methane and syngas by utilization of steam, carbon-dioxide and electricity [8–10]. Furthermore, high temperature fuel cells do not rely on precious metals such as platinum as a catalyst since nickel can be used and additionally enable direct reforming of hydrocarbons [4,11]. Despite these incentives of the technology, the key requirements for the integration in industrial scale applications are long-term stability of operation,

* Corresponding author.
E-mail address: benjamin.koenigshofer@tugraz.at (B. Königshofer).

https://doi.org/10.1016/j.apenergy.2020.116372
Received 22 June 2020; Received in revised form 27 November 2020; Accepted 15 December 2020
Available online 1 January 2021

reliability of power supply and hydrogen production and system durability. However, different operating conditions can induce performance deterioration and microstructural degradation in both FC and EC mode reducing the lifetime of the rSOC [12–16]. Recent advances in fuel cell materials and manufacturing processes reduced degradation rates down to 0.5 %/kh [17–19]. In a very recent study [20], two identical fuel electrode supported single cells with an electrochemical active surface of 16 cm^2 were operated for 1000 h. In order to examine the impact of the operating mode on the cell degradation all the operating conditions except the current direction (FC vs. EC mode) were kept constant. Hereby, it was found out that electrolysis operation accelerates performance degradation in comparison to fuel cell operation. The same conclusion was reported in [15,21,22], in which it was shown that cells optimized for operation in FC mode tend to present higher degradation rates between 2 – 5%/kh when operated in EC mode. Furthermore, deriving accurate degradation rates for alternating operation based on available data presents to be challenging, especially when operating with complex fuels and dynamic load changes. Therefore, in order to integrate and successfully operate a large scale rSOC module as a power-to-gas-to-power (and heat) technology within an industrial power plant, intensive characterization and performance determination based on the specific application is inevitable.

In order to ensure long term stability and process safety, intensive experimental investigations must be performed applying the operational conditions required for this specific application on small-scale level. While there are many investigations available focusing on the characterization and performance determination of similar planar electrolyte-supported single cells [23–26], there is far less research conducted on stacks with an active cell area of more than 127 cm^2 [27–29]. Even fewer studies utilized electrochemical impedance spectroscopy (EIS) in combination with method of distribution of relaxation times (DRT) for detailed analysis of the performance of the entire stack and the cells in the stack [30,31]. The information provided by these analysis tools in combination with the detailed monitoring and analysis of operational parameters such as temperature distribution in the stack and gas compositions, provide useful information not only for characterization but also for early stage degradation detection. Since the lifetime can be prolonged when degradation processes are detected at their preliminary stage and according countermeasures can be taken, a special focus of this work will also be on analysis of the data obtained by EIS.

Currently several research centers are working on different projects focusing on the SOFC/SOEC technology. For instance, the EU project “BALANCE” which is based on the rSOC technology but mainly focuses on the development of new-generation SOCs in terms of performance improvement and lifetime increase. Hereby on of the main targets is the achievement of efficiencies of 50% in FC mode and 90% in EC mode at a multi-kW scale, whereby a 2500 h test should demonstrate the stability of operation during longer periods [32]. Another EU project which is based on the rSOC technology is the project “REFLEX” which focuses on the development of innovative solutions for the storage of renewable energies. The main challenge is to define an optimum between high efficiency, high flexibility of operation and overall costs by improvement of rSOC components like cells, stack, power electronics or heat exchangers. Furthermore, advanced operation strategies should be defined within this project [33]. The EU project “GrInHy” focuses on the operation in electrolysis mode for H_2 production for the steel industry [34]. Another EU project “RelHy” focused on the optimization of SOECs [35]. Worldwide there are already some fuel cell power plants installed, e.g. the 59 MW Gyeonggi Green Energy in South Korea based on the molten carbonate technology [36] or the 300 kW Bloom Energy based on SOFC technology [37]. Large-scale electrolysis systems are mostly based on low temperature electrolysis cells such as the 3 MW Hydrogenics Unveils in Canada [38] or the 6 MW proton-exchange membrane electrolyzer as a part of the “H2Future” project [39]. Nevertheless, in most projects the SOFC and SOEC are split into separate modules or the reversible operation was only tested for short periods. The investigations presented in this work are related to the rSOC module (Fig. 1) installed in the combined cycle gas turbine power plant (CCGT) in Mellach/Austria within the national project Hotflex. This module presents a rated power output of 20 kW in FC mode when operated with reformate and a hydrogen production capacity of 40 m^3/h at 150 kW power supply and is set into operation in 2020. Hereby, the main purpose of the rSOC module is the production of green hydrogen from surplus produced energy as well as operation as back-up power generator.

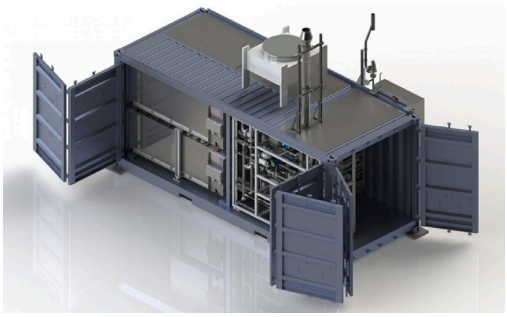

Fig. 1. rSOC module [40].

1.1. Scope of this study

This work focuses on experimental investigations on the performance of a single stack unit as the ones installed in the module at the power plant. In the further course of this project, a set of promising operation conditions based on the results obtained within this study is planned to be applied to the large-scale module at the industrial site. We want to highlight that the specific application of a rSOC module in combination with a CCGT power plant is completely unique, whereby the operational parameters for the experiments are defined in accordance with the requirements of this specific application with a special focus on high efficiency and long term stability. Hereby the stack, respectively the repeating units, are tested using several gas mixtures and operational conditions on laboratory scale in order to determine the requirements and challenges as well as to propose strategies for safe and stable operation of the large-scale rSOC module implemented in the industrial power plant. While within this project the focus in EC mode is set on steam electrolysis, in FC mode the specific reformate mixture used is predefined by the reformer installed within the module at the power plant. Furthermore, the alternating operation between EC and FC mode is analyzed. The experiments performed within this study enable fast determination of the advantages and disadvantages of specific operation conditions without influencing the lifetime of the large-scale module as well as the selection of the best appropriate operational conditions. Additionally, the electrochemical impedance measurements performed in combination with the usage of advanced analysis tools enable a deeper understanding of processes occurring during operation within a single unit of the large-scale module. This detailed analysis rests upon the high quality of the data obtained from the detailed investigations on both stack and cell level. Furthermore, the presented results build a solid foundation for optimization of the operation as well as provide a reference for the results obtained during online monitoring at the large-scale module.

2. Experimental setup

2.1. Cell and stack design

The experiments within this study were performed on a ten layer electrolyte-supported (ESC) stack composed of a Ni-GDC fuel electrode,

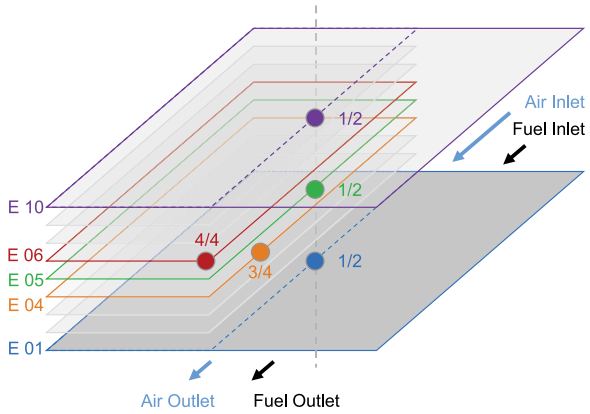

Fig. 2. Position of thermocouples (colored circles) for temperature measurement within stack [41]. The labels E 01 to E 10 refer to the cells within the stack. The ratios present the relative distance of the thermocouples from the gas inlet.

a 5YbSZ electrolyte support and a LSCF ((La,Sr)(Cr,Fe)O3) air electrode with an electrochemical active area of 127.8 cm^2 per cell. The material used for the interconnects is Crofer 22 APU. The stack is installed in a stackbox and operates in co-flow configuration whereby gas is distributed via gas flow channels and the air flow is guided through the open oxygen electrode. In order to measure the cell voltages and impedances of the repeating units within the stack, which in this case consist out of two cells each, every second interconnector is tapped via sense leads. The measurement and monitoring of the stack temperatures was realized via thermocouples integrated at the in- and outlet of the gas/air flow of stack as well as via five additional thermocouples which were mounted within the stack at different layers as presented in Fig. 2.

2.2. Test rig

The scheme of the test rig used for stack testing is presented in Fig. 3. The mixture of the different inlet gases is realized by the gas control system regulating the corresponding mass flow controllers whereby a separate steam generator was used to produce steam. The mixture of inlet gases is then pre-heated up to approx. 650 °C before entering the stack-box. After exiting the stack unit, the outlet gas passes through water-cooled condenser to the exhaust. Additionally, the testing rig was equipped with a control system unit, an electronic load, a power source, an impedance analyzer and gas analyzers ensuring detailed in-operando analysis.

2.3. Operating parameters

Within this study different operating conditions were applied to the stack in both electrolysis and fuel cell mode for a total operation time of more than 1800 h. The gas inlet mixtures were defined corresponding to requirements of a real industrial scale application and are given in Table 1. During electrolysis mode the H_2O/H_2-ratio of the inlet gas composition was varied between 4, 9 and 19. Hereby the investigations focus on the influence of low hydrogen partial pressures on the cell voltage stability and overall stack performance. Nevertheless, low hydrogen contents in the inlet gas are of desirable to achieve higher efficiencies, especially for large-scale industrial applications. Differently, in fuel cell mode the fuel composition predefined by the product of the external reformer installed at the industrial power plant. Therefore, the fuel composition stayed unchanged during the experiments, while the fuel flow is varied in order investigate the performance of the stack with focus on different combinations of fuel utilization and power output which can vary due to different scenarios demanding different operational strategies in large-scale industrial applications.

Table 1
Gas inlet mixtures.

Mixture label	Operating mode	Fuel flow	H_2	H_2O	CO	CO_2	N_2	Air flow
		SLPM	%	%	%	%	%	SLPM
E1	EC	10.88	20	80	0	0	0	10
E2	EC	9.67	10	90	0	0	0	10
E3	EC	9.16	5	95	0	0	0	10
F1	FC	7.00	48	10	12	11	19	31
F2	FC	9.00	48	10	12	11	19	40
F3	FC	11.00	48	10	12	11	19	49

The stack was operated within the operational limits of 1.3 and 3.0 V combined for two cells, below the maximum temperature of 860 °C and with a fuel utilization and steam conversion smaller than 80%. Operating the stack in EC mode the operating temperature was set to 830 °C at the air outlet which also corresponds to the performance optimum of the stack. In FC mode the operating temperature was adjusted to 800 °C in order to achieve higher power outputs and fuel utilizations within the operational limits at the specific inlet gas compositions. The temperature of the cells during the impedance measurements is given at the assigned thermocouple in Table 2. The polarization curves were recorded with different ramping techniques in accordance with the measurement protocols proposed in [42]. Beside the dynamical recording of polarization curves, a slower stepwise ramping technique is applied which ensures that a quasi-stead-state equilibrium is reached at each defined load point. The electrochemical impedance measurements were performed in galvanostatic mode, whereby an AC current with an amplitude of 4% of DC level was superimposed to the operating DC current to ensure operating within the quasi-linear are of the polarization curve. The results from the impedance measurements present the combined impedance of two cell since every second interconnector is tapped via sense leads.

3. Data validation

Large planar cells assembled in the form of the stack unit may evoke an unbalanced temperature distribution alongside the single cells as well as throughout the whole stack box [43,44]. Additionally, the gas distribution can be in-homogeneous as a result of fluctuating gas flow velocities caused by varying partial pressures [45]. These slightly fluctuating operational conditions can negatively affect the results of the EIS measurements by displaying noise or outliners. Therefore, in order to check the validity of the data the Z-Hit method to perform the Kramers–Kronig (KK) test on the measured data is deployed which is described in detail elsewhere [46–48]. In Fig. 4(a)/4(b) the real part of the measured EIS curve (orange -) and the curve calculated by the KK relations (blue -) is presented. The two curves are mostly congruent except for one part between 10–20 Hz for which an outliner with a discrepancy greater than 15% is identified and removed from the data before any further analysis. While most of the data used in this paper presented discrepancy $< 5\%$, the analysis was performed only with the data points that provided a relative error below 10% as seen in Fig. 4(c)/4(d).

The data obtained by EIS measurements is generally analyzed in the form of Nyquist diagrams. In this study an electrical circuit model developed for an ESC single cell was used for fitting the Nyquist curves, which is described in detail elsewhere [49,50]. Nevertheless, sometimes this representation of the data is not suitable to precisely divide individual electrochemical processes. A different representation of data can be calculated by the analysis via distribution of relaxation times (DRT) [51,52]. Hereby, the different processes are separated by their specific time constants which enables to extract most dominant

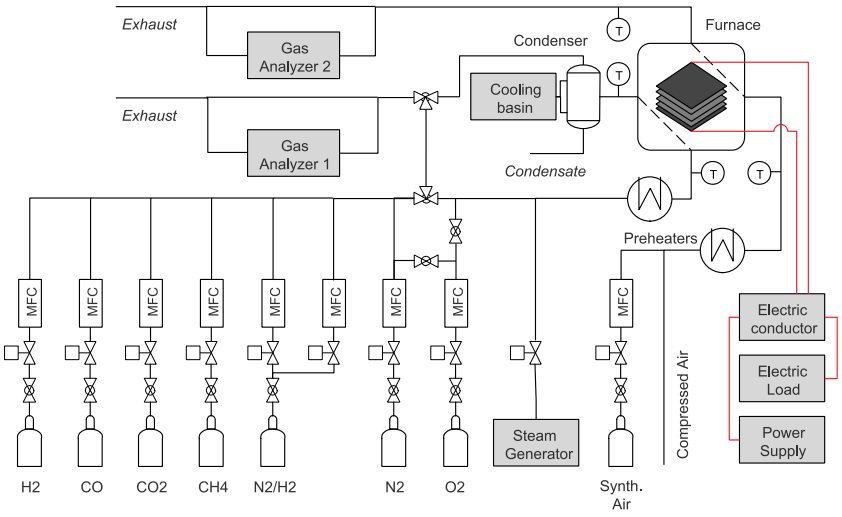

Fig. 3. Scheme of the test rig.

Table 2
Operating parameters.

Figure	Mixture label	Temperature	Thermocouple	i	FU/SC	Cells
		°C		mA/cm²	%	
Fig. 5	E1, E2, E3	830	Air outlet	0 - 780	0 - 80	stack
Fig. 6	E1	830	Air outlet	0 - 780	0 - 80	stack
Fig. 7(a), Fig. 7(b)	E1, E2, E3	830	E06-4/4	100	10	E07/08
Fig. 7(c), Fig. 7(d)	E1, E2, E3	830	E06-4/4	400	40	E07/08
Fig. 8(a), Fig. 8(b)	E2	830	Air outlet	560	57	stack
Fig. 8(c), Fig. 8(d)	E2	850	E06-4/4	560	57	E07/08
Fig. 9	F1, F2, F3	800	Air outlet	0 - 345	0 - 65	stack
Fig. 10	F2	800	Air outlet	0 - 345	0 - 58	stack
Fig. 11(a), Fig. 11(b)	F1, F2, F3	820	E04-3/4	200	30–47	E03/04
Fig. 11(c), Fig. 11(d)	F3	810–830	E06-4/4	200	30	E07/08
Fig. 11(e), Fig. 11(f)	F3	815	E05-1/2	100–300	0–48	E05/06
Fig. 12	F2	800	Air outlet	300	57	stack
Fig. 12, Fig. 16(b)	F2	845	E05-1/2	300	57	E05/06
Fig. 13, Fig. 14	E2 / F2	830 / 800	Air outlet	560 / 300	57 / 58	stack
Fig. 15, Fig. 16(a)	F2	845	E05-1/2	300	58	E05/06

frequencies of processes involved [53]. Nevertheless, the main challenge when applying such analysis tools is the proper selection of the model representing the information contained in the EIS data, whereby mostly regularization methods are used for fitting DRT curves [54,55]. The method for calculation of the distribution of relaxation times (DRT) used in this work was developed by Ciucci and Chen [54].

4. Results and discussion

The results obtained during the experiments performed on the stack unit are presented and discussed in this section. The information that can be extracted from the recorded polarization curves can be used to fulfill the requirements of fast and safe load and operational mode changes which are key properties of reversible operation. The results of the short term experiments conducted within this study enable the proposition of operational parameters suitable for the safe operation of the large-scale rSOC module. Furthermore, the results provide essential information for performance prediction as well as build a solid foundation for optimization of operation. Still, long-term experiments need to be conducted in order to determine the influence of specific operational conditions on the long-term stability or the degradation behavior of the rSOC.

4.1. Influence of operating conditions in EC mode

The stack voltages and temperatures at the stack center as function of current density were measured at different H_2O/H_2-ratios and ramping rates as presented in Fig. 5. The amount of hydrogen at the gas inlet was varied between 20 vol% (blue -), 10 vol% (orange -) and 5 vol% (green -). Hereby, the total fuel flow varied between 10.9, 9.7 and 9.2 SLPM with a constant steam flow of 8.7 SLPM. The polarization curves were recorded with two different ramping techniques within the defined voltage limits. Firstly, dynamically with 15 A/min up to 100 A and then secondly in a quasi-steady-state in 5 A steps up to 100 A with an intermediate ramping rates of 1 A/min and 15 min ramping break after each step. At a constant air outlet temperature of 830 °C the open circuit voltage (OCV) was distinctly lower at higher steam contents in accordance with the calculated Nernst voltages. Hereby, the calculated Nernst voltages at 830 °C and steam contents of 80, 90 and 95% were 8.68, 8.30 and 7.96 V, while the measured OCVs were 8.59, 8.20 and 7.78 V. The difference can be mainly attributed to the non-uniform temperature distribution within the stack. At higher current densities the voltage is mostly congruent among all gas inlet compositions due to equalized overall resistance linked to the high hydrogen partial pressures. Nevertheless, the power input (dotted lines) required at the lower H_2O/H_2-ratio of 4 was slightly higher over the

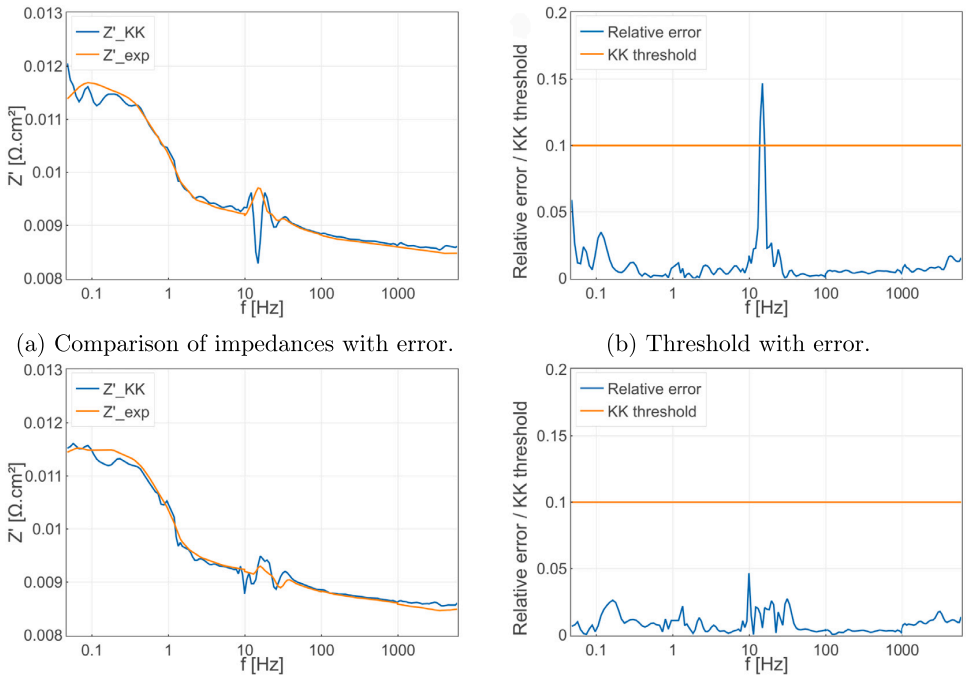

(a) Comparison of impedances with error.

(b) Threshold with error.

(c) Comparison of impedances.

(d) Threshold.

Fig. 4. Kramers–Kronig test.

whole current range. The steam conversion was also similar for all gas compositions while the electrolysis efficiency increases with higher steam content. During dynamical recording of the polarization curve the voltage almost increased linearly with increasing current. Hereby, the stack center temperature slowly decreases by 10–15 °C between 0–420 mA/cm^2 and then start rising to over 840 °C at the maximum current density. Differently, at slower ramping rates, the stack temperatures adapt to the changing conditions and a quasi-steady-state equilibrium within the stack is reached at each load step. Hereby, the stack temperatures decreases by 20–25 °C between 0–270 mA/cm^2, while nearly reaching the operational limit of 860 °C at the maximum current density. Although the water reduction reaction is considered as endothermic, the stack center temperature increases at higher current densities as a result of heat production caused by internal resistances of the cells. At lower current densities the influence of thermodynamics on the performance of the stack is greater than the influence of the electrochemical reaction's kinetics, whereby at higher current densities the effect of ionic and electronic conduction, activation and diffusion resistances on the performance increases [29]. Nevertheless, for these operational conditions the heat production in the stack at higher current densities presents the major limitation for the hydrogen production rate while the cell voltages remained unchanged within the bounds.

Fig. 6 presents the hydrogen flow at gas in- and outlet of the stack. The corresponding calculated steam conversion at maximum current density is between 81%–83% which matches well with the theoretical value of 80%, taking inaccuracies of the mass flow controllers, hydrogen loss due to leakages as well as inconsistencies in the steam generation into consideration. Additional results obtained during constant operation measuring the oxygen increase in the air flow also present steam conversion rates with deviations of < 2% compared to the theoretical values.

In Fig. 7 the results of the impedance measurements are plotted for different H_2O/H_2-ratios and current densities. The first low-frequency peak between 1 – 10 Hz shifts towards higher frequencies at both low and high current densities. This can be interpreted as a decrease of diffusion losses with increasing hydrogen content at the gas inlet according to [31,56,57]. Additionally, the amplitude of the first low-frequency peak at the H_2O/H_2-ratio of 80/20 remains mostly unchanged at both presented current densities, whereby at higher H_2O/H_2-ratios the amplitude decreases significantly with increasing current density, thus referring to the decreasing process resistance. In the Nyquist diagram the decrease of the low-frequency arc with increasing hydrogen is also clearly visible. At low current densities the ohmic resistance increases from 9.00 to 9.14 and 9.39 mΩ with decreasing hydrogen content in the inlet gas observable as presented in Nyquist diagram. This could be interpreted as the influence of the high steam amount available as a reactant, which can negatively influence the surface process resistance. It was shown that, minor amounts of steam can be adsorbed in entry areas of the cell according to [58], which was interpreted to be a possible cause for this phenomenon. Next, in [57], the authors reported that operating temperatures > 800 °C and steam molar fractions above 80% can lead do an increase of cell voltage (and therefore also the resistance) when operated at 100 mA/cm^2 as a result of a combined effect of high steam molar fraction and high temperatures. Hereby, the effect of higher temperature is considered to be more dominant than the effects of high steam concentration [59,60]. Differently, at higher current densities this effect is no longer present as a result of higher hydrogen production rates. A second peak overserved at high-frequencies between 10–300 Hz, which could be linked to air electrode processes like chemical surface exchange of O_2 and O_2^{2-}-bulk diffusion in air electrode [31,56,57]. This peak is already comparably low at 100 mA/cm^2 and seems to split up into two peaks at higher current densities. Additionally, a slight shift towards lower frequencies is observable. Generally, further peaks at frequencies between 0.2–10 kHz can be linked to fuel electrode process like the charge transfer reaction and ionic transport in the fuel electrode functional layer [31,56,57]. In the Nyquist diagram the high-frequency arc seems to be split into two separate arcs at higher current densities.

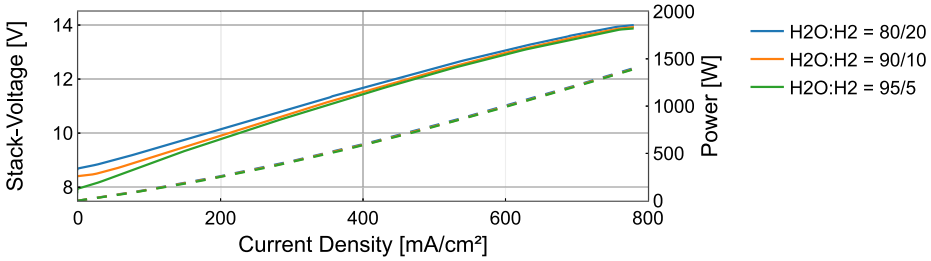

(a) Dynamically recorded stack voltages.

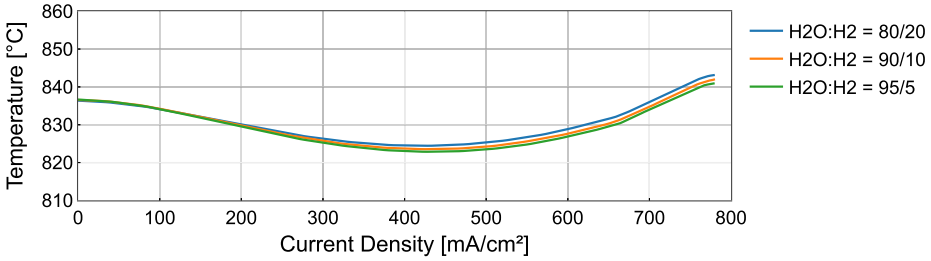

(b) Dynamically recorded stack center temperatures.

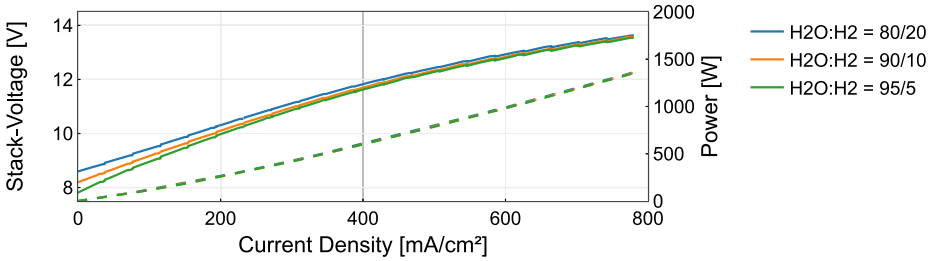

(c) Quasi-steady-state recorded stack voltages.

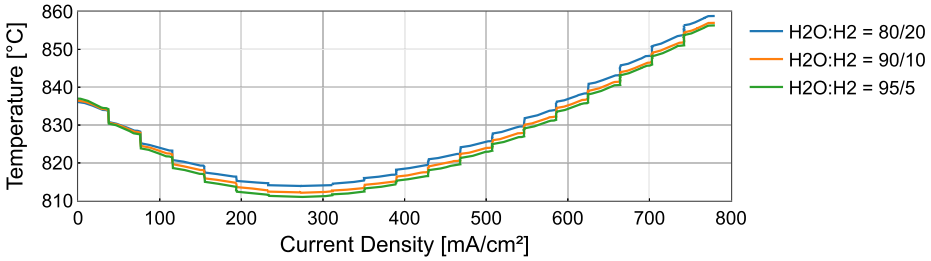

(d) Quasi-steady-state recorded stack center temperatures.

Fig. 5. Comparison of polarization curves and temperatures recorded with different ramping techniques and H_2O/H_2-ratio-ratios.

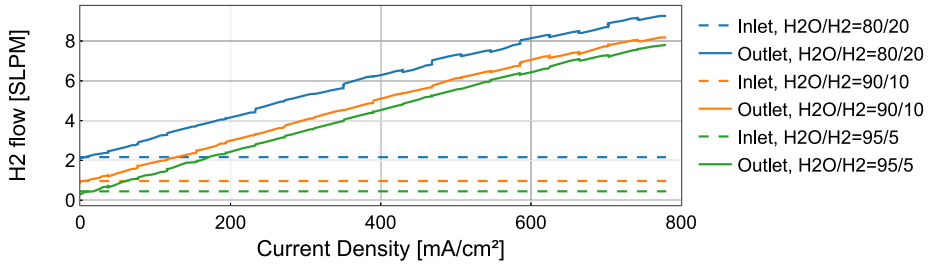

Fig. 6. Gas analysis in EC mode at inlet and outlet.

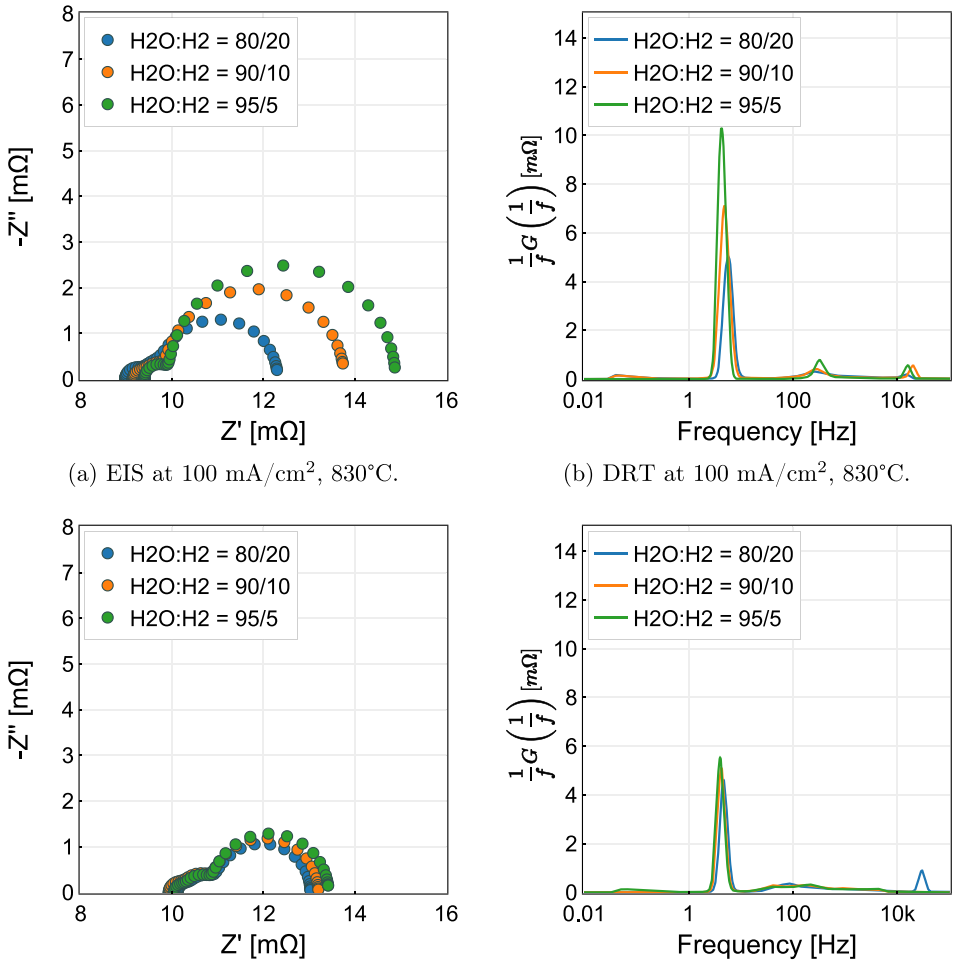

(a) EIS at 100 mA/cm^2, 830°C.

(b) DRT at 100 mA/cm^2, 830°C.

(c) EIS at 400 mA/cm^2, 830°C.

(d) DRT at 400 mA/cm^2, 830°C.

Fig. 7. Comparison of EIS and DRT in EC mode at different operating conditions.

This can be dedicated to the processes in the overlapping frequency ranges of 10–300 Hz and 0.2–10 kHz as stated above. It can be assumed that operation at higher current densities mainly influenced charge transfer reactions and the resulting changes in O_2 partial pressure also according to [61]. Furthermore, the ohmic resistance increases by approximately 0.1 Ω/cm^2 while increasing current density from 100 to 400 mA/cm2 which can only be seen in the Nyquist plot. The similarity of the impedances in Fig. 7(c)/7(d) indicates that at high steam contents slight changes of the hydrogen partial pressure the inlet gas have only very little influence at higher current densities. It can be assumed that due to the higher hydrogen partial pressures resulting from the higher production rates at high current densities significantly decreases the diffusion losses.

To conclude, for operation at lower current densities higher hydrogen contents in the inlet gas seem to be preferable due to lower diffusion losses. At higher current densities the hydrogen in the inlet gas could be further reduced in order to operate more efficiently. Nevertheless, in [62] the authors showed that high H_2O partial pressures in the fuel gas inlet can result in accelerated nickel evaporation of $Ni(OH)_2$ and therefore negatively influence the long term stability. Therefore, additional long term measurements must be conducted in order to determine the influence of the different operating conditions to specify the economical most feasible trade-off between lifetime respectively efficiency and operating costs.

4.1.1. Stability test EC mode

The results of the short-term stationary electrolysis stability test at a H_2O/H_2-ratio of 90/10 and 560 mA/cm^2 are presented in Fig. 8. The air outlet temperature was set to 830 °C in order to keep the maximum stack temperature below the operational limit of 860 °C. During the 40 h of constant operation the stack voltage as well as the temperature remained mostly unchanged. The results from the impedance measurements, which were conducted every three hours, showed slight oscillations especially of the high-frequency peaks whereby no actual trend of changes was observable. It is assumed that such slight oscillations occur due to inconsistencies in steam generation. They were more pronounced during the stability test in EC mode compared to FC mode, since amount of steam is significantly higher during the electrolysis operation (Fig. 12(a)). The highest temperature of 850 °C is measured at both the top cell (T-E10-1/2) and at the stack outlet (T-E06-4/4). The lowest temperature of 835 °C is measured at the bottom of the stack (T-E01-1/2). The temperature in the middle of the stack (T-E02-1/2) is 845 °C. Operation in EC mode presents a very narrow temperature distribution window within the stack ranging from 835–850 °C. The two-cell-voltages measured from the bottom to the top cells of the stack were 2.55, 2.52, 2.52, 2.48 and 2.49 V. Hereby, the relation between temperature and voltage can be observed whereby the minimal voltage is measured at the cells E07/08. The ohmic part of the impedance

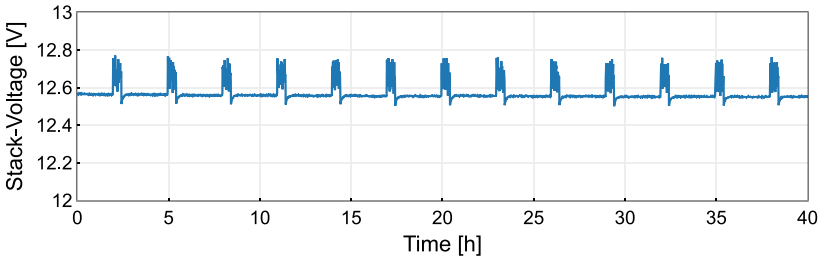

(a) Voltage during constant operation.

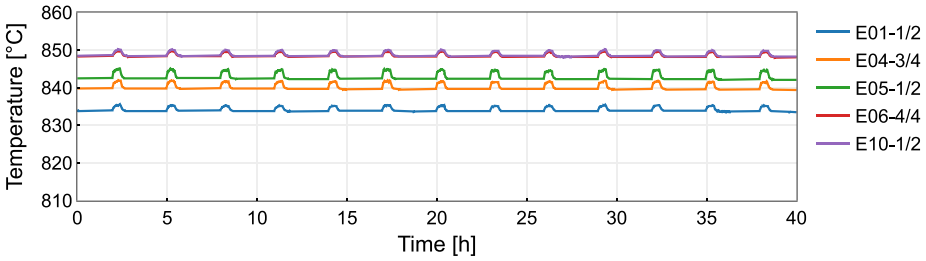

(b) Temperatures during constant operation.

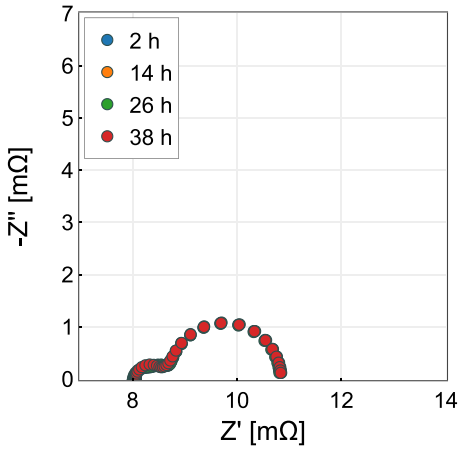

(c) EIS during constant operation.

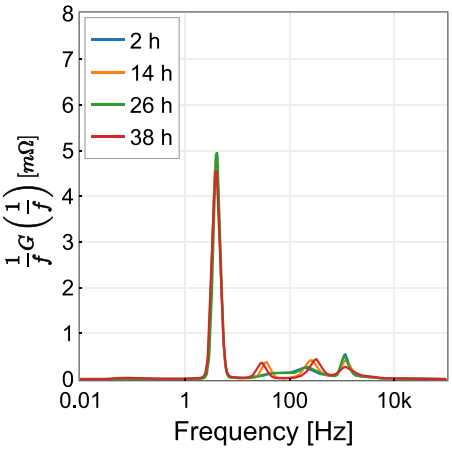

(d) DRT during constant operation.

Fig. 8. Constant operation in EC Mode at H_2O/H_2=90/10.

was 8.05 mΩ and therefore approximately 2 mΩ smaller than the one measured in the characterization measurements at 400 mA/cm^2. It can be assumed that this change is mostly related to the higher current density and higher operating temperature at the measured cells during the stability test.

4.2. Influence of operating conditions in FC mode

In FC mode the voltages and temperatures were recorded as function of current density at different inlet volume flows as presented in Fig. 9. While the inlet gas composition remained unchanged, the total fuel flow was varied between 7 SLPM (blue -), 9 SLPM (orange -) and 11 SLPM (green -). The air flow was adapted in order to maintain a constant air–fuel equivalence ratio of 5. Similar to EC mode the polarization curves were recorded with two different ramping techniques. As previously mentioned, firstly dynamically with 10 A/min up to 328 mA/cm^2 at 7 SLPM, 326 mA/cm^2 at 9 SLPM and 298 mA/cm^2 at 11 SLPM. The current ramp was stopped at the specific current density when the minimum voltage of 1.3 V for two cells combined was reached. Secondly the polarization curves were recorded quasi-steady-state in 5 A steps up to 313 mA/cm^2 at 7 SLPM and 345 mA/cm^2 at 9 and 11 SLPM mA/cm^2 with an intermediate ramping rate of 1 A/min and 15 min ramping break after each step. For a fuel flow of 9 and 11 SLPM the limiting operational factor was the minimum voltage. At 7 SLPM the current ramp was stopped when the maximum temperature of 860 °C was reached whereby the single voltages were still above the limit. At a constant air outlet temperature of 800 °C the medium temperature level in the stack is significantly higher at low fuel flows. The OCV is lower for low fuel flows whereby this trend reversed at maximum load. Although the intermediate power output (dotted lines) obtained at 7 SLPM (Fig. 9(a)) was slightly higher than at 9 and 11 SLPM, the maximum power output during quasi-steady-state conditions (Fig. 9(c)) was distinctly lower at 7 SLPM due to the temperature limitation. The fuel utilization decreases with increasing fuel flows when operating within the operational limits with this gas composition. During the dynamic ramping the voltage almost decreased

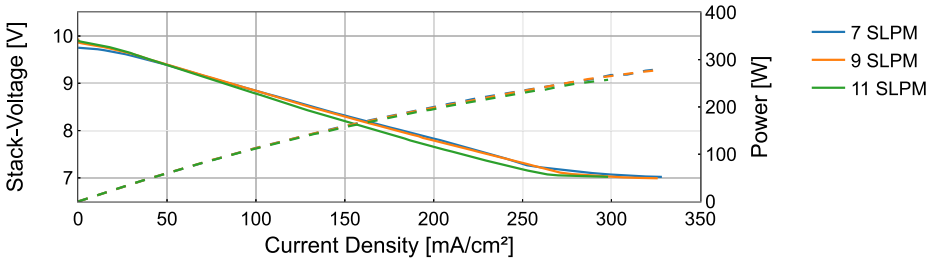

(a) Voltages at 10 A/min.

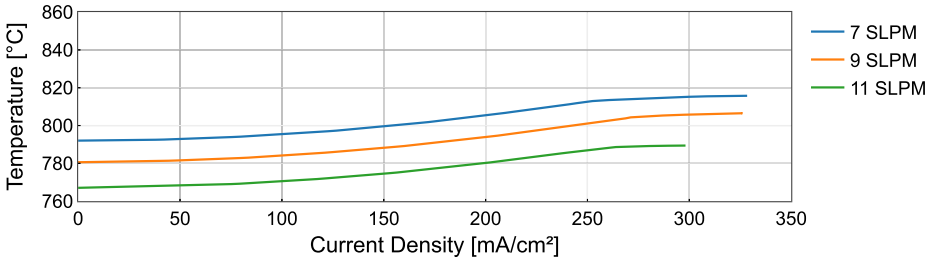

(b) Temperatures at 10 A/min.

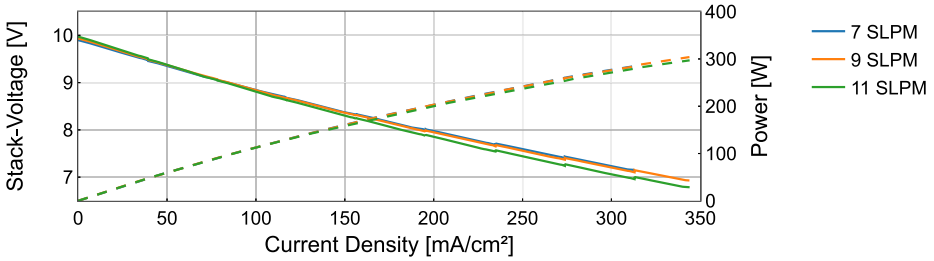

(c) Voltages at 1 A/min with 5 A/Steps and 10 min break after each step.

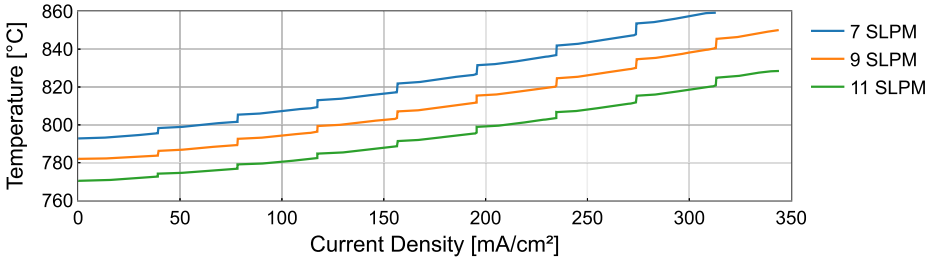

(d) Temperatures at 1 A/min with 5 A/Step and 10 min break after each step.

Fig. 9. Comparison of IV curves and temperatures recorded at different current ramps.

linearly with increasing current density and higher power outputs could be achieved at lower fuel flows. The stack center temperature slowly increased by approximately 20–25 °C at maximum load compared to given temperature at OCV. Differently, at slower ramping rates, higher power outputs were achieved at higher fuel flows, while the stack temperature increased by 65–70 °C compared to the temperature at OCV. Generally, with increasing fuel and particularly air flows the cooling of the stack was enforced which led to lower stack temperatures which further allowed higher power outputs but lower fuel utilization rates.

Fig. 10 presents the inlet and outlet concentrations of hydrogen, carbon oxide and carbon dioxide at a fuel inlet fuel flow of 9 SLPM. The blue marker (•) indicates the inlet concentration and the blue line (-) the measured outlet concentration at the specific current densities. Furthermore, the orange markers (□) present the thermodynamical equilibrium calculated by using the Gibbs energy minimization method at the specific measured stack center temperature which is indicated by the green markers (▾).

While operating at OCV 0.47 SLPM, respectively 11 vol% of H_2 inlet flow, converted into CO which can directly be linked to the reverse water gas shift reaction (RWGS). Generally, the endothermic RWGS reaction, hence the equilibrium for CO production, is favored by high temperatures above 700 °C and increasing H_2/CO_2-ratio [63–65]. This is in line with the operational conditions applied in this experiment with temperatures between 760–860 °C and an H_2/CO_2-ratio of 4.4. The exothermic oxidation of hydrogen accelerates with increasing current, while simultaneously influencing the production of CO due to increasing temperatures but decreasing H_2/CO_2-ratios. At

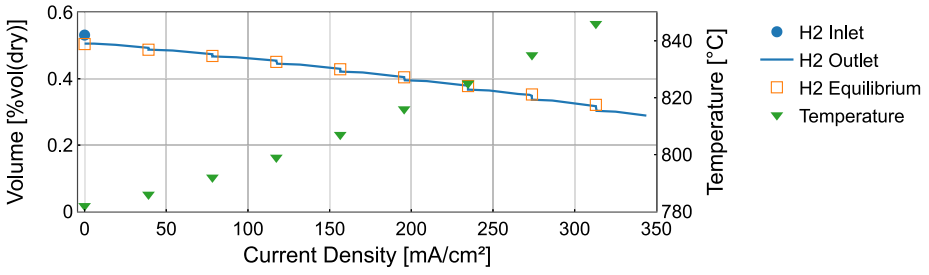

(a) H_2 balance.

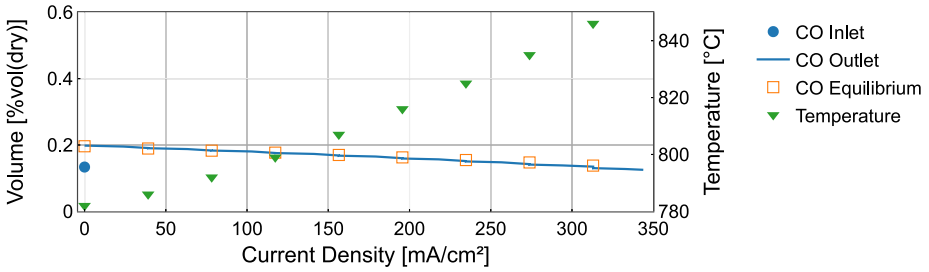

(b) CO balance.

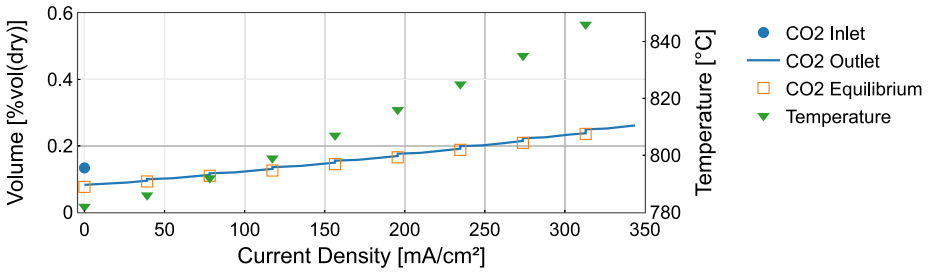

(c) CO_2 balance.

Fig. 10. Species balances in FC mode at 9 Nl/min.

approximately 160 mA/cm^2 and 810 °C, 35% of the H_2 inlet flow are utilized, whereby the equilibrium between the exothermic electrochemical utilization and endothermic chemical production of CO is reached. At the maximum current density and approximately 850 °C, 58% of the H_2 inlet flow and 28% of the CO inlet flow is utilized with the H_2/CO_2-ratio already being below 1. The higher utilization of hydrogen results also from the H_2-oxidation being thermodynamically favored compared to CO-oxidation [13,58]. The measured concentrations of methane were below 1% and were not plotted in the graphs because they play nearly no role at this high temperatures [66].

In Fig. 11(a)/11(b) the results of the impedance measurements are plotted for different fuel flows at 200 mA/cm^2 and 820 °C. The temperature of 820 °C was measured at the thermocouple given in Table 2. The first low-frequency peak between 1 – 10 Hz shifts towards higher frequencies indicating decreasing diffusion losses with increasing fuel flow [56,57]. Additionally, the amplitude of the first low-frequency peak decreases with increasing fuel flow. The higher amplitude and shift towards lower frequencies at the lower fuel flow of 7 SLPM could be related to rising concentration losses. It can be assumed that the concentration losses result from increasing amount of product species at higher fuel utilizations as well as insufficient exchange between reactants and products.[14,67]

The second high-frequency peak at between 10–100 Hz remains mostly unchanged. The low peaks at frequencies between 0.2–10 kHz present low amplitudes and appear to be unstable. While the changes at lower frequencies are also easily visible in the Nyquist diagram presented by decrease of the low-frequency arc, trends at higher frequencies are not easily distinguishable. It can be assumed, that there is no real influence of the fuel flow on the processes in this frequency range, whereby small inconsistencies of the peaks could be a results of unbalanced temperature distribution, in-homogeneous gas distribution or effect from single cells. While effecting the overall losses, the varying volume flow seems to have no influence on the ohmic resistance [68], which can also be observed in the Nyquist diagram.

In Figs. 11(c)/11(d) the results of the impedance measurements are plotted for 11 SLPM and 200 mA/cm^2 at different temperatures. With increasing temperature, the Nyquist diagram clearly presents a decrease of the ohmic resistance from 11.90, 11.25 to 10.74 mΩ. The DRT diagram presents a small shift of the peaks at frequencies between 0.1–10 kHz towards lower frequencies at higher temperatures. The two peaks shift from 0.33 and 3.3 kHz at 810 °C towards 0.25 and 1.3 kHz at 820 and 830 °C. Therefore, effect of changing the temperature between 810–830 °C is mainly indicated by small changes in the ohmic resistance which is also the main influence on the overall losses.

In Fig. 11(e)/11(f) the results of the impedance measurements are plotted for 11 SLPM and 815 °C at different current densities.

The frequency of the first low-frequency peak between 1 – 10 Hz remains unchanged, while the amplitude slightly decreases with increasing current density indicating decreasing process resistance of gas diffusion and conversion impedance [31]. When operating SOFCs with

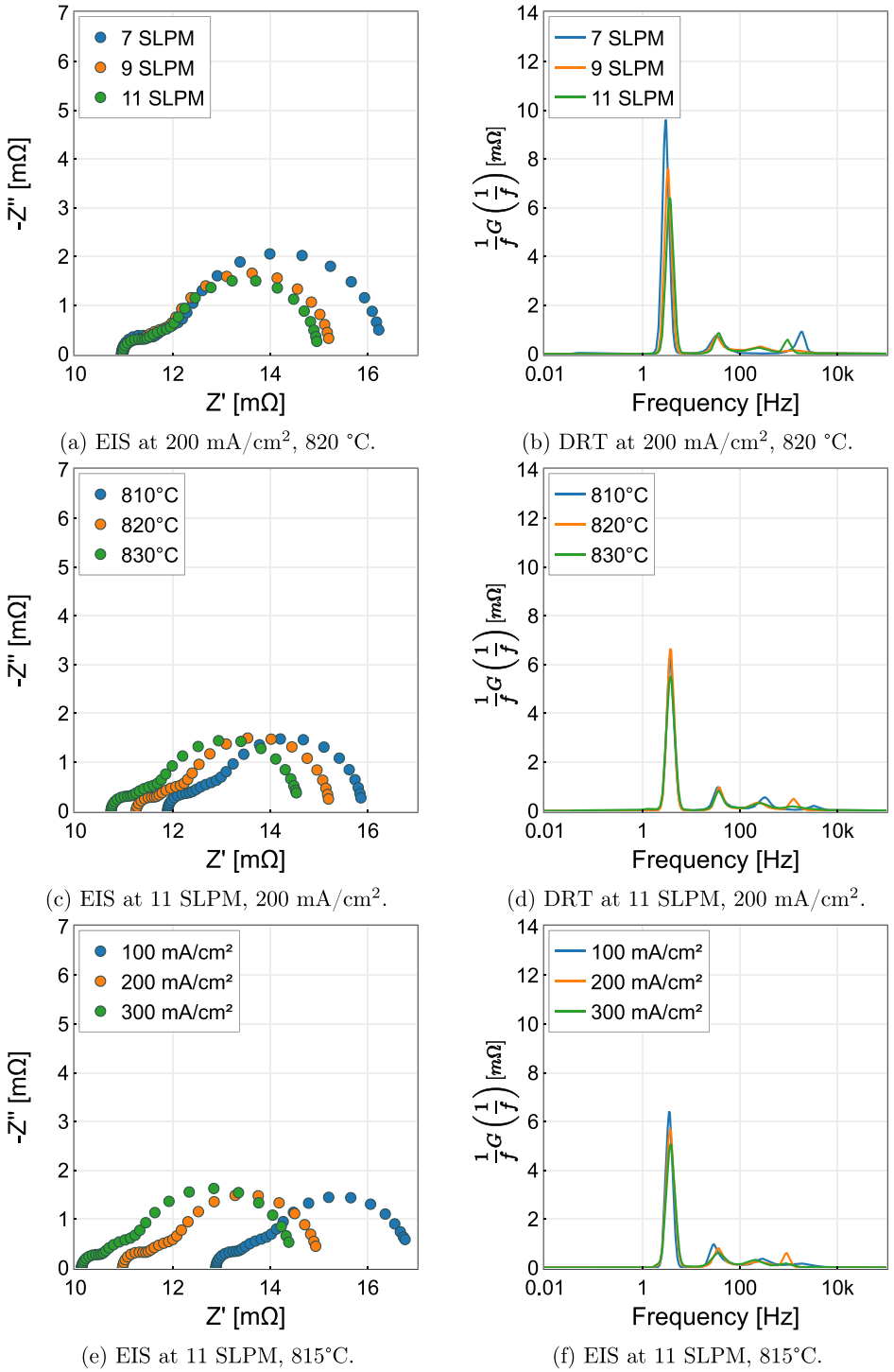

(a) EIS at 200 mA/cm^2, 820 °C.

(b) DRT at 200 mA/cm^2, 820 °C.

(c) EIS at 11 SLPM, 200 mA/cm^2.

(d) DRT at 11 SLPM, 200 mA/cm^2.

(e) EIS at 11 SLPM, 815°C.

(f) EIS at 11 SLPM, 815°C.

Fig. 11. Comparison of EIS and DRT in FC mode at different operating conditions.

such complex gas mixtures the gas transport within in the fuel electrode includes transport pathways for all fuel components $H_2/H_2O/CO/CO_2$ coupled via chemical reactions that take place such as the water-gas-shift reaction etc. As reported in [69,70], water-gas-shift reaction has most pronounced influence on the low-frequency processes and can lead to the formation of an additional low-frequency arc. This was not noticed during this experiment. Nevertheless, it was shown that these overlapping processes are quite complex and can have a largely different influence on the performance and can depend on different factors such as cell type or gas compositions [28,69,71] During operation with

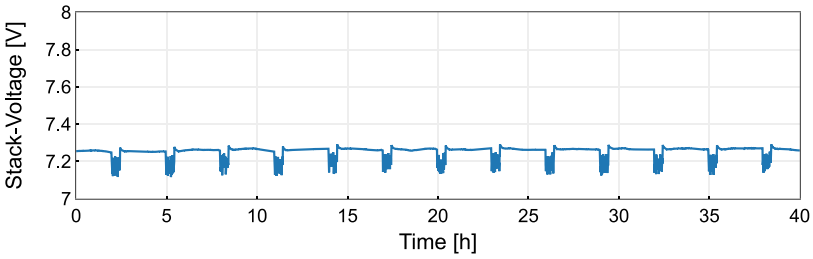

(a) Voltage during constant operation.

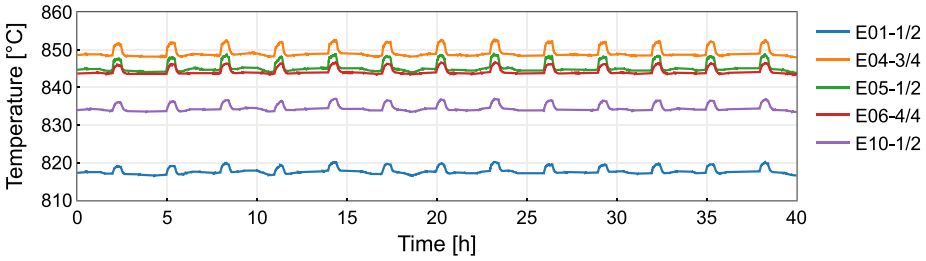

(b) Temperatures during constant operation.

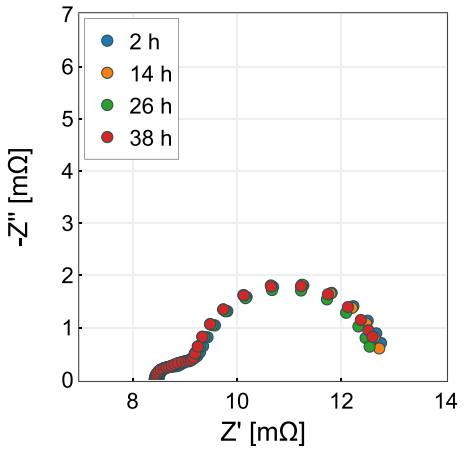

(c) EIS during constant operation.

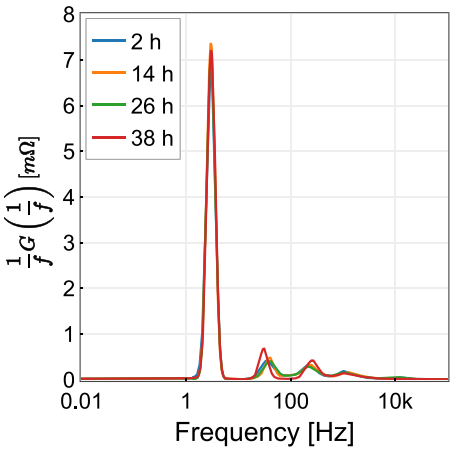

(d) DRT during constant operation.

Fig. 12. Constant operation in FC Mode at 9 Nl/min.

a comparable high H_2/CO-ratio in the inlet gas mixture a decrease of the low-frequency process resistances was observed by [72].

The amplitude of the second high-frequency peak at between 10–100 Hz also decreases with increasing current density. The peaks at frequencies between 0.1–10 kHz shift towards lower frequencies with increasing current density. The Nyquist diagram presents the influence of a decrease of the ohmic resistance with increasing current density, whereby change at between 100–200 mA/cm^2 is much more intense than the change between 200–300 mA/cm^2- It seems that this could be related to the equilibrium between the electrochemical utilization and chemical production of CO being reached between 100–200 mA/cm^2, with the chemical reactions having a stronger impact on the surface process resistance in this operational area. Therefore, operation at higher current densities generally presents decreasing overall losses, while the impact of the chemical reactions needs to be further investigated.

4.2.1. Stability test FC mode

The results of the short-term stationary fuel cell stability test at a fuel flow of 9 SLPM and 300 mA/cm^2 are shown in Fig. 12. The air outlet temperature was set to 800 °C in order to keep the maximum stack temperature below the operational limit of 860 °C. These operating conditions were then also applied for the FC mode of the alternating operation and are presented as reference.

During the 40 h of constant operation the stack voltage as well as the temperatures remained mostly unchanged. The results from the impedance measurements which were conducted every three hours showed even smaller oscillations of the high frequency peaks compared to EC mode whereby no actual trend of changes was observable. The ohmic part of the impedance was 8.45 mΩ and therefore significantly smaller than the one measured in the characterization measurements, but slightly higher than during constant EC operation. This can be related mostly to the higher operating temperature compared to the result from the characterization measurement at 300 mA/cm^2 as well as the different temperature distribution compared to EC mode. The amplitude of the DRT peaks in FC mode are generally higher than the ones measured during constant EC operation (Fig. 8), whereby in both modes the peaks are located at the same frequency ranges.

Different to EC mode the highest temperature of 850 °C is measured in the lower half of the stack at T-E04-3/4. The lowest temperature

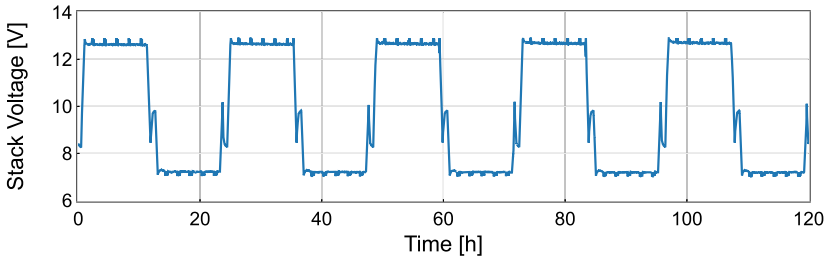

(a) Voltage during alternating operation.

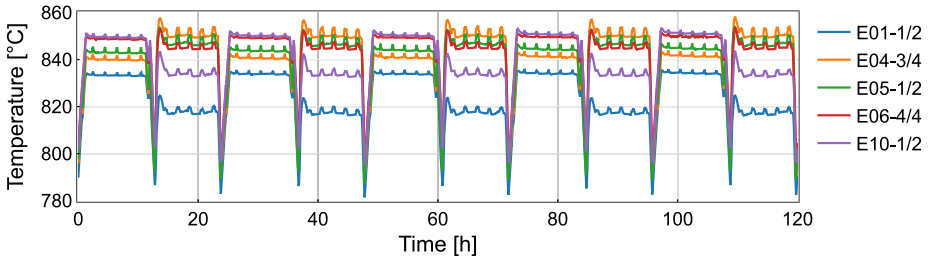

(b) Temperatures during alternating operation.

Fig. 13. Overview: Alternating operation.

of 818 °C is measured at the bottom of the stack (T-E01-1/2). Similar to EC mode the temperature in the middle of the stack (T-E02-1/2) is 845 °C. Therefore, operation in FC mode presents a wider temperature distribution throughout the stack, ranging from 818–850 °C. The two-cell-voltages measured from the bottom to the top cells of the stack were 1.42, 1.46, 1.46, 1.47 and 1.45 V whereby the maximal voltage is measured at the cells E07/08.

4.3. Alternating operation

For alternating operation of the stack, the operation parameters with the gas mixtures with the labels E2 and F2 from Table 1 were chosen, whereby 560 mA/cm^2 were supplied in EC mode and 300 mA/cm^2 were drawn in FC mode. As shown before, E2 presents a good compromise between part load suitability and efficiency and provides conditions for stable operation. Like that, F2 combines decent power output with efficiency and enables safe and steady operation within the operational limits. A very slow current ramp of 2 A/min was chosen, whereby the temperatures and voltages got enough time to adapt and the risk of exceeding operational limits during or in the period after ramping was minimized. When ramped back to OCV, the inlet gas composition was changed slowly and continuously within 15 min. After the fuel change was conducted, additional 30 min were waited so that the stack temperatures could adjust to the new gas mixture as recommended in [73]. After the temperatures have adjusted the current ramp was started again and the mode change was completed. While one goal of alternating operation being fast load and mode changes, this approach considered only the influence of alternating operation between two different operational points in EC and FC mode on the overall performance of the rSOC. The experiment lasted for a total of 120 h respectively five cycles, each consisting of 12 h in EC mode followed by 12 h in FC mode. EIS measurements were conducted every two hours in each mode at full load for a total of 25 measurements in each mode. Fig. 13 presents the stack voltage during alternating operation ranging from approx. 7.2 V at 300 mA/cm^2 in FC mode to approx. 12.6 V at 560 mA/cm^2 in EC mode, whereby the maximum stack temperature was kept below 860 °C by applying the same operating temperatures as presented during the stability tests. In Fig. 13(b) the different temperature distribution in the stack while operated in EC and FC mode are shown as described before. Furthermore, an overall temperature range between 785–855 °C during alternating operation including ramping and gas change at OCV is observable. It can also be seen, that during FC mode the temperatures present little fluctuations compared to EC mode, probably as a result of the complex gas mixture applied.

When taking a closer look at the voltages in Fig. 14 a change of the EC voltage from 12.63 V at the end of the first cycle to 12.70 V at the end of the 5th cycle can be observed. Also a slight change of the FC voltage from 7.23 V at the end of the first cycle to 7.20 V at the end of the fifth cycle can be observed. In EC mode the change is much more severe than in FC mode. While the stack temperatures in FC mode is relatively stable over the 120 h of alternating operation the temperatures in EC mode at all increased slowly by 1–2 °C. It seems that, that traces of CO and CO_2 in small ppm range, that could not be detected by the gas analyzer, are still present in the system during EC operation. Additionally, surplus H_2O could be still present within the system during FC operation [13,58]. It can be assumed that, these small quantities have a negative influence on the performance of the cell and may cause longer stabilization periods after each mode change. Anyway, these changes are not considered to be the result of permanent degradation but rather may present the challenges of operation with complex fuels and FC mode coupled with operation with high steam contents in EC mode. Nevertheless, since only short-term tests were carried out further long-term experiments are required in order to get more detailed insight.

Fig. 15 presents the Nyquist and DRT plots of the last impedance measurement of each cycle in FC mode during alternating operation and represent the behavior of the residual measurements. While there is no real trend visible in the Nyquist plot, the DRT plot shows major differences to the DRTs calculated at constant FC operation as presented in Fig. 12. Firstly, compared to constant operation in FC mode, the first low-frequency peak between 1–10 Hz shifted towards higher frequencies where it oscillated between 20–50 Hz and an amplitude of 4–8 mΩ. The other high-frequency peaks also shifted towards higher frequencies whereby the amplitude of the peak between 1–10 kHz also increased slightly. It can be assumed that this behavior refers to a new equilibrium slowly being achieved within the stack for operation FC mode during alternating operation compared to constant operation.

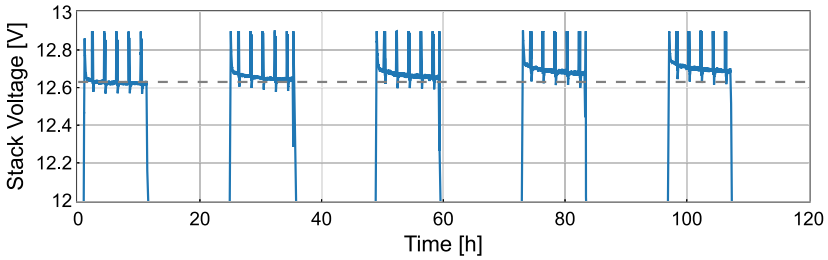

(a) EC mode.

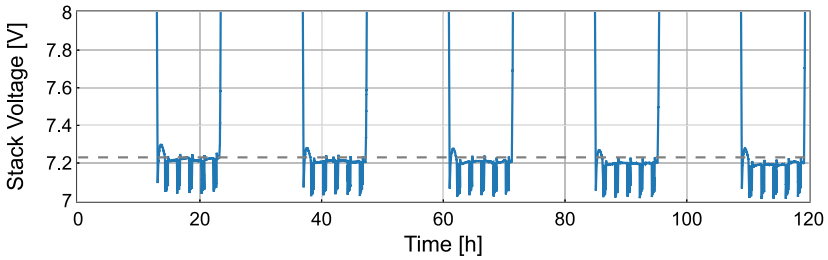

(b) FC mode.

Fig. 14. Change of stack voltages during alternating operation.

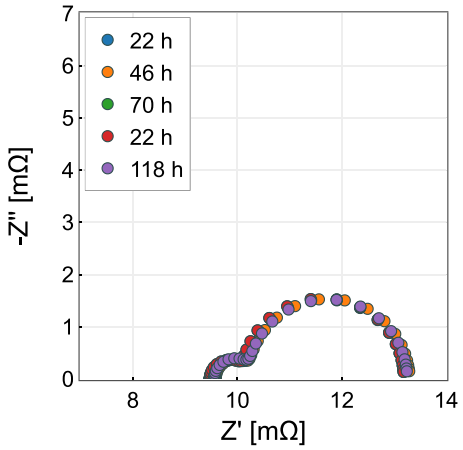

(a) EIS in FC mode.

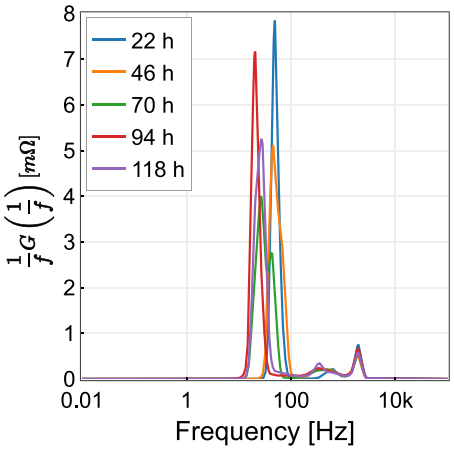

(b) DRT in FC mode.

Fig. 15. Comparison of EIS and DRT in FC mode during alternating operation.

In order to further analyze the processes appearing during alternating operation compared to constant mode operation, the change of the frequency and amplitude of the low-frequency peak in the DRT is presented in Fig. 16. This representation of data is only possible when many impedance measurements were conducted, whereby enabling an easy way for identification of changes and trends. Hereby, Fig. 16(a) presents the change of the low-frequency peak of the DRT calculated from FC mode measurements during alternating operation. It can be seen, that the frequency (blue -) changes from oscillating between 20–60 Hz to oscillating between 20–40 Hz with increasing cycle number. Although very unstable, the amplitude (orange -) of this peak presents no real trend. Differently in Fig. 16(b) the low-frequency peak calculated from FC mode measurements during constant FC operation is located significantly at lower frequencies of approximately 3 Hz with a much more stable amplitude than during alternating operation. The decrease of the frequency of the low-frequency during ongoing alternating operation could indicate an attempt of achieving of a new equilibrium within the stack possibly towards similar results than during constant FC operation.

The results of the impedance measurements present another perspective of the changes visible in the stack voltage and temperatures and confirm that alternating operation with complex fuels in FC mode combined with high steam contents in EC mode impacts the overall performance of an rSOC. Nevertheless, experiments were only conducted over a short period of time whereby it cannot be assumed that quasi-stable conditions have already been reached at the two load points during alternating operation. This must be confirmed by further measurements.

5. Conclusion

In this study, the suitability of an rSOC stack for fuel cell (FC), electrolysis (EC) and alternate operating mode was examined. The stack

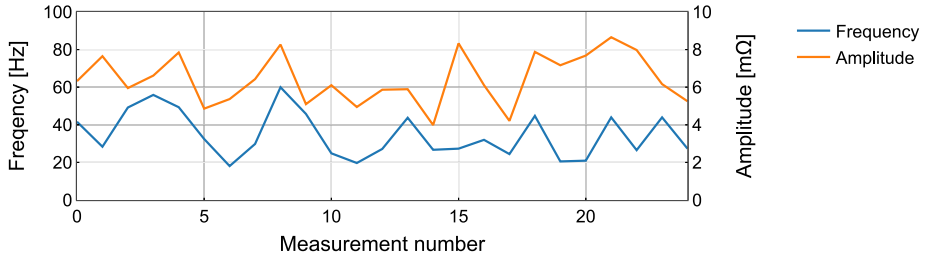

(a) FC mode during altering operation.

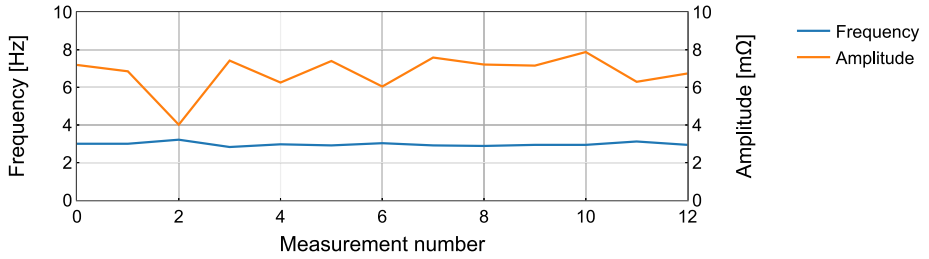

(b) FC mode during constant operation.

Fig. 16. Change of main peak of DRT in different operation modes.

Table 3
Result comparison.

Operational requirements	SOEC H_2/H_2O-ratio	SOFC Fuel flow	rSOC Mode change duration
	E1 | E2 | E3	F1 | F2 | F3	0.75 | 3 | 12 [h]
High power output / high H_2 production rate	1 | 1 | 1	3 | 2 | 1	
High efficiency	3 | 2 | 1	1 | 2 | 3	
Part load suitability	1 | 2 | 3	2 | 1 | 1	
Ability to follow specific load profiles			1 | 2 | 3
Low degradation (alternating-op.)			tbd | tbd | tbd

Operational requirements	Combination E2, F2, 12h	Application A Priority	Result
High power output / high H_2 production rate	1.5	1	1.5
High efficiency	2	2	1
Part load suitability	1.5	2	0.75
Low degradation (dynamic op.)	tbd	3	tbd
Low degradation (long-term)	tbd	1	tbd
Ability to follow specific load profiles	3	3	1
Low degradation (alternating-op.)	tbd	1	tbd

and its individual repeating units were electrochemically characterized and operated under real operating conditions in compliance with the requirements presented by the implementation of a large-scale module at a combined cycle gas turbine power plant. For the experiments conducted within this study, the stack was fed with different H_2/H_2O-ratios in EC mode and a $H_2/H_2O/CO/CO_2/N_2$ mixture with varying fuel flow in FC mode.

In EC mode the heat production caused by internal resistances of the cells at higher current densities was identified as the major limitation for the hydrogen production rate. The analysis of the impedance data showed that for operation at lower current densities higher hydrogen contents in the inlet gas seem to be preferable due to significantly lower diffusion losses. At higher current densities the measured impedances were quite similar so that the hydrogen in the inlet gas could be further reduced to enable more efficient operation. During operation with low hydrogen partial pressures no degradations effects were observed, whereby a 100% steam electrode could be applicable, which needs to be confirmed by long-term experiments. The results from FC mode presented that with increasing fuel and particularly air flows the cooling of the stack was enforced which led to lower stack temperatures which further allowed higher power outputs but lower fuel utilization rates. Additionally, too fast load changes could be critical in terms of undershooting the minimal voltage, whereby current ramps and temperature adjustments must be considered carefully. The equilibrium between chemical production through the reverse water gas shift reaction (RWGS) and electrochemical utilization of CO was reached at relatively low current densities of 160 mA/cm^2 and 810 °C. Operation at lower fuel flows presented increased concentration losses resulting from increasing amount of product species at higher fuel utilizations as well as insufficient ex-change between reactants and products. Higher current densities decreased the ohmic resistance, whereby the rate of change decreased with increasing current density. This was associated with temperature changes and the influence of the RWGS reaction on the surface process resistance at lower current densities. During 120 h of alternating operation the EC voltage and temperatures slightly

Table 4
Glossary of Symbols.

Symbol	Description
$rSOC$	Reversible solid oxide cell
$SOEC$	Solid oxide electrolysis cell
$SOFC$	Solid oxide fuel cell
EC	Electrolysis cell
FC	Fuel cell
$CCGT$	Combined cycle gas turbine
Ni-GDC	Nickel-gadolinium-doped-ceria
YbSZ	Ytterbium-stabilized-zirconia
LSCF	Lanthanum strontium cobalt ferrite
H_2	Hydrogen
H_2O	Water/Steam
CO	Carbon-monoxide
CO_2	Carbon-dioxide
N_2	Nitrogen
O_2	Oxygen
O^{2-}	Oxygen-ion
$RWGS$	Reverse water gas shift
AC	Alternating current
DC	Direct current
OCV	Open circuit voltage
IV	Current/Voltage
kh	kilohour
SLPM	Standard liters per minute
EIS	Electrochemical impedance spectroscopy
DRT	Distribution of relaxation times
KK	Kramers–Kronig

increased while the FC voltage slightly decreased with mostly unchanged temperatures. The analysis of the impedance data also showed significant changes compared to constant operation. The low-frequency peak calculated from distribution of relaxation times (DRT) shifted from between 1 – 10 Hz to oscillating between 20–50 Hz while also presenting a very unstable amplitude of the DRT low-frequency peak. It was assumed that, small quantities of CO, CO_2 and H_2, that could not be detected by the gas analyzer and remained present within the system during the whole alternating operation, had a negative influence on the performance of the cell and caused longer stabilization periods after each mode change.

Table 3 presents an overview of the results of the experiments as well as proposes a method for selection of parameters for optimization of operation. In the first part of the table the suitability of specific operational conditions to fulfill certain operational requirements is rated with 1 (good), 2 (intermediate) and 3 (bad). In the second part of the table a specific combination was chosen and the priority of the operational requirements was ranked for a specific application before the overall result was calculated.

Nevertheless, since only short-term experiments were performed this needs to be investigated in further experiments. Additional long-term experiments must be conducted in order to determine the long-term stability and degradation rates as well as to specify the industrially relevant economical most feasible trade-off between lifetime respectively efficiency and operating costs.

Declaration of competing interest

The authors declare that they have no known competing financial interests or personal relationships that could have appeared to influence the work reported in this paper.

Acknowledgments

The authors gratefully acknowledge the funding of the project “Degradation monitoring and performance optimization of SOECs” (project number I 3994) by Austrian Science Fund (FWF). Furthermore, the authors acknowledge the funding of the project “Hotflex” (project number 872391) by the Austrian Research Promotion Agency (FFG) and the Fuel Cell Hydrogen Joint Undertaking (FCHJU), Austria.

References

[1] Agency IE. World energy outlook 2010. 2010, http://dx.doi.org/10.1787/weo-2010-en.
[2] Jensen SH, Larsen PH, Mogensen M. Hydrogen and synthetic fuel production from renewable energy sources. Int J Hydrogen Energy 2007;32:3253–7. http://dx.doi.org/10.1016/j.ijhydene.2007.04.042, https://linkinghub.elsevier.com/retrieve/pii/S0360319907002480.
[3] Frank M, Deja R, Peters R, Blum L, Stolten D. Bypassing renewable variability with a reversible solid oxide cell plant. Appl Energy 2018;217:101–12. http://dx.doi.org/10.1016/j.apenergy.2018.02.115.
[4] Singhal SC, K. K. High temperature and solid oxide fuel cells: fundamentals, design and applications. Elsevier Science; 2003, http://dx.doi.org/10.1016/B978-1-85617-387-2.X5016-8, https://linkinghub.elsevier.com/retrieve/pii/B9781856173872X50168.
[5] DONITZ W. High-temperature electrolysis of water vapor-status of development and perspectives for application. Int J Hydrogen Energy 1985;10:291–5. http://dx.doi.org/10.1016/0360-3199(85)90181-8, https://linkinghub.elsevier.com/retrieve/pii/0360319985901818.
[6] Laguna-Bercero M. Recent advances in high temperature electrolysis using solid oxide fuel cells: A review. J Power Sources 2012;203:4–16. http://dx.doi.org/10.1016/j.jpowsour.2011.12.019, https://linkinghub.elsevier.com/retrieve/pii/S0378775311024384.
[7] Kupecki J, Papurello D, Lanzini A, Naumovich Y, Motylinski K, Blesznowski M, Santarelli M. Numerical model of planar anode supported solid oxide fuel cell fed with fuel containing H2S operated in direct internal reforming mode (DIR-SOFC). Appl Energy 2018;230:1573–84. http://dx.doi.org/10.1016/j.apenergy.2018.09.092, https://linkinghub.elsevier.com/retrieve/pii/S030626191831403X.
[8] Wang Y, Liu T, Lei L, Chen F. High temperature solid oxide H2O/CO2 co-electrolysis for syngas production. Fuel Process Technol 2017;161:248–58. http://dx.doi.org/10.1016/j.fuproc.2016.08.009.
[9] Alenazey F, Alyousef Y, Almisned O, Almutairi G, Ghouse M, Montinaro D, Ghigliazza F. Production of synthesis gas (H2 and CO) by high-temperature co-electrolysis of H2o and CO2. Int J Hydrogen Energy 2015;40:10274–80. http://dx.doi.org/10.1016/j.ijhydene.2015.06.034.
[10] Zhan Z, Kobsiriphat W, Wilson JR, Pillai M, Kim I, Barnett SA. Syngas production by coelectrolysis of CO 2/H 2o: The basis for a renewable energy cycle. Energy Fuels 2009;23:3089–96. http://dx.doi.org/10.1021/ef900111f.
[11] O'Hayre R, Cha S-W, Colella W, Prinz FB. Fuel cell fundamentals. Hoboken, NJ, USA: John Wiley and Sons, Inc; 2016, http://dx.doi.org/10.1002/9781119191766, http://doi.wiley.com/10.1002/9781119191766.
[12] Stoeckl B, Subotić V, Preininger M, Schwaiger M, Evic N, Schroettner H, Hochenauer C. Characterization and performance evaluation of ammonia as fuel for solid oxide fuel cells with Ni/YSZ anodes. Electrochim Acta 2019;298:874–83. http://dx.doi.org/10.1016/j.electacta.2018.12.065.
[13] Subotić V, Schluckner C, Mathe J, Rechberger J, Schroettner H, Hochenauer C. Anode regeneration following carbon depositions in an industrial-sized anode supported solid oxide fuel cell operating on synthetic diesel reformate. J Power Sources 2015;295:55–66. http://dx.doi.org/10.1016/j.jpowsour.2015.06.133.
[14] Subotić V, Baldinelli A, Barelli L, Scharler R, Pongratz G, Hochenauer C, Anca-Couce A. Applicability of the SOFC technology for coupling with biomass-gasifier systems: Short- and long-term experimental study on SOFC performance and degradation behaviour. Appl Energy 2019;256. http://dx.doi.org/10.1016/j.apenergy.2019.113904.
[15] Tietz F, Sebold D, Brisse A, Schefold J. Degradation phenomena in a solid oxide electrolysis cell after 9000 h of operation. J Power Sources 2013;223:129–35. http://dx.doi.org/10.1016/j.jpowsour.2012.09.061.
[16] Yan Y, Fang Q, Blum L, Lehnert W. Performance and degradation of an SOEC stack with different cell components. Electrochim Acta 2017;258:1254–61. http://dx.doi.org/10.1016/j.electacta.2017.11.180.
[17] Chen K, Jiang SP. Review—Materials degradation of solid oxide electrolysis cells. J Electrochem Soc 2016;163:F3070–83. http://dx.doi.org/10.1149/2.0101611jes, https://iopscience.iop.org/article/10.1149/2.0101611jes.
[18] Menzler NH, Sebold D, Guillon O. Post-test characterization of a solid oxide fuel cell stack operated for more than 30,000 hours: The cell. J Power Sources 2018;374:69–76. http://dx.doi.org/10.1016/j.jpowsour.2017.11.025.
[19] Blum L, de Haart LG, Malzbender J, Margaritis N, Menzler NH. Anode-supported solid oxide fuel cell achieves 70 000 hours of continuous operation. Energy Technol 2016;4:939–42. http://dx.doi.org/10.1002/ente.201600114.
[20] Trini M, Hauch A, Angelis SD, Tong X, Hendriksen PV, Chen M. Comparison of microstructural evolution of fuel electrodes in solid oxide fuel cells and electrolysis cells. J Power Sources 2020;450:227599. http://dx.doi.org/10.1016/j.jpowsour.2019.227599.
[21] Fang Q, Blum L, Menzler NH, Stolten D. Solid oxide electrolyzer stack with 20,000 h of operation. ECS Trans 2017;78:2885–93. http://dx.doi.org/10.1149/07801.2885ecst.
[22] Frey CE, Fang Q, Sebold D, Blum L, Menzler NH. A detailed post mortem analysis of solid oxide electrolyzer cells after long-term stack operation. J Electrochem Soc 2018;165:F357–64. http://dx.doi.org/10.1149/2.0961805jes.

[23] Chang HW, Huang CM, Shy SS. An experimental investigation of pressurized planar solid oxide fuel cells using two different flow distributors. J Power Sources 2014;250:21–9. http://dx.doi.org/10.1016/j.jpowsour.2013.10.127.

[24] Stoeckl B, Subotić V, Reichholf D, Schroettner H, Hochenauer C. Extensive analysis of large planar SOFC: Operation with humidified methane and carbon monoxide to examine carbon deposition based degradation. Electrochim Acta 2017;256:325–36. http://dx.doi.org/10.1016/j.electacta.2017.09.026.

[25] Subotić V, Schluckner C, Stöckl B, Lawlor V, Schroettner H, Hochenauer C. Strategy for carbon gasification from porous Ni-YSZ anodes of industrial-sized ASC-SOFCs and effects of carbon growth. J Electrochem Soc 2016;163:F1515–22. http://dx.doi.org/10.1149/2.0521614jes.

[26] Zheng Y, Wang J, Yu B, Zhang W, Chen J, Qiao J, Zhang J. A review of high temperature co-electrolysis of H2O and CO2 to produce sustainable fuels using solid oxide electrolysis cells (SOECs): Advanced materials and technology. Chem Soc Rev 2017;46:1427–63. http://dx.doi.org/10.1039/c6cs00403b.

[27] Kupecki J, Milewski J, Szczesniak A, Bernat R, Motylinski K. Dynamic numerical analysis of cross-, co-, and counter-current flow configuration of a 1 kw-class solid oxide fuel cell stack. 40, Elsevier Ltd; 2015, p. 15834–44. http://dx.doi.org/10.1016/j.ijhydene.2015.07.008,

[28] Preininger M, Stoeckl B, Subotić V, Mittmann F, Hochenauer C. Performance of a ten-layer reversible solid oxide cell stack (rSOC) under transient operation for autonomous application. Appl Energy 2019;254:113695. http://dx.doi.org/10.1016/j.apenergy.2019.113695, https://linkinghub.elsevier.com/retrieve/pii/S0306261919313820.

[29] Riedel M, Heddrich MP, Friedrich KA. Analysis of pressurized operation of 10 layer solid oxide electrolysis stacks. Int J Hydrogen Energy 2019;44:4570–81. http://dx.doi.org/10.1016/j.ijhydene.2018.12.168.

[30] Zhang X, O'Brien JE, O'Brien RC, Hartvigsen JJ, Tao G, Housley GK. Improved durability of SOEC stacks for high temperature electrolysis. Int J Hydrogen Energy 2013;38:20–8. http://dx.doi.org/10.1016/J.IJHYDENE.2012.09.176, https://www.sciencedirect.com/science/article/pii/S0360319912023002.

[31] Fang Q, Blum L, Menzler NH. Performance and degradation of solid oxide electrolysis cells in stack. J Electrochem Soc 2015;162:F907–12. http://dx.doi.org/10.1149/2.0941508jes.

[32] BALANCE Project, hydrogen technology to support deployment of intermittent renewable electricity sourcess. 2016, https://www.balance-project.org/.

[33] REFLEX, reversible solid oxide electrolyzer and fuel cell for optimized local energy mix. 2018, https://cordis.europa.eu/project/id/779577/de.

[34] GrInHy, green industrial hydrogen via reversible high-temperature electrolysis. 2016, https://www.green-industrial-hydrogen.com/.

[35] RelHy, innovative solid oxide electrolyser stacks for efficient and reliable hydrogen production. 2008, https://cordis.europa.eu/project/id/213009.

[36] FCE Wraps up world's largest fuel cell park in Korea, new seoul one. Fuel Cells Bull 2014;2014:6. http://dx.doi.org/10.1016/S1464-2859(14)70076-8, https://linkinghub.elsevier.com/retrieve/pii/S1464285914700768.

[37] IKEA Installs bloom energy systems in two more california stores. Fuel Cells Bull 2016;2016:7. http://dx.doi.org/10.1016/S1464-2859(16)30349-2, https://linkinghub.elsevier.com/retrieve/pii/S1464285916303492.

[38] Hydrogenics launches 3 MW electrolyser using PEM stack. Fuel Cells Bull 2017;2017:11. http://dx.doi.org/10.1016/S1464-2859(17)30195-5, https://linkinghub.elsevier.com/retrieve/pii/S1464285917301955.

[39] H2Future, hydrogen meeting future needs of low carbon manufacturing value chains. 2017, https://www.h2future-project.eu/.

[40] VERBUND Thermal power gmbh, hotflex – reversible hochtemperatur-elektrolyseanlage. 2019, https://www.verbund.com/de-at/geschaeftskunden/industrie/energiedienstleistungen/gruener-wasserstoff.

[41] Subotić V, Königshofer B, Đani Juričić, Kusnezoff M, Schröttner H, Hochenauer C, Boškoski P. Detailed insight into processes of reversible solid oxide cells and stacks using DRT analysis. Energy Convers Manage 2020;226. http://dx.doi.org/10.1016/j.enconman.2020.113509.

[42] Marco GD, Pilenga A, Honselaar M, Malkow T, Tsotridis G, Janssen A, Rietveld B, Vinke I, Kiviaho J. Testing the voltage and power as function of current density - polarisation curve for a SOFC single cell. 2010, http://ie.jrc.ec.europa.eu/.

[43] Guk E, Kim J-S, Ranaweera M, Venkatesan V, Jackson L. In-situ monitoring of temperature distribution in operating solid oxide fuel cell cathode using proprietary sensory techniques versus commercial thermocouples. Appl Energy 2018;230:551–62. http://dx.doi.org/10.1016/j.apenergy.2018.08.120, https://linkinghub.elsevier.com/retrieve/pii/S0306261918312947.

[44] Al-Masri A, Peksen M, Blum L, Stolten D. A 3D CFD model for predicting the temperature distribution in a full scale APU SOFC short stack under transient operating conditions. Appl Energy 2014;135:539–47. http://dx.doi.org/10.1016/j.apenergy.2014.08.052, https://linkinghub.elsevier.com/retrieve/pii/S0306261914008630.

[45] Huang C, Shy S, Lee C. On flow uniformity in various interconnects and its influence to cell performance of planar SOFC. J Power Sources 2008;183:205–13. http://dx.doi.org/10.1016/j.jpowsour.2008.04.059, https://linkinghub.elsevier.com/retrieve/pii/S0378775308008318.

[46] Bode HW, et al. Network analysis and feedback amplifier design. van Nostrand New York; 1995.

[47] Ehm W, Kaus R, Strunz C-ASW. Z-hit : A simple relation between impedance modulus and phase angle. providing a new way to the validation of electrochemical impedance spectra. In: Mansfeld F, Huet F, Mattos O, editors. New trends in electrochemical impedance spectroscopy and electrochemical noise analysis. Electrochemical Society Inc; 2001, p. 1–10.

[48] Agarwal P, Orazem ME, Garcia-Rubio LH. Application of measurement models to impedance spectroscopy iii. evaluation of consistency with the kramers-kronig relations. J Electrochem Soc 1995;142:4159–68.

[49] Trofimenko N, Kusnezoff M, Michaelis A. Optimization of ESC performance for co-electrolysis operation. ECS Trans 2017;78:3025–37. http://dx.doi.org/10.1149/07801.3025ecst, https://iopscience.iop.org/article/10.1149/07801.3025ecst.

[50] Preininger M, Subotić V, Stoeckl B, Schauperl R, Reichholf D, Megel S, Kusnezoff M, Hochenauer C. Electrochemical characterization of a CFY-stack with planar electrolyte-supported solid oxide cells in rSOC operation. Int J Hydrogen Energy 2018;43:12398–412. http://dx.doi.org/10.1016/j.ijhydene.2018.04.230, https://linkinghub.elsevier.com/retrieve/pii/S036031991831454X.

[51] Papurello D, Menichini D, Lanzini A. Distributed relaxation times technique for the determination of fuel cell losses with an equivalent circuit model to identify physicochemical processes. Electrochim Acta 2017;258:98–109. http://dx.doi.org/10.1016/j.electacta.2017.10.052, https://linkinghub.elsevier.com/retrieve/pii/S0013468617321503.

[52] Fuoss RM, Kirkwood JG. Electrical properties of solids. VIII. Dipole moments in polyvinyl chloride-diphenyl systems [*]. J Am Chem Soc 1941;63:385–94. http://dx.doi.org/10.1021/ja01847a013, https://pubs.acs.org/doi/abs/10.1021/ja01847a013.

[53] Schlüter N, Ernst S, Schröder U. Finding the optimal regularization parameter in distribution of relaxation times analysis. ChemElectroChem 2019;6:6027–37. http://dx.doi.org/10.1002/celc.201901863, https://onlinelibrary.wiley.com/doi/abs/10.1002/celc.201901863.

[54] Ciucci F, Chen C. Analysis of electrochemical impedance spectroscopy data using the distribution of relaxation times: A Bayesian and hierarchical Bayesian approach. Electrochim Acta 2015. http://dx.doi.org/10.1016/j.electacta.2015.03.123.

[55] Liu J, Ciucci F. The Gaussian process distribution of relaxation times: A machine learning tool for the analysis and prediction of electrochemical impedance spectroscopy data. Electrochim Acta 2020;331:135316. http://dx.doi.org/10.1016/j.electacta.2019.135316, https://linkinghub.elsevier.com/retrieve/pii/S0013468619321887.

[56] Leonide A, Sonn V, Weber A, Ivers-Tiffée E. Evaluation and modeling of the cell resistance in anode-supported solid oxide fuel cells. J Electrochem Soc 2008;155:B36. http://dx.doi.org/10.1149/1.2801372.

[57] Sonn V, Leonide A, Ivers-Tiffée E. Combined deconvolution and CNLS fitting approach applied on the impedance response of technical Ni/8YSZ cermet electrodes. J Electrochem Soc 2008;155:B675. http://dx.doi.org/10.1149/1.2908860.

[58] Schluckner C, Subotić V, Lawlor V, Hochenauer C. CFD-Simulation of effective carbon gasification strategies from high temperature SOFC Ni–YSZ cermet anodes. Int J Hydrogen Energy 2017;42:4434–48. http://dx.doi.org/10.1016/j.ijhydene.2016.11.162.

[59] Cai Q, Luna-Ortiz E, Adjiman CS, Brandon NP. The effects of operating conditions on the performance of a solid oxide steam electrolyser: A model-based study. Fuel Cells 2010;10:1114–28. http://dx.doi.org/10.1002/fuce.200900211.

[60] Riegraf M, Costa R, Schiller G, Friedrich KA, Dierickx S, Weber A. Electrochemical impedance analysis of symmetrical Ni/gadolinium-doped ceria (CGO10) electrodes in electrolyte-supported solid oxide cells. J Electrochem Soc 2019;166:F865–72. http://dx.doi.org/10.1149/2.0051913jes.

[61] Barfod R, Mogensen M, Klemenso T, Hagen A, Liu Y-L, Hendriksen PV. Detailed characterization of anode-supported SOFCs by impedance spectroscopy. J Electrochem Soc 2007;154:B371. http://dx.doi.org/10.1149/1.2433311, https://iopscience.iop.org/article/10.1149/1.2433311.

[62] Hauch A, Mogensen M, Hagen A. Ni/YSZ electrode degradation studied by impedance spectroscopy - effect of p(H2O). 192, 2011, p. 547–51. http://dx.doi.org/10.1016/j.ssi.2010.01.004,

[63] Graves C, Ebbesen SD, Mogensen M. Co-electrolysis of CO2 and H2o in solid oxide cells: Performance and durability. 192, 2011, p. 398–403. http://dx.doi.org/10.1016/j.ssi.2010.06.014,

[64] Schluckner C, Subotić V, Lawlor V, Hochenauer C. Three-dimensional numerical and experimental investigation of an industrial-sized SOFC fueled by diesel reformat - part I: Creation of a base model for further carbon deposition modeling. Int J Hydrogen Energy 2014;39:19102–18. http://dx.doi.org/10.1016/j.ijhydene.2014.09.108.

[65] Pastor-Pérez L, Baibars F, Sache EL, a HA-G, Gu S, Reina TR. CO2 valorisation via reverse water-gas shift reaction using advanced Cs doped Fe-Cu/Al2O3 catalysts. J CO2 Util 2017;21:423–8. http://dx.doi.org/10.1016/j.jcou.2017.08.009.

[66] Nguyen VN, Fang Q, Packbier U, Blum L. Long-term tests of a Jülich planar short stack with reversible solid oxide cells in both fuel cell and electrolysis modes. Int J Hydrogen Energy 2013;38:4281–90. http://dx.doi.org/10.1016/j.ijhydene.2013.01.192.

[67] Subotić V, Stoeckl B, Lawlor V, Strasser J, Schroettner H, Hochenauer C. Towards a practical tool for online monitoring of solid oxide fuel cell operation: An experimental study and application of advanced data analysis approaches. Appl Energy 2018;222:748–61. http://dx.doi.org/10.1016/j.apenergy.2018.03.182, https://linkinghub.elsevier.com/retrieve/pii/S0306261918305324.

[68] Jacobsen T, Hendriksen PV, Koch S. Diffusion and conversion impedance in solid oxide fuel cells. Electrochim Acta 2008;53:7500–8. http://dx.doi.org/10.1016/j.electacta.2008.02.019, https://linkinghub.elsevier.com/retrieve/pii/S0013468608002223.

[69] Zhu H, Kromp A, Leonide A, Ivers-Tiffée E, Deutschmann O, Kee RJ. A model-based interpretation of the influence of anode surface chemistry on solid oxide fuel cell electrochemical impedance spectra. J Electrochem Soc 2012;159:F255–66. http://dx.doi.org/10.1149/2.046207jes.

[70] Kromp A, Weber A, Ivers-Tiffee E. Electrochemistry of reformate fueled Ni/8ysz anodes for solid oxide fuel cells. ECS Trans 2013;57:3063–75. http://dx.doi.org/10.1149/05701.3063ecst.

[71] Sasaki K, Hori Y, Kikuchi R, Eguchi K, Ueno A, Takeuchi H, Aizawa M, Tsujimoto K, Tajiri H, Nishikawa H, Uchida Y. Current-voltage characteristics and impedance analysis of solid oxide fuel cells for mixed h[sub 2] and CO gases. J Electrochem Soc 2002;149:A227. http://dx.doi.org/10.1149/1.1435357.

[72] Diethelm S, Herle JV. Ethanol internal steam reforming in intermediate temperature solid oxide fuel cell. 196, 2011, p. 7355–62. http://dx.doi.org/10.1016/j.jpowsour.2010.11.063,

[73] Srikanth S, Heddrich MP, Gupta S, Friedrich KA. Transient reversible solid oxide cell reactor operation – experimentally validated modeling and analysis. Appl Energy 2018;232:473–88. http://dx.doi.org/10.1016/j.apenergy.2018.09.186.

Chapter 5

Conclusions

The thesis revisits the problem of performing on-line monitoring of the electrochemical energy conversion devices (EECD) using EIS. The main contributions described in this thesis include:

- *Implementation and validation of fast EIS* on a set of different electrochemical energy conversion devices using the same measuring architecture.
- *Implementation of the Morse wavelet* for accurate estimation of the the impedance spectra at ultra-low frequencies (<1 mHz).
- *Taking into account the noise measurement* on the measured impedance.
- *Fault detection of SOFC* by monitoring the evolution of ECM parameters.
- *The concept of modular cost-effective system* for performing EIS.

Using DRBS excitation signals with CWT to perform EIS has two advantages. First is the ability to estimate the impedance at any frequency point of interest. The second is the reduction of the required excitation time by order of magnitude compared to the classical single-sine EIS.

The usage of Morse wavelet further improved the performance of the proposed solution particularly at low frequencies. The results present the very first such analysis in the field of electrochemistry. Unlike other complex wavelets, the Morse wavelet remains analytical even for a low value of its central frequency. This is particularly important for accurate estimation of the impedance value at ultra-low frequencies ($<$ 1 mHz). As a result, the lowest observable frequency is determined by the length of the excitation signal, which was calculated to be $f_{min} = \frac{3}{T}$. The Morse wavelet has been successfully used to calculate the impedance of Li-ion battery at ultra-low frequencies ($<$ 1 mHz) with 100 points per decade in 97 minutes.

Furthermore, with broad-band excitation and CWT, it becomes possible to assess the level of noise influence on the measured impedance at each frequency point. Simulations show that the variance of the impedance results increases for frequencies with lower effective values of the input amplitude. This is a feature that is unavailable in classical single-sine EIS and has not been exploited yet.

Having impedance spectra that are not only point estimates of the mean value opens new possibilities. Changes of the impedance spectrum can be related to the changes in the internal condition of the electrochemical energy conversion devices. These changes were quantified either by using ECM or DRT. Depending on how the parameters of the ECM or DRT change, one can detect unwanted faults or degradation processes occurring

inside the device under test. The effectiveness of these approaches was used for detection of deficiencies in the fuel supply of a SOFC stack. Furthermore, same method has been successfully used to detect the drying of the PEM membrane in electrochemical hydrogen compressors.

The proposed modular experimental set-up was successfully used to perform accelerated and long-term tests, while monitoring their performances, on different EECD, such as single-cell SOFC and SOE, SOFC stacks, SOE stacks, single-cell batteries, super capacitors, etc. Using this equipment, more than 5 TB of data has been generated. Unlike currently used testing units, the proposed measurement and excitation architecture is built from readily available and cost-effective components. It offers great flexibility both in terms of power ranges as well as modes of operation. This paves the way of implementing high-precision impedance measurement loops even for in-field operation, a feat that was previously financially not viable.

Finally, the complete set of results, both methodological in terms of software and hardware, is provided in open-source format. This should further increase the practical uptake and break the vicious circle of using tailor-made measurement equipment, and closed and inflexible software implementations. The implemented libraries have been successfully tested by various teams from renowned institutions such as TU Graz, AVL, CEA Grenoble and University of Salerno. The locations of the software implementations can be found in the included papers of this dissertation.

References

[1] "Communication from the commission to the european parliament, the council, the european economic and social committee and the committee of the regions – a roadmap for moving to a competitive low carbon economy in 2050," European Comission, Brussels, 8.03.2011.

[2] E. Comission. "Eu countries' long-term strategies to meet their paris agreement commitments and the energy union objectives." (), [Online]. Available: https://ec.europa.eu/info/energy-climate-change-environment/implementation-eu-countries/energy-and-climate-governance-and-reporting/national-long-term-strategies_en.

[3] W. Zappa, M. Junginger, and M. van den Broek, "Is a 100% renewable european power system feasible by 2050?" *Applied Energy*, vol. 233-234, pp. 1027–1050, 2019, ISSN: 0306-2619. DOI: https://doi.org/10.1016/j.apenergy.2018.08.109. [Online]. Available: http://www.sciencedirect.com/science/article/pii/S0306261918312790.

[4] H. Lund and B. V. Mathiesen, "Energy system analysis of 100% renewable energy systems—the case of denmark in years 2030 and 2050," *Energy*, vol. 34, no. 5, pp. 524–531, 2009.

[5] B. V. Mathiesen, H. Lund, and K. Karlsson, "100% renewable energy systems, climate mitigation and economic growth," *Applied energy*, vol. 88, no. 2, pp. 488–501, 2011.

[6] V. Krakowski, E. Assoumou, V. Mazauric, and N. Maïzi, "Reprint of feasible path toward 40–100% renewable energy shares for power supply in france by 2050: A prospective analysis," *Applied energy*, vol. 184, pp. 1529–1550, 2016.

[7] F. Wagner, "Electricity by intermittent sources: An analysis based on the german situation 2012," *The European Physical Journal Plus*, vol. 129, no. 2, pp. 1–18, 2014.

[8] M. Z. Jacobson, M. A. Delucchi, M. A. Cameron, and B. V. Mathiesen, "Matching demand with supply at low cost in 139 countries among 20 world regions with 100% intermittent wind, water, and sunlight (wws) for all purposes," *Renewable Energy*, vol. 123, pp. 236–248, 2018.

[9] R. Amirante, E. Cassone, E. Distaso, and P. Tamburrano, "Overview on recent developments in energy storage: Mechanical, electrochemical and hydrogen technologies," *Energy Conversion and Management*, vol. 132, pp. 372–387, 2017, ISSN: 0196-8904. DOI: https://doi.org/10.1016/j.enconman.2016.11.046. [Online]. Available: https://www.sciencedirect.com/science/article/pii/S019689041631055X.

[10] A. Dehghani-Sanij, E. Tharumalingam, M. Dusseault, and R. Fraser, "Study of energy storage systems and environmental challenges of batteries," *Renewable and Sustainable Energy Reviews*, vol. 104, pp. 192–208, 2019, ISSN: 1364-0321. DOI: https://doi.org/10.1016/j.rser.2019.01.023. [Online]. Available: https://www.sciencedirect.com/science/article/pii/S1364032119300334.

[11] M. S. Guney and Y. Tepe, "Classification and assessment of energy storage systems," *Renewable and Sustainable Energy Reviews*, vol. 75, pp. 1187–1197, 2017, ISSN: 1364-0321. DOI: https://doi.org/10.1016/j.rser.2016.11.102. [Online]. Available: https://www.sciencedirect.com/science/article/pii/S1364032116308218.

[12] X. Luo, J. Wang, M. Dooner, and J. Clarke, "Overview of current development in electrical energy storage technologies and the application potential in power system operation," *Applied Energy*, vol. 137, pp. 511–536, 2015, ISSN: 0306-2619.

[13] O. Z. Sharaf and M. F. Orhan, "An overview of fuel cell technology: Fundamentals and applications," *Renewable and Sustainable Energy Reviews*, vol. 32, pp. 810–853, 2014.

[14] C. Mikolajczak, M. Kahn, K. White, and R. T. Long, *Lithium-ion batteries hazard and use assessment*. Springer Science & Business Media, 2012.

[15] E. CEN, "13306 maintenance terminology," *European committee for standardization*, 2001.

[16] D. J. Jovan and G. Dolanc, "Can green hydrogen production be economically viable under current market conditions," *Energies*, vol. 13, no. 24, p. 6599, 2020.

[17] D. Fraile, J.-C. Lanoix, P. Maio, A. Rangel, and A. Torres, "Overview of the market segmentation for hydrogen across potential customer groups, based on key application areas," *CertifHy Proj*, pp. 1–32, 2015.

[18] H. Council, "Hydrogen scaling up: A sustainable pathway for the global energy transition," 2017.

[19] J. D. Holladay, J. Hu, D. L. King, and Y. Wang, "An overview of hydrogen production technologies," *Catalysis today*, vol. 139, no. 4, pp. 244–260, 2009.

[20] TRANSITION, *A wake-up call on green hydrogen: The amount of wind and solar needed is immense*, Mar. 2020. [Online]. Available: https://www.rechargenews.com/transition/a-wake-up-call-on-green-hydrogen-the-amount-of-wind-and-solar-needed-is-immense/2-1-776481.

[21] A. Mazza, E. Bompard, and G. Chicco, "Applications of power to gas technologies in emerging electrical systems," *Renewable and Sustainable Energy Reviews*, vol. 92, pp. 794–806, 2018.

[22] S. S. Kumar and V. Himabindu, "Hydrogen production by pem water electrolysis–a review," *Materials Science for Energy Technologies*, vol. 2, no. 3, pp. 442–454, 2019.

[23] R. Hino, K. Haga, H. Aita, and K. Sekita, "38. r&d on hydrogen production by high-temperature electrolysis of steam," *Nuclear Engineering and Design*, vol. 233, no. 1-3, pp. 363–375, 2004.

[24] M. Laguna-Bercero, "Recent advances in high temperature electrolysis using solid oxide fuel cells: A review," *Journal of Power sources*, vol. 203, pp. 4–16, 2012.

[25] C. Graves, S. D. Ebbesen, S. H. Jensen, S. B. Simonsen, and M. B. Mogensen, "Eliminating degradation in solid oxide electrochemical cells by reversible operation," *Nature materials*, vol. 14, no. 2, pp. 239–244, 2015.

[26] A. Kirubakaran, S. Jain, and R. Nema, "A review on fuel cell technologies and power electronic interface," *Renewable and Sustainable Energy Reviews*, vol. 13, no. 9, pp. 2430–2440, 2009.

[27] A. B. Stambouli and E. Traversa, "Fuel cells, an alternative to standard sources of energy," *Renewable and Sustainable Energy Reviews*, vol. 6, no. 3, pp. 295–304, 2002.

[28] U. Lucia, "Overview on fuel cells," *Renewable and Sustainable Energy Reviews*, vol. 30, pp. 164–169, 2014.

[29] S. Göll, R. Samsun, and R. Peters, "Analysis and optimization of solid oxide fuel cell-based auxiliary power units using a generic zero-dimensional fuel cell model," *Journal of power sources*, vol. 196, no. 22, pp. 9500–9509, 2011.

[30] V. Subotić, A. Baldinelli, L. Barelli, R. Scharler, G. Pongratz, C. Hochenauer, and A. Anca-Couce, "Applicability of the sofc technology for coupling with biomass-gasifier systems: Short-and long-term experimental study on sofc performance and degradation behaviour," *Applied Energy*, vol. 256, p. 113 904, 2019.

[31] B. Stoeckl, V. Subotić, M. Preininger, H. Schroettner, and C. Hochenauer, "Sofc operation with carbon oxides: Experimental analysis of performance and degradation," *Electrochimica acta*, vol. 275, pp. 256–264, 2018.

[32] B. Stoeckl, V. Subotić, M. Preininger, M. Schwaiger, N. Evic, H. Schroettner, and C. Hochenauer, "Characterization and performance evaluation of ammonia as fuel for solid oxide fuel cells with ni/ysz anodes," *Electrochimica acta*, vol. 298, pp. 874–883, 2019.

[33] D. Marra, C. Pianese, P. Polverino, and M. Sorrentino, *Models for solid oxide fuel cell systems: exploitation of models hierarchy for industrial design of control and diagnosis strategies*. Springer, 2016.

[34] W. Earle Waghorne, "Viscosities of electrolyte solutions," *Philosophical Transactions of the Royal Society of London. Series A: Mathematical, Physical and Engineering Sciences*, vol. 359, no. 1785, pp. 1529–1543, 2001.

[35] W. G. Manuel, "Energy storage study 2014," *TID, Turlock, CA, Tech. Rep.*, 2014.

[36] V. F. Valdés-López, T. Mason, P. R. Shearing, and D. J. Brett, "Carbon monoxide poisoning and mitigation strategies for polymer electrolyte membrane fuel cells–a review," *Progress in Energy and Combustion Science*, vol. 79, p. 100 842, 2020.

[37] K.-S. Lee, B.-S. Lee, S. J. Yoo, S.-K. Kim, S. J. Hwang, H.-J. Kim, E. Cho, D. Henkensmeier, J. W. Yun, S. W. Nam, *et al.*, "Development of a galvanostatic analysis technique as an in-situ diagnostic tool for pemfc single cells and stacks," *International journal of hydrogen energy*, vol. 37, no. 7, pp. 5891–5900, 2012.

[38] C. Grey and J. Tarascon, "Sustainability and in situ monitoring in battery development," *Nature materials*, vol. 16, no. 1, pp. 45–56, 2017.

[39] C. Lyu, Y. Song, J. Zheng, W. Luo, G. Hinds, J. Li, and L. Wang, "In situ monitoring of lithium-ion battery degradation using an electrochemical model," *Applied Energy*, vol. 250, pp. 685–696, 2019.

[40] P. Boškoski, A. Debenjak, and B. M. Boshkoska, "Rayleigh copula for describing impedance data—with application to condition monitoring of proton exchange membrane fuel cells," *European journal of operational research*, vol. 266, no. 1, pp. 269–277, 2018.

[41] S. Chandrashekar, N. M. Trease, H. J. Chang, L.-S. Du, C. P. Grey, and A. Jerschow, "7 li mri of li batteries reveals location of microstructural lithium," *Nature materials*, vol. 11, no. 4, pp. 311–315, 2012.

[42] F. Blanc, M. Leskes, and C. P. Grey, "In situ solid-state nmr spectroscopy of electrochemical cells: Batteries, supercapacitors, and fuel cells," *Accounts of chemical research*, vol. 46, no. 9, pp. 1952–1963, 2013.

[43] V. Croze, F. Ettingshausen, J. Melke, M. Soehn, D. Stuermer, and C. Roth, "The use of in situ x-ray absorption spectroscopy in applied fuel cell research," *Journal of applied electrochemistry*, vol. 40, no. 5, pp. 877–883, 2010.

[44] D. Zhang, C. Cadet, N. Yousfi-Steiner, F. Druart, and C. Bérenguer, "Phm-oriented degradation indicators for batteries and fuel cells," *Fuel Cells*, vol. 17, no. 2, pp. 268–276, 2017.

[45] N.-H. Kim, D. An, and J.-H. Choi, "Prognostics and health management of engineering systems," *Switzerland: Springer International Publishing*, 2017.

[46] S. C. Olhede and A. T. Walden, "Generalized morse wavelets," *IEEE Transactions on Signal Processing*, vol. 50, no. 11, pp. 2661–2670, 2002.

[47] J. M. Lilly and S. C. Olhede, "Generalized morse wavelets as a superfamily of analytic wavelets," *IEEE Transactions on Signal Processing*, vol. 60, no. 11, pp. 6036–6041, 2012.

[48] A. Debenjak, P. Boškoski, B. Musizza, J. Petrovčič, and Đ. Juričić, "Fast measurement of proton exchange membrane fuel cell impedance based on pseudo-random binary sequence perturbation signals and continuous wavelet transform," *Journal of Power Sources*, vol. 254, pp. 112–118, 2014.

[49] M. Itagaki, M. Ueno, Y. Hoshi, and I. Shitanda, "Simultaneous determination of electrochemical impedance of lithium-ion rechargeable batteries with measurement of charge-discharge curves by wavelet transformation," *Electrochimica Acta*, vol. 235, pp. 384–389, 2017.

[50] N. Lohmann, P. Weßkamp, P. Haußmann, J. Melbert, and T. Musch, "Electrochemical impedance spectroscopy for lithium-ion cells: Test equipment and procedures for aging and fast characterization in time and frequency domain," *Journal of Power Sources*, vol. 273, pp. 613–623, 2015.

[51] E. Van Gheem, R. Pintelon, J. Vereecken, J. Schoukens, A. Hubin, P. Verboven, and O. Blajiev, "Electrochemical impedance spectroscopy in the presence of non-linear distortions and non-stationary behaviour: Part i: Theory and validation," *Electrochimica Acta*, vol. 49, no. 26, pp. 4753–4762, 2004.

[52] Y. Hoshi, N. Yakabe, K. Isobe, T. Saito, I. Shitanda, and M. Itagaki, "Wavelet transformation to determine impedance spectra of lithium-ion rechargeable battery," *Journal of Power Sources*, vol. 315, pp. 351–358, 2016.

[53] C. Pastor-Fernández, K. Uddin, G. H. Chouchelamane, W. D. Widanage, and J. Marco, "A comparison between electrochemical impedance spectroscopy and incremental capacity-differential voltage as li-ion diagnostic techniques to identify and quantify the effects of degradation modes within battery management systems," *Journal of Power Sources*, vol. 360, pp. 301–318, 2017.

[54] Y. Zhang, Q. Tang, Y. Zhang, J. Wang, U. Stimming, and A. A. Lee, "Identifying degradation patterns of lithium ion batteries from impedance spectroscopy using machine learning," *Nature communications*, vol. 11, no. 1, pp. 1–6, 2020.

[55] X. Yuan, H. Wang, J. C. Sun, and J. Zhang, "Ac impedance technique in pem fuel cell diagnosis—a review," *International Journal of Hydrogen Energy*, vol. 32, no. 17, pp. 4365–4380, 2007.

[56] A. Nechache, M. Cassir, and A. Ringuedé, "Solid oxide electrolysis cell analysis by means of electrochemical impedance spectroscopy: A review," *Journal of Power Sources*, vol. 258, pp. 164–181, 2014.

[57] A. R. Bredar, A. L. Chown, A. R. Burton, and B. H. Farnum, "Electrochemical impedance spectroscopy of metal oxide electrodes for energy applications," *ACS Applied Energy Materials*, vol. 3, no. 1, pp. 66–98, 2020.

[58] A. Barai, G. H. Chouchelamane, Y. Guo, A. McGordon, and P. Jennings, "A study on the impact of lithium-ion cell relaxation on electrochemical impedance spectroscopy," *Journal of Power Sources*, vol. 280, pp. 74–80, 2015.

[59] F. M. Kindermann, A. Noel, S. V. Erhard, and A. Jossen, "Long-term equalization effects in li-ion batteries due to local state of charge inhomogeneities and their impact on impedan ce measurements," *Electrochimica Acta*, vol. 185, pp. 107–116, 2015.

[60] U. Westerhoff, T. Kroker, K. Kurbach, and M. Kurrat, "Electrochemical impedance spectroscopy based estimation of the state of charge of lithium-ion batteries," *Journal of Energy Storage*, vol. 8, pp. 244–256, 2016.

[61] R. Isermann and M. Münchhof, *Identification of Dynamic Systems: An Introduction with Applications*, ser. Advanced textbooks in control and signal processing. Springer-Verlag Berlin Heidelberg, 2011, ISBN: 9783540788799.

[62] L. Ljung, *System Identification: Theory for the User*. Wiley Online Library, 1999.

[63] M. Schroeder, "Synthesis of low-peak-factor signals and binary sequences with low autocorrelation (corresp.)," *IEEE Transactions on Information Theory*, vol. 16, no. 1, pp. 85–89, 1970.

[64] "Chapter 2 - measurement of frequency response function - standard solutions," in *System identification: a frequency domain approach*, R. Pintelon and J. Schoukens, Eds., New Jersey: John Wiley & Sons, 2012, pp. 33–73.

[65] S. Moore and P. Barendse, "Online condition monitoring of lithium-ion batteries using impedance spectroscopy," in *2017 IEEE Energy Conversion Congress and Exposition (ECCE)*, IEEE, 2017, pp. 5617–5624.

[66] H. Zappen, F. Ringbeck, and D. U. Sauer, "Application of time-resolved multi-sine impedance spectroscopy for lithium-ion battery characterization," *Batteries*, vol. 4, no. 4, p. 64, 2018.

[67] C. Brunetto, A. Moschetto, and G. Tina, "Pem fuel cell testing by electrochemical impedance spectroscopy," *Electric Power Systems Research*, vol. 79, no. 1, pp. 17–26, 2009.

[68] S. R. Islam, S.-Y. Park, and B. Balasingam, "Circuit parameters extraction algorithm for a lithium-ion battery charging system incorporated with electrochemical impedance spectroscopy," in *2018 IEEE Applied Power Electronics Conference and Exposition (APEC)*, IEEE, 2018, pp. 3353–3358.

[69] R. Suresh, S. Swaminathan, and R. Rengaswamy, "Rapid impedance spectroscopy using dual phase shifted chirp signals for electrochemical applications," *International Journal of Hydrogen Energy*, vol. 45, no. 17, pp. 10 536–10 548, 2020.

[70] S. Mallat, *A Wavelet Tour of Signal Processing: The Sparse Way*, 3rd ed. Elsevier Academic Press, 2008, ISBN: 9780080922027.

[71] P. Boškoski, A. Debenjak, and B. M. Boshkoska, *Fast Electrochemical Impedance Spectroscopy: As a Statistical Condition Monitoring Tool*. Springer, 2017.

[72] M. Stepančič, Đ. Juričić, and P. Boškoski, "Fault detection of fuel cell systems based on statistical assessment of impedance data," *Energy Conversion and Management*, vol. 195, pp. 76–85, 2019, ISSN: 0196-8904. DOI: https://doi.org/10.1016/j.enconman.2019.05.004. [Online]. Available: http://www.sciencedirect.com/science/article/pii/S0196890419305436.

[73] D. Iatsenko, P. V. McClintock, and A. Stefanovska, "Linear and synchrosqueezed time–frequency representations revisited: Overview, standards of use, resolution, reconstruction, concentration, and algorithms," *Digital Signal Processing*, vol. 42, pp. 1–26, 2015, ISSN: 1051-2004.

[74] J. M. Lilly and S. C. Olhede, "Higher-order properties of analytic wavelets," *IEEE Transactions on Signal Processing*, vol. 57, no. 1, pp. 146–160, 2008.

[75] C. Torrence and G. P. Compo, "A practical guide to wavelet analysis," *Bulletin of the American Meteorological Society*, vol. 79, pp. 61–78, 1998.

[76] P. Agarwal, M. E. Orazem, and L. H. Garcia-Rubio, "Application of measurement models to impedance spectroscopy iii. evaluation of consistency with the kramers-kronig relations," *Journal of the Electrochemical Society*, vol. 142, no. 12, pp. 4159–4168, 1995.

[77] H. W. Bode *et al.*, "Network analysis and feedback amplifier design," *van Nostrand New York*, 1945.

[78] W. Ehm, R. Kaus, C.-A. Schillerand, and W. Strunz, "Z-hit – a simple relation between impedance modulus and phase angle. providing a new way to the validation of electrochemical impedance spectra," in *New Trends in Electrochemical Impedance Spectroscopy and Electrochemical Noise Analysis*, F. Mansfeld, F. Huet, and O. Mattos, Eds., 2000-24 vols., Electrochemical Society Inc, 2001, pp. 1–10, ISBN: ISBN 1-56677-291-5. [Online]. Available: http://zahner.de/pdf/zhitehm.pdf.

[79] J. Luo, K. Ying, and J. Bai, "Savitzky–golay smoothing and differentiation filter for even number data," *Signal processing*, vol. 85, no. 7, pp. 1429–1434, 2005.

[80] G. M. Smith, *How to measure current using current sensors and transducers, section zero flux sensors measurement*, Dewesoft, 9.07.2020. [Online]. Available: https://dewesoft.com/daq/how-to-measure-current-using-current-sensors%20(Last%20accessed:%2004.11.2021).

[81] M. Román Lumbreras, G. Velasco Quesada, A. Conesa Roca, and F. Jeréz, "Low consumption flux-gate transducer," *Bodo's Power Systems*, pp. 34–37, 2009.

[82] A. J. Casson, D. C. Yates, S. Patel, and E. Rodriguez-Villegas, "An analogue band-pass filter realisation of the continuous wavelet transform," in *2007 29th Annual International Conference of the IEEE Engineering in Medicine and Biology Society*, IEEE, 2007, pp. 1850–1854.

[83] J. M. Lilly and S. C. Olhede, "On the analytic wavelet transform," *IEEE transactions on information theory*, vol. 56, no. 8, pp. 4135–4156, 2010.

[84] W. Li, Q.-A. Huang, C. Yang, J. Chen, Z. Tang, F. Zhang, A. Li, L. Zhang, and J. Zhang, "A fast measurement of warburg-like impedance spectra with morlet wavelet transform for electrochemical energy devices," *Electrochimica Acta*, vol. 322, p. 134 760, 2019.

[85] D. Iatsenko, *Nonlinear Mode Decomposition*, ser. Springer Theses. Springer International Publishing, 2015.

[86] C. A. Monje, Y. Chen, B. M. Vinagre, D. Xue, and V. Feliu-Batlle, "Fractional-order systems and controls: Fundamentals and applications," in Springer Science & Business Media, 2010, ch. Chapter 13: Numerical Issues and MATLAB Implementations for Fractional-order Control Systems.

[87] P. Boškoski and A. Debenjak, "Optimal selection of proton exchange membrane fuel cell condition monitoring thresholds," *Journal of Power Sources*, vol. 268, pp. 692–699, 2014.

[88] R. J. Baxley, B. T. Walkenhorst, and G. Acosta-Marum, "Complex Gaussian ratio distribution with applications for error rate calculation in fading channels with imperfect CSI," in *IEEE GLOBECOM 2010*, 2010.

[89] G. Nusev, B. Morel, J. Mougin, Đ. Juričić, and P. Boškoski, "Condition monitoring of solid oxide fuel cells by fast electrochemical impedance spectroscopy: A case example of detecting deficiencies in fuel supply," *Journal of Power Sources*, vol. 489, p. 229 491, 2021.

[90] L. Žnidarič, G. Nusev, B. Morel, J. Mougin, Đ. Juričić, and P. Boškoski, "Evaluating uncertainties in electrochemical impedance spectra of solid oxide fuel cells," *Applied Energy*, vol. 298, p. 117 101, 2021.

[91] V. Subotić, B. Königshofer, Đ. Juričić, M. Kusnezoff, H. Schröttner, C. Hochenauer, and P. Boškoski, "Detailed insight into processes of reversible solid oxide cells and stacks using drt analysis," *Energy Conversion and Management*, vol. 226, p. 113 509, 2020.

[92] M. Heinzmann, A. Weber, and E. Ivers-Tiffée, "Advanced impedance study of polymer electrolyte membrane single cells by means of distribution of relaxation times," *Journal of Power Sources*, vol. 402, pp. 24–33, 2018.

[93] B. Königshofer, G. Pongratz, G. Nusev, P. Boškoski, M. Höber, Đ. Juričić, M. Kusnezoff, N. Trofimenko, H. Schröttner, C. Hochenauer, *et al.*, "Development of test protocols for solid oxide electrolysis cells operated under accelerated degradation conditions," *Journal of Power Sources*, vol. 497, p. 229 875, 2021.

[94] M. Orazem and B. Tribollet, *Electrochemical Impedance Spectroscopy*, ser. The ECS Series of Texts and Monographs. Wiley, 2011, ISBN: 9781118209943.

[95] A. Lasia, *Electrochemical Impedance Spectroscopy and its Applications*, ser. SpringerLink : Bücher. Springer New York, 2014, ISBN: 9781461489337.

[96] B. A. Boukamp, "A nonlinear least squares fit procedure for analysis of immittance data of electrochemical systems," *Solid state ionics*, vol. 20, no. 1, pp. 31–44, 1986.

[97] O. Kanoun, U. Tröltzsch, and H.-R. Tränkler, "Benefits of evolutionary strategy in modeling of impedance spectra," *Electrochimica acta*, vol. 51, no. 8-9, pp. 1453–1461, 2006.

[98] P. E. Jacob, S. M. M. Alavi, A. Mahdi, S. J. Payne, and D. A. Howey, "Bayesian inference in non-markovian state-space models with applications to battery fractional-order systems," *IEEE Transactions on Control Systems Technology*, vol. 26, no. 2, pp. 497–506, 2017.

[99] H. Schichlein, A. C. Müller, M. Voigts, A. Krügel, and E. Ivers-Tiffée, "Deconvolution of electrochemical impedance spectra for the identification of electrode reaction mechanisms in solid oxide fuel cells," *Journal of Applied Electrochemistry*, vol. 32, no. 8, pp. 875–882, 2002.

[100] D. Klotz, *Characterization and Modeling of Electrochemical Energy Conversion Systems by Impedance Techniques*. KIT Scientific Publishing, 2014, ISBN: 9783866449039. [Online]. Available: https://books.google.si/books?id=%5C_xsr1LvuMA8C.

[101] R. M. Fuoss and J. G. Kirkwood, "Electrical properties of solids. viii. dipole moments in polyvinyl chloride-diphenyl systems," *Journal of the American Chemical Society*, vol. 63, no. 2, pp. 385–394, 1941.

[102] A. N. Tikhonov, A. Goncharsky, V. Stepanov, and A. G. Yagola, *Numerical methods for the solution of ill-posed problems*. Springer Science & Business Media, 2013, vol. 328.

[103] F. Ciucci and C. Chen, "Analysis of electrochemical impedance spectroscopy data using the distribution of relaxation times: A bayesian and hierarchical bayesian approach," *Electrochimica Acta*, vol. 167, pp. 439–454, 2015.

Bibliography

Publications Related to the Thesis

Journal Articles

[1] G. Nusev, Đ. Juričić, M. Gaberšček, J. Moškon, and P. Boškoski, "Fast impedance measurement of li-ion battery using discrete random binary excitation and wavelet transform," *IEEE access*, vol. vol. 9, str. 46152–46 165, 2021. DOI: 10.1109/ACCESS.2021.3058368.

[2] G. Nusev, B. Morel, J. Mougin, Đ. Juričić, and P. Boškoski, "Condition monitoring of solid oxide fuel cells by fast electrochemical impedance spectroscopy: A case example of detecting deficiencies in fuel supply," *Journal of power sources*, vol. vol. 489, str. 229491-1-229491–10, 2021. DOI: 10.1016/j.jpowsour.2021.229491.

[3] B. Königshofer, P. Boškoski, G. Nusev, M. Koroschetz, M. Hochfellner, M. Schwaiger, Đ. Juričić, C. Hochenauer, and V. Subotić, "Performance assessment and evaluation of soc stacks designed for application in a reversible operated 150 kw rsoc power plant," *Applied energy*, vol. vol. 283, str. 116372-1-116372–18, 2021. DOI: 10.1016/j.apenergy.2020.116372.

[4] L. Žnidarič, G. Nusev, B. Morel, J. Mougin, Đ. Juričić, and P. Boškoski, "Evaluating uncertainties in electrochemical impedance spectra of solid oxide fuel cells," *Applied energy*, vol. vol. 298, str. 117101-1-117101–14, 2021. DOI: 10.1016/j.apenergy.2021.117101.

[5] B. Königshofer, G. Nusev, P. Boškoski, Đ. Juričić, V. Subotić, *et al.*, "Development of test protocols for solid oxide electrolysis cells operated under accelerated degradation conditions," *Journal of power sources*, vol. vol. 497, str. 229875-1-229875–16, 2021. DOI: 10.1016/j.jpowsour.2021.229875.

[6] M. Höber, B. Königshofer, P. Wachter, G. Nusev, P. Boškoski, C. Hochenauer, and V. Subotić, "Holistic approach to design, test, and optimize stand-alone sofc-reformer systems," *Processes*, vol. vol. 9, no. nol. 2, str. 348-1-348–28, 2021. DOI: 10.3390/pr9020348.

Conference Paper

[1] B. Dolenc, G. Nusev, Đ. Juričić, V. Subotić, C. Hochenauer, and P. Boškoski, "Identification of fractional-order models forcondition monitoring of solid-oxide fuel cell-systems," *IFAC papersOnline*, vol. vol. 53, no. no. 2, str. 12014–12 019, 2020. DOI: 10.1016/j.ifacol.2020.12.734.

[2] G. Nusev, P. Boškoski, and G. Dolanc, "Ocenjevanje parametrov ekvivalentnega vezja elektrokemične vodikove črpalke," in *Zbornik enajste konference AIG'19 Avtomatizacija v industriji in gospodarstvu, 9. in 10. april 2019, Maribor, Slovenija*, N. Mušk-inja and B. Tovornik, Eds., Maribor: Društvo avtomatikov Slovenije, 2019, str. 108.

[3] G. Nusev, G. Dolanc, Đ. Juričić, and P. Boškoski, "Detection of membrane drying at electrochemical hydrogen compressors," in *Proceedings of papers: issue 1*, M. Kostev and N. S. Dončov, Eds., Bitola, Niš: Faculty of Technical Sciences, St. Kliment Ohrid-ski University, Faculty of Electronic Enginering, University of Niš, Sofia, 2019, str. 99–102.

[4] G. Nusev, B. Dolenc, V. Subotić, C. Hochenauer, Đ. Juričić, and P. Boškoski, "Eis through time-domain fractional order identification," in *Abstract book*, 2018, str. 36.

[5] G. Nusev, P. Boškoski, M. Bohanec, and B. Mileva Boshkoska, "A dss model for selection of computer on module based on promethee and dex methods," in *Decision Support Systems VIII: sustainable data driven and evidence-based decision support: 4th International Conference, ICDSST 2018 Heraklion, Greece, May 22-25, 2018: proceedings*, F. Dargam, Ed., ser. Lecture notes in business information processing, LNBIP 313, Cham: Springer, 2018, str. 157–168.

[6] G. Nusev, P. Boškoski, and G. Dolanc, "Fractional order system identification method for online monitoring of humidity of electrochemical hydrogen pumps," in *Elecetri-macs 2019 Salerno*, Salerno: Electrimacs, 2019, str. 71.

[7] P. Boškoski, G. Nusev, B. Dolenc, and Đ. Juričić, "Statistical analysis of impedance data," in *Program of the 11th International Symposium on Electrochemical Impedance Spectroscopy, 2 to 7 June 2019, Lège-Cap-Ferret, France*, Lège-Cap-Ferret: [s. n.], 2019, str. 78.

[8] Đ. Juričić, G. Nusev, B. Dolenc, and P. Boškoski, "Baysian estimation of the solid oxide fuel cell model," in *Proceedings of papers: issue 1*, M. Kostev and N. S. Dončov, Eds., Bitola, Niš: Faculty of Technical Sciences, St. Kliment Ohridski University, Faculty of Electronic Enginering, University of Niš, Sofia, 2019, str. 265–268.

[9] B. Dolenc, G. Nusev, V. Subotić, C. Hochenauer, N. Gegring, Đ. Juričić, and P. Boškoski, "Fractional-order model identification for state of health assessment of solid-oxide fuel cells," in *Proceedings of the 10th IFAC Symposium on Fault Detection, Supervision and Safety for Technical Processes SAFEPROCESS 2018, Warsaw, Poland, 29-31 August 2018*, ser. IFAC papersOnline, Vol. 51, no. 24, 2018, vol. vol. 51, New York: International Federation of Automatic Control = IFAC, 2018, str. 849–854. DOI: 10.1016/j.ifacol.2018.09.674.

[10] B. Dolenc, G. Nusev, V. Subotić, N. Gehring, Đ. Juričić, and P. Boškoski, "Sofc characterisation based on an algebraic fractional-order identification approach," in *Proceedings of the 13th European SOFC & SOE Forum 2018, Lucerne, Switzerland: advanced characterisation techniques I+II*, E. Ivers-Tiffée, Ed., [S. l.]: European Fuel Cell Forum AG, 2018, str. 89–97.

[11] B. Dolenc, G. Nusev, T. Kos, P. Boškoski, D. Vrečko, D. Vrančić, and Đ. Juričić, "Novi koncept vodenja sklada trdno-oksidnih gorivnih celic na podlagi stanja naprave = the new concept of the solid-oxide fuel cells stack control based on device status," in *Zbornik desete konference Avtomatizacija v industriji in gospodarstvu, 6. in 7. april 2017, Maribor, Slovenija*, N. Muškinja and B. Tovornik, Eds., Maribor: Društvo avtomatikov Slovenije, 2017, str. 151–158.

[12] B. Dolenc, G. Nusev, P. Boškoski, B. Morel, J. Mougin, and Đ. Juričić, "Probabilistic deconvolution of solid oxide fuel cell impedance spectra," in *Elecetrimacs 2019 Salerno*, Salerno: Electrimacs, 2019, str. 53–54.

[13] Đ. Juričić, P. Boškoski, G. Nusev, M. Nerat, and B. Dolenc, "Sprotni nadzor stanja visokotemperaturnih gorivnih celic," in *Zbornik enajste konference AIG'19 Avtomatizacija v industriji in gospodarstvu, 9. in 10. april 2019, Maribor, Slovenija*, N. Muškinja and B. Tovornik, Eds., Maribor: Društvo avtomatikov Slovenije, 2019, str. 109.

[14] V. Subotić, Đ. Juričić, B. Stoeckl, B. Dolenc, P. Boškoski, M. Preininger, G. Nusev, N. H. Menzler, H. Schroettner, and C. Hochenauer, "Identification of disturbances in sofc operation and prediction of cell degradation," in *Proceedings of the 13th European SOFC & SOE Forum 2018, Lucerne, Switzerland: advanced characterisation techniques I+II*, E. Ivers-Tiffée, Ed., [S. l.]: European Fuel Cell Forum AG, 2018, str. 99.

Other Publications

[1] G. Nusev, P. Boškoski, M. Bohanec, and B. Mileva Boshkoska, "A dss model for selection of computer on module based on promethee and dex methods," in *Decision Support Systems VIII: sustainable data driven and evidence-based decision support: 4th International Conference, ICDSST 2018 Heraklion, Greece, May 22-25, 2018: proceedings*, F. Dargam, Ed., ser. Lecture notes in business information processing, LNBIP 313, Cham: Springer, 2018, str. 157–168.

Biography

Gjorgji Nusev was born on 22nd of March 1990 in Bitola, N. Macedonia. After completing the secondary school, he enrolled at the Faculty of Electrical Engineering, University of Ljubljana, R. Slovenia. In 2012, he participated in the IAESTE student exchange programme at the Department of Electronics, University of York, York, United Kingdom. In 2014, he successfully defended his diploma thesis, titled "Measuring near electric and magnetic fields for electromagnetic compatibility pre-compliance testing".

After two years of working in the industry, in 2016, he enrolled in the doctoral study programme at the Jožef Stefan International Postgraduate School. He was also accepted to the Young Researchers Programme of the Slovenian Research Agency under the supervision of Asst. Prof. Dr. Pavle Boškoski. His research field is signal processing with a focus on developing new techniques for monitoring performances of electrochemical energy conversion devices, such as batteries and fuel cells. During his studies he developed a stand-alone measurement equipment for performing electrochemical impedance spectroscopy using unconventional excitation signals, which has been successfully implemented at the Institute for Thermal Engineering, at TU Graz, Austria, and at the Institute of Atomic Energy and Alternative Energies Commission, CEA, Grenoble, France.

His research work has been presented at dozens of international conferences and published in several international journals. Also during his studies, he was actively involved in various research projects, such as:

INSIGHT - European Union's Horizon 2020 research and innovation programme

MEMPHYS - European Union's Horizon 2020 research and innovation programme

Degradation monitoring and performance optimisation of SOE - bilateral project between research agencies of Slovenia and Austria

RUBY - European Union's Horizon 2020 research and innovation programme

REACTT - European Union's Horizon 2020 research and innovation programme